BRNO UNIVERSITY OF TECHNOLOGY
FACULTY OF INFORMATION TECHNOLOGY
DEPARTMENT OF COMPUTER GRAPHICS AND MULTIMEDIA

MODERN FLIGHT CONTROL SYSTEM DESIGN AND EVALUATION

Ph.D. THESIS

AUTHOR Ing. JAN VLK

SUPERVISOR doc. Ing. PETER CHUDY, Ph.D., MBA

BRNO 2020

PROJECTS PARTICIPATION

Project **7AMB12DE004** "Evolution based control design in aeroservoelastic phenomena" has been supproted by Ministry of Education Youth and Sports.

Projects **TA-01010678** "Smart Autopilot", **TA-03010396** "Integrated Simulation Platform", **TN-01000029/02** "Artificial Intelligence Driven Autonomy" and **TH-04010325** "Flight Training Evaluation Software" have been supported by the Technology Agency of Czech Republic.

Ing. Jan Vlk: *Modern Flight Control System Design and Evaluation*, doctoral thesis Brno, Brno University of Technology, Faculty of Information Technology, 2020.

ABSTRACT

This thesis addresses the research on modern methods in automatic Flight Control System design and evaluation, as seen from the perspective of state-of-the-art and future utilization on Unmanned Aerial Systems. The thesis introduces a Flight Control System design process with a special emphasis on the Model-Based Design approach. An integral part of this process is the creation of the aircraft's mathematical model employed in the flight control laws synthesis and the composition of a simulation framework for the evaluation of the automatic Flight Control System's stability and performance. The core of this thesis is aimed at flight control laws synthesis built around a unique blend of optimal and adaptive control theory. The researched flight control laws originating from the proposed design process were integrated into an experimental digital Flight Control System. The final chapter of the thesis introduces the evaluation of the designed automatic Flight Control System and is divided into three phases. The first phase contains the Robustness Evaluation, which investigates the stability and robustness of the designed control system within the frequency domain. The second phase is the controller's Performance Evaluation employing computer simulations using created mathematical models in the time domain. As for the final phase, the designed Flight Control System is integrated into an experimental aircraft platform, serving as a testbed for future Unmanned Aerial Systems, and subjected to a series of flight tests.

KEYWORDS

Adaptive Control; Aircraft; Equations of Motion; Flight Control System; Flight Parameters; Kalman Filter; Optimal Control; State Estimation; System Linearization; Unmanned Aerial Vehicle.

ABSTRAKT

Tato práce je zaměřena na výzkum moderních metod automatického řízení letu a jejich ověření s ohledem na současný stav poznání a budoucí využití bezpilotních letadlových systémů. Práce představuje proces návrhu automatického systému řízení letu s důrazem na přístupy z oblasti návrhu založeného na modelování (Model-Based Design). Nedílnou součástí tohoto procesu je tvorba matematického modelu letounu, který byl využit k syntéze zákonů řízení a k vytvoření simulačního rámce pro evaluaci stability a kvality regulace automatického systému řízení letu. Jádro této práce se věnuje syntéze zákonů řízení založených na unikátní kombinaci teorie optimálního a adaptivního řízení. Zkoumané zákony řízení byly integrovány do digitálního systému řízení letu, jenž umožňuje vysoce přesné automatické létání. Závěrečná část práce se zabývá ověřením a analýzou navrženého systému řízení letu a je rozdělena do 3 fází. První fáze ověření obsahuje evaluaci robustnosti a analyzuje stabilitu a robustnost navrženého systému řízení letu ve frekvenční oblasti. Druhá fáze, evaluace kvality regulace, probíhala v rámci počítačových simulací s využitím vytvořených matematických modelů v časové oblasti. V poslední fázi ověření došlo k integraci navrženého systému řízení letu do experimentálního letounu, sloužícího jako testovací platforma pro budoucí bezpilotní letadlové systémy a jeho evaluaci v rámci série letových experimentů.

KLÍČOVÁ SLOVA

Adaptivní řízení; bezpilotní letadlo; estimace stavu; Kálmánův filtr; letové parametry; letadlo; linearizace systému; pohybové rovnice; robustní řízení; systém řízení letu.

BIBLIOGRAPHIC CITATION

Ing. Jan Vlk: *Modern Flight Control System Design and Evaluation*, doctoral thesis Brno, Brno University of Technology, Faculty of Information Technology, 2020.

DECLARATION

I declare that this dissertation thesis is my original work and that I have written it under the guidance of Associate Professor Peter Chudy, Ph.D., MBA. All sources and literature that I have used during my work on the thesis are correctly cited with a complete reference to the respective sources.

Brno, 2020

Ing. Jan Vlk, August 31, 2020

ACKNOWLEDGMENTS

Many thanks to my supervisor Peter Chudý, who was being patient and supportive throughout my Ph.D. studies and got me on interesting research projects. I would like to thank my present and former colleagues at the AeroWorks group, especially Milan Prustoměrský, Petr Dittrich and Karol Rydlo. Special thanks to the Evektor flight test department and flight test pilots for providing inevitable support during flight experiments and to VR Group a.s. for supporting the construction of the simulation environment. Finally, I would like to thank my parents who supported me my whole life and most of all I would like to express sincere gratitude to my wife, Michaela, for her understanding and patience during the thesis finalization.

CONTENTS

LIST OF FIGURES

LIST OF TABLES

LIST OF ACRONYMS

AAS Automatic Approach System

ADC Air Data Computer

AGL Above Ground Level

BFF Body-Fixed Frame

C2 Command and Control

CAS Control Augmentation System

CDU Control Display Unit

CG Center of Gravity

COTS Commercial of the Shelf

DE Differential Equation

DNP Digital Navigation Platform

EASA European Aviation Safety Agency

ECI Earth-Centered Inertial

EKF Extended Kalman Filter

EMA Electro-Mechanical Actuator

EOM Equations of Motion

FAA Federal Aviation Administration

FBW Fly-by-Wire

FCC Flight Control Computer

FCS Flight Control System

FMS Flight Management System

GA General Aviation

GNSS Global Navigation Satellite System

GPS Global Positioning System

HOTAS Hands on Throttle and Stick

IAS Indicated Airspeed

ICAO International Civil Aviation Organisation

ILS Instrument Landing System

IMU Inertial Measurement Unit

LQG Linear Quadratic Gaussian

LQR Linear Quadratic Regulator

LSA Light Sport Aircraft

LTI Linear Time Invariant

LTR Loop Transfer Recovery

MBD Model Based Design

MEMS Micro Electro Mechanical System

MIT Massachusetts Institute of Technology

MFD Multifunction Display

MIMO Multi-Input Multi-Output

MRAC Model Reference Adaptive Control

NED North-East-Down

PFD Primary Flight Display

PMU Propulsion Monitoring Unit

RPA Remotely Piloted Aircraft

RPAS Remotely Piloted Aircraft Systems

RPS Remote Pilot Station

SAS Stability Augmentation System

TAS True Airspeed

UAS Unmanned Aerial Systems

UAV Unmanned Aerial Vehicle

UKF Unscented Kalman Filter

WPT WayPoint

WWII World War II

Latin Letters

Symbol	Unit	Description
A	[1]	State-space system matrix
A_{cl}	[1]	Closed loop system state matrix
A_{DS}	[1]	Design system state matrix
A_{IE}	[1]	Integral error model state matrix
A_{PL}	[1]	Plant model state matrix
A_k	[1]	Recursive regression matrix
A_{ref}	[1]	Reference model state matrix
$\vec{a}^I$	[m·s^{-2}]	Absolute inertial acceleration vector
B	[1]	State-space input matrix
B_{IE}	[1]	Integral error model input matrix
B_{PL}	[1]	Plant model input matrix
B_{ref}	[1]	Reference model input matrix
b_w	[m]	Wing span
C	[1]	State-space output matrix
$\bar{c}$	[m]	Mean aerodynamic chord
C_D, C_Y, C_L	[1]	Aerodynamic force coefficients
C_l, C_m, C_n	[1]	Aerodynamic moment coefficients
D	[N]	Drag force
D_{prop}	[m]	Propeller diameter
D_{k+1}	[1]	Discrete system feedforward matrix
E	[1]	Mean value
e	[1]	Error between reference and output
e_{tr}	[1]	Tracking error
$\vec{F}$	[N]	Force vector
$(\vec{F}_P)_B$	[N]	Propulsion force vector notated in Body-Fixed frame
$F_u(s)$, $F_v(s)$, $F_w(s)$	[1]	Forming filters of translational turbulence model
$F_p(s)$, $F_q(s)$, $F_r(s)$	[1]	Forming filters of rotational turbulence model

g	[m·s^{-2}]	Gravitational acceleration
h_G	[m]	Geodetic height
H	[1]	Hamiltonian
H_G	[m]	Geopotential height
H_{k+1}	[1]	Discrete system measurement matrix
$\vec{H}^O(t)$	[kg·m^2·s^{-1}]	Angular momentum vector
$\boldsymbol{I}_{BB}$	[kg·m^2]	Inertia tensor in Body-Fixed frame
J	[1]	Advance ratio
$J(\vec{\theta}_P)$	[1]	Least square estimator criterion
K_{k+1}	[1]	Kalman gain update in online parameter estimation process
K_{LQR}	[1]	Linear Quadratic Regulator gain matrix
L	[N]	Lift force
L_{LQG}	[1]	Kalman gain in LQG controller
L_A^G, M_A^G, N_A^G	[N·m]	Aerodynamic moments acting in the center of gravity
L_u, L_v, L_w	[m]	Turbulence model scale lengths
m	[kg]	Mass
M	[1]	Mach number
$\boldsymbol{M}_{BO}$	[1]	Coordinate transformation matrix from NED frame to BFF
n_{prop}	[s^{-1}]	Propeller revolutions per second
$\vec{p}(t)$	[kg·m·s^{-1}]	Momentum vector
p_N, p_E, p_D	[m]	Position in NED coordinate frame
p, q, r	[rad·s^{-1}]	Angular rates
p_{stat}	[Pa]	Static pressure
P_{lyap}	[1]	Solution of Lyapunov equation
P_{ricc}	[1]	Solution of algebraic Riccati equation
P_{k+1}	[1]	Covariance matrix update in online parameter estimation process
Q	[N]	Crosswind force; Process noise covariance matrix
Q_C, Q_O	[1]	Controllability and observability matrix
q_i	[1]	Quaternion elements $i =, 0 \ldots, 3$
$\bar{q}$	[Pa]	Dynamic pressure
r	[1]	Reference signal

$\vec{r}^{P}$	[1]	Vector of arbitrary point P
R	[1]	Input noise covariance matrix
S	[m²]	Wing area
T	[N;K]	Thrust; Atmospheric temperature
$u(t)$	[1]	Input of dynamic system
u_{ad}	[1]	Adaptive control input
u_{bl}	[1]	Baseline control input
$v(t)$	[1]	Input noise
$V(x)$	[1]	Lyapunov function
$\vec{V}^{T}$	[m·s^{-1}]	Absolute inertial velocity vector
u_K, v_K, w_K	[m·s^{-1}]	Kinematic velocity components in BFF
$(\vec{V}_K)_B$	[m·s^{-1}]	Kinematic velocity vector notated in BFF
$w(t)$	[1]	Process noise
$x(t)$	[1]	Dynamic system state
$\vec{X}$	[1]	Vector of regressors in parameter estimation process
$(X_A^G)_B$, $(Y_A^G)_B$, $(Z_A^G)_B$	[N]	Aerodynamic forces acting in the center of gravity notated in BFF
$y(t)$	[1]	Dynamic system output
$\vec{z}$	[1]	Measurement vector in parameter estimation process

Greek Letters

α	[rad]	Angle of attack
β	[rad]	Angle of sideslip
γ	[rad]	Flight path angle
Γ_{k+1}	[1]	Discrete system noise input matrix
δ_T	[1]	Throttle deflection
δ_e	[rad]	Elevator deflection
δ_a	[rad]	Aileron deflection
δ_r	[rad]	Rudder deflection
ζ_{act}	[1]	Actuator model damping
ζ_{sens}	[1]	Sensor model damping
χ	[rad]	Flight path azimuth
μ	[rad]	Flight path bank angle
μ_G	[rad]	Geodetic latitude
$\vec{v}$	[1]	Vector of equation errors in estimation process

λ	[1]	Forgetting factor in online parameter estimation process
λ_G	[rad]	Geodetic longitude
ϕ	[rad]	Roll angle
ϕ_{k+1}	[1]	Discrete system state transition matrix
θ	[rad]	Pitch angle
$\vec{\theta}_P$	[1]	Parameter vector in estimation process
$\hat{\theta}_P$	[1]	Parameter vector estimate
ψ	[rad]	Heading angle
ψ_{k+1}	[1]	Discrete system input matrix
ρ	[kg·m^3]	Air density
$\sigma^2(\tau)$	[1]	Allan variance
σ_u, σ_v, σ_w	[1]	Turbulence model intensities
ω_{act}	[rad·s^{-1}]	Actuator model natural frequency
ω_{sens}	[rad·s^{-1}]	Sensor model natural frequency
$(\vec{\omega}_K^{OB})_B$	[rad·s^{-1}]	Vector of kinematic angular rates notated in Body-Fixed frame

1

INTRODUCTION

The market segment of Unmanned Aerial Systems (UAS) experienced a remarkable upturn over the period of last decades. The UAS utilization evolved in a response to emerging new advanced technologies and an associated high demand for application flexibility in serving the surveillance, entertainment industry and cargo transport. Various manned aircraft platforms, which were originally designed for sport and recreational flying, could play an important role in the future UAS development, providing accessible and flexible airframes enabling a cost-efficient holistic design and development. A seamless system integration into the air traffic network places strict demands on operational safety, reliability and robustness of UAS. Addressed elements serve as prerequisites for the future design of advanced automatic flight control techniques in this fast evolving segment.

Higher demands on flight endurance and load carrying capacity motivate the conversion of traditionally piloted aircraft to an Unmanned Aerial Vehicle (UAV). However, increased safety requirements have to be considered during such transformation, as well as proper training of UAV operators. Inexperienced UAV operators with limited flight experience can be ill-prepared for solving critical in flight situations related to bad weather conditions, failures or emergencies, which can suddenly evolve into serious accidents. New technologies aimed at enhanced UAV automation and safety improvements are therefore quickly being introduced to the market. However, these rapidly emerging solutions require thorough testing during the design, development and pre-production stages [14, 34].

This thesis introduces the reader to a Model Based Design (MBD) approach in the Flight Control System (FCS) development, harmonized with the state-of-the-art standards, best practices and regulatory requirements. The MBD process usually starts with the aircraft dynamic model development and simulation framework components description. This phase is followed by the control system synthesis and is concluded with system evaluation performed at first within the simulation environment and subsequently during real flight experiments.

1.1 HISTORICAL BACKGROUND

This section will briefly introduce the history of the FCS design from the first gyroscope based devices through more complex systems using the air-data and radio navigation for precision navigation tasks to state-of-the-art digital FCS.

1.1.1 *First Autopilot*

The first attempts to construct an automatic pilot are noted in England at the beginning of the 20^{th} century when Sir Hiram Maxim published a book that contained his aeronautical experiments. The automatic pilot was a gyroscope based stability augmentation system. Orville and Wilbur Wright employed a similar idea in their flight experiments as their Flyer I aircraft appeared to be highly unstable.

The first advanced gyro-based autopilot was invented by Sperry Corporation in 1912. Its functionality was presented by Lawrence Sperry, the son of Elmer Sperry, a famous inventor and founder of Sperry Corporation, during the aviation safety contest held in Paris in 1914. The Sperry's autopilot maintained straight and level flight by controlling the elevator and rudder connected to a gyroscopic heading indicator and attitude indicator via a hydraulic linkage. The ailerons were not connected, as the wing's dihedral provided sufficient roll stability. During the demonstrations, Lawrence Sperry and his french mechanic Emil Cauchin flew several times along the river of Seine while the astonished crowd and contest jury watched them speechlessly. The first fly-over was performed with Sperry's hands off the control stick, while during the following demonstrations both, the mechanic and the pilot, stepped out of the cockpit and stood on the aircraft wings [58].

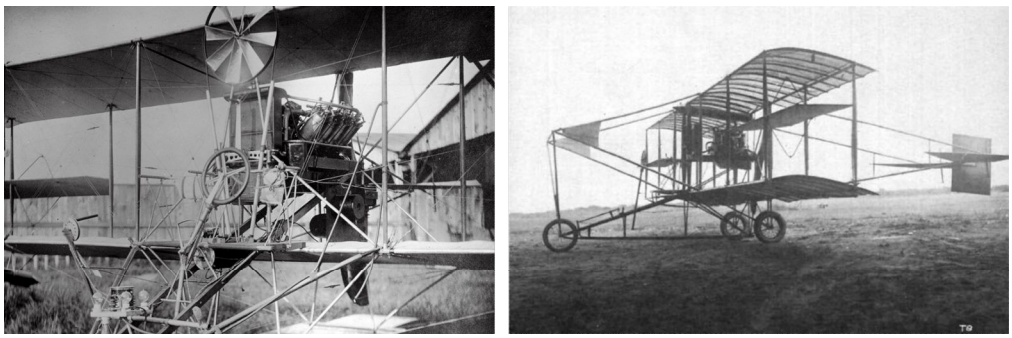

Figure 1.1: Sperry's autopilot on a Curtis biplane. Sources [4, 58]

The main motivation for installing the gyroscopic autopilot into an aircraft was the reduction of pilot workload, as piloting a plane without any automatic control device was a physically exhausting experience. To a certain level of abstraction, the

contemporary autopilot designs, provide physical and mental workload reduction, similar to Sperry's original invention.

1.1.2 *Electro-mechanical Era*

In a response to emergency circumstances, Honeywell developed a more sophisticated electro-mechanical automatic flight control system during the World War II (WWII). This device, designated as the C-1 autopilot, was the most widely used flight automation system onboard the allied WWII bombers, especially the Boeing B-17 and B-29 aircraft. The autopilot was still built around the information originating from 3 gyroscopes, sensing the aircraft attitude in roll, pitch and yaw. The electrical signals from gyroscopes were passed through amplifiers driving the electro-mechanical actuators, which controlled ailerons, elevator and rudder. Using this technology, in combination with the Norden bombsight, improved the precision of high altitude operations. The autopilot became publicly known at the end of the WWII, when it was installed in the B-29 bombers, dropping the atomic bombs on Japan. The C-1's main purpose was to reduce pilot fatigue by automatically flying the airplane in straight-level flight. Figure 1.2 shows the C-1 autopilot's control panel.

Figure 1.2: Honeywell C-1 autopilot control panel. Sources [1, 3]

The C-1 autopilot's success during the WWII led to establishing the Honeywell Aero division, which became responsible for the development and production of a series of avionic systems in the following decades [80].

However, improvements to autopilot's navigation complexity was achieved by another famous name. William P. Lear, an American inventor, businessman, and founder of the Lear Jet company introduced the F-5 autopilot, capable of automatically landing using radio-based navigation. For this invention, Lear was awarded the Collier trophy in 1949 [31].

1.1.3 *Digital autopilots and Fly-by-wire*

The development of first transistors, digital computers, and microprocessors during the 1970's drove the design of more lightweight autopilots capable of complex computational tasks. At the same time, faster, larger and higher-flying jet aircraft started replacing the propeller ones. However, one of the first fully digital control systems was designed for a space application and integrated into the Apollo program's lunar modules. The first generation of jet transport aircraft that employed a digital flight control system included the Boeing 757/767 and Airbus A310, the first airliners equipped with the "glass cockpit" technology. The flight deck of these aircraft became a combination of electronic graphical displays and proven electromechanical instruments. The advances in microprocessor technology delivering higher computational performance stimulated a broad integration of digital Flight Management System (FMS) for solving navigation tasks and as a consequence led to flight crew reduction, making the flight engineer/navigator role obsolete [8].

Figure 1.3: Vought F-8C Crusader equipped with a digital FBW system. Sources [65, 66]

The Fly-by-Wire (FBW) aircraft control concept introduced a major technological leap in aviation. The system replaced the classical mechanical controls with electric signals propagated from the control stick to the flight control computer, which then commands digitally controlled electro-mechanical actuators to drive the aircraft control surfaces. In other words, the pilot is no longer controlling the aircraft control surfaces directly but instead controls the motion of the whole aircraft using a closed-loop FCS. The FBW technology stimulated the utilization of complex digital autopilot designs and enabled safe manual aircraft control over expanded flight envelope. It also enabled an introduction of relaxed longitudinal stability aircraft aimed to achieve higher maneuverability. The first aircraft using a unique digital FBW control system was an experimental F-8C Crusader, which flew with an adopted Apollo digital flight-control computer and an inertial sensing unit. The unique feature of this F-8C aircraft was that it operated completely without mechanical control system backup. Figure 1.3 shows the NASA-operated F-8C Crusader experimental aircraft with a digital FBW system installation. The in-

troduction of a digital FBW control technology into a commercial airliner originated with the Airbus A320. Its typical sidestick, replacing the mechanical steering wheel, became a "signature" element of Airbus aircraft, defining its digital flight control philosophy. Figure 1.4 shows the flight deck of an early Airbus A-320 aircraft with a sidestick control [22].

Figure 1.4: Airbus A-320 with a sidestick. Sources [26, 90]

As stated in the previous subsections, the complexity of automatically controlling an aircraft increased from the first autopilot designs in the 1920's to present-day designs. Before introducing the digital flight control automation, pilots were much closer to direct aircraft control than they are today. The advancement in control automation put a barrier between the pilot and the actual aircraft control surfaces. The advantage of this step surfaced through in-flight pilot workload reduction, which allows her/him to redistribute attention in favor of navigation tasks and changing the pilot role to flight supervisor. However, the drawback of such relief from direct aircraft control opens discussion on reduced situational awareness and declining attention. Figure 1.5 introduces the advancements in flight automation during the 20th century. The growing gap between the pilot and the aircraft can be observed for modern FCS architectures.

1.1.4 *Remotely Piloted Aircraft Systems*

The history of the Remotely Piloted Aircraft Systems (RPAS) started with the first radio-controlled aircraft called Radioplane OQ-2 used by both, the US Army and US Navy during the WWII. These aircraft served mainly as targets for the military pilot training [67]. Unfortunately, the pilotless planes gained a bad reputation for being unreliable and expensive during the post-war era. One of the first RPAS, which helped to alter public opinion, was the RQ-2 Pioneer developed in cooperation between the USA and Israel in the 1980's. With its 5.1 m wingspan and powered by a two-cylinder two-stroke engine, this aircraft was mainly used for reconnaissance and surveillance tasks in military operation during the Persian Gulf, Bosnia, Kosovo and Iraq campaigns. Another step in the RPAS evolution is the

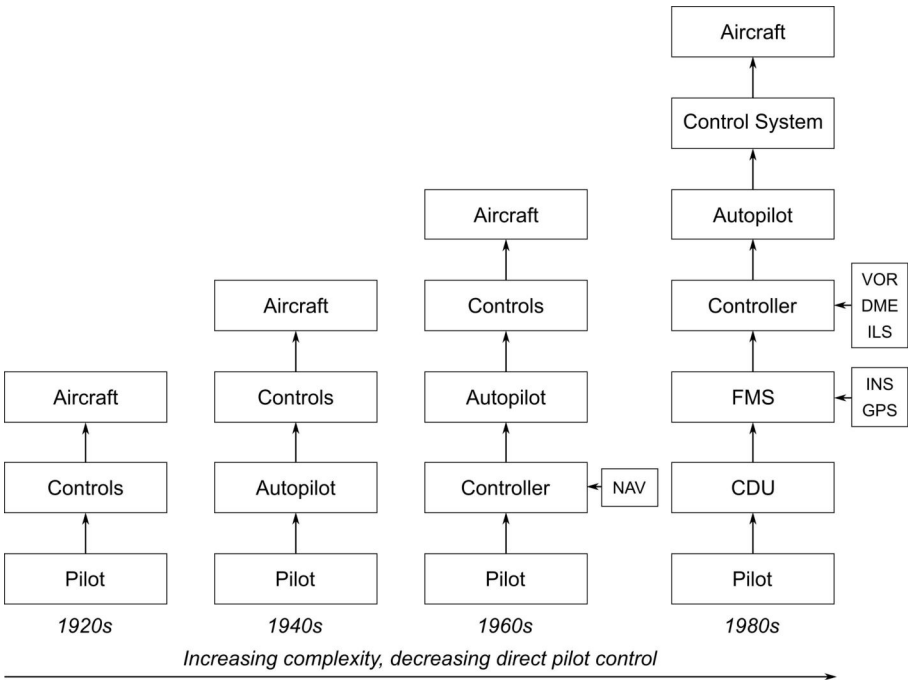

Figure 1.5: Evolution of aircraft control complexity. Source [8]

MQ-1 Predator, originally designed for aerial reconnaissance, but after an upgrade, equipped with AGM-114 Hellfire missiles. The Predator's communication with the ground control station was enabled by a satellite link providing world-wide command and control in real-time capability. Further development in RPAS segment led to the the RQ-4 Global Hawk, which is considered to be one of the largest and the most advanced RPAS. It is a high-altitude long-endurance surveillance aircraft with 40 m wingspan and a maximum speed of 629 km/h. It contains sophisticated sensor systems as synthetic aperture radar, electro-optical and thermographic camera. The Global Hawk can be operated automatically to execute a flight plan or be remotely controlled via a satellite link [2, 21, 88]. For illustration purposes, Figure 1.6 shows another modern RPAS, the MQ-9 Reaper, with its operator station containing various informative displays and the Hands on Throttle and Stick (HOTAS) control set.

Figure 1.6: RPAS operator station and MQ-9 Reaper. Sources [72, 92]

1.2 STATE-OF-THE-ART IN FLIGHT CONTROL SYSTEM DESIGN

State-of-the-art control law designs, applied to large transport aircraft FCS, benefit from employing the classical control theory using linear control techniques for a control law synthesis. The Stability Augmentation System (SAS) or Control Augmentation System (CAS) are usually composed of a cascade of transfer functions and designed by employing linear control techniques. A linear approach to control system synthesis has several advantages over the nonlinear one, e.g., the linear control system synthesis is widely introduced in the literature, along with the apparatus for linear closed-loop system stability determination. Another advantage is in the linear control system design's acceptance by the certification authorities, as the stability of the closed-loop can be determined.

The task of SAS is not to navigate the aircraft to a specific heading or climb to a defined altitude, but to assist the pilot in stabilizing the aircraft's attitude. This system is usually necessary for most high-performance aircraft with intentionally reduced stability. The SAS uses the information from onboard sensors, usually from rate gyroscopes and accelerometers, to produce negative feedback to damp out the oscillatory aircraft motion. A good practice in FCS engineering is to design the longitudinal and lateral-directional SAS separately, as the associated longitudinal and lateral-directional modes can be decoupled for most of the flight phases. Basic types of SAS are the pitch, roll, and yaw dampers that utilize the angular rate measurements to stabilize the aircraft motion. Figure 1.7 shows a block diagram of an angular rate SAS.

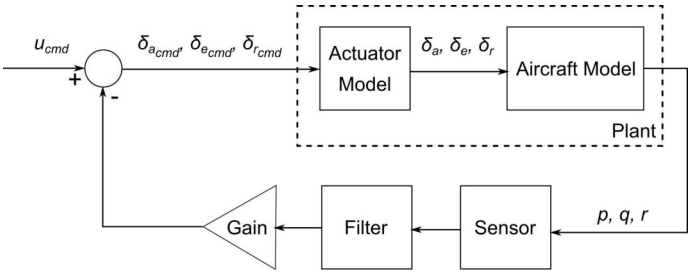

Figure 1.7: Stability Augmentation System.

A CAS is usually employed when high precision command tracking is required. Tasks executed by high-performance aircraft, as maneuvering to its physical limits, require precise control of selected variables, namely the acceleration or angular rates. When compared to SAS, which "only" improves the aircraft handling qualities, the CAS enables the pilot to perform various tasks dependent on precise command tracking, for example, high load factor maneuvering, flight path tracking during an approach and landing, or maneuvering during precise targeting. Basic variables employed in the design of respective CAS are the pitch-rate, normal and lateral

accelerations. Figure 1.8 depicts a block diagram of acceleration CAS which also contains the pitch rate stability augmentation introduced in Figure 1.7 and a PI-controller for reference acceleration tracking.

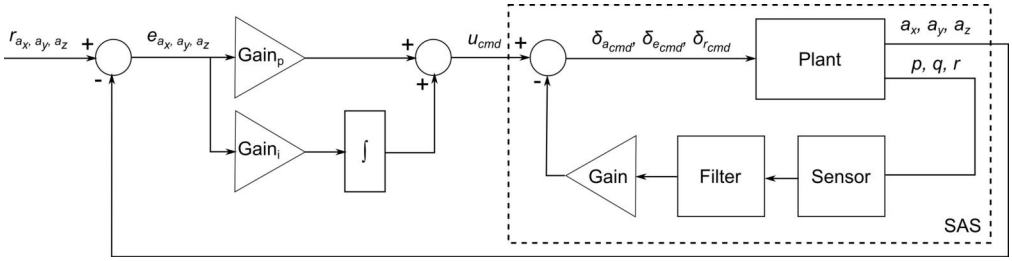

Figure 1.8: Control Augmentation System.

In most cases, the FCS system serves navigation purposes as maintaining commanded altitude, heading, Mach number or airspeed. Other modes may involve an automatic control of specified climb rate or aircraft attitude. All these modes enable pilot overload reduction during the flight. Concerning the mentioned features, the FCS design must comply with legislation specific time domain evaluation criteria, namely the steady-state error, rising time and overshoot during transient motion. The FCS design shall consider respective transient effects during the FCS engage and disengage phases. The best practice is to initiate commanded variables with current values to avoid unwanted and, in some cases, unsafe oscillations, originating from a large difference between commanded and current measured value. Figure 1.9 shows a block diagram of an altitude-hold FCS. It contains feedback loops of pitch rate stability augmentation, pitch angle hold, and above that, an altitude hold loop containing the controller G_C, in a transfer function form [87].

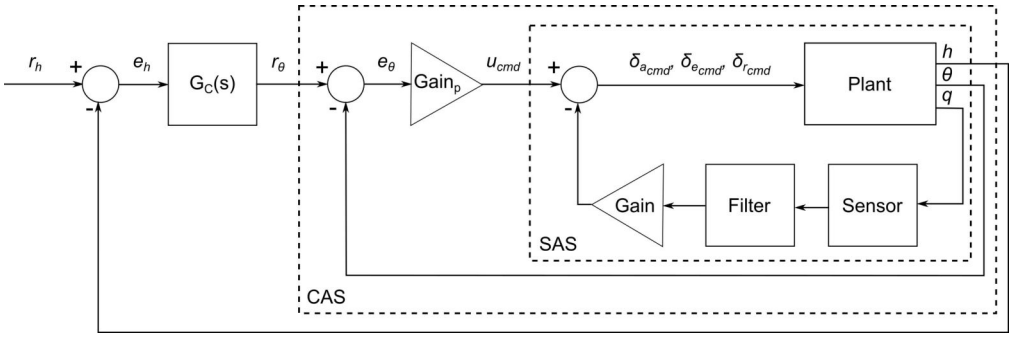

Figure 1.9: Altitude-hold mode.

One of the classical control approach limitations is that a control system's complexity rises with an increasing number of loops (angular rates, attitude, navigation, etc.) and the number of inputs/outputs (measured states and control commands). This limitation can be resolved by employing modern control design techniques that consider the aircraft model in a state-space representation and assesses the FCS for all of its inputs and outputs at once by solving one matrix equation.

This unifying approach augments the difference in classical control design, which resolves every single loop separately.

Boeing researchers Wise and Lavretsky successfully employed a modern control design technique known as Linear Quadratic Regulator (LQR). The LQR is a Multi-Input Multi-Output (MIMO) linear control approach that relies on the controlled plant in state-space representation. The LQR is according to [57] one of the most widely used control algorithms. It is a state feedback control technique with excellent robustness characteristics in gain and phase margins and outstanding regulation performance. It is successful in minimizing control usage and has a convenient implementation. This technique solves problems of regulation, but it can easily be extended to command tracking system by adding an integral term. However, this method has some drawbacks as well. For the stability margins to be guaranteed, all states have to be observable. The LQR lacks the noise attenuation capabilities, thus the best practice dictates to use a noise-canceling filter to cancel out the sensor noise. Another drawback of the LQR method is the fact that it requires tuning of weighting matrices. These matrices are necessary for feedback gain calculations. Since the LQR can be used as a baseline control technique for the FCS design, it will be described in detail in following chapters.

A common practice in the FCS integration process is to manually tune the FCS parameters. This practice consumes time and imposes additional costs. On the other hand, the approach introduced in this thesis is focused on Model-Based Design. It utilizes high fidelity aircraft dynamics model for analytic computation of controller settings.

1.3 GOALS AND CONTRIBUTION OF THE THESIS

This work's main contribution can be seen in the complexity and completeness of the FCS design process. It begins with the composition and analysis of a Light Sport Aircraft (LSA) mathematical model, which is later employed in the FCS design. The aircraft model will be used in the simulation framework core that serves the FCS evaluation. The process will continue by investigating various control system methods, their implementation on the target hardware platform and evaluation of their stability, robustness characteristics and performance during computer simulations. Availability permitting, the testing can be optionally augmented by utilization of high fidelity 6 DoF full flight simulator. The whole design process is finalized with the integration of a complete FCS into an experimental aircraft and an execution of flight tests. Figure 1.10 shows the experimental LSA, which will be used as a testing platform for the designed FCS.

Figure 1.10: Testing platform for Flight Control System design.

1.3.0.1 *High Fidelity 6 DoF Nonlinear Aircraft Model*

One of the most critical elements of a model-based FCS design is the composition of a controlled plant's high fidelity dynamics model. High fidelity mathematical representation of a real aircraft has to account for its various subsystems as the aerodynamics, mass and inertia model, sensor and actuator models, etc. to build a reliable framework for the FCS design. Model validation will be performed by comparing the model outputs to measurements collected during flight experiments. Flight measurement data collection and its processing using modern system identification techniques contributes to the high fidelity design process.

1.3.0.2 *Investigation of Modern Flight Control Methods*

Since an experimental LSA has been selected as a testing platform for the FCS implementation, the focus is aimed at linear state feedback or output feedback classes of control methods that can be augmented by the adaptation loop. The relatively limited flight envelope of an experimental LSA, defined by its applicable range of velocities and altitudes, enables a linear baseline controller design. As one of the design requirements is the overall robustness of the control system, the LQR technique will be explored. Model uncertainties will be canceled using adaptive augmentation of the baseline controller using Model Reference Adaptive Control (MRAC) method with its implementation tailored for the LSA dynamic model.

1.3.0.3 *Practical Evaluation of the Designed Flight Control System*

The FCS design process will be finalized with the flight experiment proving suitability of the researched design approach. The in-flight testing provides full evaluation potential compared to computer simulation, and underlines the relevancy of the whole design process. The experience to be gained during the flight test leads to an indisputable improvement potential for the whole FCS design process. The evaluation procedure will be composed of a series of automatic flight tasks, e.g., coordination in turns, maintaining aircraft attitude in steady level flight or optional

heading and altitude changes. The evaluation framework will be inspired by the SAE-AS94900 standard Flight Control Systems - Design, Installation, and Test of Piloted Military Aircraft. Using this standard augments the relevancy of the FCS design.

1.3.0.4 *Automatic Approach System for Light Sport Aircraft*

The Automatic Approach System (AAS), as a component of the Automatic Landing System, can be found onboard large transport aircraft. This technology requires both the aircraft and the airport to be equipped with sophisticated and expensive radio-navigation equipment, Instrument Landing System (ILS), which provides the aircraft with information about its precise position relative to the airport runway. The AAS will utilize a combination of smart affordable technologies as Inertial Measurement Unit (IMU), Global Navigation Satellite System (GNSS), and Air Data Measurement unit. The AAS can therefore play an essential role in the segment of safety features at airports not equipped with ILS. Concerning the above mentioned statement, a successful implementation of an AAS designed without radio navigation technologies can be seen as one of the main contributions of this thesis.

1.3.0.5 *Research Goals*

The thesis itself focuses on the research of modern control theory methods, their application in unmanned aviation, stability and performance evaluation during the computer simulations and flight experiments. The following list summarizes the main research goals of the thesis.

- Research and implement a high fidelity 6 DoF nonlinear model of a LSA for the FCS design and evaluation.
- Research and implement suitable aircraft control techniques.
- Evaluate researched control approaches using a high fidelity FCS design framework.
- Integrate the researched FCS control laws into an experimental digital control system onboard a LSA and perform series of practical flight test evaluations.

1.4 OUTLINE OF THE THESIS

The introductory part of this thesis, summarizing historical development of automatic flight control systems, is followed by Chapter 2 dedicated to Flight Dynamics theory, which starts with introducing the 6 DoF nonlinear aircraft model, introduces all aspects of the aircraft motion accounting for respective forces and

moments acting on the aircraft and its position changes. The aircraft motion itself is described by a set of first order differential equations called Equations of Motion (EOM). The chapter continues with the description of the linearization process, which leads to state-space representation of linear models. The linear models are used in the subsequent FCS design process steps. The general linearization algorithm is followed by forming respective linear state-space models that describe the longitudinal and lateral-directional motion of modeled aircraft.

The thesis continues with Chapter 3 that describes components for building an aircraft simulation model. The chapter starts with a description of the mass and inertia models and the definition of the gravity model. The subsequent sections introduce the aircraft propulsion system virtualization, composed of a piston engine model supplemented with propeller characteristics and models of sensor and actuator dynamics. The chapter continues with a mathematical description of the surrounding atmosphere, which contains details on continuous turbulence models further utilized within the simulation framework. The turbulence models use Dryden spectral representation taken form MIL-HDBK-1797 [23]. The subsequent section describes abstraction of aerodynamic forces and moments. The chapter is concluded with a description of the Plant model, which is a combination of the aircraft dynamics model with models of sensors and actuators.

Chapter 4 introduces the parameter estimation process employed to improve the aircraft dynamics model fidelity. The chapter describes in detail state estimation techniques, as Kalman Filter, and introduces the Equation-Error method used for aerodynamic parameter estimation. It is concluded with the results of aerodynamic parameter estimation.

Chapter 5 describes the design of the control system itself. This chapter starts with a description of the baseline controller design, which contains a LQR tailored for command tracking purposes. Furthermore, it includes a description of the Linear Quadratic Gaussian (LQG) method, which is a Kalman Filter containing extension of LQR. The Kalman Filter serves as a state estimator for the case when not all states are observable. The adaptive augmentation of the baseline controller called MRAC, which utilizes the Lyapunov stability theory of dynamic systems, is introduced as a next component of Chapter 5 and is responsible for canceling out the matched model uncertainties that may influence aircraft dynamics.

Chapter 6 describes the digital FCS implementation process. The first sections describe the implementation of the researched control laws. The chapter is concluded with the code generation process description.

The performance of the researched FCS is evaluated in Chapter 7. The first part summarizes computer simulations results and employs robustness and performance evaluation tools in frequency and time domains. The following sections

present results of flight experiments. They describe the results of the designed FCS testing during aerial navigation when the test pilot performed heading command and altitude or airspeed select tasks. The SAE-AS94900 inspired evaluation of the FCS is introduced in this chapter. The last section of this chapter introduces an AAS results through measurements of aircraft state and control actions during a test flown automatic approach procedure. The final chapter summarizes the thesis and suggests directions for future research.

2

FLIGHT DYNAMICS

This chapter introduces the description of aircraft motion through a set of first order nonlinear differential equation known as EOM. These equations define the translational and rotational velocities, derived using second Newton's law. The set also contains kinematic and navigation differential equations describing aircraft attitude, respectively, its position. The following parts describe simplifications made to the nonlinear model. This simplification process is known as linearization. Linear models in state-space representation are prerequisites to FCS design techniques investigated in this thesis for the flight control design tasks.

The mathematical notation used in this thesis is based on following standards [45, 46, 47].

2.1 SECOND NEWTON'S LAW

A mathematical description of aircraft motion is a nontrivial complex assignment. For its simplification, the dynamic model's structure considered in this thesis will evolve from rigid body point mass approximation in inertial Newtonian space. Despite its complexity, the dynamic modeling of an aircraft will start from the basic laws of physics, utilizing the Newton's second law [68]. As a first step, we will define the position of an arbitrary point P in a 3-dimensional inertial frame and assign it vector designation r^P. Figure 2.1 introduces the position of point P with respect to both Inertial and Earth-Centered Inertial (ECI) frames defined using $\vec{r}^P$, $\vec{r}^R$, $\vec{r}^{RP}$ vectors.

$$\vec{r}^P = [x, y, z] \tag{2.1}$$

The absolute (inertial) velocity of an arbitrary point P relative to the ECI frame equals

$$\begin{aligned} \vec{V}^I &= \left(\frac{d}{dt}\right)^I \vec{r}^P = (\dot{\vec{r}}^P)^I = (\vec{V}^P)^I = (\dot{\vec{r}}^R)^I + (\dot{\vec{r}}^{RP})^I \\ &= (\dot{\vec{r}}^R)^E + (\vec{\omega}^{IE}) \times (\vec{r}^R) + (\dot{\vec{r}}^{RP})^B + (\vec{\omega}^{IB}) \times (\vec{r}^{RP}), \end{aligned} \tag{2.2}$$

where $\left(\frac{d}{dt}\right)^I$ expresses the derivative in Inertial frame I. Variables $\vec{\omega}^{IE}$ and $\vec{\omega}^{IB}$ define Earth and body rotation with respect to the Inertial frame I. The absolute (inertial) acceleration of an arbitrary point P relative to ECI frame is expressed by equation 2.3 [87].

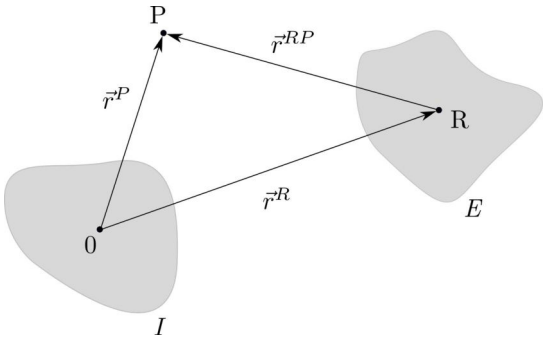

Figure 2.1: Position of an arbitrary point P with respect to Inertial (I) and ECI (E) frames. Source [87]

$$\begin{aligned}\vec{a}^{II} &= \left(\frac{d}{dt}\right)^{I}(\vec{V}^{P})^{I} \\ &= (\dot{\vec{V}}^{R})^{EB} + (\omega\vec{}^{EB}) \times (\vec{V}^{R})^{E} + 2(\vec{\omega}^{IE}) \times \left[(\vec{\omega}^{IE}) \times (\vec{r}^{R})\right] \\ &+ (\dot{\vec{\omega}}^{IB})^{B} \times (\vec{r}^{RP}) + (\vec{\omega}^{IB}) \times \left[(\vec{\omega}^{IB}) \times (\vec{r}^{RP})\right] \end{aligned} \tag{2.3}$$

The momentum change of a body in an inertial (unaccelerated) reference system is equal to the sum of the forces acting on the body, as expressed by equations 2.4 and 2.5.

$$\vec{p}(t) = \int_m \vec{V}^{I}(\vec{x}^{P}, t)\,dm \tag{2.4}$$

$$\begin{aligned}\sum \vec{F} &= \left(\frac{d}{dt}\right)^{I}\vec{p} \\ &= \left(\frac{d}{dt}\right)^{I}\int_m \vec{V}^{I}(\vec{x}^{P}, t)\,dm \end{aligned} \tag{2.5}$$

For the purpose of this abstraction, we are assuming the quasi steady mass defined by equation 2.6 and the rigid body assumption defined by equation 2.7.

$$\frac{dm}{dt} = 0 \tag{2.6}$$

$$\left(\frac{d}{dt}\right)^{B}(\vec{r}^{RP}) = 0 \tag{2.7}$$

The translational rigid body equations of motion with respect to the round rotating Earth can be described by equation

$$\begin{aligned}(\dot{\vec{V}})_{B}^{EB} = &\frac{\overbrace{\sum(\vec{F}^{G})_{B}}^{\text{External forces}}}{m} - \left[M_{BO}\left(\overbrace{(\vec{\omega}_{K}^{EO})_{O}}^{\text{Transport rate}} + \overbrace{(\vec{\omega}_{K}^{OB})_{B}}^{\text{Aircraft rotation}}\right)\right] \times (\vec{V}_{K}^{G})_{B}^{E} \\ &- \left\{M_{BO}\left[\underbrace{2(\omega\vec{}_{K}^{IE})_{O} \times (\vec{V}_{K}^{G})_{0}^{E}}_{\text{Coriolis acceleration}} + \underbrace{(\vec{\omega}_{K}^{IE})_{O} \times (\vec{\omega}_{K}^{IE})_{O} \times (\vec{r}^{G})_{O}}_{\text{Centrifugal acceleration}}\right]\right\}\end{aligned} \tag{2.8}$$

The term External forces describes the sum of all forces acting on the rigid body. The Transport rate term is the rotation caused by the round Earth surface. Aircraft rotation expresses the rotational motion of the rigid body caused by the moments acting on the rigid body. The Coriolis and Centrifugal acceleration terms are caused by the Earth's rotation.

Newton's second law of motion is also used to describe the rigid body angular momentum. The temporal change of angular momentum is equal to the sum of all external moments referenced to the center of the Earth.

$$\vec{H}^{O}(t) = \int_{m} \vec{r}^{P}(t) \times (\vec{V}^{P})^{I}(t) dm \tag{2.9}$$

$$\left(\frac{d}{dt}\right)^{I} \vec{H}^{O}(t) = \sum (\vec{M}^{O}) \tag{2.10}$$

Based on the assumed quasi-steady mass and rigid body properties introduced in equations 2.6 and 2.7 respectively, and by supplementing the assumption on quasi-steady mass distribution expressed by equation 2.11

$$\left(\frac{d}{dt}\right)^{B} I^{R} = 0, \tag{2.11}$$

it is possible to describe the rotational motion of a rigid body by employing equation 2.12 with respect to the round rotating Earth

$$(\dot{\vec{\omega}}_K^{IB})_B^B = (\boldsymbol{I}^G)_{BB}^{-1} \left[\overbrace{\sum (\vec{\boldsymbol{M}}^G)_B}^{\text{External moments}} \quad \overbrace{-(\vec{\omega}_K^{IB})_B \times (\boldsymbol{I}^G)_{BB} (\vec{\omega}_K^{IB})_B}^{\text{Inertia cross coupling}} \right] \tag{2.12}$$

Equations 2.8 and 2.12 describe the translational and rotational motion of any arbitrary point that behaves like a rigid body. Their derivation was taken from [39]. The rigid body nonlinear equations of motion, applicable to a flight simulation problem, will be expressed using the above-defined differential equations. To complete the description, we will add equations describing the attitude in Euler angles or quaternions and the position equations in the WGS-84 frame or North-East-Down (NED) frame [39].

2.2 NONLINEAR EQUATIONS OF MOTION

Before the rigid body nonlinear equations of motion for an aircraft will be defined, we will summarize the assumptions made during the modeling process in the following list [51, 86]:

- Reference point is in the Center of Gravity (CG).
- Rigid body aircraft $\left(\frac{d}{dt}\right)^B (\vec{r}^{RP}) = (\dot{\vec{r}}^{RP})^B$.
- Non-rotating Earth $(\vec{\omega}_K^{IE}) = \vec{0}$.
- Flat Earth $(\vec{\omega}_K^{EO}) = \vec{0}$.
- Quasi-steady mass $\dot{m} = \frac{dm}{dt} \approx 0$.
- Quasi-steady mass distribution $\left(\frac{d}{dt}\right)^B I^R = 0$.

Some of these assumptions will contribute to the simplification of equations 2.8 and 2.12. The previously stated assumptions are valid, as we are addressing a LSA with a fairly limited flight envelope whose dynamics is rather slow as it usually flies at subsonic speeds and small angles of attack. In another case, if for example, the high-performance fighter aircraft would be described, it would be necessary to consider the effects of rotating spherical Earth, variable aircraft mass, and the equations of motion would become much complex. The extensive description of translational and rotational equations of motion can be found in [10, 27, 85, 75].

The translational motion is influenced by different types of forces acting on the aircraft, namely the aerodynamic forces originating from the airflow over the airframe, gravitational forces caused by Earth's gravity and propulsion forces due to aircraft propulsion system.

The linear momentum time variation is equal to the sum of all external forces acting on the rigid aircraft, as introduced in equation (2.13).

$$\frac{d\vec{p}}{dt} = \sum \vec{F} = \frac{d}{dt} \int \dot{\vec{r}}^P(t) \cdot \rho(t) \cdot dV \tag{2.13}$$

The following equation represents a vector in the Body-Fixed Frame (BFF), rotating at an angular rate ω:

$$\left(\frac{d(\cdot)}{dt}\right)_I = \left(\frac{d(\cdot)}{dt}\right)_B + \vec{\omega} \times (\cdot), \tag{2.14}$$

where subscripts I and B refer to the Inertial and the BFF, respectively. Equations 2.15-2.18 show the translational equations of motion in a vector format in the BFF.

$$(\dot{\vec{V}}_K)_B = \frac{1}{m} \cdot (\vec{F}_T^G)_B - (\vec{\omega}_K)_B \times (\vec{V}_K)_B, \tag{2.15}$$

where the variable $(\vec{F}_T^G)_B$ describes the vector of total (T) forces acting in the aircraft CG (G) notated in the BFF (B) that can be described by the sum of gravitational, aerodynamic and propulsion forces

$$(\vec{F}_T^G)_B = \sum (\vec{F}^G)_B = (\vec{F}_G^G)_B + (\vec{F}_A^G)_B + (\vec{F}_P^G)_B, \tag{2.16}$$

and the variable $(\vec{V}_K)_B$ is the vector of aircraft kinematic velocities (K) expressed in the BFF

$$(\vec{V}_K)_B = [u_K, v_K, w_K]^T \tag{2.17}$$

The description of the translational motion of an aircraft in BFF coordinate frame is introduced in equation 2.18.

$$\begin{bmatrix} \dot{u}_K \\ \dot{v}_K \\ \dot{w}_K \end{bmatrix}_B = \frac{1}{m} \begin{bmatrix} X_A^G + X_P^G + X_G^G \\ Y_A^G + Y_P^G + Y_G^G \\ Z_A^G + Z_P^G + Z_G^G \end{bmatrix}_B - \begin{bmatrix} p \\ q \\ r \end{bmatrix}_B \times \begin{bmatrix} u_K \\ v_K \\ w_K \end{bmatrix}_B \tag{2.18}$$

Equivalently, the translational motion of the aircraft can be described using following parameters, true airspeed V, angle of attack α and angle of sideslip β

$$\dot{V} = -\frac{D}{m} + \frac{(X_P)_B \cos(\alpha)\cos(\beta)}{m} - g\sin(\gamma) \tag{2.19}$$

$$\dot{\alpha} = -\frac{L}{mV\cos(\beta)} + \frac{-(X_P)_B \sin(\alpha)}{mV\cos(\beta)} + \frac{g}{V\cos(\beta)}\cos(\mu)\cos(\gamma) + [q - \tan(\beta)(p\cos(\alpha) + r\sin(\alpha))] \tag{2.20}$$

$$\dot{\beta} = \frac{Q}{mV} + \frac{-(X_P)_B \cos(\alpha)\sin(\beta)}{mV} + \frac{g}{V}\cos(\gamma)\sin(\mu), \tag{2.21}$$

where variables D, L, and Q are the aerodynamic drag, lift and crosswind force and variables γ and μ are the flight path and bank angle, respectively. The resulting rotational motion is generated by the aerodynamic, inertial and propulsion moments acting on the aircraft.

The derivation of the rotational rigid-body equations of motion is also based on Newton's second law. Let $\vec{H}$ be an angular momentum, then the angular momentum time derivation equals the sum of all external moments acting on the body.

$$\frac{d\vec{H}}{dt} = \sum \vec{M} = \frac{d}{dt}(\vec{r}^P(t) \times \vec{V}^P(t) \cdot m) \tag{2.22}$$

As the angular momentum is simply given by the equation 2.23.

$$\vec{H} = \boldsymbol{I} \cdot \vec{\omega} \tag{2.23}$$

Variable $\boldsymbol{I}$ defines the inertia tensor and $\vec{\omega}$ is the angular rate vector.

$$\vec{\omega} = [p, q, r]^T \tag{2.24}$$

The vector differential that defines the time variation of angular rates was already expressed in equation 2.12, where $\sum(\vec{M}^G)_B$ is the sum of moments acting in the aircraft's CG and matrix $\boldsymbol{I}_{BB}$ is the aircraft inertia tensor defined by equation (2.25).

$$I_{BB} = \begin{bmatrix} I_{XX} & -I_{XY} & -I_{XZ} \\ -I_{XY} & I_{YY} & -I_{YZ} \\ -I_{XZ} & -I_{YZ} & I_{ZZ} \end{bmatrix} \tag{2.25}$$

A detailed form of the momentum equation is shown in equation 2.26, where the moment vector is expressed as the sum of aerodynamic a propulsion part. Since the reference point is assumed to be at the CG, the gravitational force does not contribute to the creation of additional moments around the CG.

$$\begin{bmatrix} \dot{p} \\ \dot{q} \\ \dot{r} \end{bmatrix}_B = I_{BB}^{-1} \begin{bmatrix} L_A^G + L_P^G \\ M_A^G + M_P^G \\ N_A^G + N_P^G \end{bmatrix}_B - \begin{bmatrix} p \\ q \\ r \end{bmatrix}_B \times I_{BB} \begin{bmatrix} p \\ q \\ r \end{bmatrix}_B \tag{2.26}$$

The vector $\begin{bmatrix} L_A^G & M_A^G & N_A^G \end{bmatrix}^T$ represents aerodynamic moments and vector $\begin{bmatrix} L_P^G & M_P^G & N_P^G \end{bmatrix}^T$ defines the propulsion moments acting around the aircraft's CG. The equation 2.26 can be rewritten in a derived form as

$$\begin{aligned} \dot{p} &= \frac{1}{\Delta}\left[I_{zz}L_A^G + I_{xz}N_A^G\right] \\ &+ \frac{1}{\Delta}\left[I_{xz}(I_{xx} - I_{yy} + I_{zz})pq - (I_{zz}^2 - I_{zz}I_{yy} + I_{xz}^2)qr\right] && (2.27) \\ \dot{q} &= \frac{1}{I_{yy}}M_A^G + \frac{1}{I_{yy}}\left[I_{xz}(r^2 - p^2) - (I_{xx} - I_{zz})pr\right] && (2.28) \\ \dot{r} &= \frac{1}{\Delta}\left[I_{xz}L_A^G + I_{xx}N_A^G\right] \\ &+ \frac{1}{\Delta}\left[(I_{xz}^2 - I_{xx}I_{yy} + I_{xx}^2)pq - I_{xz}(I_{xx} - I_{yy} + I_{zz})qr\right], && (2.29) \end{aligned}$$

where the variable Δ is defined by equation 2.30

$$\Delta = I_{xx} - I_{zz} - I_{xz}^2 \tag{2.30}$$

The aircraft's attitude in flight is defined using quaternions. This technique has a major advantage over the standard Euler angles stemming from avoiding the manipulation of singularities arising from the aircraft pitch angle reaching the value of $\pm\frac{\pi}{2}$. The attitude differential equations are shown in equation 2.31.

$$\begin{bmatrix} \dot{q}_0 \\ \dot{q}_1 \\ \dot{q}_2 \\ \dot{q}_3 \end{bmatrix} = \frac{1}{2}\begin{bmatrix} 0 & -p & -q & -r \\ p & 0 & r & -q \\ q & -r & 0 & p \\ r & q & -p & 0 \end{bmatrix} - \begin{bmatrix} q_0 \\ q_1 \\ q_2 \\ q_3 \end{bmatrix} \tag{2.31}$$

A mandatory condition the quaternions must fulfill is its unit normalization introduced in equation 2.32.

$$q_0^2 + q_1^2 + q_2^2 + q_3^2 = 1 \tag{2.32}$$

The following functions were employed for the transformation of the quaternions to standard Euler angles that describe the aircraft attitude with respect to the NED frame.

$$\begin{bmatrix} \phi \\ \theta \\ \psi \end{bmatrix} = \begin{bmatrix} \tan^{-1}(2\frac{q_1 q_2 + q_0 q_3}{q_0^2 + q_1^2 - q_2^2 - q_3^2}) \\ \sin^{-1}(-2[q_1 q_3 - q_0 q_2]) \\ \tan^{-1}(2\frac{q_2 q_3 + q_0 q_1}{q_0^2 - q_1^2 - q_2^2 + q_3^2}) \end{bmatrix} \tag{2.33}$$

The definition of the aircraft attitude using Euler angles is still essential, especially for its readability to humans. For the sake of completeness, we introduce the Euler angles differential equation below.

$$\begin{bmatrix} \dot{\phi} \\ \dot{\theta} \\ \dot{\psi} \end{bmatrix} = \begin{bmatrix} 1 & \sin(\phi)\tan(\theta) & \cos(\phi)\tan(\theta) \\ 0 & \cos(\phi) & -\sin(\phi) \\ 0 & \frac{\sin(\phi)}{\cos(\theta)} & \frac{\cos(\phi)}{\cos(\theta)} \end{bmatrix} \begin{bmatrix} p \\ q \\ r \end{bmatrix} \tag{2.34}$$

The aircraft position can be defined in different frames, the most used ones are the NED frame, that has cartesian coordinates and expresses aircraft position with respect to selected reference point and the spherical WGS-84 frame and describes aircraft position using geodetic latitude, longitude and height. The position equations using NED frame are introduced in 2.35. The translational velocities from equation 2.18 are transformed from BFF to NED frame.

$$\begin{bmatrix} \dot{p}_N \\ \dot{p}_E \\ \dot{p}_D \end{bmatrix}_O = \begin{bmatrix} V_N \\ V_E \\ V_D \end{bmatrix}_O = M_{OB} \begin{bmatrix} u_K \\ v_K \\ w_K \end{bmatrix}_B = V \begin{bmatrix} \cos(\chi)\cos(\gamma) \\ \sin(\chi)\cos(\gamma) \\ -\sin(\gamma) \end{bmatrix} \tag{2.35}$$

M_{OB} is a 3×3 transformation matrix defining the relationship between the NED frame and the BFF using Euler angles and trigonometric functions described in the Appendix A. Another type of position differential equation can be described by airspeed V, the flight path angle γ, and flight path azimuth χ often called track. Position in NED frame is defined by the vector

$$p_O = [p_N, p_E, p_D] \tag{2.36}$$

and accounts for a Flat-Earth assumption. Transforming the position vector from Flat-Earth to the geodetic coordinates or inversely is a common process defined by equations C.2-C.7 shown in Appendix C.

However, the geodetic coordinates can be computed by using the aircraft velocities as well

$$\dot{\lambda}_G = \left(\frac{v_K}{(N_\mu + h_G)\cos(\mu_G)} \right)_O^E \tag{2.37}$$

$$\dot{\mu}_G = \left(\frac{u_K}{M_\mu + h_G} \right)_O^E \tag{2.38}$$

$$\dot{h}_G = (-w_K)_O^E, \tag{2.39}$$

where the variable λ_G describes the geodetic longitude, variable μ_G is geodetic latitude and h_G the geodetic height. The additional variables M_μ and N_μ are defined by equations

$$\begin{aligned} M_\mu &= a\frac{1-e^2}{(1-e^2\sin^2(\mu_G))^{3/2}} \\ &= N_\mu \frac{1-e^2}{1-e^2\sin^2(\mu_G)} \end{aligned} \tag{2.40}$$

$$N_\mu = \frac{a}{\sqrt{1-e^2\sin^2(\mu_G)}} \tag{2.41}$$

The constants used in the previous equation that describe the size and shape of the Earth are shown in Table 2.1.

Table 2.1: WGS-84 Ellipsoid constants.

Description	Symbol	Value	Units
Equatorial radius	a	6378137.0	[m]
Polar radius	b	6356752.3	[m]
Flattening of the Earth	$f = \frac{a-b}{a}$	0.0034	[1]
Earth eccentricity	$e = \sqrt{f(2-f)}$	0.0818	[1]

For the purpose of this thesis, the wind is expressed as a velocity vector in BFF, as shown in equation 2.42. For the high fidelity simulation, this velocity vector is calculated from the Dryden continuous turbulence model, specified in Chapter 3.

$$(V_W)_B = \begin{bmatrix} u_W \\ v_W \\ w_W \end{bmatrix}_B \tag{2.42}$$

For the computation of the aerodynamic velocities necessary for expressing aerodynamic angles, the aircraft velocity vector and the wind velocity vector have to be subtracted.

$$(V_A)_B = \begin{bmatrix} u_A \\ v_A \\ w_A \end{bmatrix}_B = \begin{bmatrix} u_K \\ v_K \\ w_K \end{bmatrix}_B - \begin{bmatrix} u_W \\ v_W \\ w_W \end{bmatrix}_B \tag{2.43}$$

The aerodynamic airspeed V_A, angle of attack α_A and angle of sideslip β_A can be expressed using equation 2.44.

$$\begin{bmatrix} V_A \\ \alpha_A \\ \beta_A \end{bmatrix}_B = \begin{bmatrix} \sqrt{u_A^2 + v_A^2 + w_A^2} \\ \tan^{-1}\left[\frac{w_A}{u_A}\right] \\ \tan^{-1}\left[\frac{v_A}{u_A^2 + w_A^2}\right] \end{bmatrix}_B \tag{2.44}$$

In case of the no-wind condition i.e. wind velocities are equal to zero, the aerodynamic airspeed, angle of attack and angle of sideslip are equal to their kinematic counterparts V_K, α_K, β_K [87].

2.3 SYSTEM LINEARIZATION

It is a well-known fact that the dynamic behavior of most physical systems exhibits a nonlinear character. However, there are many examples of cases which behave almost linearly, when subjected to small disturbance in system variables. State-of-the-art engineering practice is to substitute the nonlinear model by its linear approximation, which is to be obtained through nonlinear system linearization around equilibrium points. The linearization process described in this thesis build up references [41, 71, 87]. State and output equations of a nonlinear dynamic system are described by equations 2.45 and 2.46.

$$\dot{x}(t) = f(x(t), u(t)) \tag{2.45}$$

$$y(t) = h(x(t), u(t)) \tag{2.46}$$

Terms $f(\cdot)$ and $h(\cdot)$ are nonlinear functions of system state $x(t)$ and system input $u(t)$. A linearized model is created around an equilibrium point x_{eq}, which is in aerospace terminology known as the trim point. One of frequently used trim points in the linearization of aircraft dynamic models is for the steady-level flight condition. The trim point has to fulfill the condition defined by equation 2.47.

$$\dot{x}_{trim} = f(x_{eq}, u_{eq}) = 0 \tag{2.47}$$

The expression basically says that aircraft states in trim condition remain constant. This close vicinity of equilibrium point is possible to express through Δ variables:

$$\Delta x(t) = x(t) - x_{eq} \quad \Rightarrow \quad x(t) = x_{eq} + \Delta x(t) \tag{2.48}$$

$$\Delta u(t) = u(t) - u_{eq} \quad \Rightarrow \quad u(t) = u_{eq} + \Delta u(t) \tag{2.49}$$

$$\Delta y(t) = y(t) - y_{eq} \quad \Rightarrow \quad y(t) = y_{eq} + \Delta y(t), \tag{2.50}$$

where u_{eq} is constant input. Linearized model is obtained using Taylor series approximation of nonlinear vector functions $f(\cdot)$ and $h(\cdot)$ arround the equilibrium point by assuming only the first order of expansion and neglecting higher orders. Equation 2.52 shows the first order of Taylor expansion.

$$\begin{aligned} \dot{x}_{eq} + \Delta\dot{x} &= f(x_{eq} + \Delta x(t), u_{eq} + \Delta u(t)) \\ &= f(x_{eq}, u_{eq}) + \left.\frac{\partial f}{\partial x}\right|_{eq} [x(t) - x_{eq}] + \left.\frac{\partial f}{\partial u}\right|_{eq} [u(t) - u_{eq}] \quad (2.51) \\ y_{eq} + \Delta y &= h(x_{eq} + \Delta x(t), u_{eq} + \Delta u(t)) \\ &= h(x_{eq}, u_{eq}) + \left.\frac{\partial h}{\partial x}\right|_{eq} [x(t) - x_{eq}] + \left.\frac{\partial h}{\partial u}\right|_{qe} [u(t) - u_{eq}] \quad (2.52) \end{aligned}$$

Because derivation of equilibrium state is equal to zero and output in equilibrium state is equal to $h(x_{eq}, u_{eq})$, we can write down equations 2.53 and 2.54.

$$\Delta\dot{x}(t) = \left.\frac{\partial f}{\partial x}\right|_{eq} \Delta x(t) + \left.\frac{\partial f}{\partial u}\right|_{eq} \Delta u(t) \quad (2.53)$$

$$\Delta y = \left.\frac{\partial h}{\partial x}\right|_{eq} \Delta x(t) + \left.\frac{\partial h}{\partial u}\right|_{eq} \Delta u(t) \quad (2.54)$$

Then it is possible to simplify state and output equations by expressing the Jacobians as constant state-space matrices, i.e., system matrix A, input matrix B, output matrix C, and feed-forward matrix D defined by equations 2.55-2.58

$$A = \left.\frac{\partial f}{\partial x}\right|_{x_{eq}, u_{eq}} \quad (2.55)$$

$$B = \left.\frac{\partial f}{\partial u}\right|_{x_{eq}, u_{eq}} \quad (2.56)$$

$$C = \left.\frac{\partial h}{\partial x}\right|_{x_{eq}, u_{eq}} \quad (2.57)$$

$$D = \left.\frac{\partial h}{\partial u}\right|_{x_{eq}, u_{eq}} \quad (2.58)$$

Equations 2.53-2.54 for near equilibrium point conditions are equivalent to state-space representation of a linear dynamic system as described by equations 2.59 and 2.60 [9, 13],

$$\dot{x}(t) = Ax(t) + Bu(t) \quad (2.59)$$

$$y(t) = Cx(t) + Du(t), \quad (2.60)$$

where A, B, C, D are expressed by Jacobi matrices assuming equilibrium point $x(t) = x_{eq}$ and $u(t) = u_{eq}$ [87]. Figure 2.2 shows the above-defined state-space system in a block diagram where the gains are assumed to be system matrices.

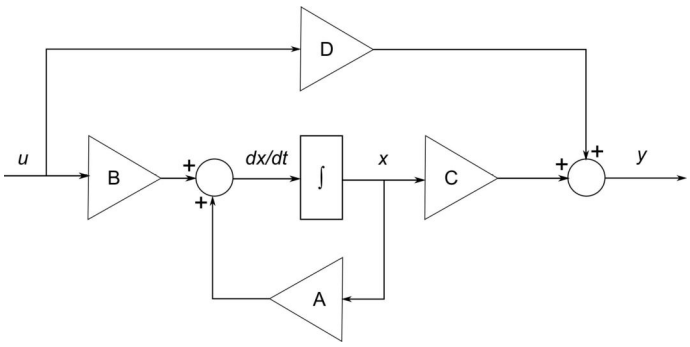

Figure 2.2: Block diagram of a dynamic system in state-space representation.

2.3.1 *Aircraft Longitudinal Motion*

The equations describing aircraft longitudinal motion can be considered decoupled if the lateral-directional state variables in differential equations describing the aircraft motion are equal to zero.

$$\beta = p = r = v_K = \phi = \psi = \chi = 0 \tag{2.61}$$

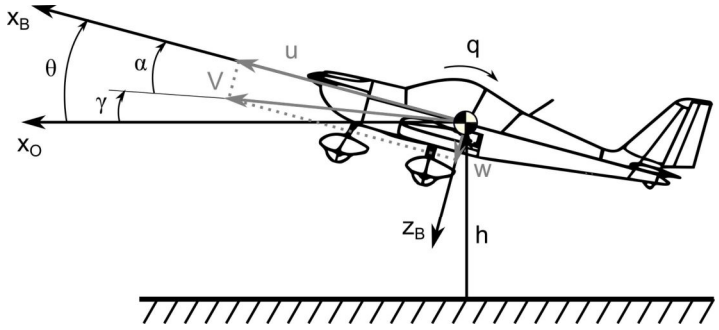

Figure 2.3: Longitudinal motion states.

The longitudinal motion state and input variables are defined in Table 2.2 [87]. The assumption of motion decoupling will lead to the simplification of previously defined equations of motion, which describe the aircraft's longitudinal motion.

$$\dot{V} = -\frac{D}{m} + \frac{(X_P)_B \cos(\alpha)}{m} - g\sin(\gamma) \tag{2.62}$$

$$\dot{\alpha} = -\frac{L}{mV} - \frac{(X_P)_B \sin(\alpha)}{mV} + \frac{g}{V}\cos(\gamma) + q \tag{2.63}$$

$$\dot{q} = \frac{1}{I_{yy}} M_A^G \tag{2.64}$$

$$\dot{\gamma} = q - \dot{\alpha} \tag{2.65}$$

$$\dot{h} = V\sin(\gamma) \tag{2.66}$$

Aerodynamic drag D, lift L and pitch moment M_A^G used in the longitudinal equations of motion are defined in Chapter 3 by equations 3.53 and 3.54. Definition of force and moment coefficients C_D, C_L and C_m used in linearization of

Table 2.2: Longitudinal states and inputs.

Variable type	Name	Nomenclature
States	Velocity	V
	Angle of attack	α
	Pitch rate	q
	Flight path angle	γ
	Geodetic height	h
Inputs	Thrust lever position	δ_T
	Elevator deflection	δ_e

longitudinal equations of motion can be found in equations 3.55, 3.57 and 3.59. The quantities $\frac{q\bar{c}}{2V}$ and $\frac{\dot{\alpha}\bar{c}}{2V}$, used in these equations, are dimensionless pitch rate and angle of attack rate, which are normalized using mean aerodynamic chord $\bar{c}$ and airspeed V.

Before the linearization itself, the longitudinal equations of motion are expressed in a form of equation 2.67, which is followed by performing partial difference of every equation according to the state, state derivative and input.

$$f(x, \dot{x}, u) = 0 \tag{2.67}$$

The results of these partial derivatives are formed into a longitudinal state-space model.

2.3.1.1 *Linearization of Velocity Equation*

The velocity equation in a form defined by equation 2.67 has below written form.

$$0 = \dot{V} + \frac{D}{m} - \frac{(X_P)_B \cos(\alpha)}{m} + g\sin(\gamma) \tag{2.68}$$

The set of equations 2.69 - 2.73 shows the partial derivative of velocity equation 2.68 with respect to longitudinal state variables.

$$\begin{aligned}
\frac{\partial f_V}{\partial V}\bigg|_0 &= \frac{1}{m}\left[\frac{\partial D}{\partial V}\bigg|_0 - \frac{\partial (X_P)_B}{\partial V}\bigg|_0 \cos(\alpha_0)\right] \\
&= \frac{1}{m}\left[\frac{\partial C_D}{\partial V}\bigg|_0 S\bar{q}_0 + 2C_D|_0 \frac{S\bar{q}_0}{V_0} + \frac{\partial (X_P)_B}{\partial V}\bigg|_0 \cos(\alpha_0)\right] \\
&= \frac{S\bar{q}_0}{m}\left[\frac{\partial C_D}{\partial V}\bigg|_0 + \frac{2C_D|_0}{V_0}\bigg|_0\right] = -X_V
\end{aligned} \tag{2.69}$$

$$\tag{2.70}$$

$$\begin{aligned}
\left.\frac{\partial f_V}{\partial \alpha}\right|_0 &= \frac{1}{m}\left[\left.\frac{\partial D}{\partial \alpha}\right|_0 - \left(\left.\frac{\partial (X_P)_B}{\partial \alpha}\right|_0 \cos(\alpha_0) - (X_P)_B\Big|_0 \sin(\alpha_0)\right)\right] - g\cos(\gamma_0) \\
&= \frac{1}{m}\bar{q}_0 S C_{D_\alpha} - \frac{1}{m}\left.\frac{\partial (X_P)_B}{\partial \alpha}\right|_0 \cos(\alpha_0) \\
&+ \frac{1}{m}\underbrace{\left[(X_P)_B\Big|_0 \sin(\alpha_0) - mg\cos(\gamma_0)\right]}_{L_0 = \bar{q}_0 S C_L|_0} \\
&= \frac{S\bar{q}_0}{m}\left[C_{D_\alpha} - C_{L_0}\right] - \frac{1}{m}\left.\frac{\partial (X_P)_B}{\partial \alpha}\right|_0 \cos(\alpha_0) = -X_\alpha \\
\left.\frac{\partial f_V}{\partial q}\right|_0 &= \frac{1}{m}\frac{\partial D}{\partial q} = \frac{S\bar{q}_0}{m}\frac{\bar{c}}{2V_0} C_{D_q} = -X_q
\end{aligned} \tag{2.71}$$

$$\left.\frac{\partial f_V}{\partial \gamma}\right|_0 = g\cos(\gamma_0) \tag{2.72}$$

$$\begin{aligned}
\left.\frac{\partial f_V}{\partial h}\right|_0 &= \frac{1}{m}\left[\left.\frac{\partial D}{\partial h}\right|_0 - \left.\frac{\partial (X_P)_B}{\partial h}\right|_0 \cos(\alpha_0)\right] \\
&= \frac{S\bar{q}_0}{m\rho_0}\left.\frac{\partial \rho}{\partial h}\right|_0 C_D|_0 - \frac{1}{m}\left.\frac{\partial (X_P)_B}{\partial h}\right|_0 \cos(\alpha_0) = -X_h
\end{aligned} \tag{2.73}$$

The set of equations 2.74 - 2.76 introduces partial derivatives of velocity equation with respect to state derivatives $\dot{V}$, $\dot{\alpha}$, $\dot{q}$, $\dot{\gamma}$, $\dot{g}$

$$\left.\frac{\partial f_V}{\partial \dot{V}}\right|_0 = 1 \tag{2.74}$$

$$\begin{aligned}
\left.\frac{\partial f_V}{\partial \dot{\alpha}}\right|_0 &= \frac{1}{m}\left[\left.\frac{\partial D}{\partial \dot{\alpha}}\right|_0 - \left.\frac{\partial (X_P)_B}{\partial \dot{\alpha}}\right|_0 \cos(\alpha_0)\right] \\
&= \frac{S\bar{q}_0}{m}\frac{\bar{c}}{2V_0} C_{D_{\dot{\alpha}}} - \frac{1}{m}\left.\frac{\partial (X_P)_B}{\partial \dot{\alpha}}\right|_0 \cos(\alpha_0) = -X_{\dot{\alpha}}
\end{aligned} \tag{2.75}$$

$$\left.\frac{\partial f_V}{\partial \dot{q}}\right|_0 = \left.\frac{\partial f_V}{\partial \dot{\gamma}}\right|_0 = \left.\frac{\partial f_V}{\partial \dot{h}}\right|_0 = 0 \tag{2.76}$$

The partial derivatives of velocity equation with respect to the longitudinal input variables δ_e, δ_T are defined bellow

$$\left.\frac{\partial f_V}{\partial \delta_e}\right|_0 = \frac{1}{m}\left.\frac{\partial D}{\partial \delta_e}\right|_0 = \frac{S\bar{q}_0}{m} C_{D_{\delta_e}} = -X_{\delta_e} \tag{2.77}$$

$$\left.\frac{\partial f_V}{\partial \delta_T}\right|_0 = -\frac{1}{m}\left.\frac{\partial (X_P)_B}{\partial \delta_T}\right|_0 \cos(\alpha_0) = -X_{\delta_T} \tag{2.78}$$

2.3.1.2 *Linearization of the Angle of Attack Equation*

The angle of attack equation 2.63 that will be linearized was expressed in the form of equation 2.67.

$$0 = \dot{\alpha} + \frac{L}{mV} - \frac{-(X_P)_B \sin(\alpha)}{mV} - \frac{g}{V}\cos(\gamma) - q \tag{2.79}$$

The following set of equations introduces the partial derivatives of the angle of attack equation with respect to the longitudinal state variables.

$$\begin{aligned}
\left.\frac{\partial f_\alpha}{\partial V}\right|_0 &= -\overbrace{\frac{1}{V_0^2}\left[\frac{L}{m} - \frac{-(X_P)_B|_0 \sin(\alpha_0)}{m} - g\cos(\gamma_0)\right]}^{\frac{1}{V_0}\dot{\alpha}_0 \approx 0} \\
&+ \frac{1}{mV_0}\left[\left.\frac{\partial L}{\partial V}\right|_0 - \left.\frac{\partial (X_P)_B}{\partial V}\right|_0 \sin(\alpha_0)\right] \\
&= \frac{\bar{q}_0 S}{mV_0^2}\left[2C_L|_0 + V_0 \left.\frac{\partial C_L}{\partial V}\right|_0\right] + \frac{1}{mV_0}\left[\left.\frac{\partial (X_P)_B}{\partial V}\right|_0 \sin(\alpha_0)\right] \\
&= -Z_V
\end{aligned} \tag{2.80}$$

$$\begin{aligned}
\left.\frac{\partial f_\alpha}{\partial \alpha}\right|_0 &= \frac{1}{mV_0}\left[\left.\frac{\partial L}{\partial \alpha}\right|_0 + \left.\frac{\partial (X_P)_B}{\partial \alpha}\right|_0 \sin(\alpha_0) + (X_P)_B|_0 \cos(\alpha_0)\right] - \frac{g}{V_0}\sin(\gamma_0) \\
&= \frac{\bar{q}_0 S}{mV_0} C_{L_\alpha} + \frac{1}{mV_0}\left[\left.\frac{\partial (X_P)_B}{\partial \alpha}\right|_0 \sin(\alpha_0)\right] \\
&+ \frac{1}{mV_0}\underbrace{\left[(X_P)_B|_0 \cos(\alpha_0) - mg\sin(\gamma_0)\right]}_{D_0 = C_D|_0 \bar{q}_0 S} \\
&= \frac{\bar{q}_0 S}{mV_0}\left[C_{L_\alpha} + C_D|_0\right] + \frac{1}{mV_0}\left[\left.\frac{\partial (X_P)_B}{\partial \alpha}\right|_0 \sin(\alpha_0)\right] = -Z_\alpha
\end{aligned} \tag{2.81}$$

$$\left.\frac{\partial f_\alpha}{\partial q}\right|_0 = \frac{1}{mV_0}\left.\frac{\partial L}{\partial q}\right|_0 - 1 = \frac{\bar{q}_0 S}{mV_0}\frac{\bar{c}}{2V_0} C_{L_q} - 1 = -Z_q - 1 \tag{2.82}$$

$$\left.\frac{\partial f_\alpha}{\partial \gamma}\right|_0 = \frac{g}{V_0}\sin(\gamma_0) \tag{2.83}$$

$$\begin{aligned}
\left.\frac{\partial f_\alpha}{\partial h}\right|_0 &= \frac{1}{mV_0}\left[\left.\frac{\partial L}{\partial \alpha}\right|_0 + \left.\frac{\partial (X_P)_B}{\partial \alpha}\right|_0 \sin(\alpha_0)\right] \\
&= \frac{\bar{q}_0 S}{mV_0 \rho_0}\left.\frac{\partial \rho}{\partial h}\right|_0 C_L|_0 + \frac{1}{mV_0}\left[\left.\frac{\partial (X_P)_B}{\partial \alpha}\right|_0 \sin(\alpha_0)\right] = -Z_h
\end{aligned} \tag{2.84}$$

The next set of equations expresses the partial derivative of angle of attack equation with respect to longitudinal state derivatives.

$$\begin{aligned}
\left.\frac{\partial f_\alpha}{\partial \dot{\alpha}}\right|_0 &= 1 + \frac{1}{mV_0}\left.\frac{\partial L}{\partial \dot{\alpha}}\right|_0 - \frac{1}{mV_0}\overbrace{\left[\left.\frac{\partial (X_P)_B}{\partial \dot{\alpha}}\right|_0\right]}^{\text{negligible}} \\
&= 1 + \frac{\bar{q}_0 S}{mV_0}\frac{\bar{c}}{2V_0} C_{L_{\dot{\alpha}}} = 1 - Z_{\dot{\alpha}}
\end{aligned} \tag{2.85}$$

$$\left.\frac{\partial f_\alpha}{\partial \dot{V}}\right|_0 = \left.\frac{\partial f_\alpha}{\partial \dot{q}}\right|_0 = \left.\frac{\partial f_\alpha}{\partial \dot{\gamma}}\right|_0 = \left.\frac{\partial f_\alpha}{\partial \dot{h}}\right|_0 = 0 \tag{2.86}$$

The following set of equations describes the partial derivatives of angle of attack equation with respect to longitudinal model inputs.

$$\left.\frac{\partial f_\alpha}{\partial \delta_e}\right|_0 = \frac{1}{mV_0}\left.\frac{\partial L}{\partial \delta_e}\right|_0 = \frac{S\bar{q}_0}{mV_0} C_{L_{\delta_e}} = -Z_{\delta_e} \tag{2.87}$$

$$\left.\frac{\partial f_\alpha}{\partial \delta_T}\right|_0 = \frac{1}{mV_0}\left.\frac{\partial (X_P)_B}{\partial \delta_T}\right|_0 \sin(\alpha_0) = -Z_{\delta_T} \tag{2.88}$$

2.3.1.3 *Linearization of the Pitch Rate Equation*

The pitch rate equation 2.64 in the form for linearization is shown in equation 2.89.

$$0 = \dot{q} - \frac{1}{I_{yy}} M_A^G \tag{2.89}$$

The following set of equations expresses the partial derivative of the pitch rate equation with respect to longitudinal state variables.

$$\left.\frac{\partial f_q}{\partial V}\right|_0 = -\frac{1}{I_{yy}}\frac{\partial M_A^G}{\partial V} = -\frac{\bar{q}_0 S\bar{c}}{I_{yy}}\left[\frac{1}{V_0}\overbrace{2C_m|_0}^{\approx 0} + \left.\frac{\partial C_m}{\partial V}\right|_0\right] = -M_V \tag{2.90}$$

$$\left.\frac{\partial f_q}{\partial \alpha}\right|_0 = -\frac{1}{I_{yy}}\frac{\partial M_A^G}{\partial \alpha} = -\frac{\bar{q}_0 S\bar{c}}{I_{yy}} C_{m_\alpha} = -M_\alpha \tag{2.91}$$

$$\left.\frac{\partial f_q}{\partial q}\right|_0 = -\frac{1}{I_{yy}}\frac{\partial M_A^G}{\partial q} = -\frac{\bar{q}_0 S\bar{c}}{I_{yy}}\frac{\bar{c}}{2V_0} C_{m_q} = -M_q \tag{2.92}$$

$$\left.\frac{\partial f_q}{\partial \gamma}\right|_0 = \left.\frac{\partial f_q}{\partial h}\right|_0 = 0 \tag{2.93}$$

The following set of equations expresses the partial derivative of the pitch rate equation with respect to longitudinal state derivative variables.

$$\left.\frac{\partial f_q}{\partial \dot{\alpha}}\right|_0 = -\frac{1}{I_{yy}}\frac{\partial M_A^G}{\partial \dot{\alpha}} = -\frac{\bar{q}_0 S\bar{c}}{I_{yy}}\frac{\bar{c}}{2V_0} C_{m_{\dot{\alpha}}} = -M_{\dot{\alpha}} \tag{2.94}$$

$$\left.\frac{\partial f_q}{\partial \dot{q}}\right|_0 = 1 \tag{2.95}$$

$$\left.\frac{\partial f_q}{\partial \dot{V}}\right|_0 = \left.\frac{\partial f_q}{\partial \dot{\gamma}}\right|_0 = \left.\frac{\partial f_q}{\partial \dot{h}}\right|_0 = 0 \tag{2.96}$$

The following set of equations expresses the partial derivative of pitch rate equation with respect to longitudinal input variables.

$$\left.\frac{\partial f_q}{\partial \delta_e}\right|_0 = -\frac{1}{I_{yy}}\frac{\partial M_A^G}{\partial \delta_e} = -\frac{\bar{q}_0 S\bar{c}}{I_{yy}} C_{m_{\delta_e}} = -M_{\delta_e} \tag{2.97}$$

$$\left.\frac{\partial f_q}{\partial \delta_T}\right|_0 = 0 \tag{2.98}$$

2.3.1.4 *Linearization of the Flight Path Angle Equation*

The following equation that describes the flight path time derivative angle will be used in the linearization process

$$0 = \dot{\gamma} - q + \dot{\alpha} \tag{2.99}$$

The partial derivatives of the flight path angle equation with respect to the longitudinal state variables are defined by following equations

$$\left.\frac{\partial f_\gamma}{\partial q}\right|_0 = -1 \tag{2.100}$$

$$\left.\frac{\partial f_\gamma}{\partial V}\right|_0 = \left.\frac{\partial f_\gamma}{\partial \alpha}\right|_0 = \left.\frac{\partial f_\gamma}{\partial \gamma}\right|_0 = \left.\frac{\partial f_\gamma}{\partial h}\right|_0 = 0 \tag{2.101}$$

The partial derivatives of the flight path angle equation with respect to the longitudinal state derivative variables are defined as

$$\left.\frac{\partial f_\gamma}{\partial \dot{\alpha}}\right|_0 = 1 \tag{2.102}$$

$$\left.\frac{\partial f_\gamma}{\partial \dot{\gamma}}\right|_0 = 1 \tag{2.103}$$

$$\left.\frac{\partial f_\gamma}{\partial \dot{V}}\right|_0 = \left.\frac{\partial f_\gamma}{\partial \dot{q}}\right|_0 = \left.\frac{\partial f_\gamma}{\partial \dot{h}}\right|_0 = 0 \tag{2.104}$$

The partial derivatives of the flight path angle equation with respect to the longitudinal input variables are defined as

$$\left.\frac{\partial f_\gamma}{\partial \delta_e}\right|_0 = \left.\frac{\partial f_\gamma}{\partial \delta_T}\right|_0 = 0 \tag{2.105}$$

2.3.1.5 *Linearization of the Height Equation*

The height equation in a form defined by equation 2.67 is shown below.

$$0 = \dot{h} - V\sin(\gamma) \tag{2.106}$$

Following equations describe the partial derivative of the height equation with respect to state variables.

$$\left.\frac{\partial f_h}{\partial V}\right|_0 = -\sin(\gamma_0) \tag{2.107}$$

$$\left.\frac{\partial f_h}{\partial \gamma}\right|_0 = -V_0\cos(\gamma_0) \tag{2.108}$$

$$\left.\frac{\partial f_h}{\partial \alpha}\right|_0 = \left.\frac{\partial f_h}{\partial q}\right|_0 = \left.\frac{\partial f_h}{\partial h}\right|_0 = 0 \tag{2.109}$$

Partial derivatives of the height equation with respect to state derivatives are described by following equations.

$$\left.\frac{\partial f_h}{\partial \dot{h}}\right|_0 = 1 \tag{2.110}$$

$$\left.\frac{\partial f_h}{\partial \dot{V}}\right|_0 = \left.\frac{\partial f_h}{\partial \dot{\alpha}}\right|_0 = \left.\frac{\partial f_h}{\partial \dot{q}}\right|_0 = \left.\frac{\partial f_h}{\partial \dot{\gamma}}\right|_0 = 0 \tag{2.111}$$

Moreover, the equation 2.112shows the partial derivatives of the height equation concerning system inputs δ_T and δ_e.

$$\left.\frac{\partial f_h}{\partial \delta_T}\right|_0 = \left.\frac{\partial f_h}{\partial \delta_e}\right|_0 = 0 \tag{2.112}$$

To summarize, we can write down all linearized longitudinal equations in following order, the airspeed, angle of attack, pitch rate, flight path angle, height and position equation.

$$\begin{aligned} 0 &= -X_V\delta V - X_\alpha\delta\alpha - X_q\delta q + g\cos(\gamma_0)\delta\gamma - X_h\delta h + \delta\dot{V} - X_{\dot{\alpha}}\delta\dot{\alpha} \\ &- X_{\delta_e}\delta(\delta_e) - X_{\delta_T}\delta(\delta_T) \end{aligned} \tag{2.113}$$

$$\begin{aligned} 0 &= -Z_V\delta V - Z_\alpha\delta\alpha - (Z_q + 1)\delta q + \frac{g}{V_0}\sin(\gamma_0)\delta\gamma - Z_h\delta h + (1 - Z_{\dot{\alpha}})\delta\dot{\alpha} \\ &- Z_{\delta_e}\delta(\delta_e) - Z_{\delta_T}\delta(\delta_T) \end{aligned} \tag{2.114}$$

$$0 = -M_V\delta V - M_\alpha\delta\alpha - M_q\delta q - M_{\dot{\alpha}}\delta\dot{\alpha} + \delta\dot{q} - M_{\delta_e}\delta(\delta_e) \tag{2.115}$$

$$0 = -\delta q + \delta\dot{\alpha} + \delta\dot{\gamma} \tag{2.116}$$

$$0 = -\sin(\gamma_0)\delta V - V_0\cos(\gamma_0)\delta\gamma + \delta\dot{h} \tag{2.117}$$

2.3.2 *Aircraft Lateral-Directional Motion*

Nonlinear state differential equations which describe the decoupled lateral-directional motion, namely the roll and yaw motion, are expressed by a set of equations 2.118-2.122. Table 2.3 contains the list of the aircraft's lateral-directional motion model states and inputs [87]. Equations 2.118-2.122 will serve as a baseline for the following linearization.

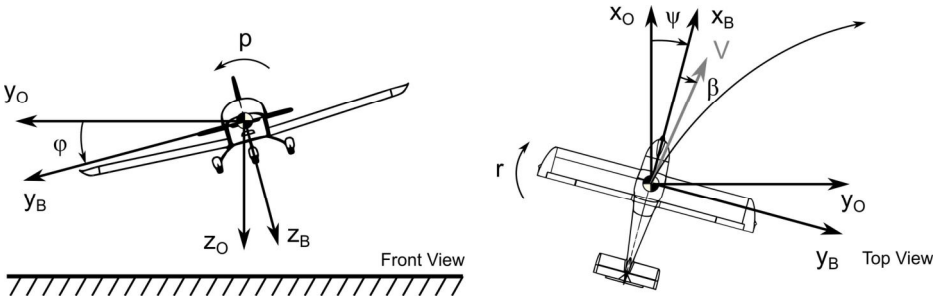

Figure 2.4: Lateral-directional motion states.

Table 2.3: Lateral-directional states and inputs.

Variable type	**Name**	**Nomenclature**
States	Angle of sideslip	β
	Roll angle	ϕ
	Heading	ψ
	Roll rate	p
	Yaw rate	r
Inputs	Aileron deflection	δ_a
	Rudder deflection	δ_r

$$\begin{aligned}\dot{\beta} &= \frac{Q}{mV} + \frac{-(X_P)_B \cos(\alpha)\sin(\beta)}{mV} + \frac{g}{V}\cos(\gamma)\sin(\mu) \\ &+ (-r\cos(\alpha) + p\sin(\alpha)) \qquad (2.118)\end{aligned}$$

$$\dot{\phi} = p + q\sin(\phi)\tan(\theta) + r\cos(\phi)\tan(\theta) \qquad (2.119)$$

$$\dot{\psi} = q\frac{\sin(\phi)}{\cos(\theta)} + r\frac{\cos(\phi)}{\cos(\theta)} \qquad (2.120)$$

$$\begin{aligned}\dot{p} &= \frac{1}{\Delta}\left[I_{zz}L_A^G + I_{xz}N_A^G\right] \\ &+ \frac{1}{\Delta}\left[I_{xz}(I_{xx} - I_{yy} + I_{zz})pq - (I_{zz}^2 - I_{zz}I_{yy} + I_{xz}^2)qr\right] \qquad (2.121)\end{aligned}$$

$$\begin{aligned}\dot{r} &= \frac{1}{\Delta}\left[I_{xz}L_A^G + I_{xx}N_A^G\right] \\ &+ \frac{1}{\Delta}\left[(I_{xz}^2 - I_{xx}I_{yy} + I_{xx}^2)pq - I_{xz}(I_{xx} - I_{yy} + I_{zz})qr\right] \qquad (2.122)\end{aligned}$$

The expression $\sin(\mu)$ from equation 2.118 can be redefined as

$$\sin(\mu) = \frac{\cos(\theta)}{\cos(\gamma)\cos(\beta)} + \tan(\gamma)\tan(\beta) \tag{2.123}$$

Aerodynamic cross-wind force Q , roll moment L_A^G and yaw moment N_A^G used in lateral-directional equations of motion are defined by equations 3.53 - 3.54. The force and moments coefficients C_Q, C_l and C_n used in the linearization of lateral-directional equations of motion are expressed in equations 3.56, 3.58 and 3.60. The quantities $\frac{pb_w}{2V}$ and $\frac{rb_w}{2V}$ are dimensionless roll an yaw rates normalized using the wingspan b_w and airspeed V.

Similarly to the linearization process of longitudinal motion, equations 2.118-2.122 have to be converted to a form defined by equation 2.67. After that, the partial derivatives of the lateral-directional motion equations with respect to state variables, input variables and state variable derivatives will be performed in order to express the linearized parameters of the state space model matrices.

The conditions expressed by equation 2.124 are considered for the linearization of the lateral-directional motion in steady-level flight.

$$\beta_0 = \phi_0 = q_0 = 0 \tag{2.124}$$

2.3.2.1 *Linearization of Angle of Sideslip Equation*

The first step in lateral-directional motion linearization is expressing the partial derivatives of the sideslip equation with respect to the lateral-directional motion state derivatives.

$$\begin{aligned}
\left.\frac{\partial f_\beta}{\partial \beta}\right|_0 &= \frac{1}{mV_0}\left[-\left.\frac{\partial Q}{\partial \beta}\right|_0 + \left.\frac{\partial (X_P)_B}{\partial \beta}\right|_0 \cos(\alpha_0)\overbrace{\sin(\beta_0)}^{0} + (X_P)_B|_0 \cos(\alpha_0)\overbrace{\cos(\beta_0)}^{1}\right] \\
&- \frac{g}{V_0}\cos(\gamma_0)\underbrace{\left.\frac{\partial \sin(\mu)}{\partial \beta}\right|_0}_{\tan(\gamma_0)} \\
&= -\frac{\bar{q}_0 S}{mV_0} C_{Q_\beta} + \frac{(X_P)_B|_0 \cos(\alpha_0)}{mV_0} - \frac{g}{V_0}\sin(\gamma_0) \\
&= -\frac{\bar{q}_0 S}{mV_0} C_{Q_\beta} + \frac{1}{mV_0}\underbrace{[(X_P)_B|_0 \cos(\alpha_0) - mg\sin(\gamma_0)]}_{D_0 = \bar{q}_0 S C_D|_0} \\
&= -\frac{\bar{q}_0 S}{mV_0}\left[C_{Q_\beta} - C_D|_0\right] = -Y_\beta
\end{aligned} \tag{2.125}$$

$$\left.\frac{\partial f_\beta}{\partial \phi}\right|_0 = -\frac{g}{V_0\underbrace{\cos(\beta_0)}_{1}}\cos(\theta_0)\underbrace{\cos(\phi_0)}_{1} = -\frac{g}{V_0}\cos(\theta_0) \tag{2.126}$$

$$\left.\frac{\partial f_\beta}{\partial p}\right|_0 = -\frac{1}{mV_0}\left.\frac{\partial Q}{\partial p}\right|_0 - \sin(\alpha_0) = -\frac{\bar{q}_0 S}{mV_0}\frac{b_w}{2V_0}C_{Q_p} - \sin(\alpha_0)$$
$$= -Y_p - \sin(\alpha_0) \tag{2.127}$$

$$\left.\frac{\partial f_\beta}{\partial r}\right|_0 = -\frac{1}{mV_0}\left.\frac{\partial Q}{\partial r}\right|_0 + \cos(\alpha_0) = -\frac{\bar{q}_0 S}{mV_0}\frac{b_w}{2V_0}C_{Q_r} + \cos(\alpha_0)$$
$$= -Y_r + \cos(\alpha_0) \tag{2.128}$$

$$\left.\frac{\partial f_\beta}{\partial \psi}\right|_0 = 0 \tag{2.129}$$

The following set of equations expresses the partial derivatives of the sideslip equation with respect to the lateral-directional motion state derivatives.

$$\left.\frac{\partial f_\beta}{\partial \dot{\beta}}\right|_0 = 1 - \frac{1}{mV_0}\left.\frac{\partial Q}{\partial \dot{\beta}}\right|_0 = 1 - \frac{\bar{q}_0 S}{mV_0}\frac{b_w}{2V_0}C_{Q_{\dot{\beta}}} = 1 - Y_{\dot{\beta}} \tag{2.130}$$

$$\left.\frac{\partial f_\beta}{\partial \dot{\phi}}\right|_0 = \left.\frac{\partial f_\beta}{\partial \dot{\psi}}\right|_0 = \left.\frac{\partial f_\beta}{\partial \dot{p}}\right|_0 = \left.\frac{\partial f_\beta}{\partial \dot{r}}\right|_0 = 0 \tag{2.131}$$

The partial derivatives of the angle of sideslip equation with respect to lateral-directional motion input variables are defined by equations 2.132 and 2.133.

$$\left.\frac{\partial f_\beta}{\partial \delta_a}\right|_0 = -\frac{1}{mV_0}\left.\frac{\partial Q}{\partial \delta_a}\right|_0 = -\frac{\bar{q}_0 S}{mV_0}C_{Q_{\delta_a}} = -Y_{\delta_a} \tag{2.132}$$

$$\left.\frac{\partial f_\beta}{\partial \delta_r}\right|_0 = -\frac{1}{mV_0}\left.\frac{\partial Q}{\partial \delta_r}\right|_0 = -\frac{\bar{q}_0 S}{mV_0}C_{Q_{\delta_r}} = -Y_{\delta_r} \tag{2.133}$$

2.3.2.2 *Linearization of Roll Angle Equation*

The first step in linearizing the roll angle equation is expressing its partial derivatives with respect to the lateral-directional motion states.

$$\left.\frac{\partial f_\phi}{\partial \phi}\right|_0 = -q\cos(\phi_0)\tan(\theta_0) + r\sin(\phi_0)\tan(\theta_0)$$
$$= -\dot{\theta}_0\tan(\theta_0) = 0 \tag{2.134}$$

$$\left.\frac{\partial f_\phi}{\partial p}\right|_0 = -1 \tag{2.135}$$

$$\left.\frac{\partial f_\phi}{\partial r}\right|_0 = -\cos(\phi_0)\tan(\theta_0) = -\tan(\theta_0) \tag{2.136}$$

$$\left.\frac{\partial f_\phi}{\partial \beta}\right|_0 = \left.\frac{\partial f_\phi}{\partial \psi}\right|_0 = 0 \tag{2.137}$$

The following set of equations expresses the partial derivatives of roll angle equation with respect to the lateral-directional motion state derivatives.

$$\left.\frac{\partial f_\phi}{\partial \dot{\phi}}\right|_0 = 1 \tag{2.138}$$

$$\left.\frac{\partial f_\phi}{\partial \dot{\beta}}\right|_0 = \left.\frac{\partial f_\phi}{\partial \dot{\psi}}\right|_0 = \left.\frac{\partial f_\phi}{\partial \dot{p}}\right|_0 = \left.\frac{\partial f_\phi}{\partial \dot{r}}\right|_0 = 0 \tag{2.139}$$

The partial derivatives of the roll angle equation with respect to lateral-directional motion input variables are defined by equation 2.140.

$$\left.\frac{\partial f_\phi}{\partial \delta_a}\right|_0 = \left.\frac{\partial f_\phi}{\partial \delta_r}\right|_0 = 0 \tag{2.140}$$

2.3.2.3 *Linearization of Heading Angle Equation*

The first step in linearizing the heading angle equation is expressing its partial derivatives with respect to the lateral-directional motion state variables.

$$\left.\frac{\partial f_\psi}{\partial \phi}\right|_0 = -q\frac{\cos(\phi_0)}{\cos(\theta_0)} + r\frac{\sin(\phi_0)}{\cos(\theta_0)} = -\frac{\dot{\theta}_0}{\cos(\theta_0)} = 0 \tag{2.141}$$

$$\left.\frac{\partial f_\psi}{\partial r}\right|_0 = -\frac{\cos(\phi_0)}{\cos(\theta_0)} = -\frac{1}{\cos(\theta_0)} \tag{2.142}$$

$$\left.\frac{\partial f_\psi}{\partial \beta}\right|_0 = \left.\frac{\partial f_\psi}{\partial \psi}\right|_0 = \left.\frac{\partial f_\psi}{\partial p}\right|_0 = 0 \tag{2.143}$$

The following set of equations expresses the partial derivatives of heading angle equation with respect to the lateral-directional motion state derivatives.

$$\left.\frac{\partial f_\psi}{\partial \dot{\psi}}\right|_0 = 1 \tag{2.144}$$

$$\left.\frac{\partial f_\psi}{\partial \dot{\beta}}\right|_0 = \left.\frac{\partial f_\psi}{\partial \dot{\phi}}\right|_0 = \left.\frac{\partial f_\psi}{\partial \dot{p}}\right|_0 = \left.\frac{\partial f_\psi}{\partial \dot{r}}\right|_0 = 0 \tag{2.145}$$

The partial derivatives of the heading angle equation with respect to lateral-directional motion input variables are defined by equation 2.146.

$$\left.\frac{\partial f_\psi}{\partial \delta_a}\right|_0 = \left.\frac{\partial f_\psi}{\partial \delta_r}\right|_0 = 0 \tag{2.146}$$

2.3.2.4 *Linearization of Roll Rate Equation*

The first step in the roll rate equation linearization is expressing its partial derivatives with respect to the lateral-directional motion state variables.

$$\left.\frac{\partial f_p}{\partial \beta}\right|_0 = -\frac{1}{\Delta}\left[I_{zz}\left.\frac{\partial L_A^G}{\partial \beta}\right|_0 + I_{xz}\left.\frac{\partial N_A^G}{\partial \beta}\right|_0\right] = -\frac{\bar{q}_0 S b_w}{\Delta}\left[I_{zz}C_{l_\beta} + I_{xz}C_{n_\beta}\right]$$
$$= -L_\beta \tag{2.147}$$

$$\left.\frac{\partial f_p}{\partial p}\right|_0 = -\frac{1}{\Delta}\left[I_{zz}\left.\frac{\partial L_A^G}{\partial p}\right|_0 + I_{xz}\left.\frac{\partial N_A^G}{\partial p}\right|_0\right] - \frac{1}{\Delta}I_{xz}(I_{xx} - I_{yy} + I_{zz})\overbrace{q_0}^{0}$$
$$= -\frac{\bar{q}_0 S b_w}{2\Delta}\frac{b_w}{2V_0}\left[I_{zz}C_{l_p} + I_{xz}C_{n_p}\right] = -L_p \tag{2.148}$$

$$\left.\frac{\partial f_p}{\partial r}\right|_0 = -\frac{1}{\Delta}\left[I_{zz}\left.\frac{\partial L_A^G}{\partial r}\right|_0 + I_{xz}\left.\frac{\partial N_A^G}{\partial r}\right|_0\right] + \frac{1}{\Delta}(I_{zz}^2 - I_{zz}I_{yy} + I_{xz}^2)\overbrace{q_0}^{0}$$
$$= -\frac{\bar{q}_0 S b_w}{2\Delta}\frac{b_w}{2V_0}\left[I_{zz}C_{l_r} + I_{xz}C_{n_r}\right] = -L_r \tag{2.149}$$

$$\left.\frac{\partial f_p}{\partial \phi}\right|_0 = \left.\frac{\partial f_p}{\partial \psi}\right|_0 = 0 \tag{2.150}$$

The following set of equations expresses the partial derivatives of the roll rate equation with respect to the lateral-directional motion state derivatives.

$$\left.\frac{\partial f_p}{\partial \dot{\beta}}\right|_0 = -\frac{1}{\Delta}\left[I_{zz}\left.\frac{\partial L_A^G}{\partial \dot{\beta}}\right|_0 + I_{xz}\left.\frac{\partial N_A^G}{\partial \dot{\beta}}\right|_0\right]$$
$$= -\frac{\bar{q}_0 S b_w}{2\Delta}\frac{b_w}{2V_0}\left[I_{zz}C_{l_{\dot{\beta}}} + I_{xz}C_{n_{\dot{\beta}}}\right] = -L_{\dot{\beta}} \tag{2.151}$$

$$\left.\frac{\partial f_p}{\partial \dot{p}}\right|_0 = 1 \tag{2.152}$$

$$\left.\frac{\partial f_p}{\partial \dot{\phi}}\right|_0 = \left.\frac{\partial f_p}{\partial \dot{\psi}}\right|_0 = \left.\frac{\partial f_p}{\partial \dot{r}}\right|_0 = 0 \tag{2.153}$$

The partial derivatives of the roll rate equation with respect to lateral-directional motion input variables are defined by equations 2.154-2.155.

$$\left.\frac{\partial f_p}{\partial \delta_a}\right|_0 = -\frac{1}{\Delta}\left[I_{zz}\left.\frac{\partial L_A^G}{\partial \delta_a}\right|_0 + I_{xz}\left.\frac{\partial N_A^G}{\partial \delta_a}\right|_0\right] = -\frac{\bar{q}_0 S b_w}{2\Delta}\left[I_{zz}C_{l_{\delta_a}} + I_{xz}C_{n_{\delta_a}}\right]$$
$$= -L_{\delta_a} \tag{2.154}$$

$$\left.\frac{\partial f_p}{\partial \delta_r}\right|_0 = -\frac{1}{\Delta}\left[I_{zz}\left.\frac{\partial L_A^G}{\partial \delta_r}\right|_0 + I_{xz}\left.\frac{\partial N_A^G}{\partial \delta_r}\right|_0\right] = -\frac{\bar{q}_0 S b_w}{2\Delta}\left[I_{zz}C_{l_{\delta_r}} + I_{xz}C_{n_{\delta_r}}\right]$$
$$= -L_{\delta_r} \tag{2.155}$$

2.3.2.5 *Linearization of Yaw Rate Equation*

The first step in yaw rate equation linearization the is expressing its partial derivatives with respect to lateral-directional motion state variables.

$$\begin{aligned}\left.\frac{\partial f_r}{\partial \beta}\right|_0 &= -\frac{1}{\Delta}\left[I_{xz}\left.\frac{\partial L_A^G}{\partial \beta}\right|_0 + I_{xx}\left.\frac{\partial N_A^G}{\partial \beta}\right|_0\right] = -\frac{\bar{q}_0 S b_w}{2\Delta}\left[I_{xz}C_{l_\beta} + I_{xx}C_{n_\beta}\right] \\ &= -N_\beta \end{aligned} \tag{2.156}$$

$$\begin{aligned}\left.\frac{\partial f_r}{\partial p}\right|_0 &= -\frac{1}{\Delta}\left[I_{xz}\left.\frac{\partial L_A^G}{\partial p}\right|_0 + I_{xx}\left.\frac{\partial N_A^G}{\partial p}\right|_0\right] - \frac{1}{\Delta}I_{xz}(I_{xz}^2 - I_{xx}I_{yy} + I_{xx}^2)\overbrace{q_0}^{0} \\ &= -\frac{\bar{q}_0 S b_w}{2\Delta}\frac{b_w}{2V_0}\left[I_{xz}C_{l_p} + I_{xx}C_{n_p}\right] = -N_p \end{aligned} \tag{2.157}$$

$$\begin{aligned}\left.\frac{\partial f_r}{\partial r}\right|_0 &= -\frac{1}{\Delta}\left[I_{xz}\left.\frac{\partial L_A^G}{\partial r}\right|_0 + I_{xx}\left.\frac{\partial N_A^G}{\partial r}\right|_0\right] + \frac{1}{\Delta}I_{xz}(I_{xx} - I_{yy} + I_{zz})\overbrace{q_0}^{0} \\ &= -\frac{\bar{q}_0 S b_w}{2\Delta}\frac{b_w}{2V_0}\left[I_{xz}C_{l_r} + I_{xx}C_{n_r}\right] = -N_r \end{aligned} \tag{2.158}$$

$$\left.\frac{\partial f_r}{\partial \phi}\right|_0 = \left.\frac{\partial f_r}{\partial \psi}\right|_0 = 0 \tag{2.159}$$

The following set of equations express the partial derivatives of the yaw rate equation with respect to the lateral-directional motion state derivatives.

$$\begin{aligned}\left.\frac{\partial f_r}{\partial \dot{\beta}}\right|_0 &= -\frac{1}{\Delta}\left[I_{xz}\left.\frac{\partial L_A^G}{\partial \dot{\beta}}\right|_0 + I_{xx}\left.\frac{\partial N_A^G}{\partial \dot{\beta}}\right|_0\right] \\ &= -\frac{\bar{q}_0 S b_w}{2\Delta}\frac{b_w}{2V_0}\left[I_{xz}C_{l_{\dot{\beta}}} + I_{xx}C_{n_{\dot{\beta}}}\right] = -N_{\dot{\beta}} \end{aligned} \tag{2.160}$$

$$\left.\frac{\partial f_r}{\partial \dot{r}}\right|_0 = 1 \tag{2.161}$$

$$\left.\frac{\partial f_r}{\partial \dot{\phi}}\right|_0 = \left.\frac{\partial f_r}{\partial \dot{\psi}}\right|_0 = \left.\frac{\partial f_r}{\partial \dot{p}}\right|_0 = 0 \tag{2.162}$$

The partial derivatives of the yaw rate equation with respect to lateral-directional motion input variables are defined by equations 2.163-2.164.

$$\begin{aligned}\left.\frac{\partial f_r}{\partial \delta_a}\right|_0 &= -\frac{1}{\Delta}\left[I_{xz}\left.\frac{\partial L_A^G}{\partial \delta_a}\right|_0 + I_{xx}\left.\frac{\partial N_A^G}{\partial \delta_a}\right|_0\right] = -\frac{\bar{q}_0 S b_w}{2\Delta}\left[I_{xz}C_{l_{\delta_a}} + I_{xx}C_{n_{\delta_a}}\right] \\ &= -N_{\delta_a} \end{aligned} \tag{2.163}$$

$$\begin{aligned}\left.\frac{\partial f_r}{\partial \delta_r}\right|_0 &= -\frac{1}{\Delta}\left[I_{xz}\left.\frac{\partial L_A^G}{\partial \delta_r}\right|_0 + I_{xx}\left.\frac{\partial N_A^G}{\partial \delta_r}\right|_0\right] = -\frac{\bar{q}_0 S b_w}{2\Delta}\left[I_{xz}C_{l_{\delta_r}} + I_{xx}C_{n_{\delta_r}}\right] \\ &= -N_{\delta_r} \end{aligned} \tag{2.164}$$

To summarize, we write down all linearized lateral-directional equations in the following order, the angle of sideslip β, roll angle ϕ, heading angle ψ, roll rate p, and yaw rate r.

$$\begin{aligned} 0 &= -Y_\beta \delta\beta - \frac{g}{V_0}\delta\phi - (Y_p + \sin(\alpha_0))\delta p - (Y_r - \cos(\alpha_0))\delta r + (1 - Y_{\dot\beta})\delta\dot\beta \\ &- Y_{\delta_a}\delta(\delta_a) - Y_{\delta_r}\delta(\delta_r) \end{aligned} \tag{2.165}$$

$$0 = -\delta p - \tan(\theta_0)\delta r + \delta\dot\phi \tag{2.166}$$

$$0 = -\frac{1}{\cos(\theta_0)}\delta r + \delta\dot\psi \tag{2.167}$$

$$0 = -L_\beta \delta\beta - L_p \delta p - L_r \delta r - L_{\dot\beta}\delta\dot\beta + \delta\dot p - L_{\delta_a}\delta(\delta_a) - L_{\delta_r}\delta(\delta_r) \tag{2.168}$$

$$0 = -N_\beta \delta\beta - N_p \delta p - N_r \delta r - N_{\dot\beta}\delta\dot\beta + \delta\dot r - N_{\delta_a}\delta(\delta_a) - N_{\delta_r}\delta(\delta_r) \tag{2.169}$$

2.4 AIRCRAFT STATE-SPACE REPRESENTATION

The aircraft model to be utilized in the FCS design contains the aircraft's longitudinal and lateral-directional motion description in the form of its state-space representation introduced in the previous section. As defined in previous section, it is possible to decouple the overall state-space model the longitudinal and lateral-directional motion. The condition for steady level flight can be defined by equations 2.170-2.175.

$$\beta = \phi = p = q = r = 0 \tag{2.170}$$

$$\dot V = \dot\alpha = \dot q = \dot\theta = \dot\gamma = \dot h = 0 \tag{2.171}$$

$$\dot\beta = \dot\phi = \dot\psi = \dot p = \dot r = 0 \tag{2.172}$$

$$V = V_0 \tag{2.173}$$

$$\alpha = \alpha_0 \tag{2.174}$$

$$\theta = \theta_0 \tag{2.175}$$

The subscript 0 in equations 2.173 - 2.175 denotes the trim condition. The longitudinal motion's state vector x_{lon} contains following listed flight quantities: airspeed V, angle of attack α, pitch rate q, flight path angle γ and altitude h. The input vector of longitudinal motion u_{lon} is composed of the throttle lever position δ_T and the elevator deflection δ_e. Based on linearized longitudinal equations 2.113 - 2.117 it is possible to express the components of the longitudinal state-space

model, i.e. the system dynamic matrix A_{lon} and system input matrix B_{lon}, that will be composed of coefficients computed during the linearization process. The experience shows, that derivatives $C_{L_{\dot{\alpha}}}$, $C_{D_{\dot{\alpha}}}$ and $C_{m_{\dot{\alpha}}}$ are very small, therefore the coefficients $Z_{\dot{\alpha}}$, $X_{\dot{\alpha}}$ and $M_{\dot{\alpha}}$ can be neglected, which simplifies the resulting state-space model.

Equations 2.176 through 2.179 introduce the longitudinal motion's state-space model with the state vector x_{lon} and the input vector u_{lon},

$$\dot{x}_{lon} = A_{lon}x_{lon} + B_{lon}u_{lon} \tag{2.176}$$

$$y_{lon} = C_{lon}x_{lon}, \tag{2.177}$$

where

$$x_{lon} = [V, \alpha, q, \gamma, h]^T \tag{2.178}$$

$$u_{lon} = [\delta_T, \delta_e]^T \tag{2.179}$$

Equations 2.180 and 2.181 introduce the internal structures of the longitudinal model's state matrix A_{lon} and the input matrix B_{lon} [87].

$$A_{lon} = \begin{bmatrix} X_V & X_\alpha & X_q & -g\cos(\gamma_0) & X_h \\ Z_V & Z_\alpha & Z_q + 1 & -\frac{g}{V_0}\cos(\gamma_0) & Z_h \\ M_V & M_\alpha & M_q & 0 & M_h \\ -Z_V & -Z_\alpha & -Z_q & \frac{g}{V_0}\cos(\gamma_0) & -Z_h \\ \sin(\gamma_0) & 0 & 0 & V_0\cos(\gamma_0) & 0 \end{bmatrix} \tag{2.180}$$

$$B_{lon} = \begin{bmatrix} X_{\delta_T} & X_{\delta_e} \\ Z_{\delta_T} & Z_{\delta_e} \\ M_{\delta_T} & M_{\delta_e} \\ -Z_{\delta_T} & -Z_{\delta_e} \\ 0 & 0 \end{bmatrix} \tag{2.181}$$

Variables X, Z, M are force and moment coefficients, that are constant for specified trim point condition defined by a combination of velocity and altitude, and are computed during linearization process derived in the previous section. Variables V_0, γ_0 are aircraft states at a trim point. In case of fully observable state vector, the output matrix C_{lon} from equation 2.177 is represented by a simple 5×5 identity matrix [37].

The lateral-directional motion model state x_{lat} is composed of flight quantities including sideslip angle β, roll angle ϕ, heading angle ψ, roll rate p and yaw rate r. Input variables of lateral-directional motion are the aileron δ_a and rudder δ_r deflections, which create the input vector u_{lat}. As the derivative of angle of sideslip doesn't have a significant effect on the lateral-directional model dynamics,

the related derivatives $Y_{\dot{\beta}}$, $L_{\dot{\beta}}$ and $N_{\dot{\beta}}$ can be neglected. This assumption simplifies the lateral-directional model's system matrix A_{lat} and input matrix B_{lat}.

The following equations define the state-space representation of lateral-directional dynamics [87].

$$\dot{x}_{lat} = A_{lat}x_{lat} + B_{lat}u_{lat} \tag{2.182}$$

$$y_{lat} = C_{lat}x_{lat} \tag{2.183}$$

$$x_{lat} = [\beta, \phi, \psi, p, r]^T \tag{2.184}$$

$$u_{lat} = [\delta_a, \delta_r]^T \tag{2.185}$$

Equations 2.186 and 2.187 introduce internal structures of the lateral-directional model's state matrix A_{lat} and the input matrix B_{lat}.

$$A_{lat} = \begin{bmatrix} Y_\beta & \frac{g}{V_0}\cos(\alpha_0) & 0 & Y_p + \sin(\alpha_0) & Y_r - \cos(\alpha_0) \\ 0 & 0 & 0 & 1 & \tan(\theta_0) \\ 0 & 0 & 0 & 0 & \frac{1}{\cos\theta_0} \\ L_\beta & 0 & 0 & L_p & L_r \\ N_\beta & 0 & 0 & N_p & N_r \end{bmatrix} \tag{2.186}$$

$$B_{lat} = \begin{bmatrix} Y_{\delta_a} & Y_{\delta_r} \\ 0 & 0 \\ 0 & 0 \\ L_{\delta_a} & L_{\delta_r} \\ N_{\delta_a} & N_{\delta_r} \end{bmatrix} \tag{2.187}$$

Variables Y, L, N are, similarly to the longitudinal case, the force and moment coefficients, which are constant for the specified trim point and are computed during the linearization process. Variables V_0, α_0, θ_0 again refer to aircraft state at trim point. The output matrix C_{lat} from equation 2.183 is a 5×5 the identity matrix as in the longitudinal motion, which means that all lateral-directional states are assumed to be observable.

3

AIRCRAFT SIMULATION MODEL

This chapter introduces the subsystems and mathematical background necessary for building an aircraft simulation model, which will be used throughout the following chapters as part of the researched designed flight control system framework. In fact, the Equations of Motion derived in the previous chapter and their linearized state-space models cover only one part of the model, namely the aircraft dynamics, as shown in Figure 3.1. The remaining necessary flight simulation subsystems will be described in the following sections. The chapter starts with a description of the mass, inertia and gravity models. The subsequent paragraphs are dedicated to the modeling of the propulsion system, and sensor and actuator dynamics. The sensor model is built up around a stochastic description of the measurement noise using the Allan variance technique to precisely express its noise characteristics. The dynamics of both, sensor and actuator models can be conveniently expressed using second-order transfer functions. The chapter continues with the description of the atmospheric model, which contains a detailed specification of the continuous turbulence model inevitable in the evaluation of the researched flight control system's performance. The final section describes in detail the aerodynamic model.

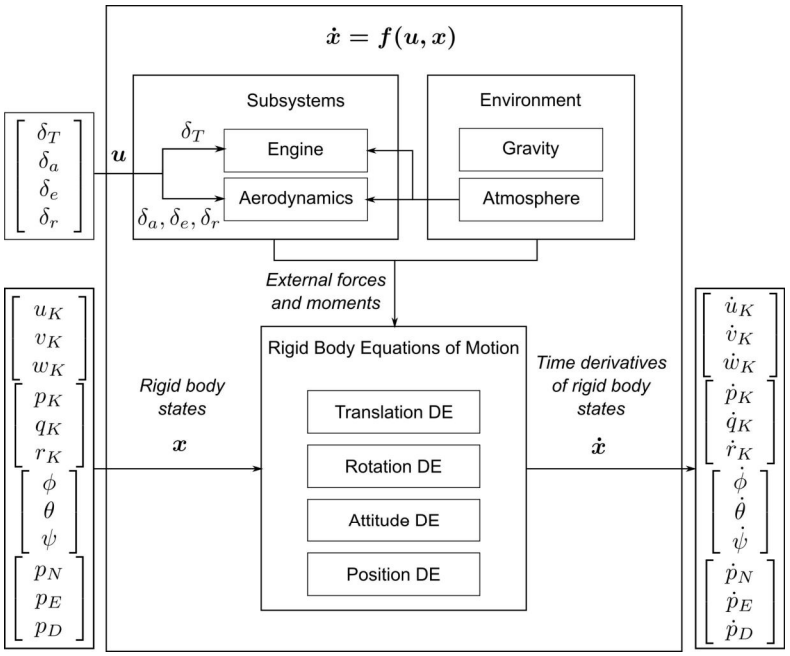

Figure 3.1: State representation of an aircraft simulation model. Source [39]

Chapter 3 is concluded with a description of a plant model, which is a combination of the aircraft and actuator dynamics. This model will be used in the subsequent chapters for the flight control system design.

3.1 MASS, INERTIA AND GRAVITY MODEL

The aircraft total weight m is computed as a sum of empty weight m_{conf} at specific balance configuration and weight of other elements m_i, accounting for the crew, fuel or payload [53]. Total weight calculation formula is shown in equation 3.1.

$$m = m_{conf} + \sum_i m_i \tag{3.1}$$

An instantaneous CG position x_{CG} is defined by elementary weights and associated known CG positions of respective configuration elements using equation 3.2.

$$x_{CG} = \frac{x_{CG_{conf}} m_{conf} + \sum_i x_{CG_i} m_i}{m} \tag{3.2}$$

In order to calculate the rotational dynamics of a simulated aircraft, it is inevitable to carefully compose the resulting inertia tensor $\boldsymbol{I}_{BB}$ [35, 49]. Equation 3.3 shows the inertia tensor's structure, while equations 3.4-3.9 introduce the tensor's elements computation.

$$\boldsymbol{I}_{BB} = \begin{bmatrix} I_{xx} & -I_{xy} & -I_{xz} \\ -I_{xy} & I_{yy} & -I_{yz} \\ -I_{xz} & -I_{yz} & I_{zz} \end{bmatrix} \tag{3.3}$$

$$I_{xx} = \int_m (y^2 + z^2) dm \tag{3.4}$$

$$I_{yy} = \int_m (x^2 + z^2) dm \tag{3.5}$$

$$I_{zz} = \int_m (x^2 + y^2) dm \tag{3.6}$$

$$I_{xy} = \int_m (xy) dm \tag{3.7}$$

$$I_{yz} = \int_m (yz) dm \tag{3.8}$$

$$I_{xz} = \int_m (xz) dm \tag{3.9}$$

The Gravity model is defined by force and moment vectors shown in equations 3.10-3.11, along with their transformations from NED frame to BFF. These transformations are necessary from the model compatibility perspective as other models as aerodynamics or propulsion are developed in BFF [89].

$$(\vec{F}_G)_B = M_{BO} \cdot \begin{bmatrix} X_G \\ Y_G \\ Z_G \end{bmatrix}_0 = M_{BO} \cdot \begin{bmatrix} 0 \\ 0 \\ m \cdot g \end{bmatrix}_0 \tag{3.10}$$

$$(\vec{M}_G)_B = M_{BO} \cdot \begin{bmatrix} L_G \\ M_G \\ N_G \end{bmatrix}_0 = \vec{0} \tag{3.11}$$

3.2 PROPULSION SYSTEM MODEL

The thrust of a propulsion system, made of for example 4-stroke reciprocity combustion engine and propeller, is computed using propeller characteristics containing advance ratio J, thrust coefficient C_T, propeller diameter D_{prop} and propeller or engine revolutions n_{prop}. At first, the advance ratio is defined by equation 3.12.

$$J = \frac{V}{n_{prop} D_{prop}} \tag{3.12}$$

The thrust coefficient C_T can be defined as a function of the advance ratio J. Using the state-of-the-art engineering practice is to approximate this function by a lookup table. The last step is expressing the thrust T using equation 3.13 [83].

$$T = C_T \rho n_{prop}^2 D^4 \tag{3.13}$$

The engine model can be defined using a function relating the engine revolutions to the throttle lever position and the instantaneous operating condition.

3.3 ACTUATOR MODEL

An important aspect of a digital FCS design is the consideration of the actuator's dynamic effects. The modeled actuator dynamics, with its time delays, influences the aircraft's overall dynamic behavior. The actuator model dynamics can be described by a second order transfer function, with properties expressed in terms of its natural frequency ω_{act} and damping ζ_{act} as shown in the equation (3.14) [30].

$$F_{act}(s) = \frac{\omega_{act}^2}{s^2 + 2\zeta_{act}\omega_{act}s + \omega_{act}^2} \tag{3.14}$$

To conveniently combine the actuator model with the state-space representations of the aircraft's longitudinal and lateral-directional motion, the transfer function $F_{act}(s)$ can be transformed into its state-space representation as introduced in equations (3.15) and (3.16).

$$\dot{x}_{act} = A_{act}x_{act} + B_{act}u_{act} \tag{3.15}$$

$$y_{act} = C_{act}x_{act} \tag{3.16}$$

The actuator's state-space model for longitudinal motion contains a state vector composed of the throttle and elevator deflections along with their associated deflection rates. The actuator model inputs for the longitudinal motion are the respective command values defined in the equation 3.19. The lateral-directional state-space actuator model, on the other hand, contains a state vector composed of aileron and rudder deflections and their associated rates. The actuator model inputs for the lateral-directional motion are the command values defined by equation 3.20. Equations 3.17 and 3.18 show the actuator model state vectors for the longitudinal and lateral-directional motion cases, while equations 3.19 and 3.20, as stated above, show the respective actuator model input vectors for the longitudinal and lateral-directional case.

$$x_{act,lon} = \left[\dot{\delta}_T, \delta_T, \dot{\delta}_e, \delta_e\right]^T \tag{3.17}$$

$$x_{act,lat} = \left[\dot{\delta}_a, \delta_a, \dot{\delta}_r, \delta_r\right]^T \tag{3.18}$$

$$u_{act,lon} = \left[\delta_{T_{cmd}}, \delta_{e_{cmd}}\right]^T \tag{3.19}$$

$$u_{act,lat} = \left[\delta_{a_{cmd}}, \delta_{r_{cmd}}\right]^T \tag{3.20}$$

The actuator's state matrix A_{act}, input matrix B_{act} and output matrix C_{act} are introduced in equations 3.21, 3.22, 3.23, 3.24 and 3.25 respectively, and have the same structure for both, the longitudinal and the lateral-directional motion.

$$A_{act,lon} = \begin{bmatrix} -2\zeta_{\delta_T}\omega_{\delta_T} & -\omega_{\delta_T}^2 & 0 & 0 \\ 1 & 0 & 0 & 0 \\ 0 & 0 & -2\zeta_{\delta_e}\omega_{\delta_e} & -\omega_{\delta_e}^2 \\ 0 & 0 & 1 & 0 \end{bmatrix} \tag{3.21}$$

$$B_{act,lon} = \begin{bmatrix} \omega_{\delta_T}^2 & 0 \\ 0 & 0 \\ 0 & \omega_{\delta_e}^2 \\ 0 & 0 \end{bmatrix} \tag{3.22}$$

Variables ζ and ω represent the actuator's damping and natural frequency for thrust and elevator actuator model, respectively. This model is a part of the longitudinal dynamics.

$$A_{act,lat} = \begin{bmatrix} -2\zeta_{\delta_a}\omega_{\delta_a} & -\omega_{\delta_a}^2 & 0 & 0 \\ 1 & 0 & 0 & 0 \\ 0 & 0 & -2\zeta_{\delta_r}\omega_{\delta_r} & -\omega_{\delta_r}^2 \\ 0 & 0 & 1 & 0 \end{bmatrix} \tag{3.23}$$

$$B_{act,lat} = \begin{bmatrix} \omega_{\delta_a}^2 & 0 \\ 0 & 0 \\ 0 & \omega_{\delta_r}^2 \\ 0 & 0 \end{bmatrix} \tag{3.24}$$

The lateral-directional motion's actuator model contains natural frequency ω and damping ζ characteristics differentiated by subscripts δ_a, δ_r for the aileron and the rudder control respectively.

The output matrix C_{act} introduced in the equation (3.25) is identical for both, the longitudinal and the lateral-directional actuator model, and consist of only two rows, as only the control surface deflections, without the respective rates, are assumed to be measurable [51].

$$C_{act} = \begin{bmatrix} 0 & 1 & 0 & 0 \\ 0 & 0 & 0 & 1 \end{bmatrix} \tag{3.25}$$

3.4 SENSOR MODEL

An unmanned aircraft's sensor network contains several measurement units that influence aircraft state variables in a different manner. The aircraft's accelerations, angular rates and Euler angles can be measured by Micro Electro Mechanical System (MEMS) IMU, usually equipped with a magnetometer to sense the magnetic field. The airspeed and pressure altitude are acquired through a pitot-static system. Finally, the position of an aircraft is sensed by a GNSS receiver. Almost all sensors add some errors into the measurement, either it is noise, drift or time delay.

3.4.1 *Sensor dynamics*

State-of-the-art sensors for UAV applications are mostly based on the MEMS technology. The dynamics of such sensor can be conveniently modeled as a second-order linear system and described by a transfer function. Example of sensor transfer function is shown in equation 3.26.

$$F_{sens}(s) = \frac{\omega_{sens}^2}{s^2 + 2\zeta_{sens}\omega_{sens}s + \omega_{sens}^2} \tag{3.26}$$

The sensor dynamics is characterized by its natural frequency ω_{sens} and by the sensor damping ζ_{sens}. A block diagram of sensor dynamics implementation is shown in Figure 3.2.

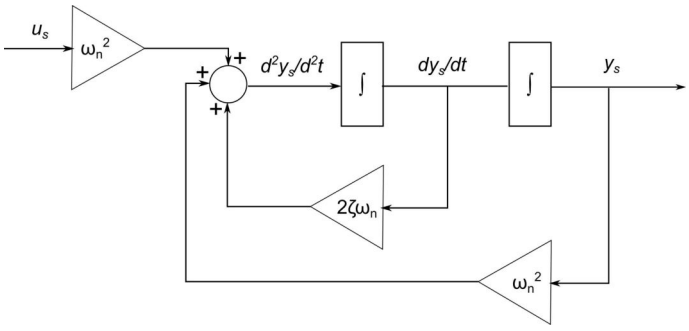

Figure 3.2: Block diagram of sensor dynamics.

3.4.2 *Noise characteristics estimation*

This section describes the process of sensor noise and bias estimations, which are needed for high fidelity sensor modeling. Once estimated these parameters are added to the clean signal in order to create precise sensor output signal comparable to the real sensor output. The sensor bias can be computed through the utilization of a simple mean calculation over selected signal length under steady conditions,

as described in equation 3.27. In the case of specific forces, the signal needs to be compensated for gravity effects [42].

$$b = \frac{1}{N}\sum_{i=1}^{N} A_i \tag{3.27}$$

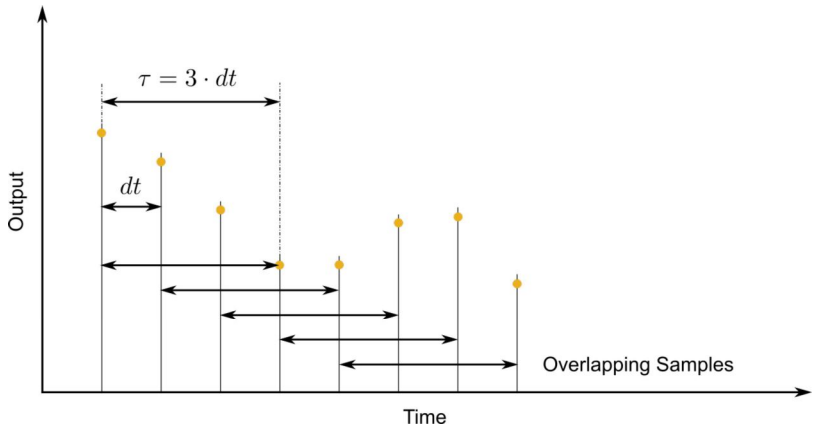

Figure 3.3: Time clusters for Allan variance calculation.

Signal noise power can be estimated by employing the Allan variance technique. This method is usually applicable to oscillator frequency stability measurements. The advantage of this approach is that it can be used without data-sheet information and based only on the measured sensor signal. For this thesis's purpose, the Allan variance calculation of a gyroscope signal will be used for the algorithm explanation. The first step of computing Allan variance is the integration of measured angular velocity samples $\omega(t)$ over the time span t, which results in angle $\theta(t)$.

The Allan variance $\sigma^2(\tau)$ can be computed as a function of τ and $<>$, which is an expression for ensemble average. Equation 3.28 shows the Allan variance formula

$$\sigma^2(\tau) = \frac{1}{2\tau^2} < (\theta_{k+2m} - 2\theta_{k+m} + \theta_k)^2 > \tag{3.28}$$

Variable τ is the so called cluster time, and its width is defined by the parameter m as defined in the following equation.

$$\tau = m \cdot dt \tag{3.29}$$

After explaining ensemble average, the result could be written by equation 3.30.

$$\sigma^2(\tau) = \frac{1}{2\tau^2(N-2m)} \sum_{k=1}^{N-2m} \left[(\theta_{k+2m} - 2\theta_{k+m} + \theta_k)^2\right] \tag{3.30}$$

The parameter N is the total number of samples and m, as mentioned above, the number of samples in an overlapping cluster time τ. This version of Allan variance algorithm is called overlapping due to the time clusters defined by the

parameter τ being overlapping, as shown in Figure 3.3. The noise characteristics can be estimated using the above-defined algorithm in a laboratory experiment, in which accelerometer and gyroscope signals are recorded under steady conditions. The noise characteristics are then extracted from measured signals. Figure 3.4 shows the Allan variance in all three axes of acceleration measurements. The Allan variance value used for the noise signal generation is the functional value of

$$\tau = 10^0 \tag{3.31}$$

Figure 3.5 shows the measured acceleration noise in steady conditions and the generated acceleration noise signal using Allan variance.

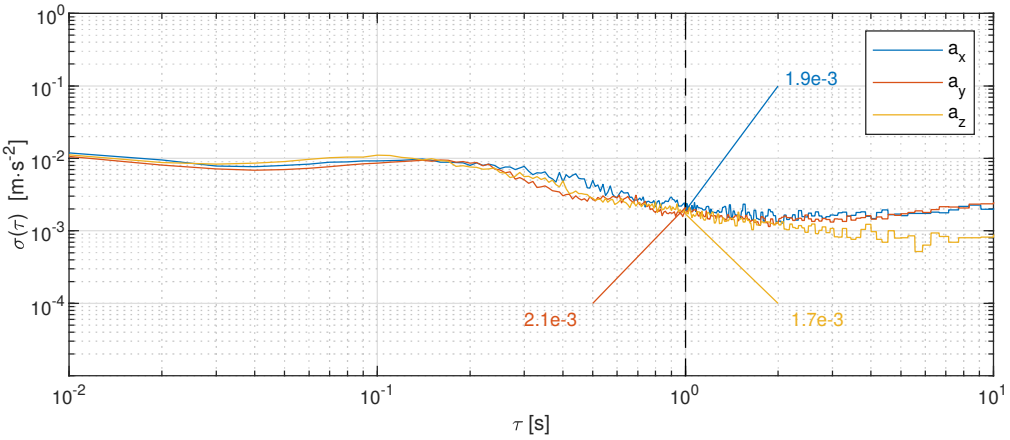

Figure 3.4: Allan variance of acceleration measurements.

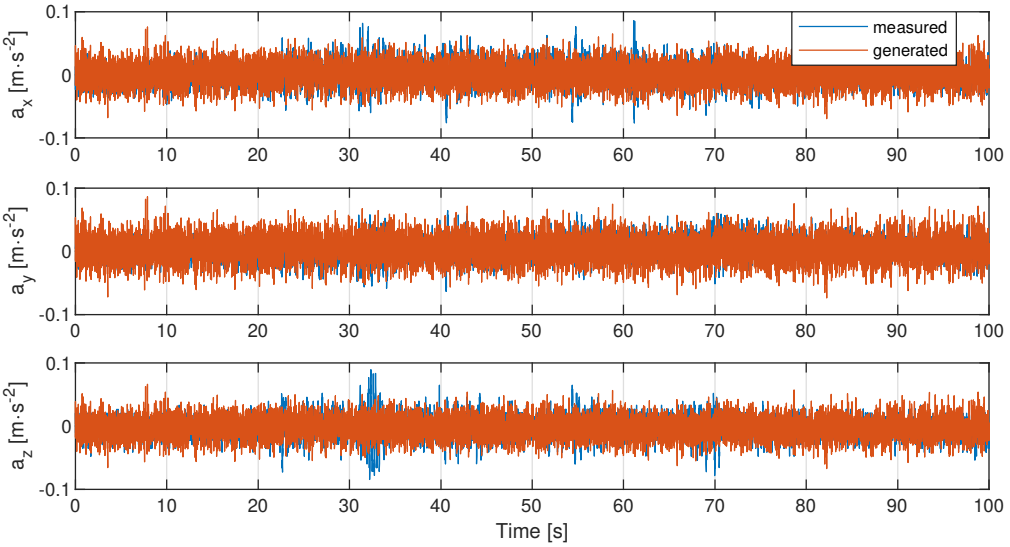

Figure 3.5: Noisy acceleration signals in three axes.

The same process of Allan variance estimation can be applied to measurements of angular velocities. Figure 3.6 shows Allan variances of gyroscope measurements and Figure 3.7 depicts the comparison of measured angular rate noise and generated angular rate noise with the utilization of the Allan variance method.

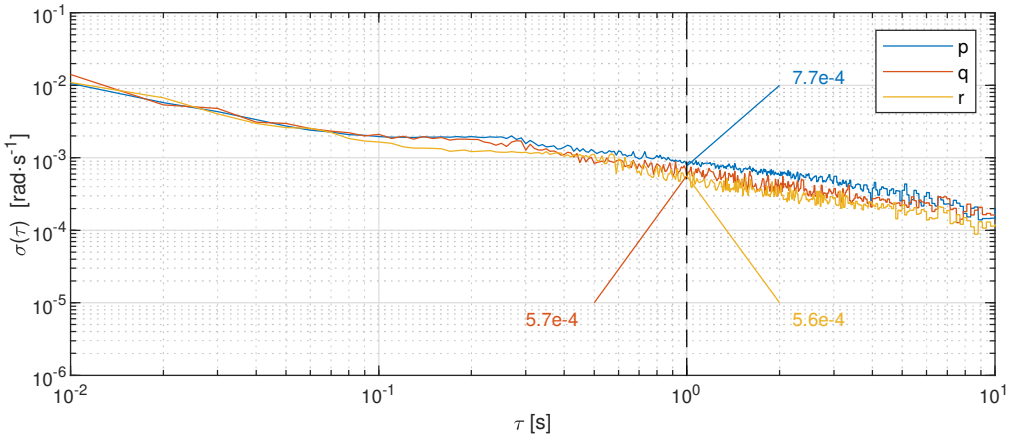

Figure 3.6: Allan variance of angular rate measurements.

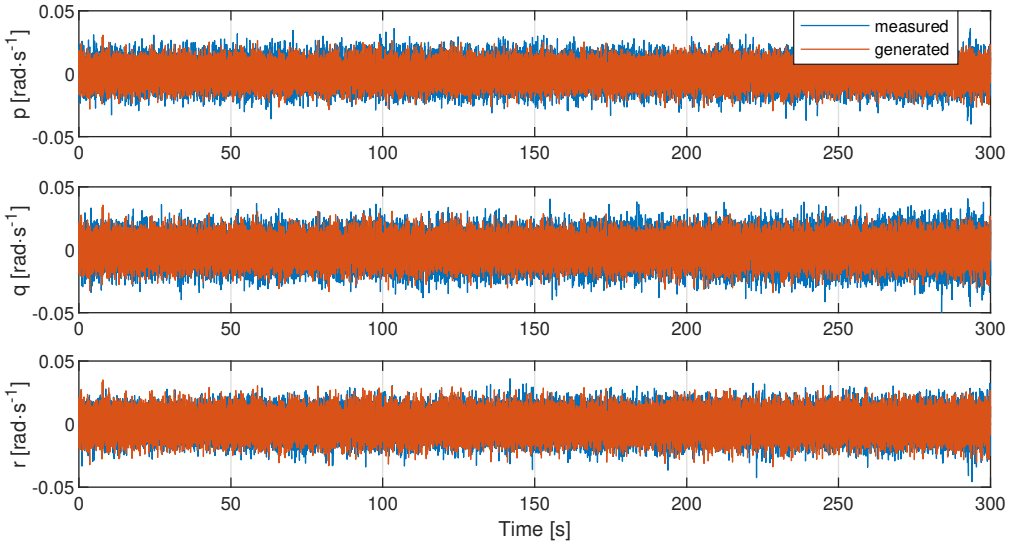

Figure 3.7: Noisy angular rate signals in three axes.

3.5 ATMOSPHERIC MODEL

Future implementations of an aircraft dynamic model include an atmospheric model compliant to the international standard ISO 2533, which is useful for altitude ranges from -2 to 20 km (from the troposphere to lower stratosphere)[48]. This model is used to calculate important physical quantities, namely the air temperature T, air density ρ, Mach number M and dynamic pressure $\bar{q}$. The first step in using the ISO 2533 model is to calculate the geopotential height H_G, which is necessary for the calculation of the air temperature, static pressure and air density.

$$H_G = \frac{r_E \cdot h}{r_E + h} \tag{3.32}$$

Following expressions define the above mentioned physical quantities for geopotential heights from -2 to 11 km:

$$T = (1 + \gamma_{TR} \cdot \frac{H_G}{T_S}) \cdot T_S \tag{3.33}$$

Table 3.1: Atmospheric constants.

Name	Nomenclature	Value	Units
Sea Level Temperature	T_S	288.15	[K]
Sea Level Density	ρ_S	1.225	$[kg \cdot m^{-3}]$
Sea Level Pressure	p_S	1.013×10^5	[Pa]
Troposphere constant	n_{TR}	1.235	[1]
Lapse Rate	γ_{TR}	-6.5×10^{-3}	$[K \cdot m^{-1}]$
11 Km Temperature	T_{11}	216.65	[K]
11 Km Density	ρ_{11}	0.364	$[kg \cdot m^{-3}]$
11 Km Pressure	p_{11}	2.263×10^4	[Pa]
Ideal Gas Constant	R	287.05	$[J \cdot kg^{-1}K^{-1}]$
Adiabatic index	κ	1.41	[1]

$$p_{stat} = (1 + \gamma_{TR} \cdot \frac{H_G}{T_S})^{\frac{n_{TR}}{n_{TR}-1}} \cdot p_S \tag{3.34}$$

$$\rho = (1 + \gamma_{TR} \cdot \frac{H_G}{T_S})^{\frac{1}{n_{TR}-1}} \cdot \rho_S \tag{3.35}$$

The isothermal character of the stratosphere higher layers leads to different modified for temperature, static pressure and air density computation for altitudes between 11 and 20 km. Constants for both atmospheric layers are given in Table 3.1.

$$T = T_{11} \tag{3.36}$$

$$p_{stat} = p_{11} \cdot e^{-\frac{g_0}{R \cdot T_{11}} \cdot (H_G - 11000)} \tag{3.37}$$

$$\rho = \rho_{11} \cdot e^{-\frac{g_0}{R \cdot T_{11}} \cdot (H_G - 11000)} \tag{3.38}$$

Finally, with the availability for the air density and airspeed, it is possible to define the dynamic pressure and Mach number essential for expressing aerodynamic forces and moments.

$$\bar{q} = \frac{1}{2} \cdot \rho \cdot V \tag{3.39}$$

$$M = \frac{V}{\sqrt{\kappa \cdot R \cdot T}} \tag{3.40}$$

3.5.1 *Continuous Atmospheric Turbulence Model*

The continuous atmospheric turbulence model as described in this thesis was taken from the standard MIL-HDBK-1797 [23]. The model estimates continuous turbulence contributions to aircraft translational and rotational velocities based on the aircraft altitude, velocity, attitude and user setting of wind speed at 20ft altitude (low altitude model) supplemented by the probability of exceedance coefficient (high altitude model). The user may adjust parameters according to requested turbulence severity. Table 3.2 shows parameter settings for 3 levels of turbulence severity: light, moderate and severe.

Table 3.2: Severity parameters for high and low altitude conditions turbulence models.

Severity	**Wind velocity at 20 ft [kts]**	**Probability of exceedance [1]**
Light	15	10^{-2}
Moderate	30	10^{-3}
Severe	45	10^{-5}

3.5.1.1 *Forming Filters*

Equations 3.41-3.46 describe linear filters which process white noise on input and generate transtational and rotational velocities affecting the aircraft state. Linear filter parameters are adjusted with respect to scale lengths L_u, L_v, L_w, turbulence intensities $\sigma_u, \sigma_v, \sigma_w$, aircraft airspeed V and altitude h. Filter structure is identical for low and high altitude conditions. Following subsection describes differences in scale lengths and turbulence intensities. Parameter b_w represents the aircraft's wing span [23].

$$F_u(s) = \sigma_u \sqrt{\frac{2L_u}{\pi V}} \cdot \frac{1}{1 + \frac{L_u}{V}s} \tag{3.41}$$

$$F_v(s) = \sigma_v \sqrt{\frac{L_v}{\pi V}} \cdot \frac{1 + \frac{\sqrt{3}L_v}{V}s}{(1 + \frac{L_v}{V}s)^2} \tag{3.42}$$

$$F_w(s) = \sigma_w \sqrt{\frac{L_w}{\pi V}} \cdot \frac{1 + \frac{\sqrt{3}L_w}{V}}{(1 + \frac{L_w}{V}s)^2} \tag{3.43}$$

$$F_p(s) = \sigma_w \sqrt{\frac{0.8}{V}} \cdot \frac{(\frac{\pi}{4b_w})^{1/6}}{L_w^{1/3}(1 + (\frac{4b_w}{\pi V})s)} \tag{3.44}$$

$$F_q(s) = \frac{\pm\frac{s}{V}}{1 + (\frac{4b_w}{\pi V})s} \cdot F_w(s) \tag{3.45}$$

$$F_r(s) = \frac{\pm\frac{s}{V}}{1 + (\frac{3b_w}{\pi V})s} \cdot F_v(s) \tag{3.46}$$

3.5.1.2 *Low Altitude Model*

The low altitude model describes scale lengths and turbulence intensities for altitudes below 1000 ft. Scale lengths are affected only by the aircraft altitude, while turbulence intensities are influenced by wind speed W_{20} at 20ft above the ground. The velocity vector orientation in low altitude model is defined in the BFF [23].

$$L_u = L_v = \frac{h}{(0.177 + 0.000823h)^{1.2}} \tag{3.47}$$

$$L_w = h \tag{3.48}$$

$$\sigma_w = 0.1W_{20} \tag{3.49}$$

$$\sigma_u = \sigma_v = \frac{\sigma_w}{(0.177 + 0.000823h)^{0.4}} \tag{3.50}$$

3.5.1.3 *Medium/High Altitude Model*

The high altitude model describes turbulence behavior above 2000 ft. The scale lengths are constant as shown in equation 3.51, and turbulence intensities are defined by a 2D lookup table, the graphical representation of which is shown in Figure 3.8. Inputs to the lookup table are the aircraft altitude and the probability of exceedance, set by the user according to requested turbulence severity. The velocity vector of the high altitude model is defined in BFF.

$$L_u = L_v = L_w = 1750\text{ft} \tag{3.51}$$

$$\sigma_u = \sigma_v = \sigma_w \tag{3.52}$$

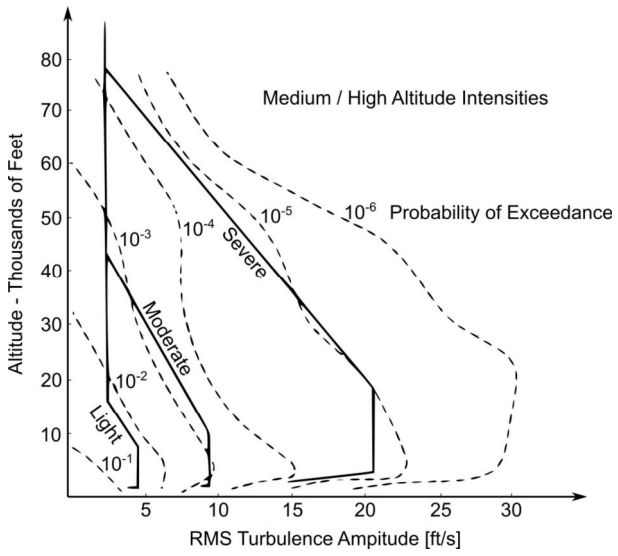

Figure 3.8: Continuous turbulence intensities based on the probability of exceedance. Source [23]

The medium altitude velocities and angular rates between 1000 ft and 2000 ft are determined as a linear interpolation between low and high altitude results and are expressed in the BFF axis frame [23].

3.5.1.4 *Turbulence Model Structure*

The inputs to the turbulence model described by a block diagram in Figure 3.9 are the geodetic altitude h, Euler angles ϕ, θ, ψ, airspeed V, wind speed at 20 ft above ground W_{20} and the probability of exceedance. Outputs that influence the aircraft simulation model are turbulence induced velocities and angular rates in BFF. The turbulence model contains three main subsystems, as shown in Figure 3.9, the Low Altitude Model, the High Altitude Model, and the function for assembling the turbulence contributions. The white noise generator block computes turbulence intensities and scale lengths. The Turbulence Filter blocks include implementation of linear filters from equations 3.41-3.46.

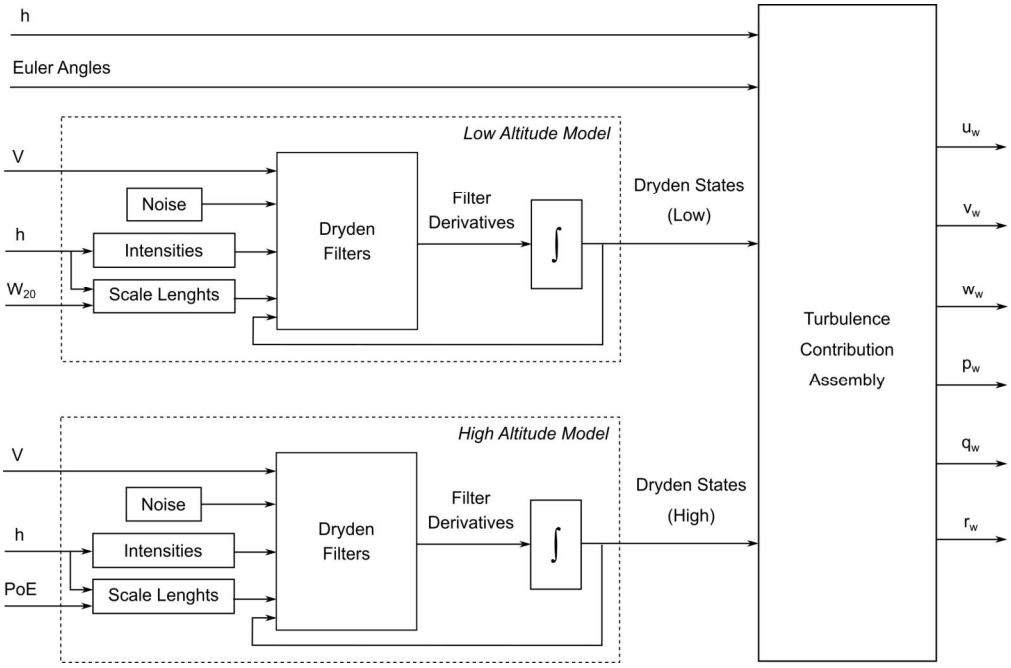

Figure 3.9: Continuous atmospheric turbulence model.

3.6 AERODYNAMIC MODEL

Aerodynamic forces and moments are influenced by the shape of the aircraft and its configuration. Equations 3.53 and 3.54 introduce aerodynamic forces and moments as functions of the mean aerodynamic chord $\bar{c}$, wing area S, wingspan b_w, air density ρ, airspeed V, and aerodynamic force and moment coefficients of the modeled aircraft [60].

$$\begin{bmatrix} D \\ Q \\ L \end{bmatrix} = \underbrace{\frac{1}{2}\rho V^2 S}_{\bar{q}} \begin{bmatrix} C_D \\ C_Q \\ C_L \end{bmatrix} \tag{3.53}$$

$$\begin{bmatrix} L_A \\ M_A \\ N_A \end{bmatrix} = \underbrace{\frac{1}{2}\rho V^2 S}_{\bar{q}} \begin{bmatrix} b_w & 0 & 0 \\ 0 & \bar{c} & 0 \\ 0 & 0 & b_w \end{bmatrix} \begin{bmatrix} C_l \\ C_m \\ C_n \end{bmatrix} \tag{3.54}$$

Applicable drag C_D, side-force C_Q and lift C_L coefficients, together with the roll C_l, pitch C_m and yaw C_n moment coefficients are defined by the following set of equations [51, 87].

$$C_D = C_{D_0} + C_{D_\alpha}\alpha + C_{D_{\dot{\alpha}}}\frac{\dot{\alpha}\bar{c}}{2V} + C_{D_q}\frac{q\bar{c}}{2V} + C_{D_{\delta_e}}\delta_e \tag{3.55}$$

$$C_Q = C_{Q_\beta}\beta + C_{Q_{\dot{\beta}}}\frac{\dot{\beta}b_w}{2V} + C_{Q_p}\frac{pb_w}{2V} + C_{Q_r}\frac{rb_w}{2V} + C_{Q_{\delta_a}}\delta_a + C_{Q_{\delta_r}}\delta_r \tag{3.56}$$

$$C_L = C_{L_0} + C_{L_\alpha}\alpha + C_{L_{\dot{\alpha}}}\frac{\dot{\alpha}\bar{c}}{2V} + C_{L_q}\frac{q\bar{c}}{2V} + C_{L_{\delta_e}}\delta_e \tag{3.57}$$

$$C_l = C_{l_\beta}\beta + C_{l_{\dot{\beta}}}\frac{\dot{\beta}b_w}{2V} + C_{l_p}\frac{pb_w}{2V} + C_{l_r}\frac{rb_w}{2V} + C_{l_{\delta_a}}\delta_a + C_{l_{\delta_r}}\delta_r \tag{3.58}$$

$$C_m = C_{m_0} + C_{m_\alpha}\alpha + C_{m_{\dot{\alpha}}}\frac{\dot{\alpha}\bar{c}}{2V} + C_{m_q}\frac{q\bar{c}}{2V} + C_{m_{\delta_e}}\delta_e \tag{3.59}$$

$$C_n = C_{n_\beta}\beta + C_{n_{\dot{\beta}}}\frac{\dot{\beta}b_w}{2V} + C_{n_p}\frac{pb_w}{2V} + C_{n_r}\frac{rb_w}{2V} + C_{n_{\delta_a}}\delta_a + C_{n_{\delta_r}}\delta_r \tag{3.60}$$

3.7 PLANT MODEL

The plant model is made of a combination of the aircraft and the actuator state-space model connected via control surface deflections. The output of the plant is a combination of the already defined state vector of the longitudinal or lateral-directional aircraft model and the actuator state as defined by the equation 3.61

$$x_{pl} = [x_{lat/lon}, x_{act}]^T \tag{3.61}$$

The plant system for a longitudinal and lateral-directional motion can be defined by equations 3.62 and 3.63.

$$\dot{x}_{pl} = \underbrace{\begin{bmatrix} A_{lat/lon} & B_{lat/lon}C_{act} \\ 0^{4\times5} & A_{act} \end{bmatrix}}_{A_{pl}} x_{pl} + \underbrace{\begin{bmatrix} 0^{5\times2} \\ B_{act} \end{bmatrix}}_{B_{pl}} u_{act} \tag{3.62}$$

$$y_{pl} = \underbrace{\begin{bmatrix} 1 & 0 \end{bmatrix}}_{C_{pl}} \begin{bmatrix} x_{lon/lat} \\ x_{act} \end{bmatrix} \tag{3.63}$$

When assigning equations 2.180, 2.181, 3.21, 3.22 to the equation 3.62 we get the plant dynamic matrix $A_{pl\,lon}$ expressed by the equation 3.64 and input matrix $B_{pl\,lon}$ shown in equation 3.65.

$$A_{pl\,lon} = \begin{bmatrix} X_V & X_\alpha & X_q & -g\cos\gamma_0 & X_h & 0 & X_{\delta_T} & 0 & X_{\delta_e} \\ Z_V & Z_\alpha & Z_q & -\frac{g}{V_0}\cos\gamma_0 & Z_h & 0 & Z_{\delta_T} & 0 & Z_{\delta_e} \\ 0 & M_\alpha & 0 & M_q & M_h & 0 & M_{\delta_T} & 0 & M_{\delta_e} \\ -Z_V & -Z_\alpha & -Z_q & +\frac{g}{V_0}\cos\gamma_0 & -Z_h & 0 & 0 & 0 & 0 \\ \sin\gamma_0 & 0 & 0 & -V_0\cos\gamma_0 & 0 & 0 & 0 & 0 & 0 \\ 0 & 0 & 0 & 0 & 0 & -2\zeta_{\delta_T}\omega_{\delta_T} & -\omega_{\delta_T}^2 & 0 & 0 \\ 0 & 0 & 0 & 0 & 0 & 1 & 0 & 0 & 0 \\ 0 & 0 & 0 & 0 & 0 & 0 & 0 & -2\zeta_{\delta_e}\omega_{\delta_e} & -\omega_{\delta_e}^2 \\ 0 & 0 & 0 & 0 & 0 & 0 & 0 & 1 & 0 \end{bmatrix} \tag{3.64}$$

$$B_{pl\,lon} = \begin{bmatrix} 0 & 0 \\ 0 & 0 \\ 0 & 0 \\ 0 & 0 \\ 0 & 0 \\ \omega_{\delta_T}^2 & 0 \\ 0 & 0 \\ 0 & \omega_{\delta_e}^2 \\ 0 & 0 \end{bmatrix} \tag{3.65}$$

The dynamic matrix of lateral-directional plant model is shown in equation 3.66. Similarly, as the input matrix of longitudinal plant model, we can describe the input matrix of the lateral-directional plant model by equation 3.67

$$A_{pllat} = \begin{bmatrix} Y_\beta & \frac{g}{V_0} & 0 & Y_p + s(\alpha_0) & Y_r - c(\alpha_0) & 0 & Y_{\delta_a} & 0 & Y_{\delta_r} \\ 0 & 0 & 0 & 1 & t(\theta_0) & 0 & 0 & 0 & 0 \\ 0 & 0 & 0 & 0 & \frac{1}{c(\theta_0)} & 0 & 0 & 0 & 0 \\ L_\beta & 0 & 0 & L_p & L_r & 0 & L_{\delta_a} & 0 & L_{\delta_r} \\ N_\beta & 0 & 0 & N_p & N_r & 0 & N_{\delta_a} & 0 & N_{\delta_r} \\ 0 & 0 & 0 & 0 & 0 & -2\zeta_{\delta_a}\omega_{\delta_a} & -\omega_{\delta_a}^2 & 0 & 0 \\ 0 & 0 & 0 & 0 & 0 & 1 & 0 & 0 & 0 \\ 0 & 0 & 0 & 0 & 0 & 0 & 0 & -2\zeta_{\delta_r}\omega_{\delta_r} & -\omega_{\delta_r}^2 \\ 0 & 0 & 0 & 0 & 0 & 0 & 0 & 1 & 0 \end{bmatrix} \tag{3.66}$$

$$B_{pllat} = \begin{bmatrix} 0 & 0 \\ 0 & 0 \\ 0 & 0 \\ 0 & 0 \\ 0 & 0 \\ \omega_{\delta_a}^2 & 0 \\ 0 & 0 \\ 0 & \omega_{\delta_r}^2 \\ 0 & 0 \end{bmatrix} \tag{3.67}$$

Both dynamic and input matrices of longitudinal and lateral-directional plant models contain information about the aircraft and actuator dynamics. Equation 3.68 describes the output matrix, which is the same for the longitudinal, as well as lateral-directional plant model. The plant model is shown in a form in which it will be later utilized in the sections dedicated to the FCS design process.

$$C_{pl} = \begin{bmatrix} 1 & 0 & 0 & 0 & 0 & 0 & 0 & 0 & 0 \\ 0 & 1 & 0 & 0 & 0 & 0 & 0 & 0 & 0 \\ 0 & 0 & 1 & 0 & 0 & 0 & 0 & 0 & 0 \\ 0 & 0 & 0 & 1 & 0 & 0 & 0 & 0 & 0 \\ 0 & 0 & 0 & 0 & 1 & 0 & 0 & 0 & 0 \end{bmatrix} \tag{3.68}$$

4

PARAMETER ESTIMATION

The process of building an aircraft mathematical model from flight testing campaigns generally relies on System Identification techniques. The aim of this chapter is introduce the aerodynamic model parameter estimation algorithms. There are two main approaches to creating models. The first one is called the mathematical modeling and is based on the knowledge of laws of physics used for the description of system dynamics. This approach is rather analytical. The other approach uses the system's input-output data collected during test campaigns. This approach is rather experimental. The analytical approach has limited use in modeling systems with complex structure and unknown parameters. At this point, the parameter estimation approach on experimental data needs to be used. The mathematical models obtained through identification have following features:

- It is relatively easy to create them, but their validity can be limited to the surroundings of a certain working point.
- Mathematical models created via identification usually do not have true physical meaning.
- Assistance of domain expert is usually necessary during the process of the mathematical model identification.

The expert opinion about choosing the right model structure or selecting and pre-processing the correct input-output data for parameter estimation can be a better strategy than performing the trial and error process of choosing the right model structure and data set.

The motivation for creating mathematical models can be driven from the desire of better understanding the modeled systems. An identified mathematical model of an aircraft can be employed either in the process of control system design or for creating high fidelity flight simulators. The identified aircraft model can be used for a baseline FCS design and can also serve as a reference model in the adaptive flight control design , which will be introduced in the subsequent chapters. Figure 4.1 describes a general aircraft parameter estimation process using the input-output data, a priory model values and selected model structure.

Following paragraphs will introduce the basic aerodynamic model structure used in the parameter estimation along with the Equation Error Method estimation technique, which will be explained later. The chapter is concluded with the

input-output data used for the identification along with the resulting model. The estimation algorithms presented in this chapter are inspired by [49, 51]. The interested reader is referred to [28, 33, 61, 70] for more in-depth insight into system identification and parameter estimation.

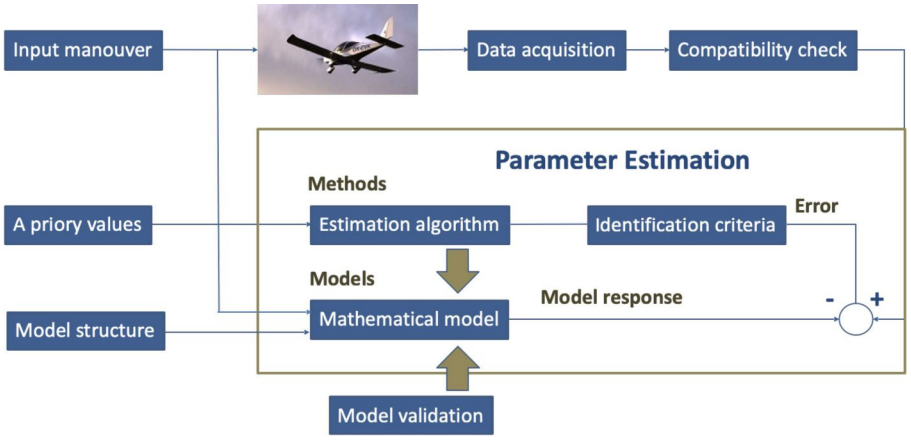

Figure 4.1: System identification process.

4.1 MODEL FOR PARAMETER ESTIMATION

The aircraft model used for parameter estimation describes contains a structure made of force and moment coefficients. Equations 4.1 - 4.6 show a sample model structure that to be used for actual parameter estimation.

$$C_D = C_{D_0} + C_{D_\alpha}\alpha + C_{D_{\delta_e}}\delta_e \tag{4.1}$$

$$C_Y = C_{Y_0} + C_{Y_\beta}\beta + C_{Y_{\delta_r}}\delta_r \tag{4.2}$$

$$C_L = C_{L_0} + C_{L_0}\alpha + C_{L_{\delta_e}}\delta_e \tag{4.3}$$

$$C_l = C_{l_0} + C_{l_\beta}\beta + C_{l_{\delta_a}}\delta_a + C_{l_{\delta_r}}\delta_r + C_{l_p}\frac{pb_w}{2V} + C_{l_r}\frac{rb_w}{2V} \tag{4.4}$$

$$C_m = C_{m_0} + C_{m_\alpha}\alpha + C_{m_{\delta_e}}\delta_e + C_{m_q}\frac{q\bar{c}}{2V} \tag{4.5}$$

$$C_n = C_{n_0} + C_{n_\beta}\beta + C_{n_{\delta_a}}\delta_a + C_{n_{\delta_r}}\delta_r + C_{n_p}\frac{pb_w}{2V} + C_{n_r}\frac{rb_w}{2V} \tag{4.6}$$

The model can be described in a simplified form by equation 4.7.

$$z = X\theta_P + \nu \tag{4.7}$$

where the parameters to be estimated are formed in the vector θ_P. An example of the parameter vector for a roll moment coefficient C_l is shown in equation 4.8.

$$\theta_P = [C_{l_0}, C_{l_\beta}, C_{l_{\delta_a}}, C_{l_{\delta_r}}, C_{l_p}, C_{l_r}]^T \tag{4.8}$$

The vector of measured states, called regressors, of the roll moment coefficient C_l is formed in equation 4.9.

$$X = [1, \beta, \delta_a, \delta_r, \frac{pb_w}{2V_0}, \frac{rb_w}{2V_0}] \tag{4.9}$$

The vector of the so called measurements z that forms left side of equation 4.7, is for the roll moment coefficient example expressed by equation 4.10.

$$z = [C_l(1), C_l(2), \ldots, C_l(N)]^T \tag{4.10}$$

Parameter N represents the number of measured data points used for parameter estimation. Since the data contains the measured noise and errors, and the model itself is only an approximation, it is suitable to define the vector of equation errors ν that is expressed by equation 4.11

$$\nu = [\nu(1), \nu(2), \ldots, \nu(N)]^T \tag{4.11}$$

The dimensionless force and moment coefficients, expressed in the equation 4.10, are computed from variables measured during the flight experiment with using the knowledge of the equations of motion and laws of physics. Forces coefficients in BFF are computed using the acceleration measurements and thrust estimates.

$$C_X = \frac{ma_x - T}{\bar{q}S} \tag{4.12}$$

$$C_Y = \frac{ma_y}{\bar{q}S} \tag{4.13}$$

$$C_Z = \frac{ma_z}{\bar{q}S} \tag{4.14}$$

These coefficients are converted in the next step using rotation about the measured angle of attack to the stability axis frame, which is often used for expressing the aerodynamic force and moment coefficients. This rotation does not affect the side-force coefficient C_Y, which remains the same.

$$C_D = -C_X \cos(\alpha) - C_Z \sin(\alpha) \tag{4.15}$$

$$C_L = -C_Z \cos(\alpha) + C_X \sin(\alpha) \tag{4.16}$$

Moment coefficient computations are based on the moment equations of motion and the knowledge of moments of inertia and rotational accelerations that are usually computed as a numerical derivative of angular rate signals.

$$C_l = \frac{I_x}{\bar{q}Sb_w}\left[\dot{p} - \frac{I_{xz}}{I_x}(pq + \dot{r}) + \frac{(I_z - I_y)}{I_x}qr\right] \tag{4.17}$$

$$C_m = \frac{I_y}{\bar{q}S\bar{c}}\left[\dot{q} + \frac{(I_x - I_z)}{I_y}pr + \frac{I_{xz}}{I_y}(p^2 - r^2)\right] \tag{4.18}$$

$$C_n = \frac{I_z}{\bar{q}Sb_w}\left[\dot{r} - \frac{I_{xz}}{I_z}(\dot{p} - qr) + \frac{(I_y - I_x)}{I_z}pq\right] \tag{4.19}$$

4.2 EQUATION ERROR METHOD

In its most basic form, the Equation Error Method becomes the parameter estimator based on the minimization of the sum of squared differences, i.e., the least-squares estimator. This type of estimator requires a type of model that is linear in parameters. The advantages of the least-squares estimator are simple implementation and low computational complexity. The aerodynamic force and moment coefficients equations 4.1-4.6 fulfill the condition of linearity in parameter fits to the required model structure expressed in equation 4.10. As stated above, the least square estimator minimizes the sum of squared differences defined by criterion $J(\theta_P)$ within the equation 4.20.

$$\begin{aligned} J(\theta_P) &= \frac{1}{2}(z - X\theta_P)^T(z - X\theta_P) \\ &= \frac{1}{2}[\theta_P^T X^T X\theta_P - \theta_P^T X^T z - z^T X\theta_P + z^T z] \end{aligned} \tag{4.20}$$

The vector of parameters θ_P that minimizes quadratic criterion $J(\theta_P)$ is defined by equation 4.21

$$\frac{dJ(\theta_P)}{d\theta_P} = -z^T X + \theta_P^T (X^T X) = 0 \tag{4.21}$$

and by expressing the parameter vector θ_P form equation 4.21 its least square estimate can be expressed by equation 4.22.

$$\hat{\theta}_P = (X^T X)^{-1} X^T z \tag{4.22}$$

The analysis of parameter estimate given by equation 4.22 can be done assuming that the regressor X is without error, and the noise within the measurement z is white and Gaussian. In that case, the output estimate $\hat{y}$ can be expressed using equation 4.23, which leads to computation of measurement variance σ^2 defined by equation 4.24. Resulting estimate covariance matrix P_{ij} and standard deviation s, which is the squared root of estimate covariance, can be expressed using equations 4.25 and 4.26.

$$\hat{y} = X\hat{\theta}_P \tag{4.23}$$

$$\hat{\sigma}^2 = \frac{(z - \hat{y})^T(z - \hat{y})}{N - n_p} \tag{4.24}$$

$$\begin{aligned} cov(\hat{\theta}_P) &= E[(\hat{\theta}_P - \theta_P)(\hat{\theta}_P - \theta_P)^T] = \hat{\sigma}^2 (X^T X)^{-1} \\ &= [P_{ij}] \quad \text{where} \quad i, j = 1, 2, \ldots, n_p \end{aligned} \tag{4.25}$$

$$s(\hat{\theta}_{P_j}) = \sqrt{P_{jj}} \tag{4.26}$$

4.2.1 *Differentiation of Noisy Data*

The equations 4.17-4.19 for the computation of the roll, pitch and yaw moment coefficients contain the angular acceleration signals $\dot{p}$, $\dot{q}$ and $\dot{r}$ on their right sides. As direct measurement of angular accelerations is difficult due to limited availability and high cost of precise angular accelerometers, most algorithms compute the angular accelerations using numerical derivatives of their angular rate signals. This task can be very challenging since the angular rate measurements, especially those provided by MEMS gyroscopes, are usually very noisy, and all the noise present in a signal is multiplied after differentiation. The solution to this problem is, according to [51], a combination of data smoothing algorithm with a differentiation afterward. One way to perform the smoothed differentiation is to sequentially fit noisy data with a polynomial, which is then differentiated. Another approach is to smooth noisy data with an optimal Fourier smoother and than compute the derivative in the frequency domain. This approach's advantage is that it does not process the data sequentially, but computes the derivative for the whole maneuver. The polynomial used for sequential fitting can be a simple second-order polynomial continuously fitted through 5 consecutive data-points. The polynomial is expressed by equation 4.27

$$y = at^2 + bt + c \tag{4.27}$$

Coefficients a, b and c are estimated using the least-square algorithms. Another option can be in the utilization of the smooth noise-robust differentiator as the Sawitzky-Golay filters with improved noise suppression based on least-squares smoothing [79]. Table 4.1 shows different order numerical differentiators that can be used for computing angular accelerations for the purpose of aerodynamic parameters estimation [38].

Table 4.1: Numerical differentiators.

Order	Smooth Noise-Robust Differentiators
5	$\frac{2(f_1-f_{-1})+f_2-f_{-2}}{8h}$
7	$\frac{5(f_1-f_{-1})+4(f_2-f_{-2})+f_3-f_{-3}}{32h}$
9	$\frac{14(f_1-f_{-1})+14(f_2-f_{-2})+6(f_3-f_{-3})+f_4-f_{-4}}{128h}$
11	$\frac{42(f_1-f_{-1})+48(f_2-f_{-2})+27(f_3-f_{-3})+8(f_4-f_{-4})+f_5-f_{-5}}{512h}$

4.3 ONLINE PARAMETER ESTIMATION

The previously described parameter estimation method is applicable to a complete set of collected data available after completing measurement campaign. This type of method is called an offline parameter estimation, and it is perfectly suitable for the baseline controller design purposes. However, for the advanced control design techniques, it is more appropriate to derive model parameters from state variables measurement online. The online parameter estimation can be described as a process in which new incoming data is used to update an existing model. The time variation of model parameters caused by changes in flight conditions, mass redistribution caused by fuel burn, or the structural damage and failures can be detected using online parameter estimation algorithms. The practical utilization of online parameter estimation can cover the in-flight monitoring of parameters for stability and control, testing or online fault detection. One of the algorithms that can perform real-time parameter update is Recursive Least Squares [62]. The main advantages of the online parameter estimation are summarized in the following list [51]:

- The parameters are calculated online without the necessity of processing the whole dataset.
- Time-varying parameter tracking.
- Identification of problems in parameter estimates.
- Parameters are available throughout the flight, which can help identify the length of signals appropriate for excitation.

The main disadvantages can be seen in the following list:

- Model structure must be fixed.
- Estimated parameter variance can continually decrease, which is called covariance windup.
- The trade-off between rapid response to time variation of parameters and smooth time histories of parameter estimates.
- The numerical problems can be caused by signal periods with low excitation.
- The data processing cannot be used during the online parameter estimation.

Figure 4.2 shows the utilization of the online parameter identification within the scheme of an adaptive flight control system. Majority of adaptive control systems are based on some online control system modification. In this case, the Online

Parameter Estimation block, that combines the state estimation and aerodynamic model identification, modifies the flight control system indirectly throughout an onboard aerodynamic model. This model feeds the control laws with computed forces and moments. Finally, the control laws generate commands for the actuators attached to the control surfaces. The online parameter estimation method, which combines the state estimation with model identification, is related to a two-step technique.

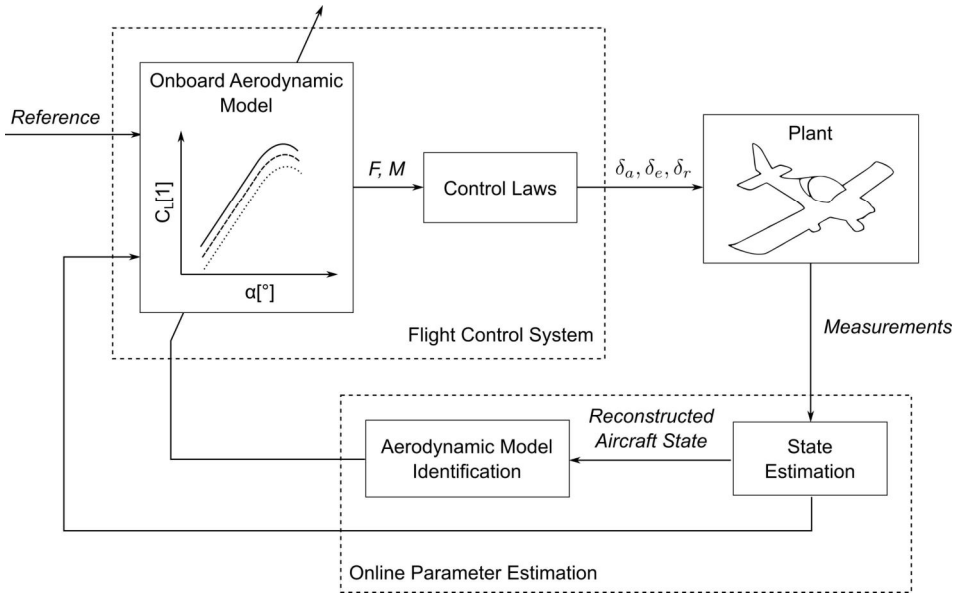

Figure 4.2: Online parameter estimation within adaptive flight control system.

The recursive least squares parameter estimation algorithm will be defined using equations written in a recursive form, with a new update of variable expressed by index $k+1$. The first step of the online parameter estimation process is the definition of the recursive regression matrix and its update by equations 4.28 - 4.30.

$$A_k = A(x_k) \tag{4.28}$$

$$A_{k+1} = \begin{bmatrix} A_k \\ a_{k+1} \end{bmatrix} \tag{4.29}$$

$$a_{k+1} = a(x_{k+1}) \tag{4.30}$$

The variable x_k is the current state measurement, the notation of equation 4.31 is used for the measurement vector update.

$$Y_k = \begin{bmatrix} y_1 & y_2 & \dots & y_k \end{bmatrix}^T \qquad Y_{k+1} = \begin{bmatrix} Y_k \\ y_{k+1} \end{bmatrix} \tag{4.31}$$

The process of online parameter estimation using the recursive least squares algorithm starts with obtaining the initial parameter estimate $\hat{\theta}_0$ and covariance matrix P_0. The recursive loop is initiated by obtaining a new set of measured data

(x_{k+1}, y_{k+1}), which is followed by formulating the regression matrix for a new data point as shown in equation 4.32.

$$a_{k+1} = \begin{bmatrix} 1 & p_1(x_{k+1}) & \dots & p_M(x_{k+1}) \end{bmatrix} \tag{4.32}$$

The subsequent step is calculating the Kalman gain K_{k+1} based on the regressor matrix from the equation 4.32 and the current covariance matrix P_k.

$$K_{k+1} = P_k a_{k+1}^T (a_{k+1} P_k a_{k+1} + I)^{-1} \tag{4.33}$$

Equation 4.34 shows how the Kalman gain K_{k+1} is used for the computation of the parameter update.

$$\hat{\theta}_{k+1} = \hat{\theta}_k + K_{k+1}(y_{k+1} - a_{k+1}\hat{\theta}_k) \tag{4.34}$$

The last step of online parameter estimation is the covariance matrix update computation introduced in equation 4.35, then the process enters to the new iteration step.

$$P_{k+1} = P_k - K_{k+1} a_{k+1} P_k \tag{4.35}$$

A problem with using classical recursive least squares may occur since the new data has the same weight as the old ones. This problem can be resolved by introducing the so-called forgetting factor λ, which is a weighting factor applicable to the new data. The only step that will be different in the process of recursive least squares estimation is the computation of the Kalman gain, where the identity matrix I is replaced by the identity matrix scaled by the forgetting factor λI as shown in equation 4.36.

$$K_{k+1} = P_k a_{k+1}^T (a_{k+1} P_k a_{k+1} + \lambda I)^{-1} \tag{4.36}$$

4.4 STATE ESTIMATION TECHNIQUES

The state estimation is a technique that computes the state of a dynamic system from the measured variables. The use-cases of state estimation, which is widely used throughout the control system design, include the signal noise suppression, signal reconstruction (in aerospace applications known as flight path reconstruction) and data fusion that improves the accuracy of the state estimate by combining different sensors, widely used in navigation systems as Global Positioning System (GPS) or robotics application. One of the most utilized techniques for state estimation, which will be described in this section, is the Kalman filter. The Kalman filter was co-invented by Rudolph Kalman in 1958 during his work on the Apollo project navigation computer and became quickly popular, especially among the engineering community. The reason was its transparency. In contrast to

the Wiener filter, which is based on frequency description and spectral factorization, the Kalman filter operates in the time domain and with system state variables. More details about the state estimation topics can be found in [5, 20, 50]. Kalman filter is a linear optimal state estimator in the means of minimal variance, and its basic working principle is the calculation of weighted average between the measured and predicted state, where the weight (Kalman gain) depends on the uncertainty of the measurement, the higher the uncertainty, the lower the weight. It can be expressed by a general equation 4.37

$$x_{estimated} = x_{predicted} + K \cdot (z_{measured} - z_{predicted}) \tag{4.37}$$

The motivation of using state estimation within the task of parameter estimation is that the result of parameter estimation, i.e., the identified model is directly influenced by the quality of input-output data used. If the data is noisy and biased or some necessary variables are missing, it is highly likely that the parameter estimator's performance will be poor. In other words, if there is garbage at the input to the parameter estimator, there will be garbage at the output as well. Another utilization of state estimation techniques is related to the control system design. The state estimator, namely the Kalman filter, is an integral part of the LQG control technique, which will be researched in detail in Chapter 5. The LQG control approach combines the Kalman filter with the state feedback control. The Kalman filter assumes stochastic, affine, linear and time-variant system in a form defined by equations 4.38 and 4.39.

$$\dot{x}(t) = A(t)x(t) + B(t)u(t) + G(t)w(t) \quad x(t_0) = x_0 \tag{4.38}$$

$$z(t) = H(t)x(t) + D(t)u(t) + v(t) \quad t = t_i, \quad i = 1, 2, \dots \tag{4.39}$$

Matrices A, B, G, H, D are assumed to be known and possibly time-varying. The variable $w(t)$ is the process continuous white noise and $v(t)$ is the measurement white noise. The noise characteristics, namely the process noise mean $E[w(t)]$, process noise covariance $E\left[w(t)w(t)^T\right]$, measurement noise mean $E[v(t)]$ and measurement noise covariance $E\left[v(t)v(t)^T\right]$ are introduced in equations 4.40-4.43

$$E[w(t)] = 0 \tag{4.40}$$

$$E\left[w(t)w(t)^T\right] = Q(t) \tag{4.41}$$

$$E[v(t)] = 0 \tag{4.42}$$

$$E\left[v(t)v(t)^T\right] = R(t) \tag{4.43}$$

Before the definition of the Kalman filter algorithm it is necessary to discretize the continuous system expressed in equations 4.38 and 4.39, which results in a following discrete linear system described by equations 4.44 and 4.45.

$$\dot{x}_{k+1} = \Phi_{k+1}x_{k+1} + \Psi_{k+1}u_{k+1} + \Gamma_{k+1}w_{k+1} \tag{4.44}$$

$$z_{k+1} = H_{k+1}x_{k+1} + D_{k+1}u_{k+1} + v_{k+1} \tag{4.45}$$

Table 4.2: Kalman filter variables definition.

Description	Variable
Current real system state	x_k
One step ahead real system state	x_{k+1}
Current optimal estimated system state	$\hat{x}_{k,k}$
One step ahead state prediction	$\hat{x}_{k+1,k}$
One step ahead optimal state estimation	$\hat{x}_{k+1,k+1}$

Variable Φ_{k+1} represents the system transition matrix, Ψ_{k+1} is the input distribution matrix, and Γ_{k+1} defines the noise input matrix. Table 4.2 defines some variables that will be used throughout the Kalman filter description.

The first step in the Kalman filter definition is expressing the one step ahead state prediction described by equation 4.46, which is followed by the computation of the state prediction error covariance matrix expressed by equation 4.47.

$$\hat{x}_{k+1,k} = \Phi_{k+1,k}\hat{x}_k + \Psi_{k+1,k}u_k, \quad \hat{x}_{0,0} = \hat{x}_0 \tag{4.46}$$

$$P_{k+1,k} = \Phi_k P_{k,k}\Phi_k^T + \Gamma_{k+1,k}Q_d\Gamma_{k+1,k}^T, \quad P_{0,0} = P_0 \tag{4.47}$$

The subsequent step is the Kalman gain calculation, which represents the relative weight of difference between the measurement and estimate.

$$K_{k+1} = P_{k+1,k}H_{k+1}^T(H_{k+1}P_{k+1,k}H_{k+1}^T + R_{k+1})^{-1} \tag{4.48}$$

Afterwards the measurement update of the state estimate is introduced in equation 4.49.

$$\hat{x}_{k+1,k+1} = \hat{x}_{k+1,k} + K_{k+1}\underbrace{(z_{k+1} - H_{k+1}\hat{x}_{k+1,k})}_{\text{Measurement error}} \tag{4.49}$$

As stated in equation 4.37 the optimal estimate $\hat{x}_{k+1,k+1}$ is a combination of the biased state estimate $\hat{x}_{k+1,k}$ and the estimated measurement error scaled by the Kalman gain K_{k+1}. The state estimation error covariance matrix is computed at the end of the recursive cycle using equation 4.50. In other words, the sample covariance matrix $P_{k+1,k+1}$ can be expressed in terms of the old covariance matrix $P_{k+1,k}$.

$$P_{k+1,k+1} = (I - K_{k+1}H_{k+1})P_{k+1,k} \tag{4.50}$$

The Kalman filter described by equations 4.46-4.50 is intentionally introduced in its recursive form as it is the most appropriate way for easy and straightforward implementation. After performing the last step, that is the computation of the state estimation error covariance matrix, the recursive cycle starts again from the equation 4.46, therefore it is referred to as a state prediction computation.

To determine the noise covariance matrices Q and R, it is possible to use the knowledge of the sensor calibration process. If the system input vector is defined by equation 4.51, then each input has a standard deviation defined by vector Σ_u specified in equation 4.52.

$$u = [u_1, \ldots, u_n]^T \tag{4.51}$$

$$\Sigma_u = [\sigma_{u1}, \ldots, \sigma_{un}] \tag{4.52}$$

Equivalently if the measurement vector z is expressed by equation 4.53, then the corresponding standard deviation vector Σ_z is defined by equation 4.54

$$z = [z_1, \ldots, z_m] \tag{4.53}$$

$$\Sigma_z = [\sigma_{z1}, \ldots, \sigma_{zm}] \tag{4.54}$$

The noise covariance matrices Q and R can be defined in the form of a diagonal matrix containing the squared input and measurement standard deviations.

$$Q = \begin{bmatrix} \sigma_{u1}^2 & 0 & 0 \\ 0 & \ddots & 0 \\ 0 & 0 & \sigma_{un} \end{bmatrix}, \quad R = \begin{bmatrix} \sigma_{z1}^2 & 0 & 0 \\ 0 & \ddots & 0 \\ 0 & 0 & \sigma_{zm} \end{bmatrix} \tag{4.55}$$

Considerations in the following list need to be made when implementing the ordinary linear Kalman filter.

- System assumed in the state estimator needs to be linear.
- System model (matrices A, B, H, D) needs to be known.
- Noise covariance matrices Q, R need to be known.
- The R matrix should be based on sensor noise measurements.
- Stochastic input noise represents both sensor noise and model uncertainties.
- The initial guess of the covariance matrix P_0 should be selected large for unknown initial state error.
- Initial state estimate $\hat{x}_0$ can be selected arbitrarily.
- The system has to be fully observable to guarantee the Kalman filter convergence.

As stated above, the ordinary Kalman filter can only estimate the state of a linear system. However, in practice, the system and measurement equations can become nonlinear. In that case, the Extended Kalman Filter (EKF) that linearizes the system and measurement equation around their nominal values can be used. However,

when using the EKF, the state estimates are no longer guaranteed to converge to an optimally estimated state. Other versions of the Kalman filter, as the Iterated EKF or Unscented Kalman Filter (UKF), only improve the convergence of the state estimate. Similarly to the case of EKF they do not guarantee an optimal state estimate.

4.5 PARAMETER ESTIMATION RESULTS

This section demonstrates the parameter estimation results of an aircraft aerodynamic model. The Equation Error Method algorithm and the aerodynamic model structure described in the previous sections have been employed in the aircraft parameter estimation process. The input-output measurement data used in the parameter estimation process came from a real flight experiment performed on an experimental LSA.

Figure 4.3 shows 3D graphs of the longitudinal force and moment coefficients, namely the lift and pitch moment coefficient. The red dots inside the graphs represent the discrete identified parameters while the surface is an extrapolation over the flight envelope. Coefficients of the longitudinal motion are presented as functions of the angle of attack α and elevator deflection δ_e.

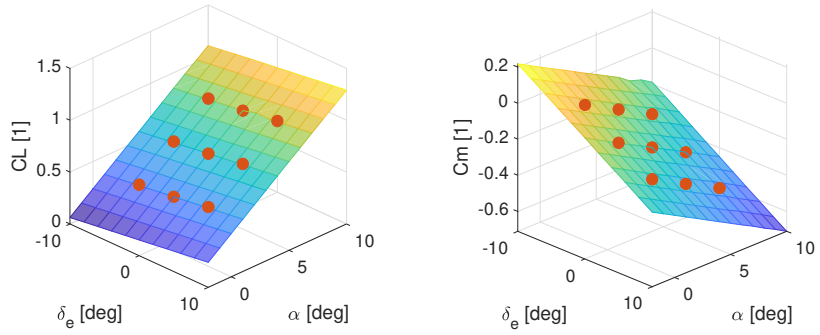

(a) Lift (b) Pitch moment

Figure 4.3: Aerodynamic coefficients of longitudinal motion.

Figure 4.4, on the other hand, contains the lateral-directional motion's force and moment coefficients, namely the side force, roll and yaw moment coefficients. The lateral-directional parameters are presented as functions of the angle of attack α and angle of sideslip β.

Parameter estimation results will be used in the following chapters during the research, design and development of an automatic flight control system for an experimental aircraft platform.

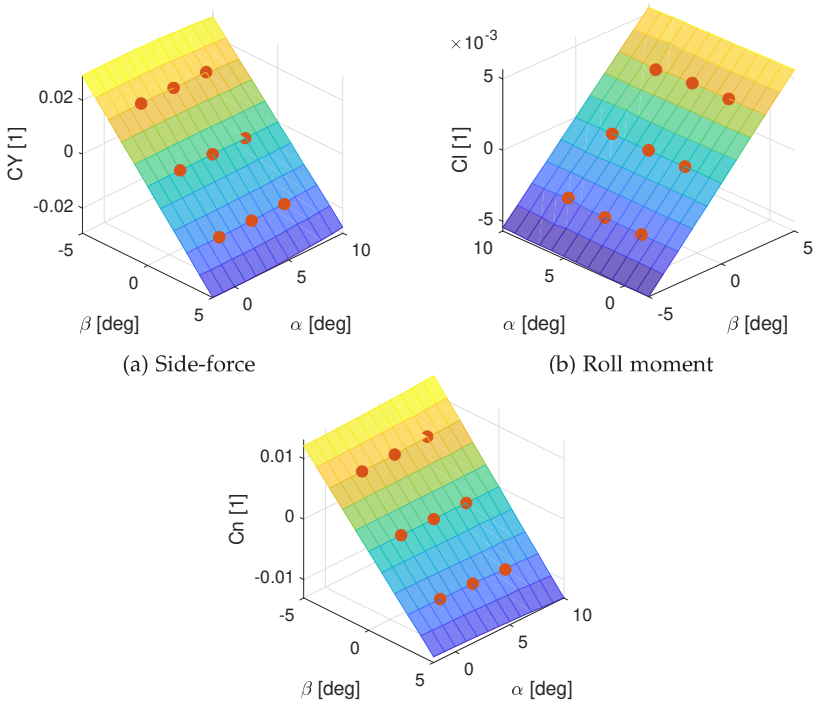

(a) Side-force

(b) Roll moment

(c) Yaw moment

Figure 4.4: Aerodynamic coefficients of lateral directional motion.

5

CONTROL SYSTEM SYNTHESIS

This chapter contains the theoretical background and practical aspects of modern Flight Control System (FCS) design. The chapter starts with a definition of optimal FCS design techniques based on Linear Quadratic Regulator (LQR) and Linear Quadratic Gaussian (LQG) approaches with optional adaptive augmentation of the baseline control system.

The LQR is a state feedback control method known to provide an excellent design robustness capability. However, two deficiencies emerge when considering the LQR implementation into an automatic flight control system. The first implementation deficiency of the LQR method is that it is a state feedback approach requiring all system states to be measurable. The second implication is the fact that this method is unable to provide sufficient noise attenuation. In order to mitigate the previously introduced challenges, an optimal estimation technique (Kalman filter), along with optimal regulation, can be used to create an output feedback strategy known as LQG. In other words, the LQG control is a combination of Kalman filter and LQR. Even though the LQG provides reduced tracking performance and stability margins when compared to LQR, its robustness can be regained by employing the so-called Loop Transfer Recovery (LTR) technique. The cost for the recovery includes an obvious trade-off between the controller's stability margins and its noise attenuation capability. The linear-quadratic control topic is described in more detail in the following references [11, 32, 54, 78, 91].

5.1 LINEAR QUADRATIC REGULATOR

As stated above, the LQR is a state feedback control technique that computes optimal feedback gain matrices for given state-space represented systems with respect to a quadratic cost function, which is minimized. The feedback gain matrix is associated with a solution of the Riccati equation [57]. The LQR design technique has certain advantages over the classical control design methods or Eigen-structure assignment based methods, as it guarantees adequate stability margins.

An LQR design process starts with the definition of a controlled linear system in its state-space form, as expressed by equations 5.1 and 5.2. Equation 5.3 defines the boundary condition, i.e. the system's state x in time t_0 equals the constant x_0.

$$\dot{x} = Ax + Bu \tag{5.1}$$

$$y = Cx \tag{5.2}$$

$$x(t_0) = x_0, \quad x \in R^{n_x}, u \in R^{n_u} \tag{5.3}$$

Variable x represents system state and variable u represents system input. Parameters n_x and n_u specify the state, resp. input vector dimensions. The system dynamic matrices A, B are assumed to be time-invariant.

The LQR control law is expressed by equation 5.4

$$u_{cmd} = K_{LQR} \cdot x, \tag{5.4}$$

where the gain matrix K_{LQR} is designed to minimize the quadratic performance index at infinite time interval $(0, \infty)$ described in equation 5.5.

$$J = \int_0^\infty (x^T Q x + u^T R u) dt \tag{5.5}$$

$$Q = Q^T \geq 0 \tag{5.6}$$

$$R = R^T \geq 0 \tag{5.7}$$

The weight matrices Q and R are assumed to be symmetric and positive definite, as indicated by equations 5.6 and 5.7. And their selection directly influences the solution of Riccati equation P defined by equation 5.17, and correspondingly the feedback gain K_{LQR}, defined by equation 5.19. Large elements of matrix Q penalize the system state x, which leads to higher feedback gains K_{LQR} and to higher control effort. Large elements of matrix R penalize the input u, which leads to smaller feedback gains K_{LQR} and to smaller control effort. With respect to controllability and observability, definitions introduced in Section 7.1, we want to have the pair of matrices (A, B) controllable and pair of matrices $(A, \sqrt{Q})$ observable. The observability of the pair $(A, \sqrt{Q})$ is important, as it guarantees that the unstable system states x will be penalized in quadratic performance index J defined by equation 5.5 and their contributions in the performance index will be minimized. The following equations are dedicated to the derivation of the gain matrix K_{LQR}. The first step is expressing the Hamiltonian for LQR in a form defined by equation 5.8.

$$H = x^T Q x + u^T R u + \frac{\partial J^*}{\partial x}(Ax + Bu) \tag{5.8}$$

The gradient of Hamiltonian with respect to input u, shown in equation 5.9, should be equal to zero in order to define the optimal control law.

$$\frac{\partial H}{\partial u} = 2Ru + B^T \nabla_x J^*(x, t) = 0 \tag{5.9}$$

The optimal control can then be expressed as equation 5.10.

$$u^* = -\frac{1}{2}R^{-1}B^T\nabla_x J^*(x,t) \tag{5.10}$$

By substituting the optimal control u^* into the Hamiltonian expressed by equation 5.8 we can define the so called Hamilotn-Jacobi-Bellman equation 5.11 [57].

$$-\frac{\partial J^*}{\partial t} = x^TQx + \frac{1}{4}\frac{\partial J^*}{\partial x}BR^{-1}B^T\nabla_x J^* + \frac{\partial J^*}{\partial x}Ax - \frac{1}{2}\frac{\partial J^*}{\partial x}BR^{-1}B^T\nabla_x J^* \tag{5.11}$$

When we assume that optimal cost function J^* is in a quadratic form as shown in equation 5.12

$$J^* = x(t)^TP(t)x(t), \tag{5.12}$$

then we can express the partial derivative of J^* with respect to time by equation 5.13 and the gradient of J^* with respect to state x by equation 5.14.

$$\frac{\partial J^*(x,t)}{\partial t} = x^T\dot{P}x \tag{5.13}$$

$$\nabla_x J^*(x,t) = 2P(t)x \tag{5.14}$$

By substituting equations 5.13 and 5.14 into Hamilton-Jacobi-Bellman equation 5.11 and factoring out the x variable the ordinary differential equation called Riccati equation can be formed as

$$-\dot{P}(t) = P(t)A + A^TP(t) + Q - P(t)BR^{-1}B^TP(t) \tag{5.15}$$

Assuming the limiting boundary condition defined by equation 5.16

$$\lim_{t\to\infty} P(t) = 0_{n_x\times n_x}, \tag{5.16}$$

the Riccati equation 5.15 has unique constant solution P_{ricc} which can be found by solving the algebraic Riccati equation 5.17.

$$A^TP_{ricc} + P_{ricc}A - (P_{ricc}B)R^{-1}(B^TP_{ricc}) + Q = 0 \tag{5.17}$$

The solution of Riccati equation P_{ricc} and substitution of equation 5.14 into 5.10 defines the optimal control law defined by equation 5.18.

$$u^* = -R^{-1}B^TP_{ricc}x = -K_{LQR}x \tag{5.18}$$

The feedback matrix K_{LQR} can be then expressed by equation 5.19.

$$K_{LQR} = R^{-1}(B^TP_{ricc}) \tag{5.19}$$

The LQR design process involves selecting weight matrices Q and R. Common practice is to set both matrices as diagonal and initiate the values according to the Bryson's rule. The Bryson's rule is a good starting point of tuning the weight

matrices because it is a simple normalization of variables in cost function defined by equation 5.5 [37].

$$Q = \begin{bmatrix} \frac{1}{(x_1)^2_{max}} & 0 & 0 \\ 0 & \ddots & 0 \\ 0 & 0 & \frac{1}{(x_n)^2_{max}} \end{bmatrix} \tag{5.20}$$

$$R = \rho \begin{bmatrix} \frac{1}{(u_1)^2_{max}} & 0 & 0 \\ 0 & \ddots & 0 \\ 0 & 0 & \frac{1}{(u_m)^2_{max}} \end{bmatrix} \tag{5.21}$$

To sum up the theory necessary for a LQR control system synthesis, Table 5.1 contains all important expressions derived in this section.

Table 5.1: LQR control synthesis summary.

Description	**Expression**
System dynamics	$\dot{x} = Ax + Bu \quad x(0) = x_0$
Performance index	$J = \int_0^\infty (x^T Q x + u^T R u) dt$
Algebraic Riccati equation	$PA + A^T P - PBR^{-1}B^T P + Q = 0$
Optimal control	$u = -R^{-1}B^T P x = -K_{LQR} x$

5.1.1 *Command Tracking*

The LQR, in its basic form, forces the controlled states to reach zero, which is a known regulation problem. However, most of the practical application of automatic control requires the output of the system to track the reference signal, which changes its value. This problem is known as command tracking. In order to transform from regulation to command tracking, an integral error dynamics must be considered to remove the steady-state error [57, 97]. If the tracking error is defined as an integral of the difference between command and output signals as shown in equation 5.22, the linear state space defined previously by equations 5.1 and 5.2 might be augmented as shown in equation 5.23.

$$e_i = \int_{t_0}^{t_1} (r - y) dt \tag{5.22}$$

$$\begin{bmatrix} \dot{x} \\ \dot{e}_i \end{bmatrix} = \begin{bmatrix} A & 0 \\ -C & 0 \end{bmatrix} \begin{bmatrix} x \\ e_i \end{bmatrix} + \begin{bmatrix} B \\ 0 \end{bmatrix} u + \begin{bmatrix} O \\ I \end{bmatrix} r \tag{5.23}$$

As $t \to \infty$ the regulation of the error $e \to 0$, which is equivalent to the command tracking $y \to r$. The integral control action added to the basic LQR control design

provides desired command tracking capability and guarantees a zero steady-state error. Authors Wise and Lavretsky developed a systematic approach in augmenting the state-space model, and referring to it as the Servomechanism Design model. By embedding the model of the class of signals to be tracked and applying the LQR design, the state regulation provides for an accurate command tracking.

The aforementioned Servomechanism Design Model can be split into two parts:

- A servo tracking controller for command tracking.
- A state-feedback component for stabilization.

The dimension of the command signal r is assumed to be lower or equal to the dimension of the system output y defined by equation 5.2. Its model can be expressed by differential equation 5.24.

$$\overset{(p)}{r} = \sum_{i=1}^{p} a_i \overset{(p-i)}{r} \tag{5.24}$$

It is possible to define some typical command signal models using differential equations via parameter p and coefficients a_i as shown in the Table 5.2.

Table 5.2: Typical command signals.

Signal Type	**Differential Equation**	**Model Parameters**
Constant	$\dot{r} = 0$	$p = 1,\ a_1 = 0$
Ramp	$\ddot{r} = 0$	$p = 2,\ a_1 = a_2 = 0$
Sinusoid	$\ddot{r} = -\omega_0^2 r$	$p = 2,\ a_1 = 0,\ a_2 = -\omega_0^2$

The next step is to define the error signal using equation 5.25,

$$e = r - y_c, \tag{5.25}$$

where y_c is a subset of the output vector y, which the controller should track. The regulated system output y_c can then be defined as

$$y_c = C_c x + D_c u, \tag{5.26}$$

where matrix C_c is an output matrix that selects the states to be tracked. The in equation 5.25, mentioned error signal e, aimed to augment the linear state-space model, can be defined as p^{th} order time derivative $\overset{(p)}{e}$.

$$\overset{(p)}{e} = \overset{(p)}{r} - \overset{(p)}{y_c} \tag{5.27}$$

$$\overset{(p)}{e} - \sum_{i=1}^{p} a_i \overset{(p-i)}{e} = \underbrace{\overset{(p)}{r} - \sum_{i=1}^{p} a_i \overset{(p-i)}{r}}_{=0} - \left(\overset{(p)}{y_c} - \sum_{i=1}^{p} a_i \overset{(p-i)}{y_c} \right) \tag{5.28}$$

Assuming equation 5.24 for the definition of the reference signal model, the first term on the right side of equation 5.28 disappears and it is possible to express the (p-i)th time derivative of a regulated system output using equation 5.29.

$$y_c^{(p-i)} = C_c x^{(p-i)} + D_c u^{(p-i)} \tag{5.29}$$

New formulation of the error dynamics equation 5.28 can be derived by substituting terms $y_c^{(p)}$ and $y_c^{(p-i)}$.

$$e^{(p)} - \sum_{i=1}^{p} a_i e^{(p-i)} = -C_c \underbrace{\left[x^{(p)} - \sum_{i=1}^{p} a_i x^{(p-i)} \right]}_{\xi} - D_c \underbrace{\left[u^{(p-i)} - \sum_{i=1}^{p} a_i u^{(p-i)} \right]}_{\mu} \tag{5.30}$$

Definition of new variables ξ and μ is introduced in equations 5.31 and 5.32.

$$\xi = x^{(p)} - \sum_{i=1}^{p} a_i x^{(p-i)} \tag{5.31}$$

$$\mu = u^{(p)} - \sum_{i=1}^{p} a_i u^{(p-i)} \tag{5.32}$$

The time derivative of variable ξ can be defined by equation 5.33

$$\dot{\xi} = x^{(p+1)} - \sum_{i=1}^{p} a_i x^{(p-i+1)} \tag{5.33}$$

and knowing the definition of linear state-space model introduced in equation 5.1 we can write the state-space representation of equation 5.33.

$$\dot{\xi} = A \left[x^{(p)} - \sum_{i=1}^{p} a_i x^{(p-i)} \right] + B \left[u^{(p)} - \sum_{i=1}^{p} a_i u^{(p-i)} \right] \tag{5.34}$$

$$\dot{\xi} = A\xi - B\mu \tag{5.35}$$

The equations 5.34 and 5.35 above exactly represents the original system state-space model, and the Servomechanism Design Model can be obtained by combining the error dynamics equation with the differential equation 5.35. The new state z of the Servomechanism Design Model and its dimension n_z can be defined by equations 5.36 and 5.36.

$$z = \left[e, \dot{e}, \ldots, e^{(p-1)}, \xi \right]^T \tag{5.36}$$

$$n_z = n_x + p \times n_r \tag{5.37}$$

Parameters n_x and n_r represent system state x resp. reference signal r dimensions. The Servomechanism Design Model can be obtained by differentiation of the state z, as expressed in equation 5.38.

$$\dot{z} = \tilde{A}z + \tilde{B}\mu \tag{5.38}$$

The new system dynamics matrix $\tilde{A}$ and new system input matrix $\tilde{B}$ are defined as shown below in equations 5.39 and 5.40.

$$\tilde{A} = \begin{bmatrix} 0 & I & 0 & \dots & 0 & 0 \\ 0 & 0 & I & \ddots & 0 & 0 \\ 0 & 0 & \ddots & \ddots & 0 & 0 \\ 0 & 0 & \dots & 0 & I & 0 \\ a_p I & a_{p-1} I & \dots & a_2 I & a_1 I & -C_c \\ 0 & 0 & \dots & 0 & 0 & A \end{bmatrix} \tag{5.39}$$

$$\tilde{B} = \begin{bmatrix} 0 \\ 0 \\ \vdots \\ -D_c \\ B \end{bmatrix} \tag{5.40}$$

When Servomechanism Design Model matrices $\tilde{A}$ and $\tilde{B}$ are used for computation of feedback matrix K_{LQR}. The newly defined state z and its components will in steady state be forced to zero while the state vector x itself can be nonzero [57].

5.1.2 *LQR-based Flight Control System Synthesis*

Since controlling an aircraft requires command tracking capabilities, e.g., maintaining specified airspeed, altitude or heading, the basic LQR algorithm has to be augmented with an integral error dynamics, which guarantees the steady-state error minimization of the controlled variables. The LQR based FCS design requires availability of a linear state-space system. Based on the assumption from Chapter 2, that a linearized aircraft model can be decoupled into longitudinal and lateral-directional motion models, the FCS for both models will be researched individually. Figure 5.1 shows the design scheme for an LQR based FCS. It contains three main subsystems, namely the Plant, which is a combination of the aircraft and actuator dynamics, the negative state feedback matrix K_{LQR}, and an Integral Error Dynamics.

The LQR might be employed assuming the full availability of the Design System state x_{DS}, yielding a control law as graphically illustrated in Figure 5.1.

$$u = -K_{LQR} \cdot x_{DS} \tag{5.41}$$

At first, the baseline controller for the longitudinal motion model will be expressed. The plant state is defined in the form of the following vector

$$x_{PL_{lon}} = [V, \alpha, q, \gamma, h, \dot{\delta}_T, \delta_T, \dot{\delta_e}, \delta_e]^T, \tag{5.42}$$

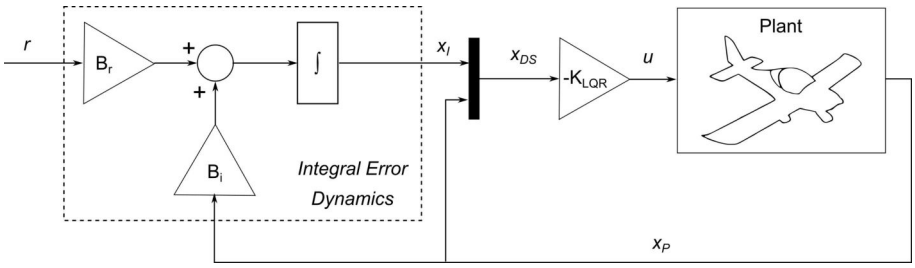

Figure 5.1: The LQR system scheme.

which is a combination of the longitudinal motion model state and the actuator model state. Selected controlled variables in the reference signal r are the commanded airspeed V_{cmd} and altitude h_{cmd}.

$$r = [V_{cmd}, h_{cmd}]^T \tag{5.43}$$

The Integral Error dynamics state vector x_{IE} contains respective airspeed and altitude errors, as introduced in equation 5.44.

$$x_{IE} = [e_V, e_h]^T \tag{5.44}$$

The Integral Error dynamics for the longitudinal motion FCS is described below by the equation 5.45.

$$\overbrace{\begin{bmatrix} \dot{e}_V \\ \dot{e}_h \end{bmatrix}}^{\dot{x}_{IE}} = \overbrace{\begin{bmatrix} 0 & 0 \\ 0 & 0 \end{bmatrix}}^{A_{IE}} \overbrace{\begin{bmatrix} e_V \\ e_h \end{bmatrix}}^{x_{IE}} + \overbrace{\begin{bmatrix} -1 & 0 & 0 & 0 & 0 & 0 & 0 & 0 & 0 \\ 0 & 0 & 0 & 0 & -1 & 0 & 0 & 0 & 0 \end{bmatrix}}^{B_{IE}} x_{PL_{lon}} + \underbrace{\begin{bmatrix} 1 & 0 \\ 0 & 1 \end{bmatrix}}_{B_r} \underbrace{\begin{bmatrix} V_{cmd} \\ h_{cmd} \end{bmatrix}}_{r} \tag{5.45}$$

The system for the longitudinal FCS design is a combination of an Integral Error dynamics and a Plant model as show in equation 5.46.

$$\underbrace{\begin{bmatrix} \dot{x}_{PL_{lon}} \\ \dot{x}_{IE} \end{bmatrix}}_{\dot{x}_{DS}} = \underbrace{\begin{bmatrix} A_{PL_{lon}} & 0^{9\times 2} \\ B_{IE} & A_{IE} \end{bmatrix}}_{A_{DS}} \underbrace{\begin{bmatrix} x_{PL_{lon}} \\ x_{IE} \end{bmatrix}}_{x_{DS}} + \underbrace{\begin{bmatrix} B_{PL_{lon}} \\ 0^{2\times 1} \end{bmatrix}}_{B_{DS}} u + \begin{bmatrix} 0^{9\times 2} \\ B_r \end{bmatrix} r \tag{5.46}$$

The lateral-directional plant model's state vector is composed of the sideslip β, roll ϕ and heading ψ angle, roll p and yaw r rates, the aileron δ_a and rudder δ_r deflections, and their respective rates as shown in equation 5.47.

$$x_{PL_{lat}} = [\beta, \phi, \psi, p, r, \dot{\delta_a}, \delta_a, \dot{\delta_r}, \delta_r]^T \tag{5.47}$$

The controlled variables for the lateral-directional FCS are the sideslip and heading angle commands, which define the content of the reference signal r.

$$x_{IE} = [e_\beta, e_\psi]^T \tag{5.48}$$

$$r = [\beta_{cmd}, \psi_{cmd}]^T \tag{5.49}$$

The integral error dynamics state vector x_{IE} for the lateral-directional FCS can be expressed using equation 5.50.

$$\overbrace{\begin{bmatrix}\dot{e}_\beta\\ \dot{e}_\psi\end{bmatrix}}^{\dot{x}_{IE}} = \overbrace{\begin{bmatrix}0&0\\0&0\end{bmatrix}}^{A_{IE}}\overbrace{\begin{bmatrix}e_\beta\\ e_\psi\end{bmatrix}}^{x_{IE}} + \overbrace{\begin{bmatrix}-1&0&0&0&0&0&0&0\\0&0&-1&0&0&0&0&0\end{bmatrix}}^{B_{IE}} x_{PL_{lat}} + \underbrace{\begin{bmatrix}1&0\\0&1\end{bmatrix}}_{B_r}\underbrace{\begin{bmatrix}\beta_{cmd}\\ \psi_{cmd}\end{bmatrix}}_{r} \tag{5.50}$$

Similarly to the longitudinal FCS design, the Design System used for the lateral-directional controller can be defined in the form of equation 5.51.

$$\underbrace{\begin{bmatrix}\dot{x}_{PL_{lat}}\\ \dot{x}_{IE}\end{bmatrix}}_{\dot{x}_{DS}} = \underbrace{\begin{bmatrix}A_{PL_{lat}}&0^{9\times2}\\ B_{IE}&A_{IE}\end{bmatrix}}_{A_{DS}}\underbrace{\begin{bmatrix}x_{PL_{lat}}\\ x_{IE}\end{bmatrix}}_{x_{DS}} + \underbrace{\begin{bmatrix}B_{PL_{lat}}\\ 0^{2\times1}\end{bmatrix}}_{B_{DS}} u + \begin{bmatrix}0^{9\times2}\\ B_r\end{bmatrix} r \tag{5.51}$$

The Design System defined by matrices A_{DS} and B_{DS}, from equations 5.46 and 5.46. is used for the computation of the feedback gain matrix K_{LQR}, which is then used for expressing the closed-loop system. The closed system, shown in equation 5.52, will have an identical structure for the longitudinal and the lateral-directional model.

$$\dot{x}_{cl} = \left(\begin{bmatrix}A_{PL}&0^{9\times2}\\ B_{IE}&A_{IE}\end{bmatrix} - \begin{bmatrix}B_{PL}\\ 0^{2\times1}\end{bmatrix} K_{LQR}\right) x_{cl} + \begin{bmatrix}0^{9\times2}\\ B_r\end{bmatrix} r \tag{5.52}$$

5.2 LINEAR QUADRATIC GAUSSIAN CONTROL

As mentioned in the previous subsection, the LQR algorithm provides for excellent stability margins when transforming the regulation problem into command tracking by adding integral error dynamics states. However, some design limitations must be considered, e.g., the necessity to measure the complete state vector, and an implementation of additional filtering algorithm in the presence of noise. In case a complete state vector measurement is not possible, there are two strategies to overcome this issue. Either, utilize the output feedback algorithm, that based on previous research doesn't provide satisfactory results, or perform a state estimation. The LQG controller design is covered in more detail in references [11, 24, 25].

Lets consider the linear time-invariant Gaussian system introduced in equations 5.53 and 5.54.

$$\dot{x} = Ax + Bu + w,\quad x \in \mathbb{R}^n,\ u \in \mathbb{R}^m, w \in \mathbb{R}^n \tag{5.53}$$

$$y = Cx + n,\quad y \in \mathbb{R}^p,\ n \in \mathbb{R}^p \tag{5.54}$$

Parameters w and n are zero-mean, white, uncorrelated Gaussian stochastic processes representing the process and measurement noise. Their covariances Q and R can be expressed as shown in equations 5.55 and 5.56.

$$Q = E\left[w(t)w^T(t)\right] \tag{5.55}$$

$$R = E\left[n(t)n^T(t)\right] \tag{5.56}$$

The process noise covariance matrix Q and the measurement noise covariance matrix R shall be positive definite and shall not be mistaken for the LQR weighting matrices. In this case, Q and R are Kalman filter design matrices, and they form the Minimum Energy Estimation quadratic cost function defined in equation 5.57.

$$J_{MEE} = \int_{-\infty}^{t} \left[w^T(\tau)Q^{-1}w(\tau) + n^T(\tau)R^{-1}n(\tau)\right] d\tau \tag{5.57}$$

The proper choice of the above-defined covariance matrices is part of the Kalman gain computing process. They are usually selected according to the following assumptions, which are stated concerning the above-defined Minimum Energy Error quadratic cost:

- For small Q elements, a high penalty is given to the corresponding process disturbance terms, forcing them to be small, which is equivalent to saying that we trust the employed plant model and subsequently, the state estimation process.
- For small R elements, a high penalty is given to the corresponding measurement noise terms, forcing them to be small. This is equivalent to saying that we trust the measurements, and the Kalman filter will respond fast to the changes in the output. Since the R matrix elements represent the sensor noise covariance, it is usually good practice to obtain these values directly from sensor datasheets.

Assuming the LQR feedback gain matrix K_{LQR} has been successfully designed, it is possible to combine the optimal control with the optimal state estimation and to obtain an output feedback controller by employing the Kalman filter defined in Chapter 4. Equation 5.58 introduces the Kalman filter in a form of state-space representation suitable for employing in the LQG design.

$$\dot{\hat{x}} = (A - L_{LQG}C)\hat{x} + Bu_{cmd} + L_{LQG}y \tag{5.58}$$

Variable y represents the system output vector expressed by equation 5.54, L_{LQG} is the previously mentioned Kalman gain matrix. The control law that contains the system state estimate $\hat{x}$ is defined using equation 5.59.

$$u_{cmd} = -K_{LQR} \cdot \hat{x} \tag{5.59}$$

The feedback gain K_{LQR} is obtained by using the LQR algorithm described in the previous subsection by the equation 5.19.

5.2.1 *LQG Closed Loop System's Stability Assessment*

The stability assessment of the LQG closed-loop system starts with the definition of the system dynamics that is a combination of the linear stochastic system dynamics described in equation 5.53 and the control law defined in equation 5.59

$$\dot{x} = Ax - BK_{LQR}\hat{x} + w, \tag{5.60}$$

where w represents a zero mean, white, uncorrelated Gaussian stochastic process. The estimation error is defined by equation 5.61

$$e = x - \hat{x}, \tag{5.61}$$

which leads to the definition of the following error dynamics equation

$$\begin{aligned}
\dot{e} &= \dot{x} - \dot{\hat{x}} \\
&= \underbrace{Ax - BK_{LQR}(x-e) + w}_{\dot{x}} - \underbrace{(A - L_{LQG}C - BK_{LQR})(x-e) - L_{LQG}(Cx+n)}_{\dot{\hat{x}}} \\
&= (A - L_{LQG}C)e + w - L_{LQG}n,
\end{aligned} \tag{5.62}$$

which can be written as a closed-loop in state-space representation taking a form of equation 5.63.

$$\begin{bmatrix} \dot{x} \\ \dot{e} \end{bmatrix} = \begin{bmatrix} A - BK_{LQR} & BK_{LQR} \\ 0 & A - L_{LQG}C \end{bmatrix} \begin{bmatrix} x \\ e \end{bmatrix} + \begin{bmatrix} I \\ I \end{bmatrix} w + \begin{bmatrix} 0 \\ -L \end{bmatrix} n \tag{5.63}$$

Due to the triangular structure of the closed-loop system and since both of the expressions $A - BK_{LQR}$ and $A - LC$ are Hurwitz matrices (all eigenvalues have strictly negative real part), the Separation Principle (which states the optimal control and state estimation problems can be decoupled if certain conditions are fulfilled) ensures that the closed-loop system will be asymptotically stable [37].

5.2.2 *LQG-based Flight Control System Synthesis*

For Linear Time Invariant (LTI) systems with normally distributed process and measurement noise, the optimal state estimator with respect to the minimal variance is the Kalman Filter [57]. The system for a LQG controller design is described by the equation 5.64.

$$\dot{x}_{DS} = A_{DS}x_{DS} + B_{DS}u_c + \begin{bmatrix} 0^{9\times 2} \\ B_r \end{bmatrix} r + w_{DS} \tag{5.64}$$

Subscript DS stands for Design System, which is a combination of Plant and Integral Error dynamics. Variable w_{DS} represents the Design System's process

noise. The estimator used in the LQG control design can be expressed by equations 5.65 and 5.66, which is the Kalman filter form defined in equation 5.58.

$$\dot{\hat{x}}_{DS} = \hat{A}_{DS}\hat{x}_{DS} + \begin{bmatrix} 0^{9\times 2} \\ B_r \end{bmatrix} r + L_{LQG}(y_{DS} - \hat{y}_{DS}) \tag{5.65}$$

$$\hat{y}_{DS} = \hat{C}_{DS}\hat{x}_{DS} \tag{5.66}$$

Figure 5.2 shows the combination of the feedback gain matrix K_{LQR} and a Kalman Filter in a closed loop with a state-space Plant description. Variables $\hat{x}$ and $\hat{y}$ represents system's state and output estimates, while variables w and n are the process and measurement noise that appeared in equations 5.53 and 5.54.

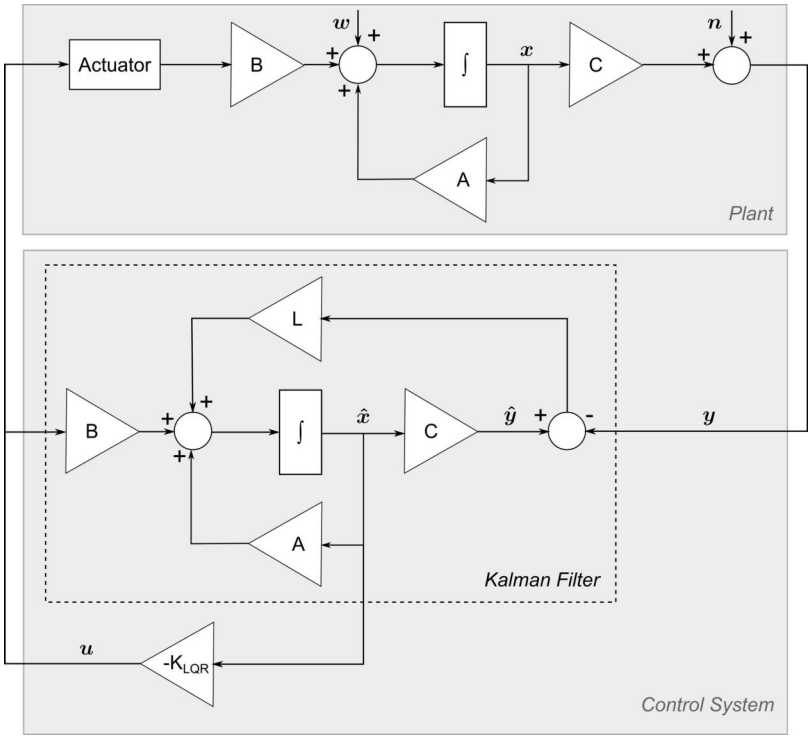

Figure 5.2: The LQG control system scheme.

The LQG closed loop system is expressed by equation 5.67.

$$\dot{x}_{cl} = \begin{bmatrix} \dot{x}_{PL} \\ \dot{x}_{IE} \\ \dot{\hat{x}}_{DS} \end{bmatrix} = A_{cl}x_{cl} + \begin{bmatrix} 0^{9\times 2} \\ B_r \\ \begin{bmatrix} 0^{9\times 2} \\ B_r \end{bmatrix} \end{bmatrix} r + \begin{bmatrix} w_{DS} \\ 0^{2\times 1} \\ 0^{11\times 1} \end{bmatrix} \tag{5.67}$$

The closed-loop system state matrix A_{cl} is composed of all subsystems as the Plant, Integral Error dynamics and Kalman Filter dynamics, as introduced in the following equation 5.68 [25].

$$A_{cl} = \begin{bmatrix} A_{PL} & 0^{9\times 2} & -B_{PL}K_{LQR} \\ B_{IE} & A_{IE} & 0^{2\times 11} \\ L_{x_{PL}}C_{PL} & L_{x_{IE}} & A_{kf} \end{bmatrix}, \tag{5.68}$$

where the state matrix of the Kalman Filter A_{kf} is expressed by equation 5.69.

$$A_{kf} = \left(\begin{bmatrix} \hat{A}_{PL} & 0^{9\times 2} \\ B_{IE} & A_{IE} \end{bmatrix} - \begin{bmatrix} \hat{B}_{PL} \\ 0^{2\times 11} \end{bmatrix} K_{LQR} - L_{LQG}\hat{C}_{DS} \right) \tag{5.69}$$

5.2.3 *Loop Transfer Recovery*

A significant advantage of the LQG controller design approach lies in the possibility to estimate the missing states, i.e., so the designer doesn't need to have complete knowledge of the state vector. The next advantage is in the noise attenuation capabilities. However, the cost for these features is the system's closed-loop robustness reduction. The idea behind the Loop Transfer Recovery (LTR) technique is to modify the LQG design in order to restore the LQR closed-loop system's robustness. The modification of the LQR gains is not recommended. Instead, tuning of the Kalman filter gain is proposed as a better way to achieve the excellent robustness features of the LQR approach [84].

The LTR method parametrizes both process and measurement noise covariances utilized in the solution of the Riccati equation 5.17. The original covariances Q, R are recalculated according to the following expressions introduced in equations 5.70 and 5.71 [96].

$$Q_n = Q + \frac{\nu+1}{\nu}\bar{B}\bar{B}^T \tag{5.70}$$

$$R_n = \frac{\nu+1}{\nu}R \tag{5.71}$$

Matrix $\bar{B}$ is created by adding columns to matrix B.

$$\bar{B} = [BX],\ X \in^{n_x\times(n_y-n_u)} \tag{5.72}$$

The matrix X should complete the column rank of matrix B in a way such that the matrix $C\bar{B}$ is invertible and that the corresponding extended system $C(sI-A)^{-1}\bar{B}$ should be a minimum phase, which means the system and its inversion are stable. The reason for the minimum phase requirement is, the system dynamics $C(sI-A)^{-1}\bar{B}$ is inverted within the Kalman filter, and if it contains negative zeros, the closed-loop system becomes unstable. The extended Riccati equation

is a combination of equation 5.17 and equations 5.70, 5.71 and it is expressed in equation 5.73 [84].

$$\begin{aligned} AP_{ricc} &+ P_{ricc}A^T + Q + \bar{B}\bar{B}^T - P_{ricc}C^TR^{-1}CP_{ricc} \\ &+ \frac{1}{\nu}(\bar{B}\bar{B}^T - P_{ricc}C^TR^{-1}CP_{ricc}) = 0 \end{aligned} \tag{5.73}$$

5.3 MODEL REFERENCE ADAPTIVE CONTROL

In practice, the dynamic model used for the controller design is not fully identical to the real controlled plant due to the parametric uncertainties (e.g. differences in aerodynamic parameters). Therefore, even a robust LQR design introduced in the previous section may not provide sufficient robustness to meet the design requirements. Moreover, the design could be too conservative to provide good tracking performance, which leads to a gain adaptation controller design.

The motivation for designing the adaptive control systems is summarized in the following list [43].

- Current FCS design (LQR) assumes an exact knowledge of aircraft dynamics available through respective state-space matrices A, B, C, D.
- Covering larger part of the flight envelope (due to adaptation of control system parameters) than linear FCS, which is designed for only one point of the flight envelope.
- Current LQR based FCS design is not fault-tolerant.
- Various uncertainties can influence the aircraft model's fidelity.
- The aircraft dynamics can change due to unexpected structural or system failures.

The concept used in this work for adaptive augmentation of the LQR baseline FCS is called Model Reference Adaptive Control (MRAC). The core idea behind the MRAC design is the online modification or adaptation of controller gains considering the error between the Plant and the desired reference system. Within the so-called Direct MRAC approach, the controller gains are computed by an adaptation law in order to minimize the error between the plant and reference system response. Figure 5.3 shows the MRAC based adaptive control design concept.

The stability concept used in the MRAC design is Lyapunov's direct stability method in combination with the so-called Massachusetts Institute of Technology (MIT) rule, which creates the adaptation law basis. As this approach guarantees only the stability and not the asymptotic stability, the Barbalat's Lemma is used

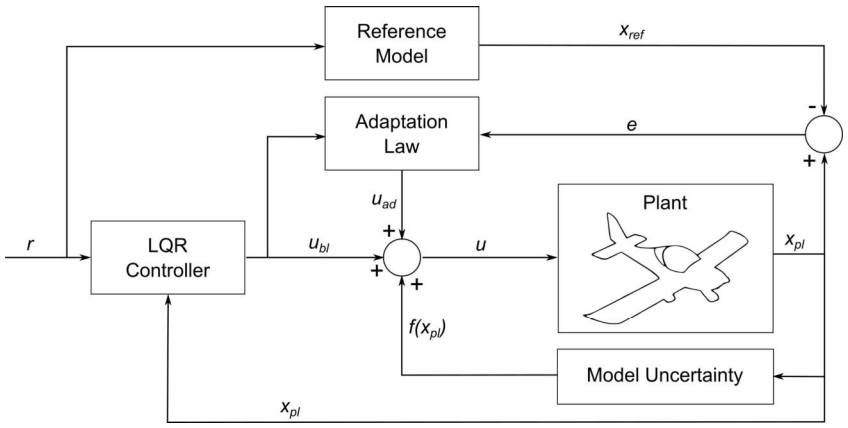

Figure 5.3: MRAC system block diagram.

for proving the asymptotic stability of the error. The following subsection will introduce the Lyapunov stability concept, namely the Lyapunov direct method, that will play a critical role in the adaptive control law derivation process. The Lyapunov stability theory is well covered in references [56, 64, 77].

5.3.1 *Lyapunov Stability of Dynamic Systems*

The Lyapunov stability theory employed in this thesis is focused on the class of nonautonomous unforced dynamic systems defined by equation 5.74.

$$\dot{x} = f(t, x) \tag{5.74}$$

Function f is defined as piece-wise and continuous with origin in $x = 0$. The equilibrium point $x^\star$ in nonzero initial time t_0 is defined as shown in equation 5.75.

$$f(t, x^\star) = 0, \quad \forall t \geq t_0 \tag{5.75}$$

Definition 5.3.1. Stability of Equilibrium in the Sense of Lyapunov *The equilibrium point $x^\star = 0$ of nonautonomous unforced dynamics defined by equation 5.74 is stable if for any $\epsilon > 0$ and $t_0 \geq 0$ there exists $\delta(\epsilon, t_0) > 0$ such that for all initial conditions $\|x(t_0)\| < \delta$ and for all $t \geq t_0 \geq 0$ the corresponding system trajectories are bounded as in $\|x(t)\| < \epsilon$. The equilibrium is uniformly stable if it is stable and δ is independent of t_0. The equilibrium point is unstable if it is not stable.*

Definition 5.3.2. Global Stability *The origin is globally stable if it is stable and*

$$\lim_{\epsilon \to \infty} \delta(\epsilon, t_0) = \infty. \tag{5.76}$$

Definition 5.3.3. Asymptotic Stability *The equilibrium point* $x^\star = 0$ *of equation 5.74 is asymptotically stable if it is stable and there exists a positive constant* $c = c(t_0)$ *such that* $x \to 0$ *as* $t \to \infty$ *for all* $\|x(t_0)\| \leq c$.

Definition 5.3.4. Uniform Asymptotic Stability *The equilibrium point* $x^\star = 0$ *of equation 5.74 is uniformly asymptotically stable if it is uniformly stable and there exists a positive constant* c *independent on* t_0 *such that* $x \to 0$ *as* $t \to \infty$ *for all* $\|x(t_0)\| \leq c$, *uniformly in* t_0, *where the limit uniformity is understood in the following sense*

$$\exists c \, \forall \eta > 0 \, \exists T(\eta) \, \forall t \geq t_0 + T(\eta) \, \forall \|x(t)\| \leq c \Rightarrow \|x(t)\| \leq \eta \tag{5.77}$$

Definition 5.3.5. Global Uniform Asymptotic Stability *The origin is globally uniformly asymptotically stable if it is uniformly asymptotically stable and* $\lim_{\epsilon \to \infty} \delta(\epsilon) = \infty$.

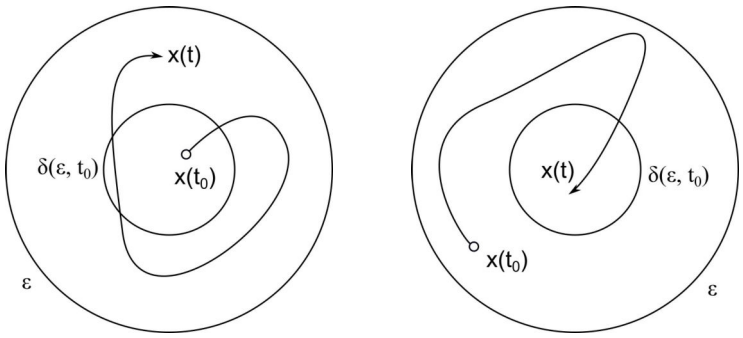

(a) Stability (b) Uniform asymptotic stability

Figure 5.4: Geometrical representation of Lyapunov stability concept.

A uniformly asymptotic stable closed system is a highly desirable goal in the control system design process as the asymptotically stable system's performance is resistant to system perturbations and disturbances. It forces the controller tracking errors well to asymptotically converge to zero in time. Only the uniform stability is often achieved during the adaptive control system design, which means that the tracking error is still converging asymptotically to zero. At the same time, other signals remain uniformly stable and bounded.

5.3.1.1 *Direct Method*

The Lyapunov's direct method is basically used for the uniform stability analysis of the class of systems defined by equation 5.74. The key to the uniform stability assessment is finding the positive definite differentiable function $V(x)$ called

Lyapunov function candidate, with time derivative along the system solution $x(t)$ defined by equation 5.78

$$\dot{V}(x) = \sum_{i=1}^{n} \frac{\partial V}{\partial x_i}\dot{x}_i = \sum_{i=1}^{n} \frac{\partial V}{\partial x_i} f_i(t,x) = \nabla V(x) f(t,x) \tag{5.78}$$

$$\nabla V(x) = \left[\frac{\partial V}{\partial x_1}, \frac{\partial V}{\partial x_2}, \ldots, \frac{\partial V}{\partial x_n}\right] \tag{5.79}$$

Term $\nabla V(x)$, defined by equation 5.79, is the row vector gradient of $V(x)$ along the trajectories of system dynamics specified by equation 5.74. We can observe the dependency of Lyapunov function derivative $\dot{V}(x)$ not only on $V(x)$ but on the system dynamics $f(t,x)$ as well. Now it is possible to define the Lyapunov's direct method.

Theorem 5.3.1. Lyapunov's Direct Method for Assessing Uniform Stability of Nonautonomous Systems *Let $x^\star = 0 \in R^n$ be an equilibrium point for the nonautonomous dynamics defined by equation 5.74, whose initial conditions are drawn from a domain $D \subset R^n$, with $x^\star \in D$ and $t_0 = 0$. Suppose that on the domain D there exists a continuously differentiable locally positive-definite function $V(x) : D \to R$, whose time derivative along the system trajectories is locally negative semidefinite as shown in equation 5.80, for all $t \geq 0$ and for all $x \in D$.*

$$\dot{V}(x) = \nabla V(x) f(t,x) \leq 0 \tag{5.80}$$

Then the system's equilibrium $x^\star = 0$ is locally uniformly stable in the sense of Lyapunov. If in equation 5.80 $\dot{V}(x) < 0$ for all nonzero x and for all $t \geq 0$ (the time derivative along the system trajectories is locally negative definite), than the origin is locally uniformly asymptotically stable.

If the Lyapunov function doesn't fulfill the condition given by the equation 5.80, it can not be stated that the system is unstable. It is only necessary to find another suitable Lyapunov function.

5.3.1.2 *Stability of LTI Systems*

The Lyapunov direct method can be used for stability assessment of Linear Time-Invariant (LTI) systems.

Theorem 5.3.2. Lyapunov Stability of LTI Systes *The equilibrium state $x^\star = 0$ of the Linear Time-Invariant LTI system given by equation 5.81*

$$\dot{x} = Ax \tag{5.81}$$

is asymptotically stable if, and only if given any symmetric positive-definite matrix Q, there exists a symmetric positive-definite matrix P, which is the unique solution of the set of $n(n+1)$ linear equations

$$A^T P + PA = -Q \tag{5.82}$$

Therefore

$$V(x) = x^T P x \tag{5.83}$$

is a Lyapunov function for equation 5.81.

The proof of the theorem mentioned above can be given by expressing the Lyapunov function derivative given by equation 5.83 and by substituting from the Lyapunov equation 5.82 as shown in equation 5.84.

$$\dot{V}(x) = x^T \left[A^T P + PA\right] x = -x^T Q x < 0 \tag{5.84}$$

Equation 5.84 satisfies the condition given in theorem 5.3.1 and we can state that the equilibrium point $x^* = 0$ is asymptotically stable.

5.3.2 *Derivation of Adaptive Control Law*

As shown in Figure 5.3 the complete input to the plant is composed of 3 main signals, namely the baseline controller input u_{bl} provided by the LQR control system, the adaptive augmentation input u_{ad} and the model uncertainty. The adaptive augmentation's main purpose is the uncertainty suppression. The adaptive control law derivation process with LQR baseline controller is summarized in the following list [40, 44, 57]:

1. Define the plant dynamics with model uncertainty.
2. Augment the plant dynamics with an Integral Error dynamics and create a Design System
3. Close the loop with LQR based control law.
4. Define matching conditions and the reference model for MRAC.
5. Define the control law composed of baseline controller and adaptation rule.
6. Define the tracking error between the reference state and the plant state.
7. Express error dynamics.
8. Define the Lyapunov function candidate.
9. Solve the Lyapunov equation.
10. Express the Lyapunov function derivative.
11. Form an adaptation law.

Lets consider the plant dynamics with a state-dependent matched uncertainty $f(x_{PL})$,

$$\dot{x}_{PL} = A_{PL}x_{PL} + B_{PL}\Lambda(u + f(x_{PL})), \tag{5.85}$$

$$f(x_{PL}) = \theta^T\phi(x_{PL}), \tag{5.86}$$

where unknown parameter λ represents the input uncertainty. The matched uncertainty $f(x_{PL})$ is composed of an unknown parameter matrix θ and known n-dimensional regressor vector $\phi(x_{PL})$.

The combination of a Plant and an Integral Error dynamics is to be used as a system for the following MRAC design, resulting in a state-space representation shown in equation 5.90. The system is called the Design System since it is used for MRAC controller design and thus contains the subscript DS.

$$A_{DS} = \begin{bmatrix} A_{PL} & 0^{9\times 2} \\ B_{IE} & A_{IE} \end{bmatrix} \tag{5.87}$$

$$B_{DS} = \begin{bmatrix} B_{PL} \\ 0^{2\times 2} \end{bmatrix} \tag{5.88}$$

The whole open loop extended plant dynamics is expressed in equation 5.90. Its state x_{DS} is defined by equation 5.89.

$$x_{DS} = [x_{PL}, x_{IE}]^T \tag{5.89}$$

It contains the plant dynamics state x_{PL} defined by equations 5.42, 5.47 and the Integral Error dynamics state x_{IE} described in equations 5.44, 5.48 as well as the reference input r expressed by equations 5.43, 5.49.

$$\dot{x}_{DS} = A_{DS}x_{DS} + B_{DS}\Lambda(u + \theta^T\phi(x_{PL})) + B_{ref}r \tag{5.90}$$

Now we can set up the matching condition expressed by equations 5.91 and 5.92, which define the dynamics of a Reference model (subscript ref), which is to be followed by the Plant with an uncertainty.

$$A_{ref} = A_{DS} + B_{DS}\Lambda K_{LQR}^T \tag{5.91}$$

$$B_{ref} = \begin{bmatrix} 0^{9\times 2} \\ B_r \end{bmatrix} \tag{5.92}$$

The Reference model inputs are the signal commands and the output is an ideal state x_{ref}. The dynamics of the Reference model is described by equation 5.93.

$$\dot{x}_{ref} = A_{ref}x_{ref} + B_{ref}r \tag{5.93}$$

The total control input u is composed of three main components as defined by equation 5.94 namely the base-line control input u_{bl}, defined in foregoing

section, and an adaptation component u_{ad}, responsible for canceling the unknown matched uncertainties $f(x_{PL})$ introduced into the Plant dynamics [57].

$$u = u_{bl} + u_{ad} + f(x_{PL}) \tag{5.94}$$

The baseline control input u_{bl} is calculated as a product of the negative LQR feedback gain K_{LQR} and the Design System state x_{DS}. The adaptation input u_{ad} is composed of an input gain matrix estimate $\hat{K}_u$ and an uncertainty gain matrix estimate $\hat{\theta}$.

$$u = \underbrace{-K_{LQR}x_{DS}}_{u_{bl}} + \underbrace{(-\hat{K}_u^T u_{bl} - \hat{\theta}^T\phi(x_{PL}))}_{u_{ad}} + \underbrace{\theta^T\phi(x_{PL})}_{f(x_{PL})} \tag{5.95}$$

To express the estimate of the previously mentioned gain matrices $\hat{K}_u$ and $\hat{\theta}$, it becomes necessary to compute the tracking error as a difference between the Design System's state and the state of the reference system, which is introduced in equation 5.96.

$$e_{tr} = x_{DS} - x_{ref} \tag{5.96}$$

Based on the equation 5.96 it is possible to define the error dynamics equation 5.97, which will in the next steps lead to the definition of a Lyapunov function $V(e_{tr}, \Delta\bar{\theta})$.

$$\dot{e}_{tr} = A_{ref}e_{tr} - B_{DS}\Lambda\Delta\bar{\theta}^T\bar{\phi} \tag{5.97}$$

Term $\bar{\theta}$ represents an extended adaptive parameter matrix and $\bar{\phi}$ is an extended regressor defined by equations 5.98 and 5.99 respectively.

$$\bar{\theta} = [K_u, \theta] \tag{5.98}$$

$$\bar{\phi} = [u_{bl}, \phi] \tag{5.99}$$

The difference between the adaptive parameter matrix θ and its estimate $\hat{\theta}$ is expressed by equation 5.100 and it is necessary for the Lyapunov function $V(e_{tr}, \Delta\bar{\theta})$ computation.

$$\Delta\bar{\theta} = \bar{\theta} - \hat{\bar{\theta}} \tag{5.100}$$

In order to express the parameter update laws and to assure the closed-loop stability of error dynamics, we define the quadratic Lyapunov function $V(e_{tr}, \Delta\bar{\theta})$, known as the "kinetic energy" of the errors in the system, defined by equation 5.101.

$$V(e_{tr}, \Delta\bar{\theta}) = e_{tr}^T P_{lyap} e_{tr} + trace(\Delta\bar{\theta}^T\Gamma_{\bar{\theta}}^{-1}\Delta\bar{\theta}\Lambda) \tag{5.101}$$

Matrix $\Gamma_{\bar{\theta}}$ is a symmetric positive definite and defines the learning rate of an adaptive controller and matrix P_{lyap} is the solution of Lyapunov algebraic equation introduced in equation 5.102. The Lyapunov equation solution is used as a measure to guarantee the stability of an error dynamics in a closed-loop system.

$$P_{lyap}A_{ref} + A_{ref}^T P_{lyap} = -Q \tag{5.102}$$

The solution of the equation 5.102 is employed to estimate the input and uncertainty gain matrices. In order to define the structure of the MRAC update laws, the time derivative of the above mentioned Lyapunov function $\dot{V}(e_{tr}, \Delta\bar{\theta})$ results in equation 5.103.

$$\dot{V}(e_{tr}, \Delta\bar{\theta}) = -e_{tr}^T Q e_{tr} - 2e_{tr}^T P_{lyap} B_{DS} \Lambda \Delta\bar{\theta}^T \bar{\phi} + 2trace(\Delta\bar{\theta}^T \Gamma_{\bar{\theta}}^{-1} \dot{\hat{\theta}} \Lambda) \tag{5.103}$$

Then we apply the vector trace identity $a^T b = trace(ba^T)$ to express the derivative of the Lyapunov function in a form suitable for the MRAC update laws synthesis, which results in equation 5.104. This design strategy aims to dissipate the energy and thus push the derivative of the Lyapunov function to be non-positive, which assures that the Lyapunov function will be non increasing.

$$\dot{V}(e, \Delta\bar{\theta}) = -e^T Q e + 2trace(\Delta\bar{\theta}^T \{\Gamma_{\bar{\theta}}^{-1} \dot{\bar{\theta}} - \bar{\phi} e_{tr}^T P_{lyap} B_{DS}\} \Lambda) \tag{5.104}$$

The condition of a negative semi-definite derivation of the Lyapunov function, which guarantees the stability of a closed-loop system according to Lyapunov's direct method for assessing uniform stability of nonautonomous systems described in [64], is achieved by the definition of the update law in equation 5.105.

$$\dot{\bar{\theta}} = \Gamma_{\bar{\theta}} \bar{\phi}(u_{bl}, x_{PL}) e_{tr}^T P_{lyap} B_{DS} \tag{5.105}$$

The matrix $\Gamma_{\bar{\theta}}$ can be expressed by equation 5.106 and contains the adaptation rates for uncertainties Γ_u and Γ_θ.

$$\Gamma_{\bar{\theta}} = \begin{bmatrix} \Gamma_u & 0_{n \times m} \\ 0_{N \times m} & \Gamma_\theta \end{bmatrix} \tag{5.106}$$

The update law in a form of equation 5.105 guarantees the time derivative of Lyapunov function $\dot{V}(e_{tr}, \Delta\bar{\theta})$ becomes

$$\dot{V}(e_{tr}, \Delta\bar{\theta}) = -e^T Q e \leq 0 \tag{5.107}$$

and thus negative semi-definite. According to Barbalat's lemma defined in reference [57] the tracking error e_{tr} is forced to zero asymptotically as $t \to \infty$. Considering the $\bar{\theta}$ and $\bar{\phi}$ are composed variables as shown in equations 5.98 and 5.99, the update law defined by equation 5.105 can be split into equations 5.108 and 5.109 to define update laws for variables K_u and $\hat{\theta}$.

$$\dot{\hat{K}}_u = \Gamma_u u_{bl} e_{tr}^T P_{lyap} B_{DS} \tag{5.108}$$

$$\dot{\hat{\theta}} = \Gamma_\theta \phi(x_p) e_{tr}^T P_{lyap} B_{DS} \tag{5.109}$$

Update laws in representation defined by equations 5.108 and 5.109 is suitable for the MRAC algorithm implementation.

5.3.3 *Projection Algorithm*

As the MRAC algorithm itself does not fully guarantee the parameter convergence, a robustness modification of MRAC laws known as the "projection algorithm" has to be employed. The projection algorithm holds the estimated parameters within predefined boundaries and does not allow for a parameter drift, causing unexpected controller behavior [44]. The projection algorithm's first step is to define the convex function that defines the boundaries within a parameter space. This function is introduced in equation 5.110

$$f(\hat{\theta}) = \frac{1}{\epsilon}\sum_{i=1}^{n}\left|\frac{\hat{\theta}_i}{\theta_{i,max}}\right|^p - \frac{1}{\epsilon} + 1 \leq 0, \tag{5.110}$$

where the variable $\hat{\theta}_i$ is the estimate of i^{th} adaptive parameter and the variable $\theta_{i,max}$ is the boundary of i^{th} adaptive parameter estimate. The variables p and ϵ define parameter space boundaries. The gradient of the convex function necessary to compute the projection is defined by equation 5.111.

$$\nabla f(\hat{\theta}) = \frac{2(1+\epsilon)}{\epsilon\theta_{max}}\hat{\theta} \tag{5.111}$$

The projection algorithm itself is defined for 3 cases:

- No scaling, if not in transition zone, i.e. $f(\hat{\theta}) < 0$
- No scaling, if $f(\hat{\theta}) \geq 0$ and vertical component of $\dot{\hat{\theta}}$ points away from the boundary
- Scaling, if $f(\hat{\theta}) \geq 0$ and the vertical component of $\dot{\hat{\theta}}$ points to the boundary

Three projection cases shown in equation 5.112 were described in reference [59].

$$\dot{\hat{\theta}} = \text{Proj}(\hat{\theta}, \dot{\hat{\theta}}) = \begin{cases} \dot{\hat{\theta}} & \text{if} \quad f(\hat{\theta}) < 0 \\ \dot{\hat{\theta}} & \text{if} \quad f(\hat{\theta}) \geq 0, \nabla f(\hat{\theta})^T\dot{\hat{\theta}} \\ \dot{\hat{\theta}} - f(\hat{\theta})\frac{\nabla f(\hat{\theta})^T}{\|\nabla f(\hat{\theta})\|}\dot{\hat{\theta}}\frac{\nabla f(\hat{\theta})}{\|\nabla f(\hat{\theta})\|} & \text{if} \quad f(\hat{\theta}) \geq 0, \nabla f(\hat{\theta})^T\dot{\hat{\theta}} \end{cases} \tag{5.112}$$

5.3.4 *Hedging*

Hard input nonlinearities due to the actuator saturation can cause a serious challenge to the adaptive control system operation. The solution is to employ a technique known as hedging, which modifies the reference model dynamics defined by equation 5.93 and enhances it by the difference between saturated input $R_s(u)$ and computed input u [6, 63]. Equation 5.113 describes the input saturation while equation 5.114 expresses the difference Δu.

$$R_s(u) = \begin{cases} u & \text{if} \quad u_{min} < u < u_{max} \\ u_{max} & \text{if} \quad u > u_{max} \\ u_{min} & \text{if} \quad u < u_{min} \end{cases} \tag{5.113}$$

$$\Delta u = R_s(u) - u \tag{5.114}$$

The new dynamics of the reference model, including the information about actuators saturation, is defined by equation 5.115.

$$\dot{x}^*_{ref} = A_{ref} x^*_{ref} + B_{ref} r + B_{PL}(\Delta u) \tag{5.115}$$

The modified reference model state x^*_{ref} is used for computing the new tracking error $e_U = x_{DS} - x^*_{ref}$ which propagate to a new definition of update laws [57], as shown in equations 5.116 and 5.117, respectively.

$$\dot{\hat{K}}_u = \Gamma_u u_{bl} e_U^T P B_{DS} \tag{5.116}$$

$$\dot{\hat{\theta}} = \Gamma_\theta \phi(x_P) e_U^T P B_{DS} \tag{5.117}$$

6

DIGITAL FLIGHT CONTROL SYSTEM IMPLEMENTATION

The rapid prototyping environment MATLAB® /Simulink® was selected for the FCS implementation due to its strong capabilities in control system design and analysis.

The FCS algorithms introduced in Chapter 5 were at first implemented in the Simulink® environment using its block diagrams. The utilization of the block diagrams instead of the classical programming improves readability, traceability and enables convenient and allows easy modifications of the implemented system, making it useful for rapid prototyping. The next step in the implementation process was the code generation for a target hardware platform used in the experimental aircraft platform.

6.1 LINEAR QUADRATIC REGULATOR IMPLEMENTATION

The LQR controller implemented in Simulink® environment is shown in Figure 6.1. The controller structure is based on the algorithm introduced in Chapter 5. The reference input vector r is composed of 3 command signals, the airspeed V_{cmd}, altitude h_{cmd} and heading ψ_{cmd}. The controller structure itself contains two main parts, namely the Integral Error Dynamics (used for the command tracking) and feedback gain K_{LQR}. The simulation model also contains Actuator Saturation, representing actuator's physical limits, Plant Dynamics and Sensor Noise.

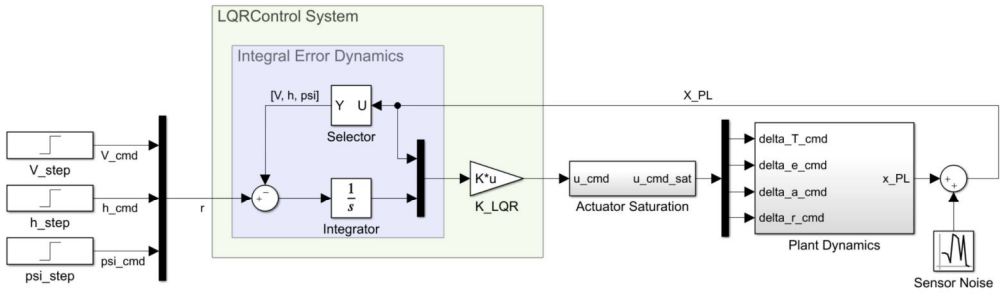

Figure 6.1: LQR simulation model implemented in Simulink® .

The Plant Dynamics structure introduced in Figure 6.2 contains the throttle, elevator, aileron and rudder actuator models connected to the Aircraft Dynamics subsystem in state-space representation. Inputs of the Plant Dynamics subsystems are the commanded control signals generated by the control system. Actuator mod-

els process control signals. Every actuator model generates control deflection and rate signal. The control deflections create the input vector to the Aircraft Dynamics subsystem. The output vector of the Plant Dynamics model x_{PL} is composed of the aircraft states and actuator deflections and rates.

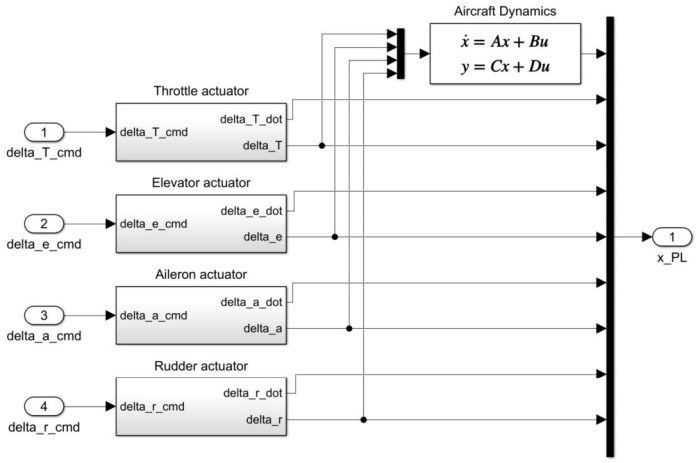

Figure 6.2: Plant dynamics structure.

The actuator dynamics is modeled using a second-order transfer function. The throttle actuator structure shown in Figure 6.3, based on the actuator model introduced in Chapter 3.

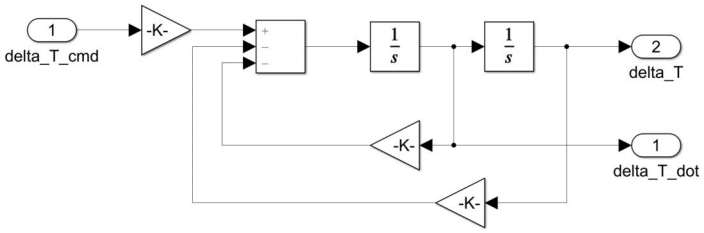

Figure 6.3: Actuator dynamics structure.

6.2 LINEAR QUADRATIC GAUSSIAN CONTROLLER IMPLEMENTATION

The LQG control system implementation in a form of Simulink® block diagram is shown in Figure 6.4. The control system was implemented using the algorithms introduced in Chapter 5. Three main components of LQG controller are the Integral Error Dynamics, Kalman filter and LQR state feedback K_{LQR}. The Plant Dynamics subsystem remaining the same as introduced in Figure 6.2.

The Kalman filter is implemented as a state-space model, which containing the information about controlled plant dynamics in the form of state-space matrices A, B, C, combined with the difference between estimated output $\hat{y}$ and Design System output y_{DS} multiplied by Kalman gain L.

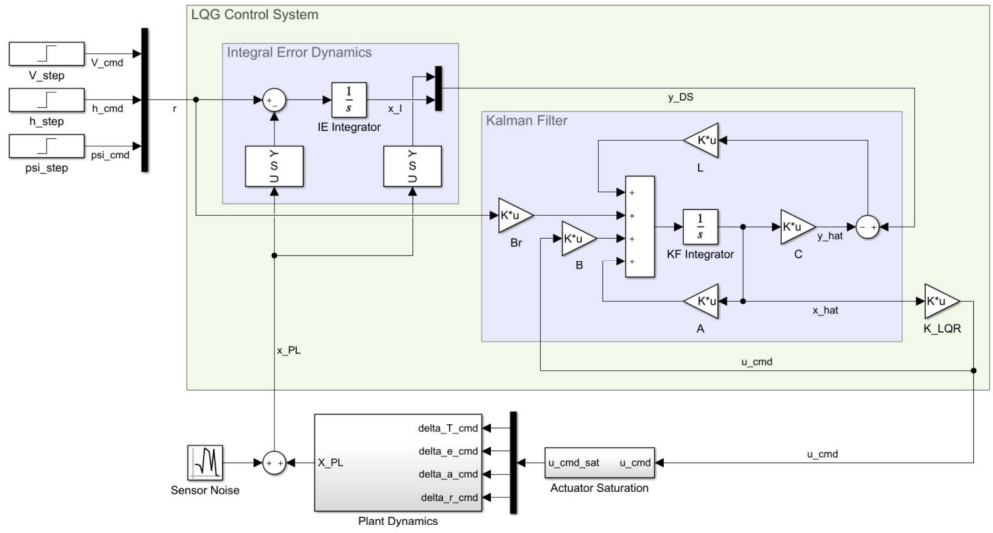

Figure 6.4: LQG simulation model implemented in Simulink® .

6.3 MODEL REFERENCE ADAPTIVE CONTROL IMPLEMENTATION

The MRAC implementation using the Simulink® block diagrams is shown in Figure 6.5. Its design augments the previously described LQR controller selected as the baseline control system. The MRAC system is composed of the Reference Model and Input and State Update Laws. The Reference Model, is extended with the Hedging input u_H to overcome the actuator saturation.

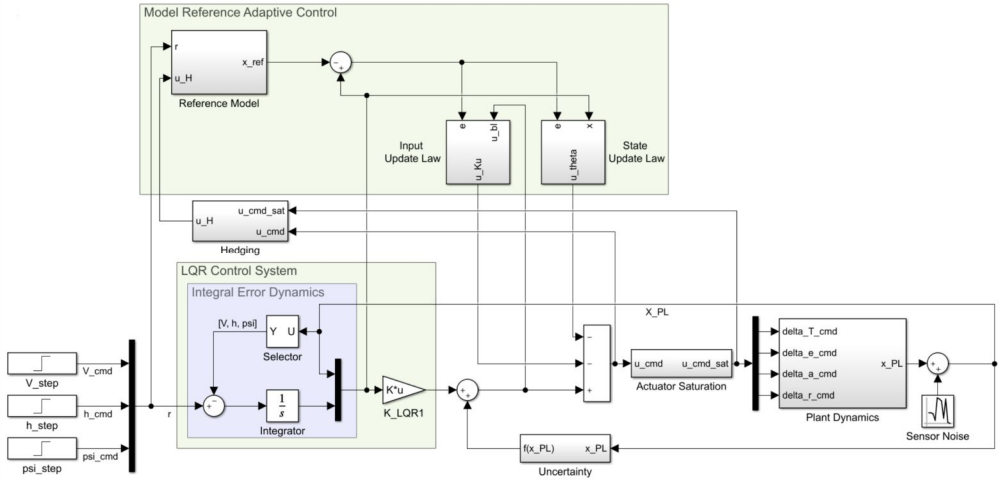

Figure 6.5: MRAC simulation model implemented in Simulink® .

Structure of the Reference Model subsystem is shown in Figure 6.6. The Reference Model dynamics was implemented in a form of a state-space representation defined by matrices A_{ref} and B_{ref} expressed by equations 5.91 and 5.92.

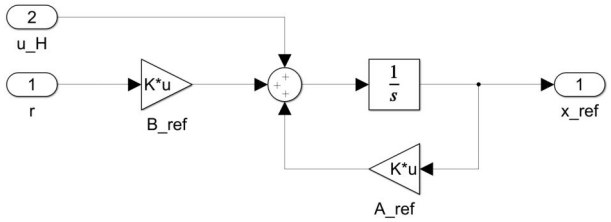

Figure 6.6: MRAC Reference Model subsystem.

The Update Laws defined by equations 5.108 and 5.109 were implemented using a Matlab Function block as introduced in Figure 6.7.

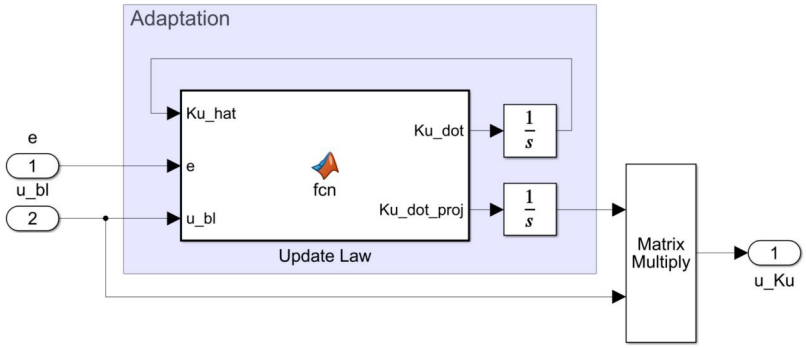

Figure 6.7: MRAC Input Update Law subsystem.

Hedging modification described in Chapter 5 was implemented as a subtraction of the saturated and non-saturated input command signal multiplied by the reference model input matrix B_{ref} as shown in Figure 6.8.

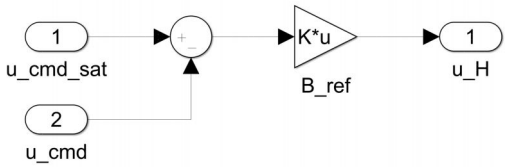

Figure 6.8: MRAC Hedging subsystem.

The following block of MATLAB® code contains the implementation of the Update Law function shown in Figure 6.7. The Update Law implementation was enhanced by a Projection algorithm described in Chapter 5 due to the parametric drift elimination.

```
function [Ku_dot, Ku_dot_proj] = fcn(Ku_hat,e,u_bl,MRAC)
% This fuction computes adaptive contribution Ku derivatives enhanced
% with Projection algorithm
% Inputs:
%       Ku_hat - Ku parameter estimate
%       e - Tracking error
%       u_bl - Baseline controller input
%       MRAC - Structure containing MRAC parameters
% Outputs:
%       Ku_dot - Derivative of Ku parameter estimate
%       Ku_dot_proj - Derivative of Ku parameter (Projection algorithm
%       employed)

f = zeros(1,2);
grad_f = zeros(2,2);
Ku_dot_new = zeros(size(grad_f));
Ku_dot_aux = (MRAC.gamma_theta*u_bl*e'*MRAC.P*MRAC.B);

for i = 1:length(MRAC.Ku_max)
    theta_abs = sqrt(Ku_hat(i,1)^2 + Ku_hat(i,2)^2 );
    f(i) = ((1 + MRAC.epsilon(i))*theta_abs^2 ...
        - MRAC.Ku_max(i)^2)/(MRAC.epsilon(i)*MRAC.Ku_max(i)^2);
    grad_f(:,i) = (2*(1 + MRAC.epsilon(i))/(MRAC.epsilon(i) ...
     *MRAC.Ku_max(i))*Ku_hat(i,:))';

    if ((f(i) > 0) && (Ku_dot_aux(:,i)'*grad_f(:,i)) < 0)
          Ku_dot_new(:,i) = Ku_dot_aux(:,i) ...
             - (grad_f(:,i)*grad_f(:,i)' ...
             /norm(grad_f(:,i))^2)*Ku_dot_aux(:,i)*f(i);
    else
          Ku_dot_new(:,i) = Ku_dot_aux(:,i);
    end
end

Ku_dot_proj = (Ku_dot_new)';
Ku_dot = (MRAC.gamma_theta*u_bl*e'*MRAC.P*MRAC.B)';
```

6.4 CODE GENERATION

The control algorithms implemented using functional blocks in Simulink® can be converted into low-level code like C/C++ directly within MATLAB® environment. This process is called code generation. The generated code can be integrated into a larger project or compiled through a third-party toolchain, and the executable files can be deployed to the target hardware. The code generation process is introduced in block diagram in Figure 6.9 [36].

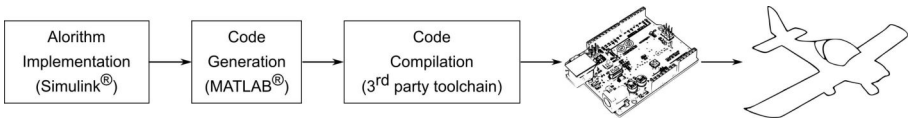

Figure 6.9: Code generation and deployment to the target hardware. Source [36]

The FCS implementations details described in the previous subsections were used mainly for the design and evaluation purposes. They contained the modeled aircraft dynamics and were implemented as continuous-time models. However, the model used for the code generation shall be implemented as a discrete-time model and shall contain only the FCS with defined inputs and outputs.

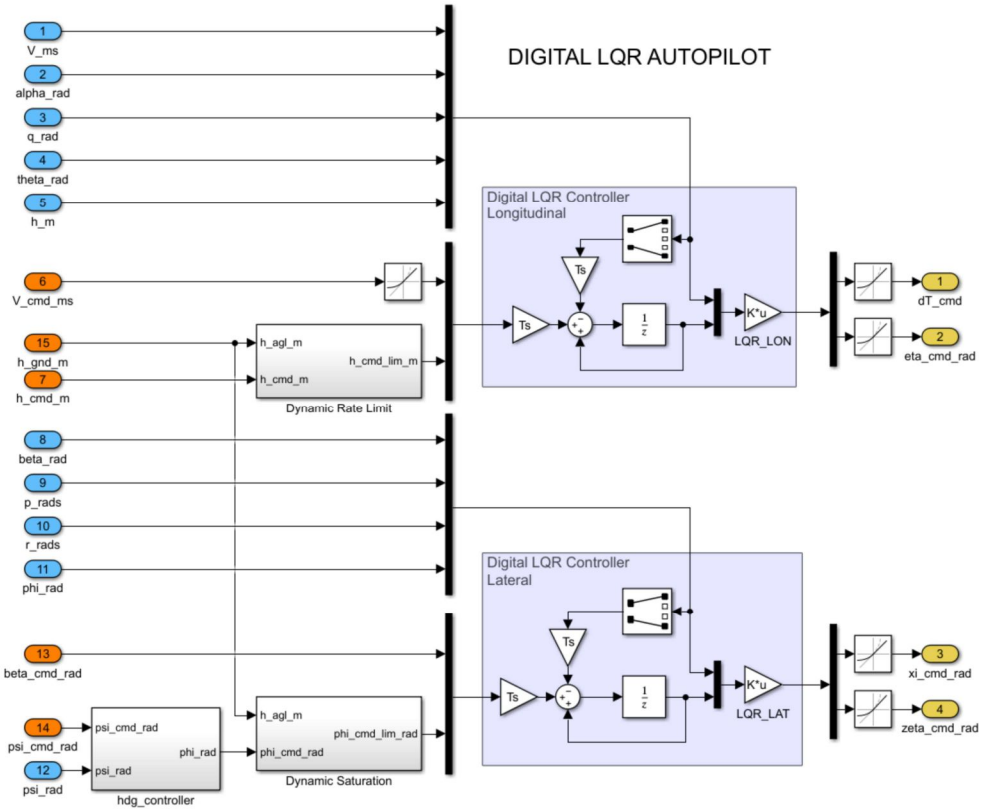

Figure 6.10: Simulink® FCS model used for code generation.

Figure 6.10 shows the FCS implementation in Simulink® used for code generation with colored inputs and outputs. The blue input ports are used for the aircraft state measurements while the orange input ports are used as command inputs. The yellow output ports send the computed control surfaces and throttle lever deflections to the actuators.

7

DIGITAL FLIGHT CONTROL SYSTEM EVALUATION

This chapter introduces the robustness, performance and flight test evaluations performed with the researched Flight Control System (FCS). The robustness evaluation employs frequency response based techniques as frequency response plots, resulting stability margins or sensitivity functions. The performance evaluation uses offline computer simulations, resulting in time-domain performance analysis using step response characteristics. The robustness evaluation focuses on the baseline controller as it employs techniques suitable for linear systems. This evaluation concept can not be used for adaptive control system designs due to its parameter changes. The performance evaluation validates both, the baseline and the adaptive control design's, time-domain performance. The longitudinal and lateral-directional control systems are to be evaluated separately. The actual flight test evaluation will be investigated in two parts. The first part will focus on the compliance to the criteria inspired by SAE-AS94900 standard for the FCS design, while within the second part an automatic approach to an airport will be tested. Chapter 7 starts with an overview of the employed evaluation techniques.

7.1 EVALUATION TECHNIQUES FOR FLIGHT CONTROL SYSTEM DESIGN

In an automatic flight control system design, it is necessary to comply to various criteria issued by the aviation authorities through regulatory requirements. The European Aviation Safety Agency (EASA) and Federal Aviation Administration (FAA) require designers to prove the design's robustness, stability and performance. Automatic flight control design techniques based on linear control strategies may utilize various well-described evaluation techniques in frequency and time domains [81].

7.1.1 *System Controlability and Observability*

Primary task of control systems is to find control input $u(t)$ within interval $[t_0, t_1]$ which changes initial state $x(t_0)$ to requested end state $x(t_1)$. Two techniques addressing the controllability and observability are used in the control system design. A linear system is controllable if there exists a control input $u(t)$ which transfers all its initial states $x(t_0) \neq 0$ to the origin of state space $x(t_1) = 0$ [37].

The measure of how well the system state $x(t)$ can be determined based on its output $y(t)$ is called state observability. If the whole system state is observable, such a system is called observable. Controllability and observability are essential prerequisites in control system design (e.g. stabilization of unstable systems or optimal control).

- **Controllability matrix** - Controllability of a linear system defined by equations 2.59-2.60 is possible to be proven with a controllability matrix. A linear dynamic system is controllable if the rank of its controllability matrix defined by the equation 7.1 is equal to system state dimension, thus it fulfills condition given by equation 7.2. Controllability matrix is defined by a dynamic matrix A and input matrix B of the above mentioned linear state-space system [55].

$$Q_C = \begin{bmatrix} B & AB & A^2B & \cdots & A^{n-1}B \end{bmatrix}, \tag{7.1}$$

  where n is the system state dimension.

- **Observability matrix** - Observability of a linear system defined by equations 2.59-2.60 can be proved by observability matrix. A linear dynamic system is observable in case the observability matrix rank is equal to the system state dimension. The observability matrix is expressed by equation 7.2 and it is defined by a dynamic matrix A and output matrix C of the above mentioned linear state-space system [55].

$$Q_O = \begin{bmatrix} C \\ CA \\ CA^2 \\ \cdots \\ CA^{n-1} \end{bmatrix}, \tag{7.2}$$

  where n is the system state dimension.

7.1.2 *Frequency Response Plots*

The control system analysis in the frequency domain plays an important role in the FCS design process. It enables to understand the system from the stability and robustness perspective. Two types of frequency response plots are being used in the control system design, namely the Nyquist and Bode plot.

A Nyquist plot is a parametric plot of an open-loop transfer function frequency response. The real part of the system's frequency response function is drawn on the x-axis, and the imaginary part is drawn on the y-axis. The shape of the Nyquist plot can determine the stability of the system as well as its stability margins. The stability of the closed-loop system can be determined from a Nyquist plot by using the Nyquist stability criterion, which defines the number of unstable closed-loop poles as a sum of the number of unstable open-loop poles and the number of clockwise encirclements by the Nyquist plot around the point -1 at the real axis [37].

Another frequently used frequency response plot is the Bode plot that contains two graphs, magnitude and phase characteristics dependent on frequency. Bode plot can be employed for the FCS design since it enables to read various system properties. Some of the important properties obtained from Bode plot are the stability margins, namely the gain and phase margin, described closely in the following subsection, system bandwidth defined by the frequency at which the magnitude plot decreases below the threshold -3dB or resonance frequency, usually indicated by a peak in magnitude plot, etc. [27]. Nyquist and Bode plot examples are shown in Figure 7.1.

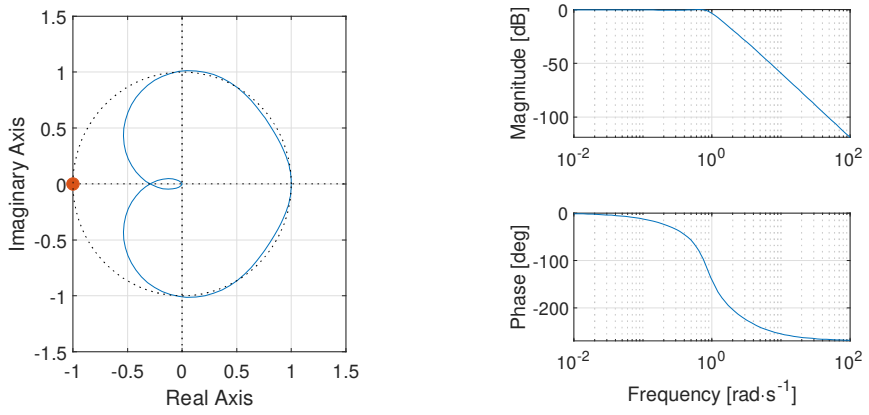

(a) Nyquist plot

(b) Bode plot

Figure 7.1: Frequency response plots.

7.1.3 *Stability Margins*

The stability margins are used to evaluate the system's stability in a frequency response representation. Two stability margins are being evaluated, the gain margin and phase margin. The gain margin is the amount of gain increase or decrease required to make the loop gain unity at the frequency where the phase angle reaches -180°. In other words, the gain margin is $1/g$ if g is the gain at the -180° phase frequency. Similarly, the phase margin is the difference between the phase of the response and -180° threshold when the loop gain equals 1.0, which is equal to the value of 0dB in the Magnitude plot. The frequency at which the magnitude is 0dB is called the unity-gain frequency or gain crossover frequency. It is generally found that gain margins of 3dB or more, combined with the phase margins between 30° and 60°, result in reasonable trade-offs between bandwidth and stability [87]. Figure 7.2 shows the derivation of phase and gain margin.

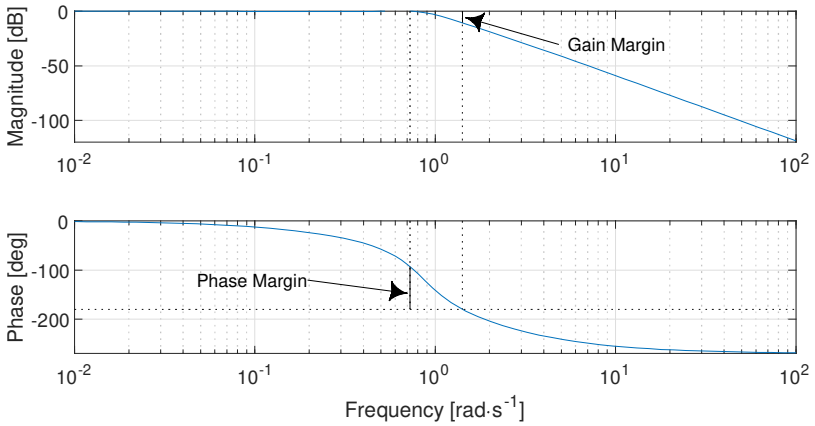

Figure 7.2: Gain and phase margins shown in Bode plot.

Stability margins are some of the upmost important parameters for the certification of a FCS. The requirements given by SAE-AS94900 dictates the margins to be within 8 dB in gain and 60° in phase.

7.1.4 *Sensitivity Function*

The sensitivity function, also referred to as sensitivity, measures how sensitive a signal is to an added disturbance. Sensitivity is a closed-loop measure. Feedback reduces the sensitivity in the frequency band, where the open-loop gain is greater than 1.0 [57]. Figure 7.3 shows the sensitivity functions in a form of a Bode plot.

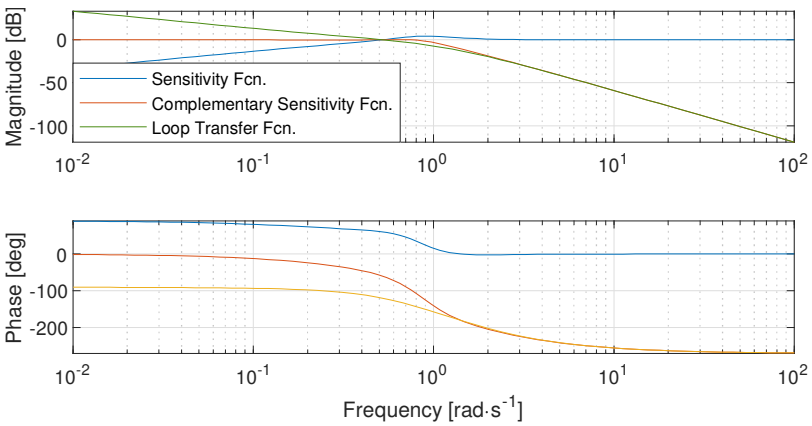

Figure 7.3: Sensitivity function in Bode plot.

7.1.5 *Time Domain Performance Criteria*

The most popular time-domain performance criteria are taken from a dynamic system's reaction to a step input signal, called step response. Rise time describes the time a controlled system needs to rise from 10% to 90% of the steady-state value. Settling time is the moment when the signal remains in ±5% range interval measured from the reference value. The last frequently used time-domain criterion is the overshoot, which expresses the percentage amount of first peak overshoot above the step input signal [37]. Figure 7.4 shows the time domain performance criteria in the step response plot.

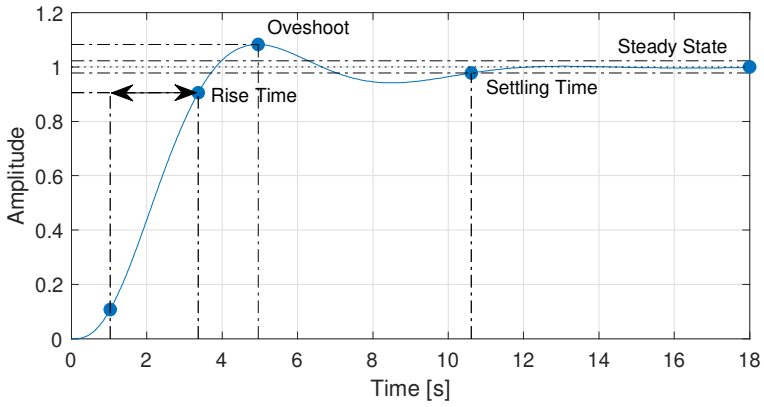

Figure 7.4: Time domain performance criteria.

7.2 ROBUSTNESS EVALUATION

The robustness characteristics of designed controllers can be investigated within the frequency domain. The LQG based control techniques generally have worse robustness properties than the LQR based approach due to the additional dynamics introduced by the Kalman filter. Different controller designs can be compared using the robustness evaluation. A favorable robustness can be observed for the case of the LQR design approach, while its noise attenuation exhibits fairly poor results. The LQG design offers good results in noise cancellation but exhibits fairly low stability margins. A good compromise between these two techniques is the utilization of the LTR approach, which improves the stability margins with the noise attenuation potential.

7.2.1 *Longitudinal Controller Robustness*

Tables 7.1 and 7.2 show the computed gain and phase margins in throttle and elevator actuator cuts.

Table 7.1: Comparison of robustness in actuator cut (δ_T) for different controllers.

Controller type	**Gain Margin [dB]**	**Phase Margin [°]**
LQR	∞	80.82
LQG	-18.71	-19.95
LTR(ν = 10)	-13.21	-117.78
LTR(ν = 1)	40.11	103.57
LTR(ν = 0.1)	177.71	52.77
LTR(ν = 0.01)	126.68	84.44

Table 7.2: Comparison of robustness in actuator cut (δ_e) for different controllers.

Controller type	**Gain Margin [dB]**	**Phase Margin [°]**
LQR	-36.16	83.69
LQG	10.25	31.61
LTR(ν = 10)	5.39	28.01
LTR(ν = 1)	8.92	43.49
LTR(ν = 0.1)	26.04	112.39
LTR(ν = 0.01)	12.87	89.81

Figures 7.5 and 7.6 show Bode plots for plant input loop-cuts at throttle and elevator actuators. Stability margins recovery can be observed with the LTR parameter being tuned. Bode plots show an additional roll-off at high frequencies caused by the state estimator and thus good noise attenuation performance for the LQG/LTR techniques. The LQR design suffers from insufficient noise attenuation performance as it does not contain any state estimator. In the case of noisy measurements, a noise suppression algorithm has to be implemented (e.g., notch filter), which introduces additional time delays in the control loop performance.

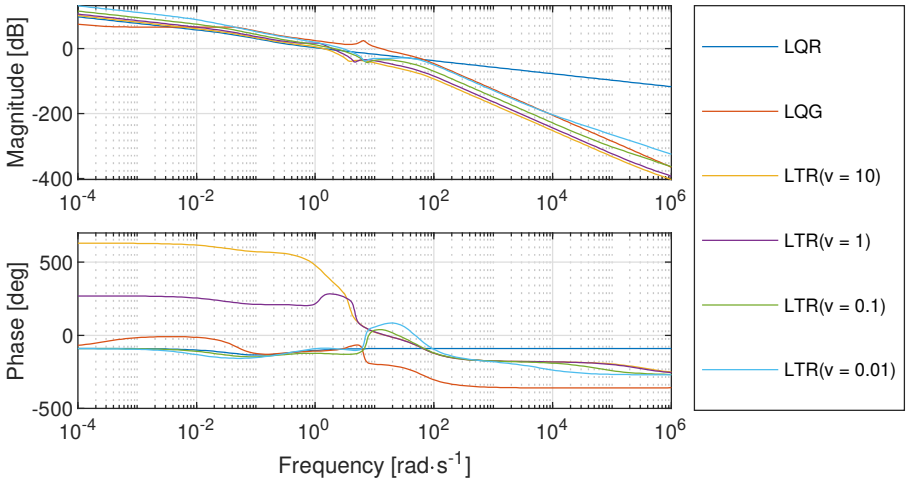

Figure 7.5: Bode plots in throttle actuator cut of different employed controllers.

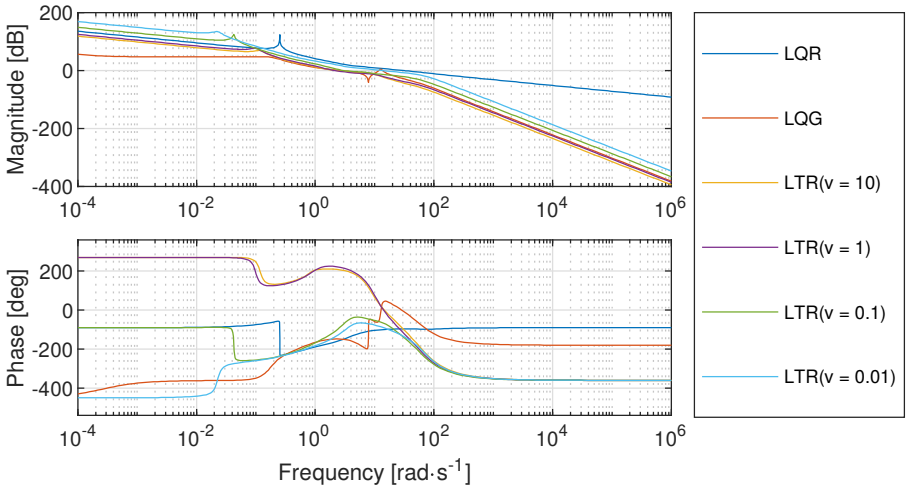

Figure 7.6: Bode plots in elevator actuator cut of different employed controllers.

Figures 7.7 and 7.8 show the Nyquist curves for the Plant input loop-cuts and present the stability margins recovery for the LTR parameter examination, as was also the case for the Bode plots above. The best controller designs, assessed from the perspective of the respective gain and phase margins, are according to the Nyquist plots the LTR based designs with parameters $\nu_1 = 0.1$ and $\nu_2 = 0.01$. These designs represent a balanced combination of robustness and noise attenuation.

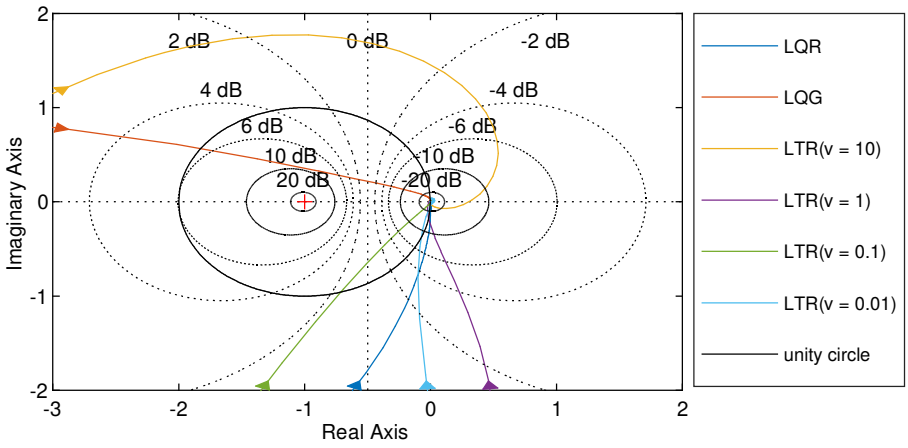

Figure 7.7: Nyquist plots in throttle actuator cut of different employed controllers.

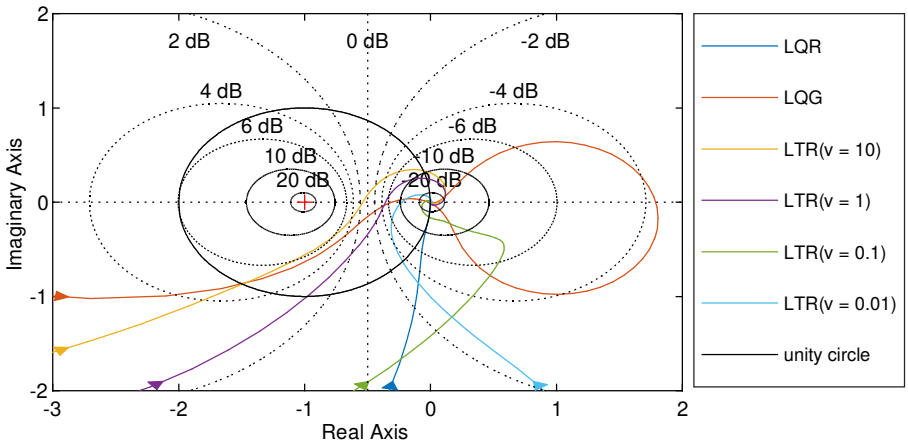

Figure 7.8: Nyquist plots in elevator actuator cut of different employed controllers.

Figures 7.9 and 7.10 present the sensitivity functions for velocity and altitude loops. The sensitivity function is for the investigated case defined as a transfer function from an input reference signal to an output regulation error. The maximum sensitivity peaks are presented in Tables 7.1 and 7.2 and show adequate sensitivity to process disturbances [94].

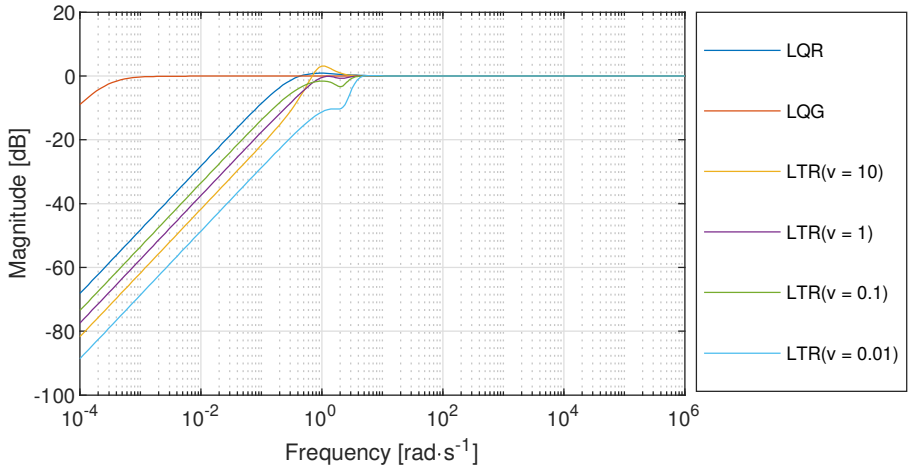

Figure 7.9: Sensitivity functions for different controller types - sensor cut in velocity measurement loop.

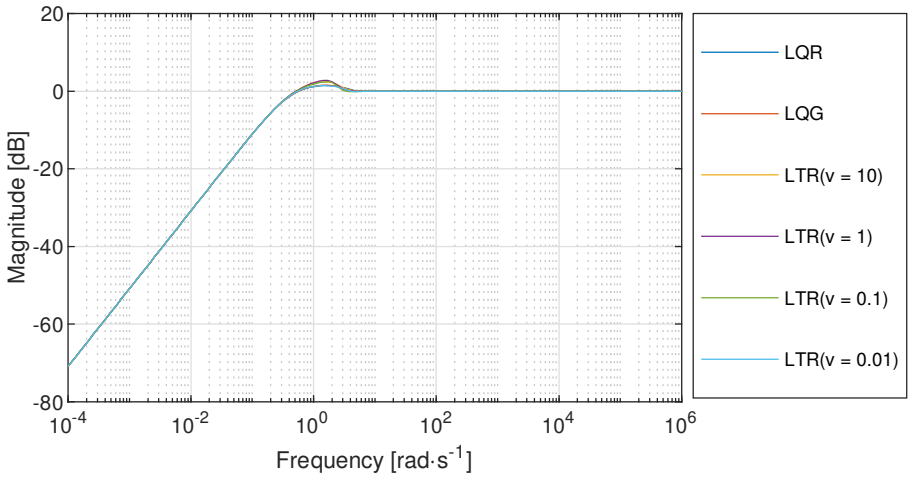

Figure 7.10: Sensitivity functions for different controller types - sensor cut in altitude measurement loop.

Table 7.3: Comparison of sensitivity function maximum in sensor cuts (V, h) for different controllers.

Controller type	**Max. Sensitivity - V [1]**	**Max. Sensitivity - h [1]**
LQR	1.18	1.11
LQG	1.19	1.00
LTR(v = 10)	1.32	1.43
LTR(v = 1)	1.38	1.01
LTR(v = 0.1)	1.32	1.01
LTR(v = 0.01)	1.18	1.02

7.2.2 *Lateral-directional Controller Robustness*

This subsection provides insight into the robustness characteristics of the researched lateral-directional FCS. Different types of controllers, namely the LQR, LQG, and its modifications using the LTR techniques are compared in frequency domain characteristics. The stability margins in actuator cut and sensitivity function maximums in sensor cut loop transfer functions are presented in Tables 7.4 and 7.5.

Table 7.4: Comparison of robustness in actuator cut (δ_a) for different controllers.

Controller type	**Gain Margin [dB]**	**Phase Margin [°]**
LQR	∞	66.48
LQG	4.93	17.61
LTR(ν = 10)	18.67	53.30
LTR(ν = 1)	-18.55	45.14
LTR(ν = 0.1)	14.67	40.83
LTR(ν = 0.01)	-5.52	-37.66

Table 7.5: Comparison of robustness in actuator cut (δ_r) for different controllers.

Controller type	**Gain Margin [dB]**	**Phase Margin [°]**
LQR	∞	92.56
LQG	4.29	34.69
LTR(ν = 10)	38.18	47.18
LTR(ν = 1)	36.43	65.97
LTR(ν = 0.1)	26.39	39.79
LTR(ν = 0.01)	25.15	-81.02

The values of gain and phase margins in Tables 7.4 and 7.5 show the robustness deterioration when compared to the LQR and LQG controller. The stability margins of the LQG control were restored utilizing the LTR modification. The best values of gain margin, phase margin and sensitivity function maximum were achieved when setting the LTR parameter $\nu = 10$.

Figures 7.11 and 7.12 show Bode plots of loop transfer functions formed in aileron and rudder input loop-cuts. The Bode plots show again the insufficient high frequency noise attenuation capabilities of the LQR controller when compared to the LQG or LTR and stability robustness improvement of the LTR designs.

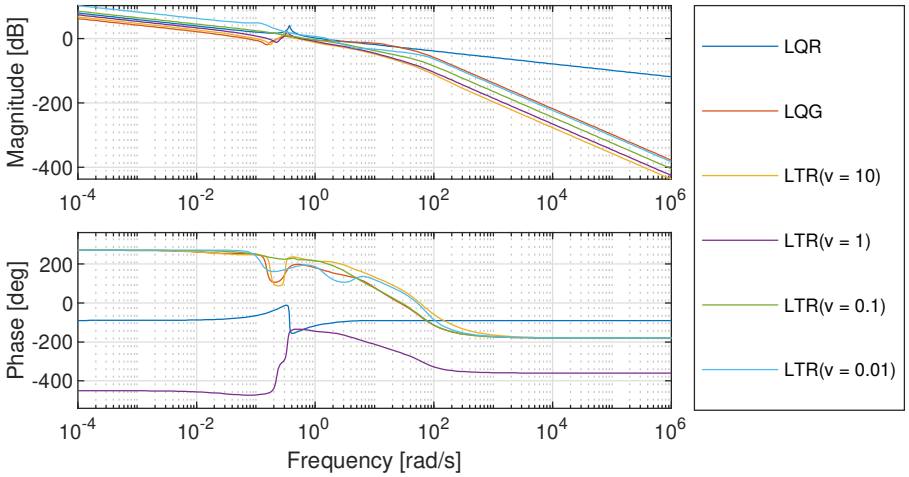

Figure 7.11: Bode plots in aileron actuator cut of different employed controllers.

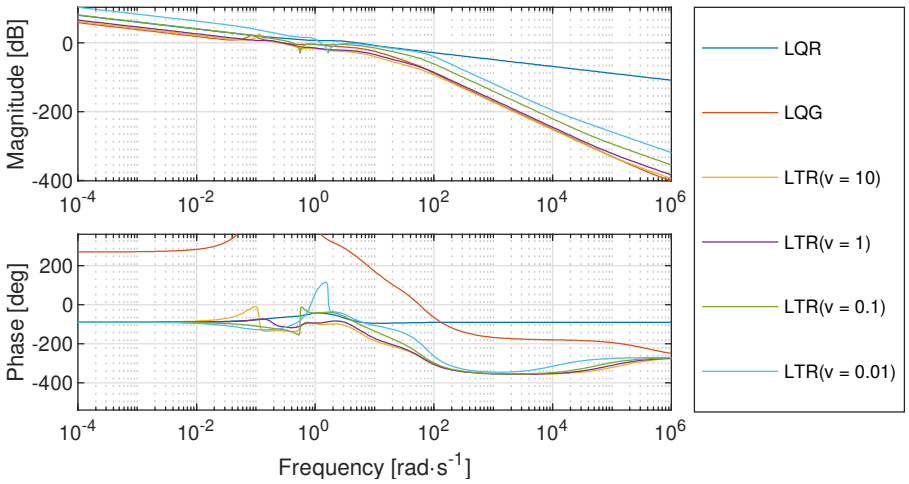

Figure 7.12: Bode plots in rudder actuator cut of different employed controllers.

Figures 7.13 and 7.14 show the Nyquist plots representing the loop transfer function's frequency response in aileron and rudder actuator cuts. The best stability and robustness characteristics according to the Nyquist plot were performed by the LQR, while the LTR modifications improved the stability characteristics of theLQG control system.

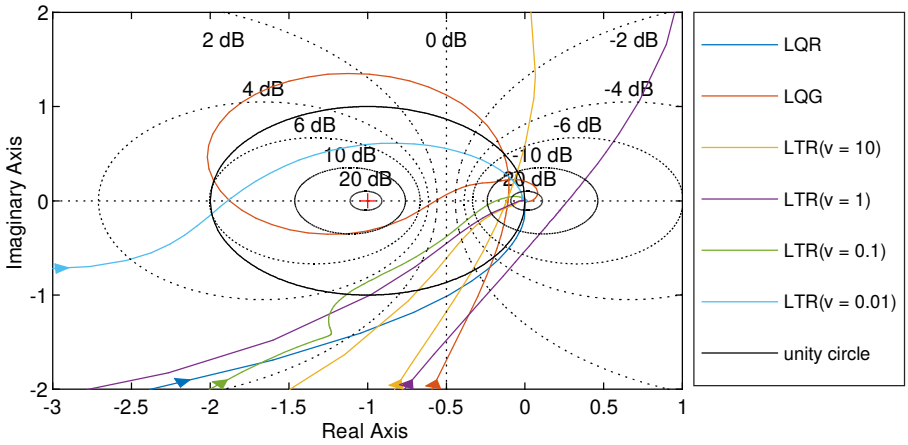

Figure 7.13: Nyquist plots in aileron actuator cut of different employed controllers.

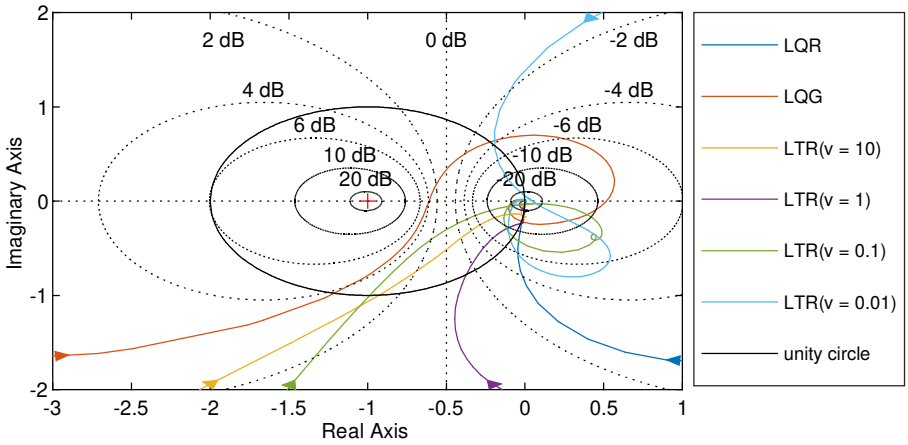

Figure 7.14: Bode plots in rudder actuator cut of different employed controllers.

The sensitivity functions computed at the plant outputs β and ψ (so called sensor cuts) are shown in Figures 7.15 and 7.16.

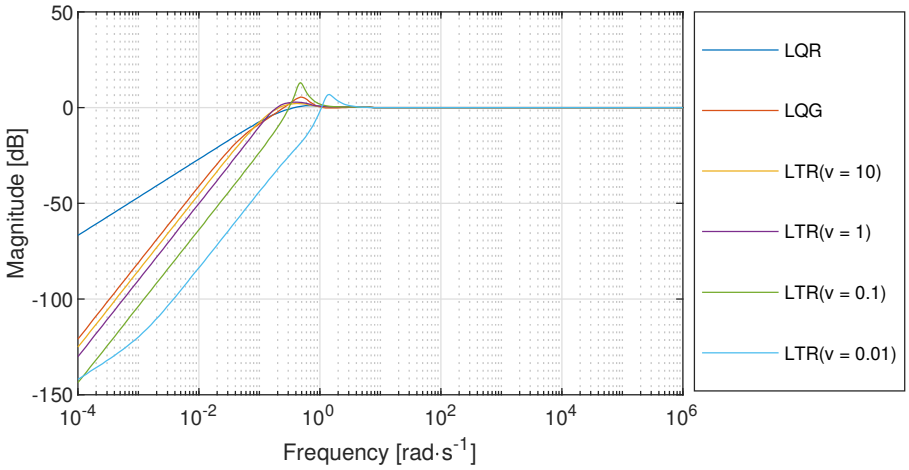

Figure 7.15: Sensitivity functions for different controller types - sensor cut in angle of sideslip loop.

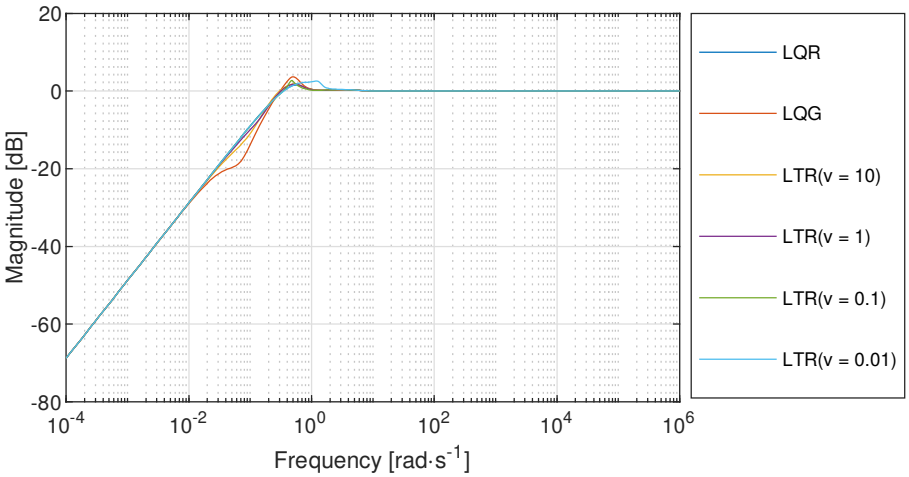

Figure 7.16: Sensitivity functions for different controller types - sensor cut in heading loop.

Table 7.6: Comparison of sensitivity function maximum in sensor cuts (β, ψ) for different controllers.

Controller type	**Max. Sensitivity - β [1]**	**Max. Sensitivity - ψ [1]**
LQR	1.19	1.12
LQG	1.53	1.87
LTR(ν = 10)	1.23	1.27
LTR(ν = 1)	1.23	1.38
LTR(ν = 0.1)	1.37	4.46
LTR(ν = 0.01)	1.34	2.20

7.3 PERFORMANCE EVALUATION

The FCS performance can be evaluated by observing the step responses of the closed-loop system. Step response characteristics, namely the rise time, settling time, overshoot, peak value and peak time can be selected as the main performance indicators. The baseline and adaptive controller performances are to be analyzed separately, and both are divided into longitudinal and lateral-directional parts, respectively.

7.3.1 *Baseline Controller Evaluation*

The baseline controller performance was evaluated in computer simulations using the aircraft dynamics in a form of a state-space model introduced in Chapter 2 with modeled actuator dynamics and sensor noise described in Chapter 3. The two designs, the LQR and LQG were considered as baseline controllers, and their performances were compared.

7.3.1.1 *Longitudinal control*

Five different state variables (airspeed V, angle of attack α, pitch rate q, flight path angle γ and altitude h) and 2 control input variables (elevator δ_e and throttle δ_T deflection) were observed for a time-domain performance analysis. The airspeed and altitude were chosen as controlled variables. Step changes of reference airspeed and altitude were performed during the simulation. Figures 7.17, 7.18 and 7.19 show the step response of controlled variables for LQR and LQG control design approaches. As the LQG control employed the Kalman filter for the state estimation, it shows better noise attenuation performance. The control variables, the throttle δ_T and elevator δ_e deflections remained within the saturation limits given by the physical limits of the aircraft.

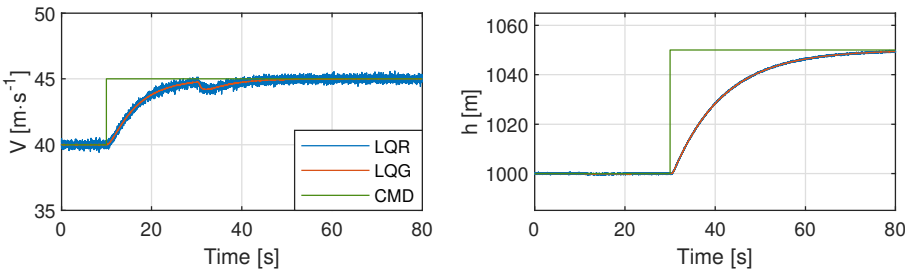

Figure 7.17: Comparison of longitudinal LQR & LQG controllers - command tracking.

The time performance characteristics mentioned in the previous paragraph are shown in Table 7.7. Both controlled variables have almost no steady-state error and

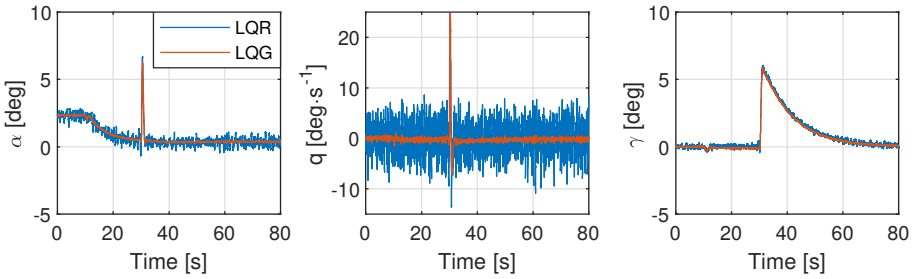

Figure 7.18: Comparison of longitudinal LQR & LQG controllers - plant states.

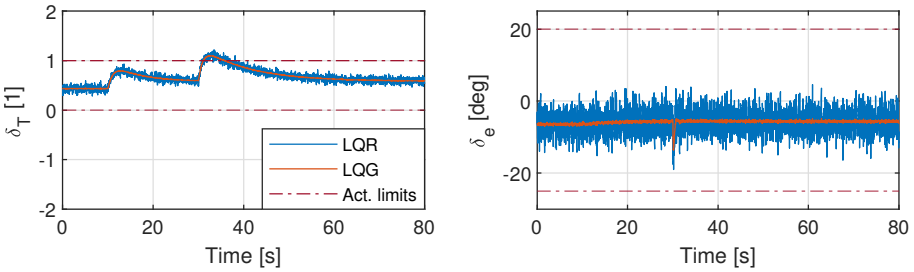

Figure 7.19: Comparison of longitudinal LQR & LQG controllers - plant inputs.

small overshoot. Short settling time and rise time proves that weight matrices Q and R were selected correctly [94].

Table 7.7: Time performance characteristics for controlled longitudinal variables in climb.

Command step	ΔV (+5 m·s^{-1})	Δh (+30 m)
Rise Time [s]	3.13	0.84
Settling Time [s]	5.74	7.09
Overshoot [%]	0.00	7.74
Peak [1]	59.99	5.39
Peak Time [s]	8.94	1.88

7.3.1.2 *Lateral-directional control*

The control task performed by the lateral-directional controller is composed of heading angle ψ command tracking and angle of sideslip β regulation to 0 in order to perform the coordinated turn. Figure 7.20 shows the lateral-directional variables controlled by the LQR and LQG controllers.

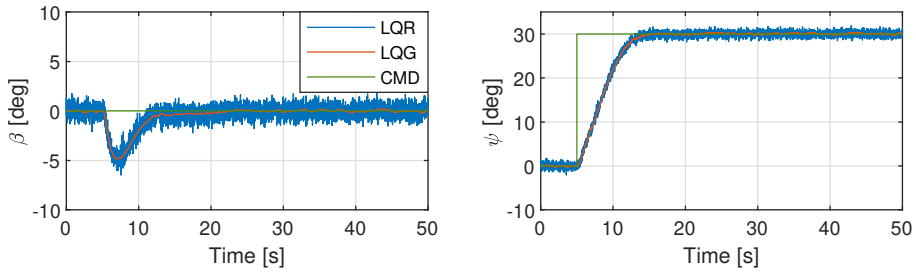

Figure 7.20: Lateral-directional LQR & LQG controllers comparison - command tracking.

Figure 7.21 shows the lateral-directional model states during the heading ψ control task. The Kalman filter state estimates are displayed for the case of the LQG controller, which is the reason why the LQG variables contain less noise. Figure 7.22 displays lateral-directional plant inputs during the heading angle command tracking task. The control deflections did not exceed the actuator's physical limits, due to a conservative controller setting.

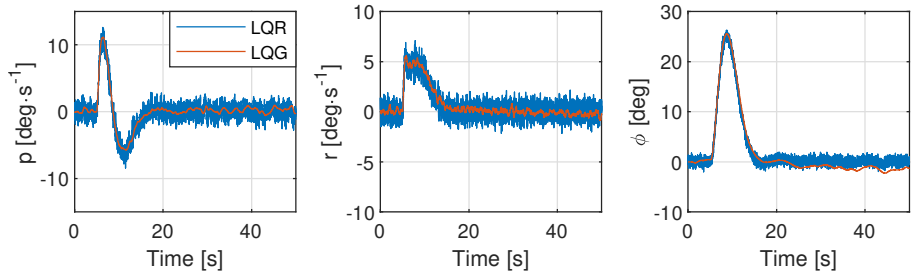

Figure 7.21: Comparison of lateral-directional LQR & LQG controllers - plant states.

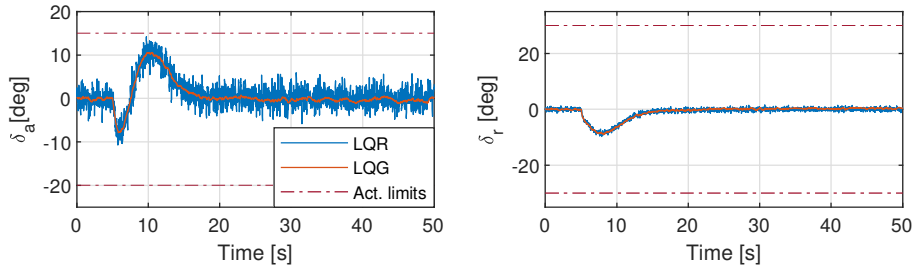

Figure 7.22: Comparison of lateral-directional LQR & LQG controllers - plant inputs.

Table 7.8: Time performance characteristics for controlled lateral-directional variables in level flight.

Command step	$\Delta\beta$ (0°)	$\Delta\psi$ (+ 30°)
Rise Time [s]	0.00	5.88
Settling Time [s]	22.81	13.61
Overshoot [%]	-	0.01
Peak [-]	4.86	30.00
Peak Time [s]	7.13	26.84

7.3.2 *Adaptive Control System Evaluation*

The performance of the adaptive FCS was tested with a simulation model based on the data collected during flight experiments with the utilization of system identification algorithms. The control system maintained preselected airspeed while performing step changes in altitude. During the simulation, a matched uncertainty was introduced to the model in the 250th second. The matched uncertainty affects only the moment equation in the Plant Dynamics and can be directly compensated for by the control surface deflection. The uncertainty was composed of a control effectiveness loss of 50% and a linear state-dependent uncertainty defined by the equations 7.3 and 7.4.

$$f(\alpha, q) = k_\alpha \alpha + k_q q \tag{7.3}$$

$$f(\beta, p, r) = k_\beta \beta + k_p p + k_r r \tag{7.4}$$

where $k_\alpha, k_q, k_\beta, k_p, k_r$ are parameters of uncertainty. The parameter values used in the computer simulations are shown in Table 7.9.

Table 7.9: Control surfaces uncertainty parameter values.

Control element	k_α [1]	k_q [1]	k_β [1]	k_p [1]	k_r [1]
Uncertainty - δ_e	-2.53	-1.06	-	-	-
Uncertainty - δ_a	-	-	-0.21	0.03	-0.99
Uncertainty - δ_r	-	-	-0.21	-13.15	3.13

7.3.2.1 *Adaptive longitudinal control*

During the first simulation, the uncertainty mentioned above was injected into a closed-loop system, which contained only the baseline controller without any adaptation. The uncertainty caused rough oscillations in the altitude control loop, and the closed-loop system became unstable. The instability caused by untcertainty mentioned above is observable in Figure 7.23 after 250th second of simulation.

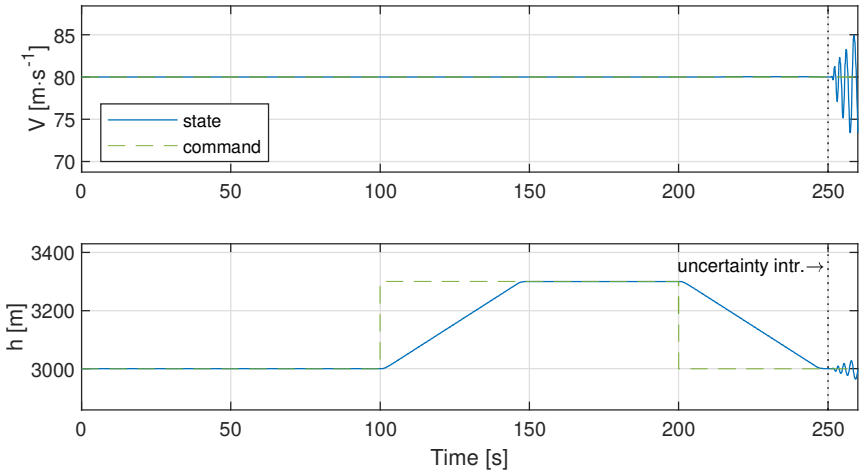

Figure 7.23: Airspeed and altitude control using baseline controller.

Figure 7.24 shows tracked signals of airspeed V and altitude h under active adaptation process. An uncertainty that started the adaptation process was introduced in the 250th second. A small oscillatory response to the first step input occurred after the introduction of the uncertainty. Right after the second step response, the controller maintained minimal overshoot and similar rise time as before the introduction of the uncertainty.

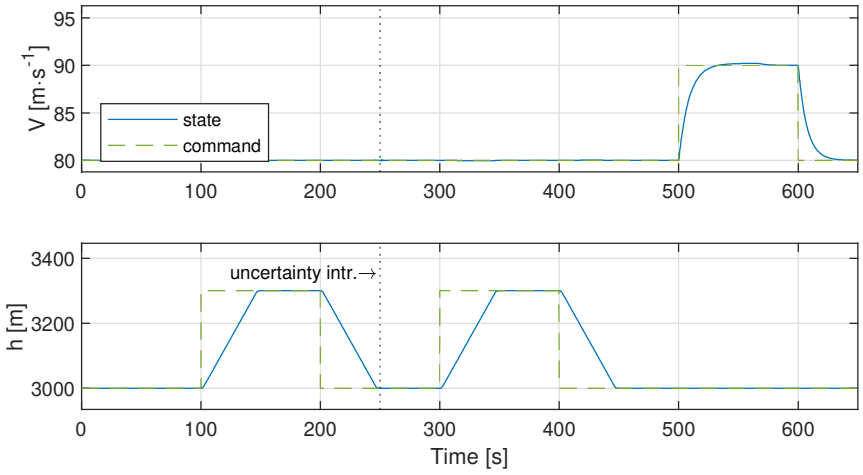

Figure 7.24: Airspeed and altitude control using MRAC

Figure 7.25 shows the remaining states (angle of attack α, pitch rate q and flight path angle γ) in the simulation model to demonstrate the adaptation process. Again, small oscillations are present after the introduction of uncertainty. However, the adaptive controller stabilizes the closed-loop system.

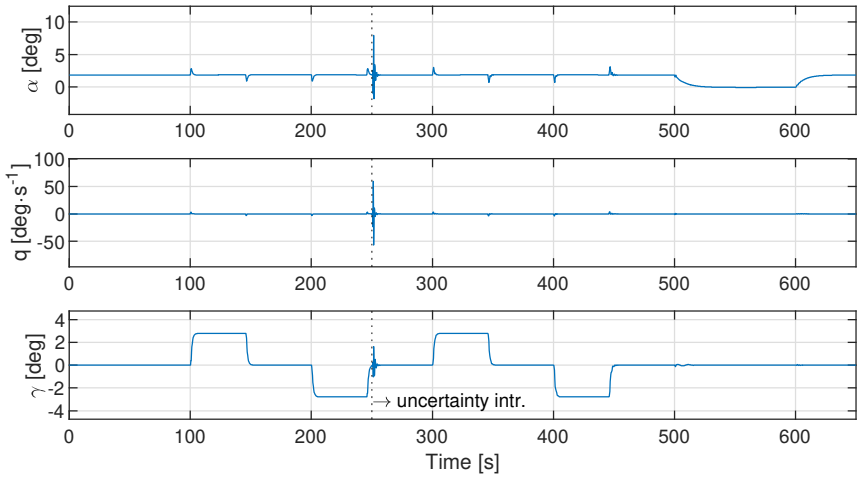

Figure 7.25: Longitudinal state variables under MRAC.

The control surface deflections (throttle δ_T and elevator δ_e) are shown in Figure 7.26 and again demonstrate the ability of the adaptive controller to overcome the uncertainty. The control variables remained within the actuator's physical limits. In case the actuators would saturate, the hedging algorithm would modify the reference model to compensate for the saturation effect.

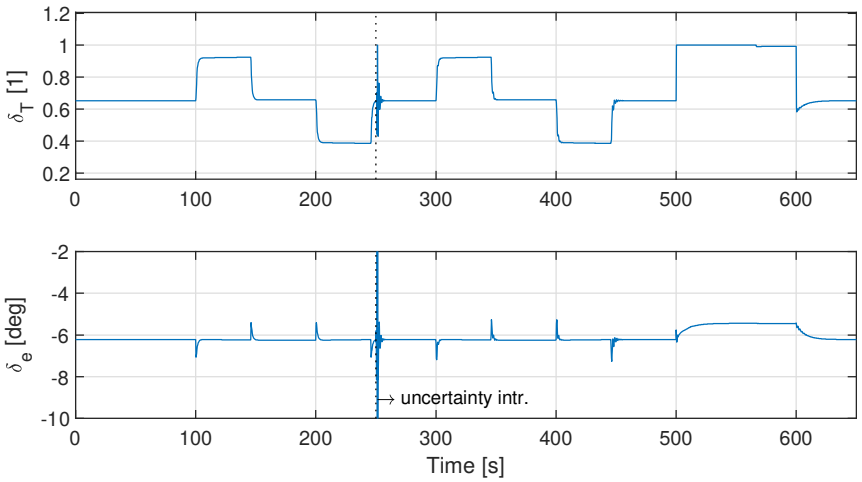

Figure 7.26: Longitudinal input variables under MRAC.

Figure 7.27 demonstrates the change of the adaptive parameters $\hat{\theta}$ and K_u when compensating for the injected uncertainty described in equations 7.3 and 7.4. All eight monitored parameters converge to the optimal values. In the case of a parameter drift, the projection algorithm described in Section 5.3 would keep the parameters within the defined boundaries [93].

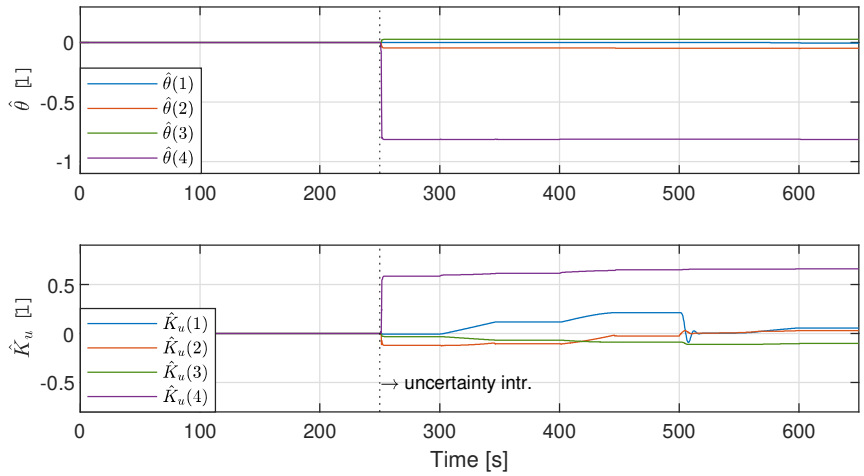

Figure 7.27: Evolution of longitudinal adaptive parameters.

7.3.2.2 *Adaptive lateral-directional control*

The second set of simulations was focused on lateral-directional motion control. The adaptive control system was supposed to track the given heading while maintaining a minimal sideslip angle with the presence of the above-defined uncertainty introduced in the 250th second of the simulation run. Figure 7.28 shows the behavior of the LQR baseline controller without any adaptation under the influence of uncertainty. Violent oscillations can be observed after the onset of the introduced uncertainty.

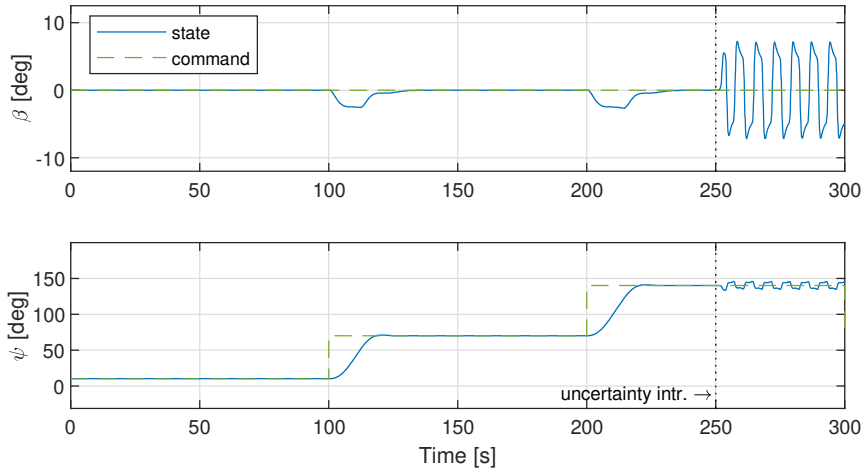

Figure 7.28: Sideslip and heading control using baseline controller.

Figure 7.29 depicts the tracking capabilities of a lateral MRAC controller. The FCS maintains favorable tracking performance of heading angle even after the onset of uncertainty and keeps minimal overshoots and steady-state error. The sideslip angle remains within the 3 degrees interval, which is acceptable.

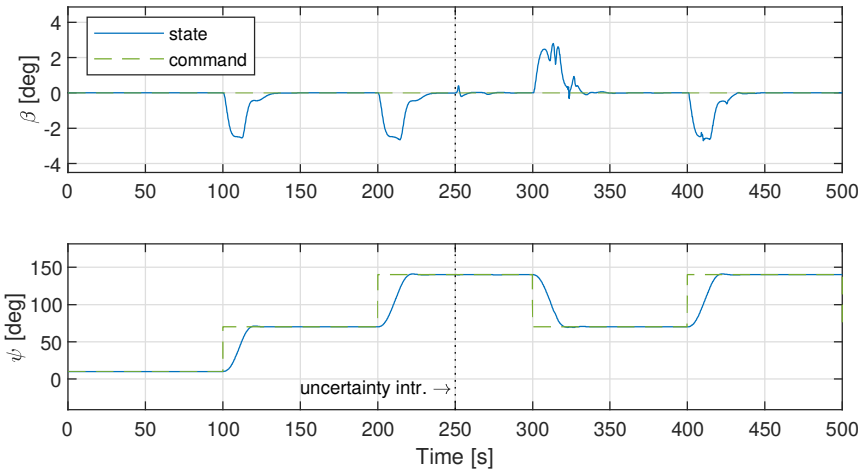

Figure 7.29: Sideslip and heading control using MRAC.

The remaining lateral-directional states i.e., roll and yaw rates, and the roll angle, can be seen in Figure 7.30. This figure shows a slight oscillation during the first step response after the uncertainty onset. The MRAC controller shows adaptation and a smooth transition during a heading change maneuver in the 400th second.

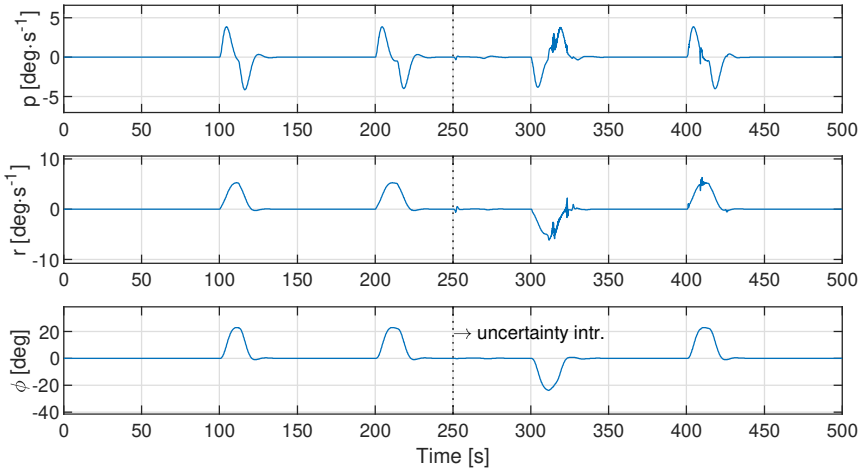

Figure 7.30: Lateral-directional state variables under MRAC.

As seen in Figure 7.31, the control surface deflection remains within the actuator's physical limit. The adaptation process can be seen after the onset of the uncertainty. The reaction to the first step under the uncertainty conditions is slightly oscillatory, while the MRAC controller's reaction to the second heading change is smoother with a minor change in the amplitude.

Figure 7.32 demonstrates the change of adaptive parameters $\hat{\theta}$ and K_u in order to compensate for the injected uncertainty introduced in equations 7.3 and 7.4. As can be seen in Figure 7.32, all eight monitored parameters converge to their optimal values. In the case of a parameter drift, the projection algorithm described in the previous section would keep the parameters within the defined boundaries.

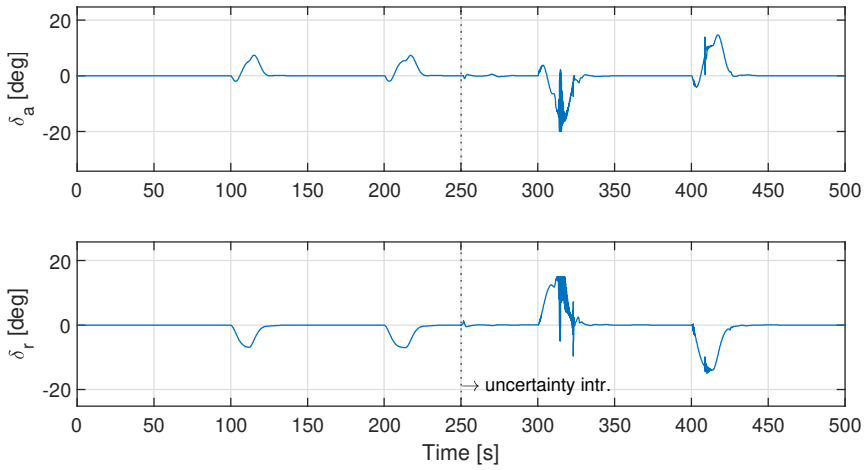

Figure 7.31: Lateral-directional input variables under MRAC.

The uncertainty for the lateral-directional motion control case was introduced during a steady level flight. However, the MRAC controller needs to adapt a sufficient system excitation, which is why significant parameter changes are observable at the 300th second of the simulation during a heading change and not instantly when the uncertainty is introduced [93].

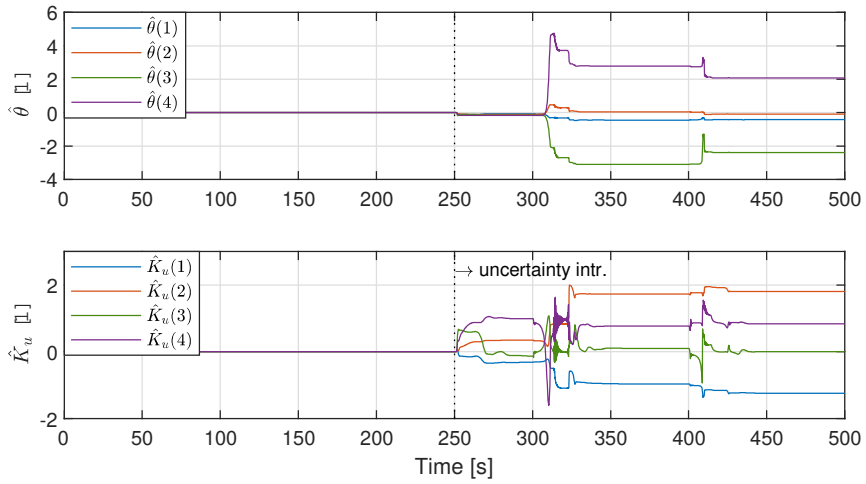

Figure 7.32: Evolution of lateral-directional adaptive parameters.

7.3.2.3 *Adaptive control performance evaluation*

As the adaptation gains change throughout the simulation, the only relevant evaluation criteria are the time domain performance characteristics as the rise time, settling time, overshoot, peak value and peak time. Values of mentioned criteria were monitored after a state-dependent uncertainty was introduced into the simulation. Table 7.10 shows time-domain performance characteristics for longitudinal and lateral-directional simulation cases [93].

Table 7.10: Time-domain performance characteristics for longitudinal and lateral-directional cases.

Command step	ΔV (+10 m·s^{-1})	Δh (+300 m)	$\Delta\psi$ (+70°)
Rise Time [s]	17.28	36.58	12.01
Settling Time [s]	67.33	46.31	19.32
Overshoot [%]	0.24	0.00	1.32
Peak Value [-]	90.22	3300.00	70.91
Peak Time [s]	66.67	100.00	22.64

As the lateral-directional MRAC controller was designed to track the target heading signal while driving the sideslip angle to zero, the time domain performance characteristics are shown only for the heading angle.

7.4 FLIGHT TEST EVALUATION

The operational functionality of the FCS algorithms designed for the automatic flight and automated landing approach has been experimentally confirmed in flight experiments performed with an experimental LSA. This section is divided into two subsections. The first subsection describes the automatic flight results with manually inserted command values of altitude, airspeed and heading. The second subsection is focused on a complex task of automatic landing approach.

7.4.1 *Flight Control System Evaluation*

An important part of the FCS evaluation is the examination of qualitative indicators of automatic control. The reference SAE-AS94900 [76] was employed in evaluation of the FCS design.

7.4.1.1 *Coordination in Steady Banked Turns*

Figure 7.33 shows the aircraft trajectory in an FCS coordinated turn during practical flight experiments. The figure also contains the time series of the angle of sideslip β and lateral acceleration a_y. The quantitative limits for this task specified by reference [76] are shown in respective graphs.

- Increment of angle of sideslip β shall not exceed $\pm 2°$.
- Lateral acceleration a_y shall not exceed 0.03 g during steady banks.

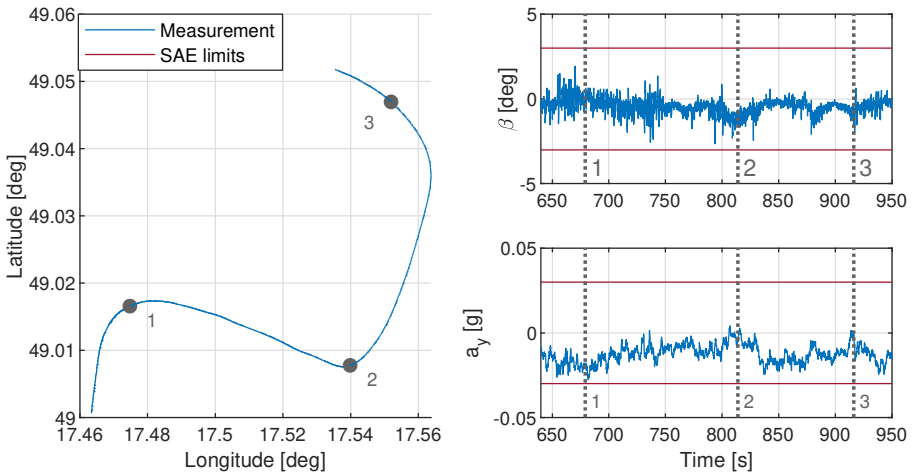

Figure 7.33: Coordinated steady banked turns.

Based on the evaluation of observed criteria defined by regulation [76] the designed FCS fulfills the conditions expressed in paragraph 3.2.4.1.3.1.

7.4.1.2 *Lateral Acceleration Limits During Roll Maneuver*

Figure 7.34 depicts aircraft motion characteristics during roll maneuver with activated FCS. The graphs show time series of lateral acceleration a_y, roll rate p and roll angle ϕ in aircraft's BFF. Every graph contains the quality of control limits taken from paragraph 3.2.4.1.3.2 "Lateral acceleration limits, rolling" of the reference [76]. A short overview of the mentioned criteria is listed below:

- The lateral acceleration a_y in aircraft BFF shall not exceed $\pm 0.1g$ for flight condition with roll rate up to $30°{\cdot}s^{-1}$.
- The limits shall be fulfilled for flight in constant altitude and continuous rolling from one side to the other for maximum roll rate achieved by the FCS.

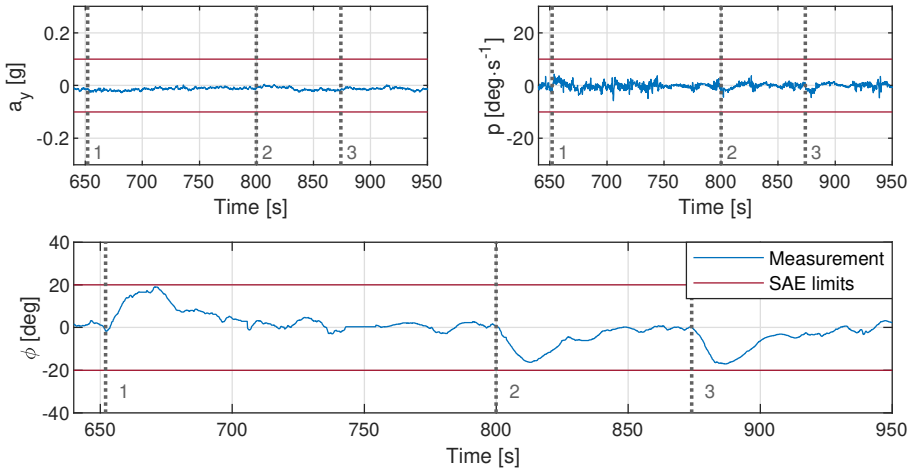

Figure 7.34: Aircraft characteristics during roll motion.

The limit roll angle of 20° comes from an internal setting of the FCS, while the limit roll rate value $10°{\cdot}s^{-1}$ comes from paragraph 3.2.4.2.3 "Heading select" of the reference [76]. Based on the criteria defined by the reference [76], the designed FCS complies to the requirements of paragraph 3.2.4.1.3.2 of mentioned regulation.

7.4.1.3 *Coordination in Steady Level Flight*

Figure 7.35 depicts the aircraft trajectory in FCS controlled steady level flight during a flight test. The figure with aircraft trajectory is completed with plots showing time series of the aerodynamic angle of sideslip β and lateral acceleration a_y during steady level flight. The limit values for FCS performance evaluation are shown in graphs of the angle of sideslip β and lateral acceleration a_y, respectively. The short list of performance criteria defined by paragraph 3.2.4.1.3.3 "Coordination in straight and level flight" of reference [76] are described below:

- The angle of sideslip shall not exceed $\pm 1°$ from the steady-state value in steady level flight.
- The lateral acceleration a_y at the center of gravity shall not exceed $\pm 0.02g$.

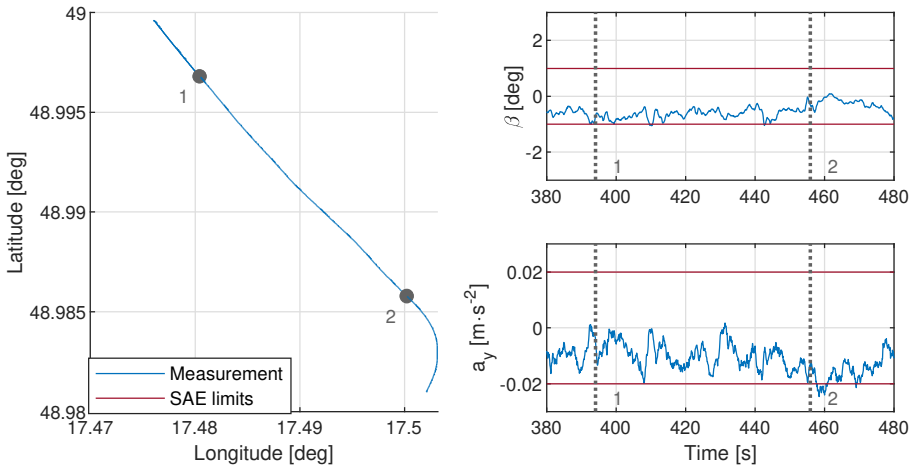

Figure 7.35: Angle of sideslip in steady level flight.

Considering the measurements acquired during the practical flight evaluation, the designed autopilot fulfills criteria of paragraph 3.2.4.1.3.3 from reference [76].

7.4.1.4 *Attitude Hold*

Figure 7.36 shows the aircraft trajectory in a steady level flight during the FCS flight test. The aircraft trajectory is augmented by time series of aircraft attitudes described by respective Euler angles, i.e., roll angle ϕ and pitch angle θ measured in steady level flight. Both graphs with measured aircraft attitude contain respective limit values taken from paragraph 3.2.4.2.1 "Attitude Hold (Pitch and Roll)" of reference [76]. A short list of mentioned criteria is described below:

- For non-turbulent air, the static precision shall be kept within the limits $\pm 0.5°$ for pitch angle and $\pm 1°$ for roll angle with respect to steady-state values.
- In case of a flight in the turbulent atmosphere, the offset in pitch angle shall be lower than $5°$ RMS, and the offset in roll angle shall not exceed $10°$ RMS.

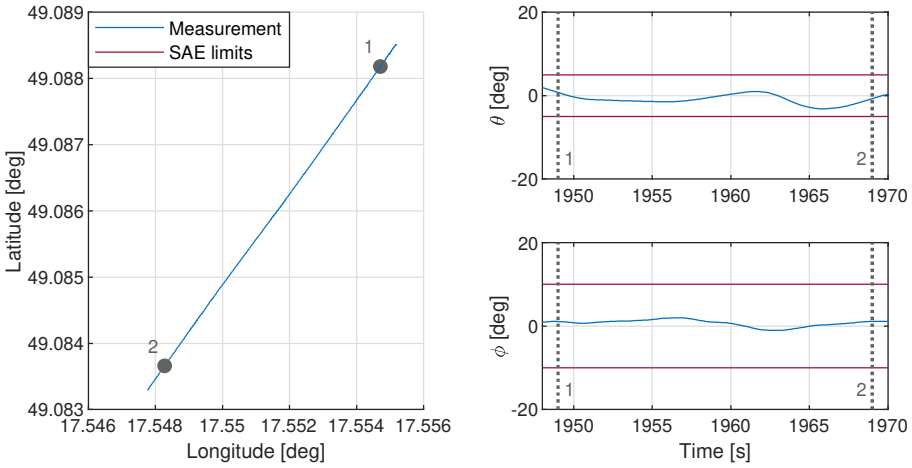

Figure 7.36: Attitude hold mode in steady level flight.

Referring to pitch and roll angle measurements in attitude hold mode it can be concluded that the designed autopilot fulfills conditions of paragraph 3.2.4.2.1 taken from the reference [76].

7.4.1.5 *Heading Hold*

Figure 7.37 introduces an aircraft trajectory during a steady level flight controlled by the researched FCS for the purpose of the flight performance evaluation. The aircraft trajectory is shown in combination with a graph of heading measurement during the steady level flight. The heading measurement graph contains flight performance evaluation limits taken from paragraph 3.2.4.2.2 "Heading Hold" of reference [76]. A short list of mentioned criteria is shown below:

- The steady offset to the reference heading under calm air conditions shall be kept within the range of $\pm 0.5°$.
- The offset from the reference heading atmospheric turbulence shall not exceed 5° RMS

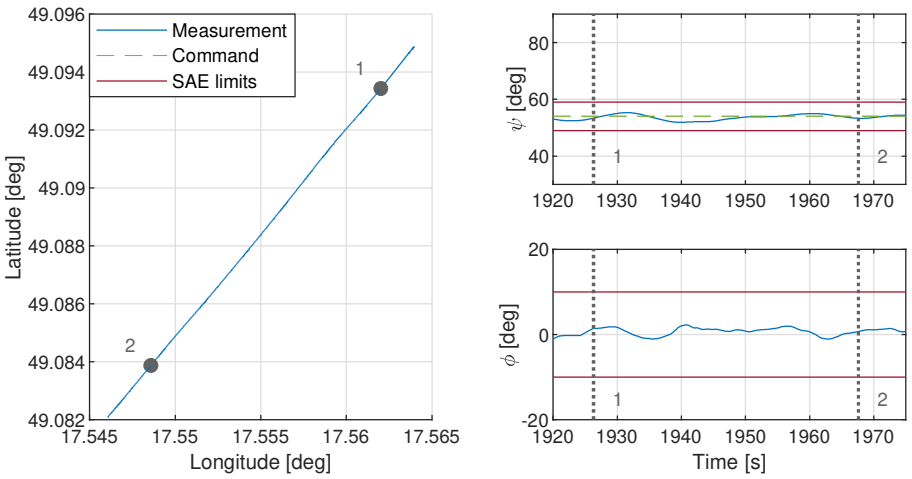

Figure 7.37: Heading hold mode in steady level flight.

Based on the recorded heading measurement during the flight performance evaluation, it can be concluded that the researched autopilot fulfills conditions defined by the paragraph 3.2.4.2.2 of reference [76].

7.4.1.6 *Heading Select*

Figure 7.38 shows the aircraft trajectory during a heading change controlled by the FCS as a part of the flight experiment. The figure also contains the aircraft's trajectory during heading change maneuver, commanded and measured heading and measured roll rate p. Both graphs contain limits for control quality evaluations taken from the paragraph 3.2.4.2.3 "Heading Select" of reference [76]. A short overview of the mentioned criteria is listed below:

- After activation, the FCS shall perform a coordinated turn towards the selected direction with minimal heading change, while maintaining the tolerances mentioned in the subsection Heading Hold.
- The autopilot shall not overshoot the selected heading by more than 1.5° in clean configuration and by more than 2.5° in configuration with flaps.
- The coordinated turn enter and exit shall be quick and continuous.
- The roll rate p shall not exceed $10°{\cdot}s^{-1}$.

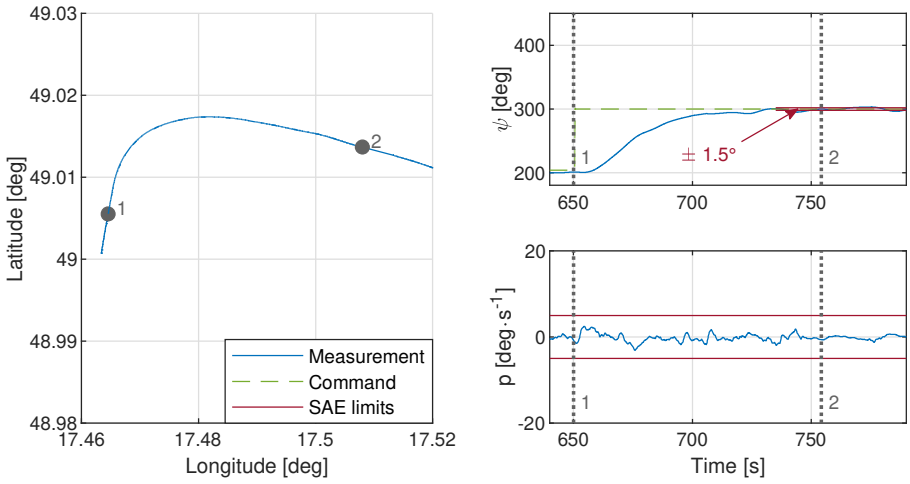

Figure 7.38: Heading select mode in level right turn.

Based on the evaluation of monitored criteria defined by reference [76], it can be concluded that the researched FCS fulfills conditions of paragraph 3.2.4.2.3.

7.4.1.7 *Altitude Select and Hold*

Figure 7.39 shows the aircraft trajectory controlled by the FCS during a flight test. The figure with aircraft trajectory is shown in combination with the time series of aircraft pressure altitude h and normal acceleration a_z. These graphs contain FCS evaluation limits, which were taken from paragraph 3.2.4.2.4 "Altitude Hold and Altitude Select" of reference [76]. A short review of the mentioned criteria is listed below:

- For the vertical speed below $\pm 2000\ \mathrm{ft} \cdot \mathrm{min}^{-1}$, engaging the autopilot shall lead to maintaining current pressure altitude or setting commanded altitude that would be maintained by the autopilot. Acceleration in z-axis shall not exceed ± 0.5 g.
- Minimal control accuracy for altitude below 30000 ft:
  - For roll angle 0°-1°, the altitude accuracy shall be within the range ± 30 ft.
  - For roll angle 1°-30°, the altitude accuracy shall be within the range ± 60 ft or 0.3%, consider the larger limit.
- After autopilot engage or after any vertical speed instability lower than or equal to $2000\ \mathrm{ft} \cdot \mathrm{min}^{-1}$, the specified instability shall be recovered until 30 s.
- Periodical oscillations shall have a period of at least 20 s.

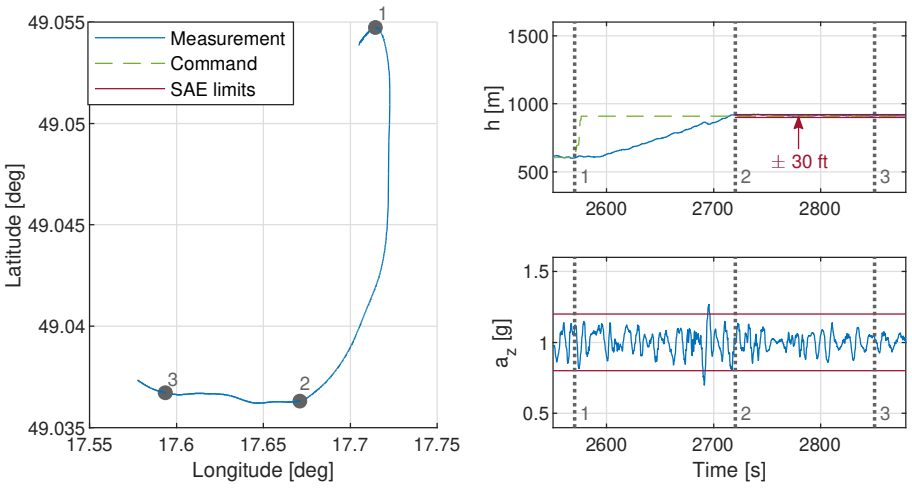

Figure 7.39: Altitude select mode.

Based on the evaluation of monitored criteria defined by reference [76], the researched FCS fulfills conditions of paragraph 3.2.4.2.4.

7.4.1.8 *Airspeed Hold*

Figure 7.40 shows an aircraft trajectory in steady level flight maintained by the FCS during flight experiments. The figure with flight trajectory is shown in combination with a graph of airspeed time history during automatic flight. It shows limits of flight quality criteria, which were taken from paragraph 3.2.4.2.6 Airspeed Hold in reference [76]. A short list of mentioned criteria is described below:

- The airspeed during FCS engagement is taken as a reference value.
- The airspeed shall be maintained within ±2% boundary of reference value or ±5 kts.
- Any periodical oscillation within the above mentioned limits shall have a minimum period of 20 s.

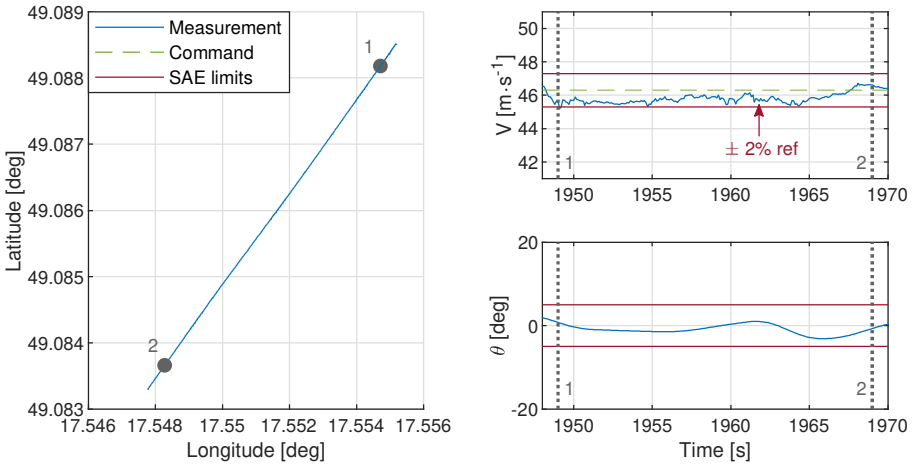

Figure 7.40: Indicated Airspeed hold mode in steady level flight.

Based on the above-described requirements defined by the reference [76] it is obvious that the designed FCS fulfills the conditions specified by paragraph 3.2.4.2.6. The airspeed remains within a ±2% boundary during the observed period, the pitch angle does not exceed ±5° limit specified in the previous subsections.

7.4.2 *Automatic Approach System Evaluation*

The functionality of the researched algorithm for the automatic flight, including autonomous approach for landing was proven feasible through a series of flight experiments performed on an experimental LSA equipped with a digital FCS introduced in Chapters 5 and 6. The flight experiments were performed at the LKKU airport at the end of the year 2018 [17].

Figure 7.41: Experimental aircraft approach to LKKU RWY 20 in an automatic mode.

The experiment was designed to consist of a flight along a predefined rectangular trajectory inspired by a regular flying circuit pattern. During the flight experiment, the test pilot approached the 1st WayPoint (WPT) of the trajectory illustrated in Figure D.1 in a steady level flight at altitude 1000 ft AGL and 60 kts Indicated Airspeed (IAS). The actual automatic approach mode was engaged by the pilot using a dedicated push-button on the control stick. Figure 7.41 shows the experimental aircraft's instrument panel, containing the digital autopilot's Primary Flight Display (PFD) and Multifunction Display (MFD) set to an automatic approach for landing mode during the landing maneuver.

The weather conditions including the wind speed and direction, air temperature, and QNH encountered during the presented experiment are listed in Table 7.11. Effects of wind, occasional atmospheric turbulence and low temperatures were successfully managed by the researched digital FCS, which steered the aircraft towards the runway.

Figure 7.42 shows the flight test trajectory conveniently defined by four WPTs and the position of the LKKU's runway in the WGS-84 coordinate system. The blue line indicates the aircraft's position while the red marker indicates the point when the autopilot has been engaged the autopilot is engaged. Grey circles mark WPT position of the flight test trajectory.

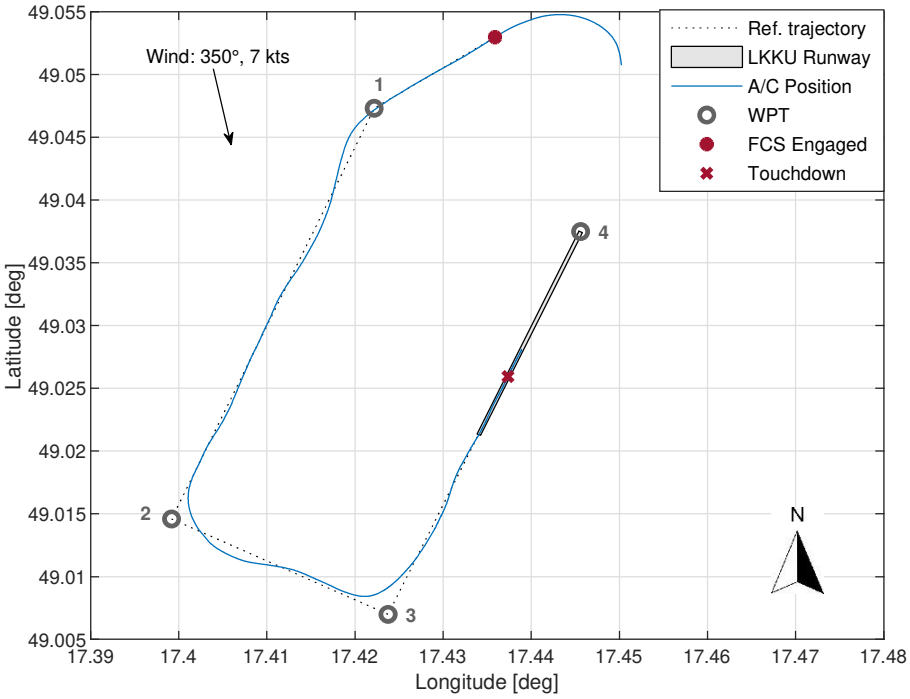

Figure 7.42: Trajectory flown during the automatic landing approach experiment.

Table 7.11: Weather conditions at LKKU at the time of the experiment.

Quantity	**Value**	**Unit**
Wind Speed	7	[kts]
Wind Direction	350	[°]
Temperature	-2	[°C]
QNH	1014	[hPa]

As illustrated in Figure 7.42, the FCS guides the experimental aircraft directly towards the 1st WPT and than follows the predefined flying pattern. Minor oscillations can be observed after passing 1st and 2nd WPT. These can be attributed to the wind conditions, which are represented by an arrow in Figure 7.42.

Figure 7.43 shows the principal quantities controlled by the FCS, namely the airspeed V, altitude h and aircraft heading ψ. Altitude and airspeed command values are defined by fixed step functions related to the current WPT towards which the aircraft is flying. The vertical speed was limited to -2 $m{\cdot}s^{-1}$ during most of the descent and -1 $m{\cdot}s^{-1}$ right before touchdown. This limit is responsible for the ramp shape of the altitude command signal. The heading command is computed continuously, in order to navigate the aircraft along the predefined trajectory considering the actual aircraft position. The algorithm for computing the heading command is introduced in Appendix C. It is noticeable to mention that minor differences in

maintaining the target airspeed V occurred during the descent. However, the FCS was able to guide the aircraft to the runway.

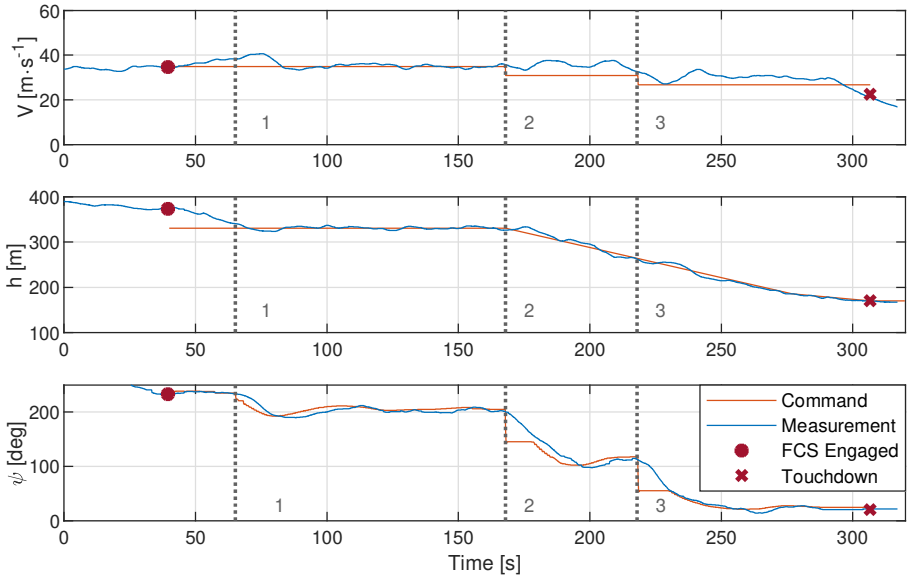

Figure 7.43: Measured flight quantities during automatic landing approach.

Figures 7.44 and 7.45 depict the rest of the aircraft states, namely the values which describe the lateral-directional motion i.e. the lateral acceleration a_y, roll rate p and roll angle ϕ. The roll angle ϕ rotation to -20°, introducing a turn in the trajectory is observable after passing each WPT. The lateral acceleration a_y is maintained close to 0 g, as the FCS is performing a coordinated turn and compensates the lateral acceleration through the use of the rudder. The roll rate p is maintained within $\pm 10°\cdot s^{-1}$ interval. The longitudinal motion is described by normal acceleration a_z, pitch rate q and pitch angle θ. The decrease in pitch angle θ is observable after passing 2nd WPT as the FCS initiates a descent. Since the digital FCS was set conservatively, the accelerations almost never exceeded the ± 0.2 g acceleration range [95]. Both Figures 7.44 and 7.45 illustrate the design limits of the FCS inspired by the reference [76].

The digital 4-axis FCS controlled the elevator, rudder, ailerons and throttle lever. Figure 7.46 shows their deflections during an automatic flight and approach for landing. It is observable that the FCS is set very conservatively since changes in control surface deflections are rather slow and do not exceed operational limits illustrated by respective red boundaries.

Since the complete flight experiment was performed in clean aircraft configuration, it was not allowed to use flaps as aerodynamic breaks. This explains the steady-state error in airspeed during the descent maneuver, when thrust control reached its lowest limit. Other aircraft states remained within the design limits introduced in subsections 7.4.1.1 - 7.4.1.8.

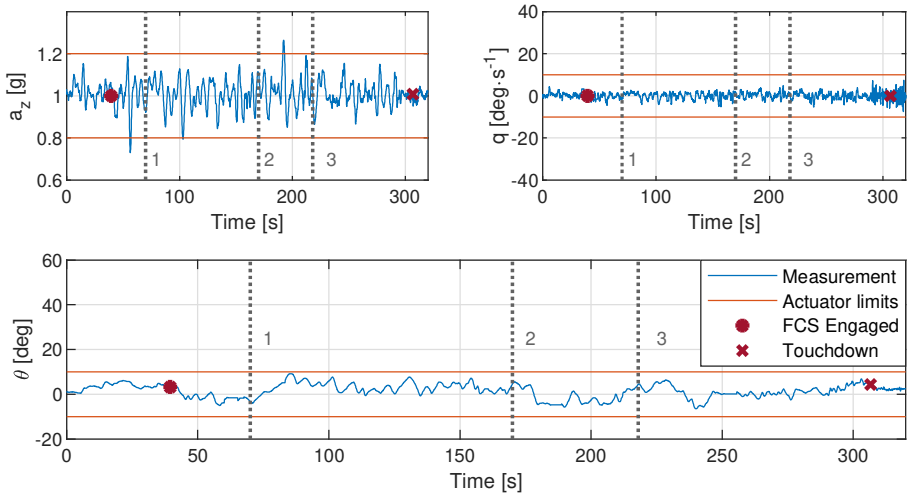

Figure 7.44: Longitudinal variables.

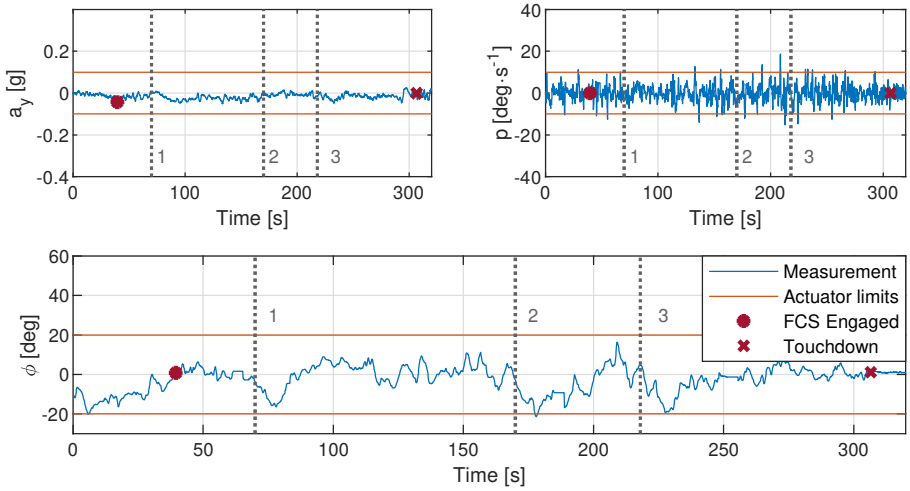

Figure 7.45: Lateral-directional variables.

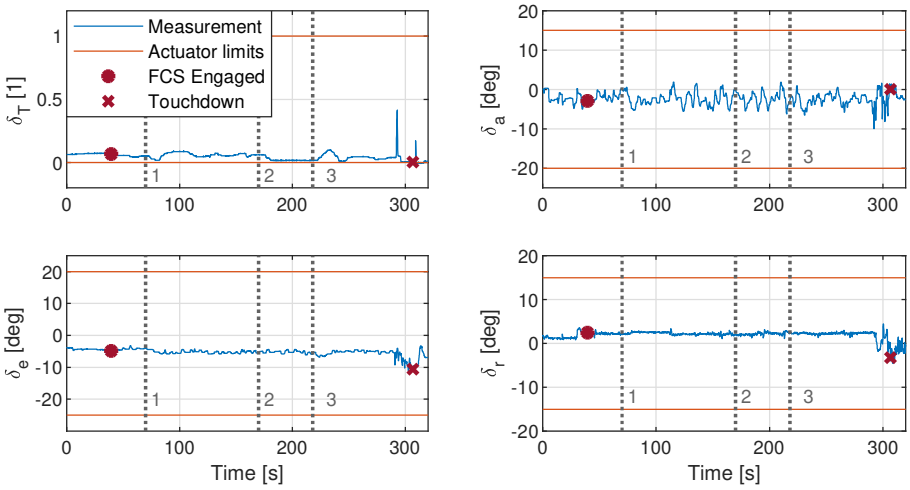

Figure 7.46: Control deflections.

7.4.2.1 *Automatic Landing Approach Performance Evaluation*

The performance evaluation criteria were inspired by the reference [82] focused on the development of the auto-land system for a general aviation class of aircraft. The document recommends that pitch angle before the touchdown shall be larger than 5° otherwise, the front gear could be damaged during the automatic landing. The vertical speed before the touchdown shall remain within the interval of $\langle 0.3; 2.0 \rangle$ $m \cdot s^{-1}$. Greater values could be unpleasant for the pilot. The automatic landing approach system shall prevent the aircraft from stall, thus the airspeed V during touchdown shall remain above the stall speed, which is declared by the manufacturer at 42 kts, which is 21.6 $m \cdot s^{-1}$. The designed automatic approach system for fixed-wing experimental LSA complied with the above-mentioned requirements, as can be seen in Table 7.12, which summarizes the performance metrics results, consisting of different aircraft variables measured during the final phase of an automatic landing approach. These variables are the pitch attitude θ, vertical speed VS, airspeed V and normal acceleration a_z [95].

Table 7.12: Measured flight quantities during the automatic approach final phase.

Quantity	**Value**	**Unit**
Pitch angle	5.4	[°]
Vertical speed	-0.33	[$m \cdot s^{-1}$]
Airspeed	25	[$m \cdot s^{-1}$]
Normal acceleration	1.01	[g]

8

CONCLUSION

This chapter summarizes and discusses the research on modern FCS introduced in this thesis in light of the main goals and contributions specified in Chapter 1. This chapter is logically divided into three sections. The first section serves as the thesis summary and contains a concluding remark on most of its chapters. The second section lists main contributions and the last section proposes the direction of future research focused on the modern FCS technologies.

8.1 SUMMARY

This thesis demonstrates a modern FCS design, implementation, and stability and performance evaluation using computer simulations and flight tests tailored for a fixed-wing LSA. Chapter 2 was dedicated to the definition of the aircraft's 6DoF nonlinear model. A precise model and selected structure of the controlled plant, in our case representing an experimental LSA, is essential in designing a well performing FCS. The nonlinear aircraft dynamic model was developed from Newton's laws, in a form of Equations of Motion. The nonlinear system was then linearized to express the aircraft dynamics in a form of a linear state-space model suitable for the FCS research and development. Chapter 3 focused on the description of respective subsystems that represent a suitable simulation environment and which enabled the first tests of researched control strategies. Models describing the aircraft propulsion, aerodynamic properties, actuator and sensor dynamics, or atmospheric model, represent an integral part of the simulation framework. Leveraging the aircraft's aerodynamic model fidelity was achieved through utilization of the parameter estimation methods described in Chapter 4. The aerodynamic force and moment coefficients were estimated using the Equation Error method over a range of measured flight parameters. This chapter also presents the state estimation technique, namely the Kalman filter, employed in the FCS design. Chapter 5 introduced the necessary theory on three control system methods, which enabled their proper understanding and follow on research. This chapter started with a robust LQR controller and its adjustment to the command tracking task. Then a more complex LQG controller containing the Kalman filter was researched. The chapter was concluded with the MRAC technique that augments previously defined control system to overcome model uncertainties. Chapter 6 described the implementation of the

designed FCS using MATLAB® / Simulink® environment. This chapter introduced the implementation of the control system methods from Chapter 5 and the low-level code generation for the target hardware platform. Chapter 7 presented the designed FCS's stability and performance evaluations results. The FCS evaluation was divided into three main parts. The first part was focused on the FCS stability and robustness evaluation in the frequency domain. Its conclusion confirm the LQR being a more robust FCS design method than the LQG. The second part was dedicated to the investigation of the time-domain performance of implemented designs in computer simulations. The LQG controller showed significant noise-attenuation capabilities due to the Kalman filter's presence in the design. The MRAC augmentation, on the other hand, presented its ability to overcome model uncertainties that influenced the aircraft dynamics. The chapter was concluded by presenting the flight experiment results that proved the suitability of the researched FCS.

8.2 THESIS CONTRIBUTIONS

The following list summarizes the main contributions of this thesis.

- High fidelity 6DoF nonlinear aircraft simulation model of an experimental LSA platform refined with estimated aerodynamic coefficients originating from parameter estimation process on measured flight data.
- The FCS design based on the robust LQR control strategy, with its implementation tailored specifically for a LSA.
- The MRAC based adaptive augmentation of a linear FCS evaluated in computer simulations.
- Three-phase evaluation of the designed FCS, including robustness and stability evaluation, time-domain performance evaluation in the simulation environment and a flight experiment evaluation.

8.3 FUTURE DEVELOPMENT

The future development should account for a higher level of aircraft autonomy. Features as automatic take-off and landing should provide a useful extension to the proposed FCS. The next step could account for a transformation from the experimental LSA platform to RPAS by designing the ground control station with Command and Control (C2) link to the aircraft, taking the pilot out of the flight deck and controlling the aircraft remotely.

Part I

APPENDIX

A

COORDINATE FRAMES IN FLIGHT CONTROLS

For the proper definition of physical quantities, the simulation model uses five different coordinate frames: World Geodetic System 1984 (WGS-84), North-East-Down frame (NED), Body-Fixed frame, Aerodynamic frame and Stability frame. This section also includes the most important transformation relationships between frames expressed by transformation matrices.

A.1 WGS 84 - COORDINATES

The WGS-84 coordinate system defines the aircraft's position using three components (two angles and the height above the ellipsoid), geodetic longitude, geodetic latitude and geodetic height as shown in Figure A.1 [69].

- Geodetic Longitude: λ - Angle measured between zero meridian plane and the meridian plane of point P.
- Geodetic Latitude: μ - Angle measured between Equatorial plane and surface normal of point P in the meridian plane of point P.

A.2 NED FRAME

The main purpose of the NED frame is to specify the aircraft's attitude/orientation. It has the origin in the reference point of the aircraft as can be seen in Figure A.1. The frame moves with this reference point and rotates to keep the defined NED alignment [12, 73, 74]. The NED frame index is o and respective axis are:

- x_0 axis is pointing to the geographic North, and it is parallel with the local geoid surface,
- y_0 axis is pointing to the geographic East, and it is also parallel to the local geoid surface,
- z_0 axis is pointing downwards, and it is perpendicular to the local geoid surface.

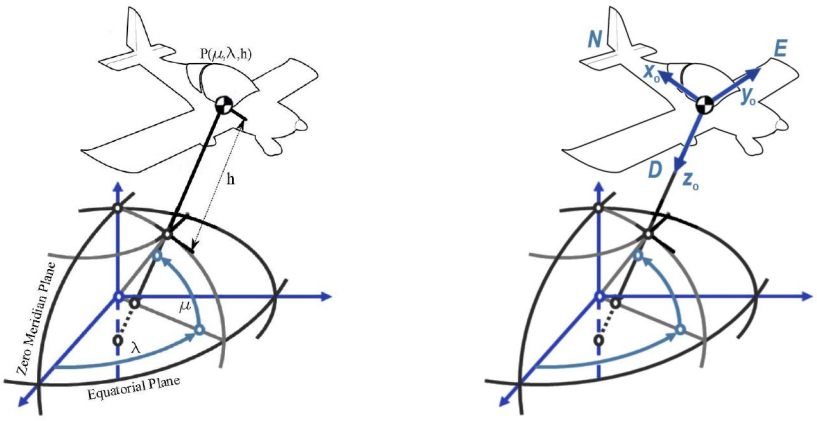

(a) WGS-84 (b) NED

Figure A.1: Position describing frames.

A.3 BODY-FIXED FRAME

This frame is commonly used to define all forces and moments acting on the aircraft and express other quantities (acceleration, velocities, attitude, etc.). The origin of the Body-Fixed frame is at the Center of Gravity and the frame moves with the origin [29, 45, 73]. The index of the Body-Fixed frame is B and respective axis are:

- x_B axis is pointing the aircraft nose in the plane of symmetry,
- y_B axis is pointing to the right wing of the aircraft,
- z_B axis is perpendicular to plane defined by x_B and y_B axes and pointing downwards.

A.4 AERODYNAMIC FRAME

The aerodynamic frame defines the motion and attitude of the aircraft according to aerodynamic flow. It is essential for defining the aerodynamic forces (lift, drag, lateral force). Its origin is in the aircraft's reference point, and the frame moves with this reference point [29, 45, 73]. The index of the Aerodynamic frame is A.

- x_A axis is aligned to aerodynamic velocity $\vec{V}_A$,
- y_A axis is pointing to the right, and it is perpendicular to the plane defined by x_A and z_A axes,
- z_A axis is pointing downwards in the aircraft's plane of symmetry, and it is perpendicular to the plane defined by x_A and y_A axes.

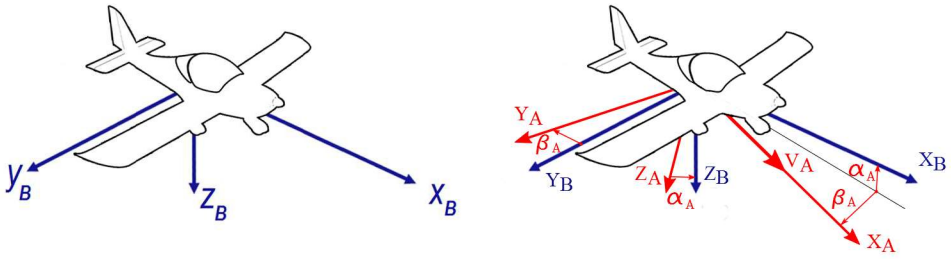

(a) Body-Fixed (b) Aerodynamic

Figure A.2: Attitude describing frames.

A.5 STABILITY FRAME

The stability frame, similar to the aerodynamic frame, defines the aircraft's attitude towards the oncoming airflow but the lateral direction of the airflow described by the angle of sideslip β_A is neglected. This frame is usually employed for expressing the aerodynamic force and moment coefficients, and it is used as a linearization frame [7, 45, 73]. The index of this frame is S and respective axis are>

- x_S axis is the aerodynamic velocity projection to the xz axis of the aircraft's Body-Fixed frame,
- y_S points to the right, and it is perpendicular to xz axis of the aircraft's Body-Fixed frame,
- z_S axis is pointing downwards in the aircraft's plane of symmetry, and it is perpendicular to the plane defined by x_S and y_S axes.

A.6 FRAME TRANSFORMATION

Occasionally, it is necessary to convert physical quantities from one frame to another, e.g., converting aerodynamic forces to the Body-Fixed frame for their utilization in Equations of Motion or converting the aircraft's velocities in the Body-Fixed frame to the NED frame to express the change of the aircraft's position. In this case, so-called Transformation matrices are used. The following matrices define the transformation between the NED frame and Body-Fixed frame (M_{B0}), between the aerodynamic frame and Body-Fixed frame (M_{BA}), between stability frame and Body-Fixed frame M_{BS} and between aerodynamic frame and stability frame M_{SA}. In equations A.1, A.2, A.3 and A.4 is used special notation (*c* stands for cosinus and *s* stands for sinus functions) [87, 73].

$$M_{BO} = \begin{bmatrix} c(\psi)c(\theta) & s(\psi)c(\theta) & -s(\theta) \\ c(\psi)s(\theta)s(\phi) - s(\psi)c(\phi) & s(\psi)s(\theta)s(\phi) + c(\psi)c(\phi) & c(\theta)s(\phi) \\ c(\psi)s(\theta) + s(\psi)s(\phi) & s(\psi)s(\theta)c(\phi) - c(\psi)s(\phi) & c(\theta)c(\phi) \end{bmatrix} \tag{A.1}$$

$$M_{BA} = \begin{bmatrix} c(\alpha_A)c(\beta_A) & -c(\alpha_A)s(\beta_A) & -s(\alpha_A) \\ s(\beta_A) & c(\beta_A) & 0 \\ s(\alpha_A)c(\beta_A) & -s(\alpha_A)s(\beta_A) & c(\alpha_A) \end{bmatrix} \tag{A.2}$$

$$M_{BS} = \begin{bmatrix} c(\alpha_A) & 0 & -s(\alpha_A) \\ 0 & 1 & 0 \\ s(\alpha_A) & 0 & c(\alpha_A) \end{bmatrix} \tag{A.3}$$

$$M_{SA} = \begin{bmatrix} c(-\beta_A) & 0 & -s(-\beta_A) \\ 0 & 1 & 0 \\ s(-\beta_A) & 0 & c(-\beta_A) \end{bmatrix} \tag{A.4}$$

B

AIRCRAFT GEOMETRY

The basic geometric characteristics of the experimental aircraft used in the dynamic model are shown in Table B.1.

Table B.1: Geometric characteristics. Source [16]

Description	**Symbol**	**Value**	**Units**
Wing span	b_w	8.646	[m]
Mean aerodynamic chord	$\bar{c}$	1.25	[m]
Wing area	S	10.6	[m^2]
CG position in x-axis	x_{CG}	1.9086	[m]
Aerodynamic center position in x-axis	x_{AC}	2.1443	[m]

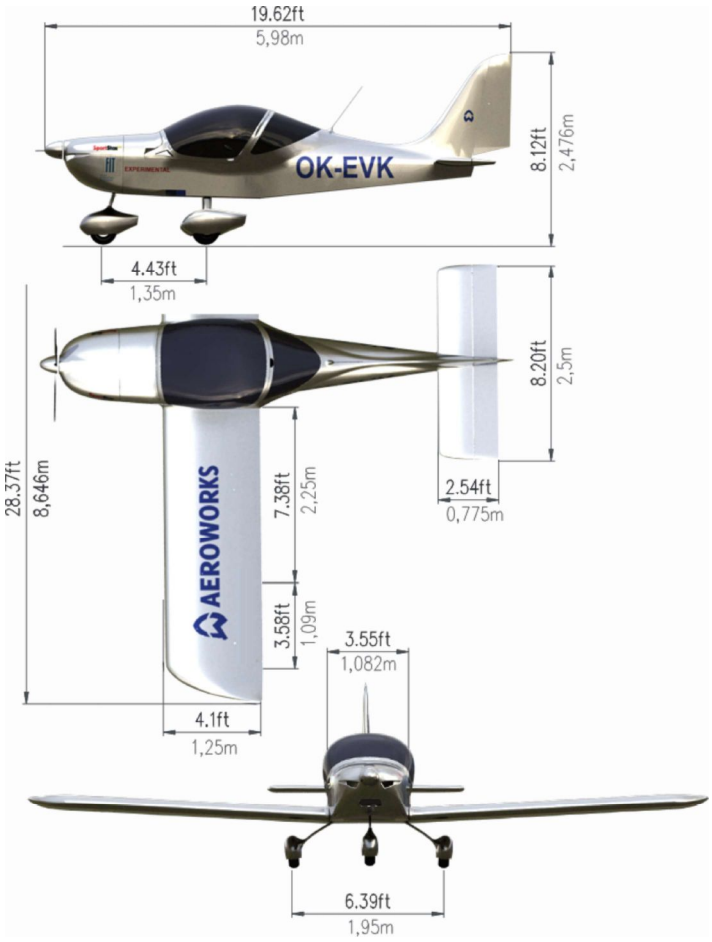

Figure B.1: Aircraft geometry. Source [16]

C

GUIDANCE ALGORITHM

An aircraft flight trajectory definition for FCS is usually composed of a series of WPTs with additional associated flight quantities. Each WPT is therefore represented by its position in the WGS-84 coordinate system, namely the geodetic latitude and longitude, target altitude and airspeed, which are to be maintained during the automatic flight.

$$WPT = [LAT_{wpt}, LON_{wpt}, ALT_{wpt}, IAS_{wpt}] \tag{C.1}$$

The navigation computer's task is to compute the heading command from the actual aircraft position to the respective WPT defining individual flight trajectory legs. The goal is to minimize the Cross-Track, which is the shortest distance between the own aircraft and the trajectory leg between two WPTs and its geometrical definition is shown in Figure C.1. Furthermore Figure C.1 shows the basic navigation geometry with the distances between WPTs and the aircraft, and respective navigation angles (α_{nav}, β_{nav}) important for the computation of the target heading in the NED coordinate system.

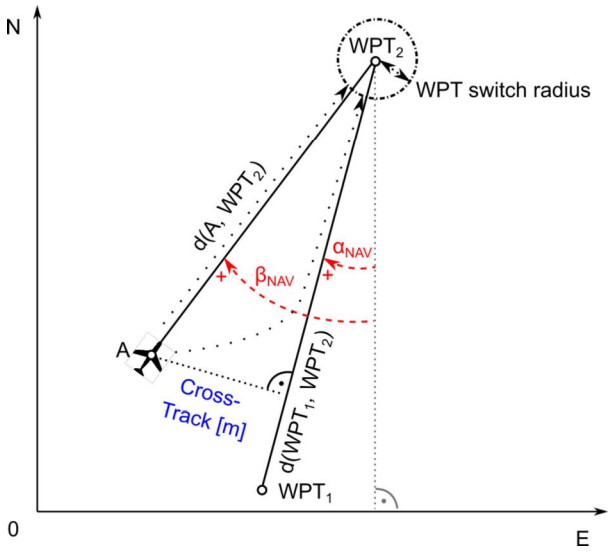

Figure C.1: Aerial navigation scheme.

The target heading computation is described by a block diagram shown in Figure C.2. At first, WPTs and aircraft positions in WGS-84 coordinates are trans-

formed to the Flat-Earth coordinates. The first step is to compute small changes of latitude and longitude defined by equations C.2 and C.3,

$$dLAT = LAT - LAT_0, \tag{C.2}$$

$$dLON = LON - LON_0, \tag{C.3}$$

where LAT_0 and LON_0 define the aircraft's initial position. The next step in converting the Latitude, Longitude and Altitude (LLA) set to NED coordinates is to compute the radiuses of curvature in the prime vertical R_N and in the meridian R_M using equations C.4 and C.5

$$R_N = \frac{R}{\sqrt{1-(2f-f^2)\sin(LAT_0)^2}}, \tag{C.4}$$

$$R_M = R_N \frac{1-(2f-f^2)}{1-(2f-f^2)\sin(LAT_0)^2}, \tag{C.5}$$

where f stands for the Earth flattening and parameter R represents the Earth's radius. The last step is to compute the position changes in NED coordinates using formulas expressed in equations C.6 and C.7 [27, 87].

$$dN = \frac{dLAT}{atan(\frac{1}{R_M})} \tag{C.6}$$

$$dE = \frac{dLON}{atan(\frac{1}{R_N \cos(LAT_0)})} \tag{C.7}$$

The navigation angles ($\alpha_{NAV}, \beta_{NAV}$) describe the heading between the 1st and 2nd WPT and between own aircraft and the 2nd WPT. Respective navigation angles are expressed by equations C.8 and C.9.

$$\alpha_{nav} = atan2(p_{E_{WPT_2}} - p_{E_{WPT_1}}, p_{N_{WPT_2}} - p_{N_{WPT_1}}) \tag{C.8}$$

$$\beta_{nav} = atan2(p_{E_{WPT_2}} - p_{E_A}, p_{N_{WPT_2}} - p_{N_A}) \tag{C.9}$$

The actual Cross-Track is to be computed with the utilization of both navigation angles.

$$CrossTrack = d(A, WPT_2)\sin(\beta_{nav} - \alpha_{nav}) \tag{C.10}$$

The Cross-Track is used as an input to the controller that minimizes the normal distance between the own aircraft and the planned trajectory. This is executed through a simple proportional controller. The last step before expressing target heading, to be acquired and than maintained by the FCS, is to determine if the aircraft flies directly towards the next WPT by choosing the shortest distance or if it follows the trajectory defined by the 1st and 2nd WPT.

The evaluation criterion is the difference between the navigation angles α_{NAV} and β_{NAV}, which is known as the angle of intercept. If the angle of intercept is

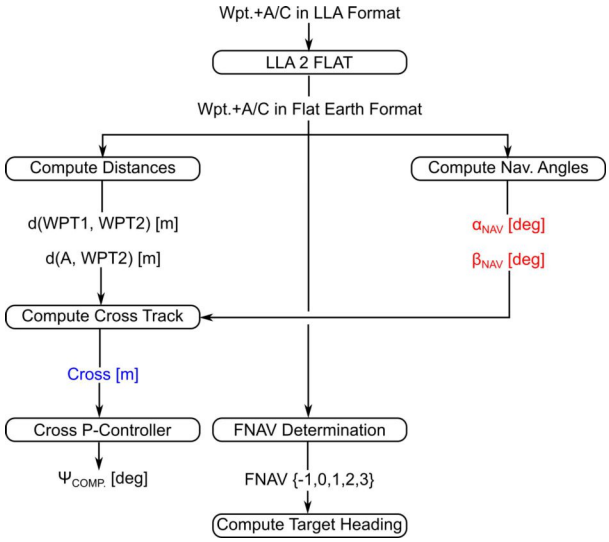

Figure C.2: Target heading computation diagram.

larger than the 45° threshold, the navigation computer selects the shortest distance to the next WPT. Thus the target heading ψ_T is set to β_{NAV} according to the equation C.12. Otherwise, the target heading ψ_T is set in a way to follow the flight plan leg between WPTs using equation C.11. The compensation angle ψ_{COMP}, defined by equation C.13, is proportional to the distance of CrossTrack shown in Figure C.1.

$$\psi_T = \alpha_{NAV} + \psi_{COMP} \tag{C.11}$$

$$\psi_T = \beta_{NAV} \tag{C.12}$$

$$\psi_{COMP} = K_{P_{cross}} \cdot \text{CrossTrack} \tag{C.13}$$

Selection of the following WPT is performed at the moment when the aircraft intercepts the upcoming flight plan defined WPT. Figure C.2 illustrates the target heading computation process.

D

AUTOMATIC LANDING APPROACH

The trajectory for an automatic approach experiment has been composed of WPTs set into a rectangular-shape pattern, as shown in Figure D.1. After engaging the automatic approach mode, the digital 4-axis FCS sets the target heading either to the 1st or directly to 2nd WPT according to the aircraft's actual position. The automatic approach procedure is divided into several phases (Initiation, Downwind, Base and Final Leg). Each phase is represented by a state of a final state machine implemented within the FCS's navigation computer [52, 95].

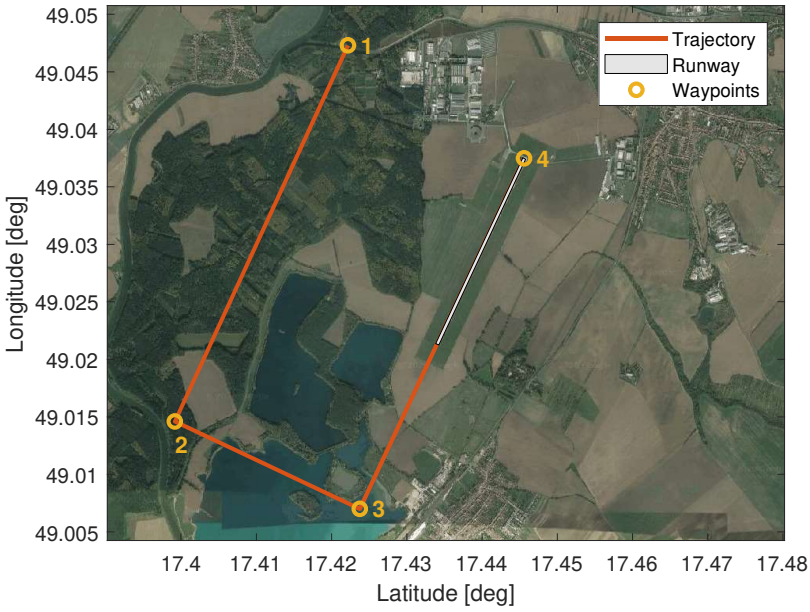

Figure D.1: Flight trajectory for automatic approach experiments.

The automatic approach mode is engaged in a steady level flight, trimmed to airspeed of 60 kts at the altitude of 1000 ft Above Ground Level (AGL).

Further phases can be divided into three sections, namely the downwind, base leg and landing approach. The FCS required to maintain steady level flight at 60 kts along the leg between the 1st WPT and the 2nd WPT during the downwind section. After passing the 2nd WPT, the FCS gets to the base leg and initiates a descent at a vertical speed limited to -2 $m \cdot s^{-1}$. The digital FCS works in its full configuration, which means it controls the airspeed, altitude and heading, while minimizing the aircraft's sideslip angle. The landing approach starts after passing the 3rd WPT of the trajectory as shown in Figure D.1. The aircraft heading is aligned with the

runway, and the autopilot maintains 60kts IAS, while the vertical speed maintains its limit of -2m·s^{-1}.

When approaching closely to the runway, the pilot disengaged the FCS, flared and landed the aircraft manually, to comply to the approved flight test protocol.

E

FCS ARCHITECTURE

This appendix introduces the digital FCS architecture and describes its components in detail. This chapter is based on research projects technical reports [15, 17, 18].

The digital FCS is composed of the PFD with an embedded Flight Control Computer (FCC) and other units built around this central element as shown in Figure E.1. FCS units include a Multifunction Display, Electro-Mechanical Actuator (EMA), an Automatic Trim System, Digital Navigation Platform (DNP) and Propulsion Monitoring Unit (PMU). The whole system is operated via touch controlled graphical user interface within the PFD and MFD, and via dedicated push buttons on the control stick.

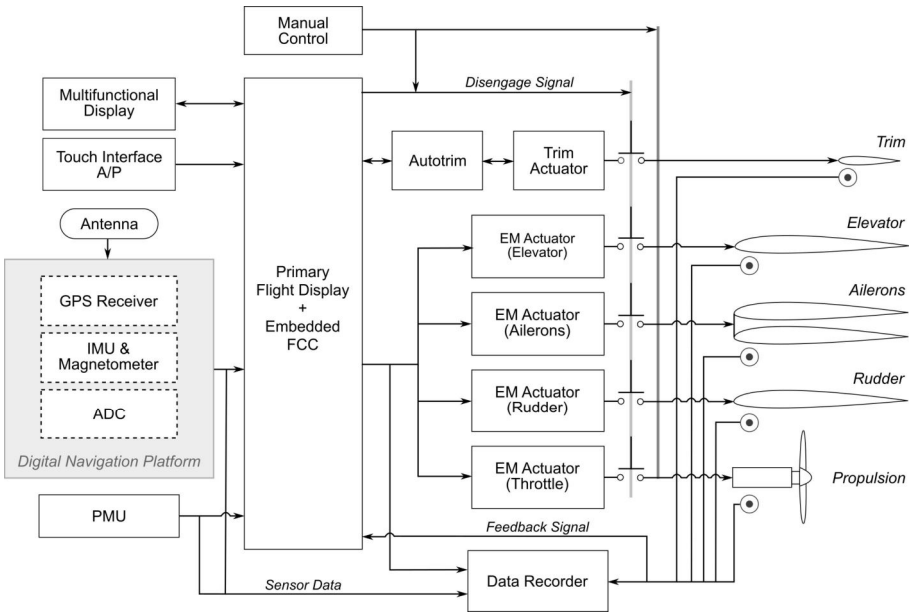

Figure E.1: Digital FCS architecture. Source [18]

The hardware solution contains components for a complete integration into an aircraft, as illustrated in Figure E.1. The software implementation allows the user to automatically control the aircraft through the digital FCS using various stabilization modes. The user can select between the stabilization of selected airspeed, altitude and heading. Another option is to fly automatically along a trajectory defined by a set of waypoints, which includes the automatic landing approach feature.

The block diagram, shown in Figure E.2, contains hardware units of the digital FCS for aircraft integration. The figure contains illustration of power supply, and

data channels. CANaerospace standard was used for data transfer between digital FCS components.

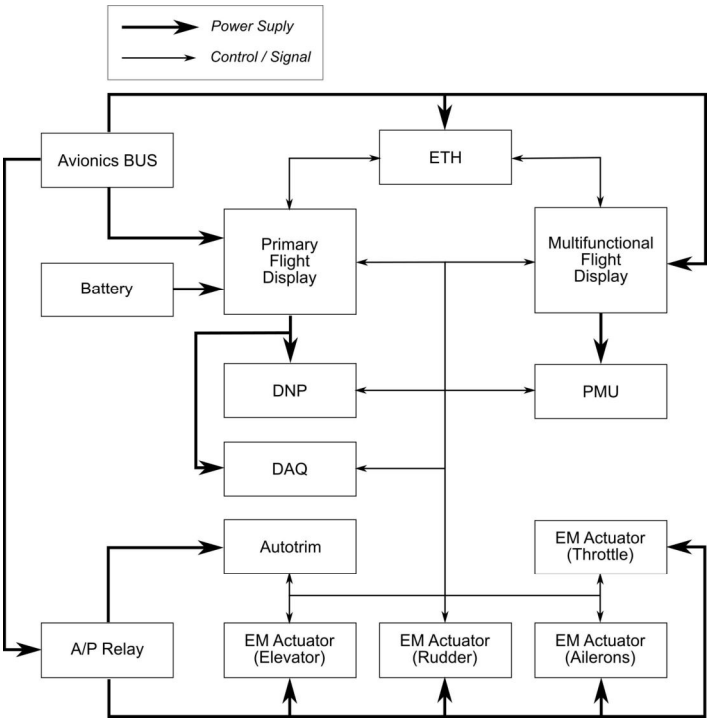

Figure E.2: Block diagram of digital FCS hardware solution. Source [15]

The main FCS hardware units are:

- Primary Flight Display
- Multifunction Flight Display
- Digital Navigation Platform including Air Data Computer, IMU with magnetometer and a GPS receiver
- Propulsion Monitoring Unit
- Autotrim system
- Set of digitally controlled EMA
- Data Acquisition Unit

The EMA are integrated in parallel to the aircraft mechanical control path within the digital FCS. The EMA receive control signals from FCC and enable to perform precise attitude as well as airspeed control. Actuators are disconnected after the FCS is disengaged and the aircraft control is returned to the manual regime. Table E.1 describes the position of the FCS components in the experimental aircraft.

Table E.1: Digital FCS positioning in the experimental aircraft.

FCS component	Position
PFD	Instrument panel
MFD	Instrument panel
EM actuator (elevator)	Under the pilot seat
EM actuator (ailerons)	Under the pilot seat
EM actuator (rudder)	Cockpit part of the fire barrier
EM actuator (throttle)	Cockpit part behind the instrument panel
DNP	Baggage compartment, close to aircraft CG
Autotrim system	Baggage compartment
PMU	Cockpit part of the fire wall
DAQ	Baggage compartment
Network router	Cockpit part behind the instrument panel

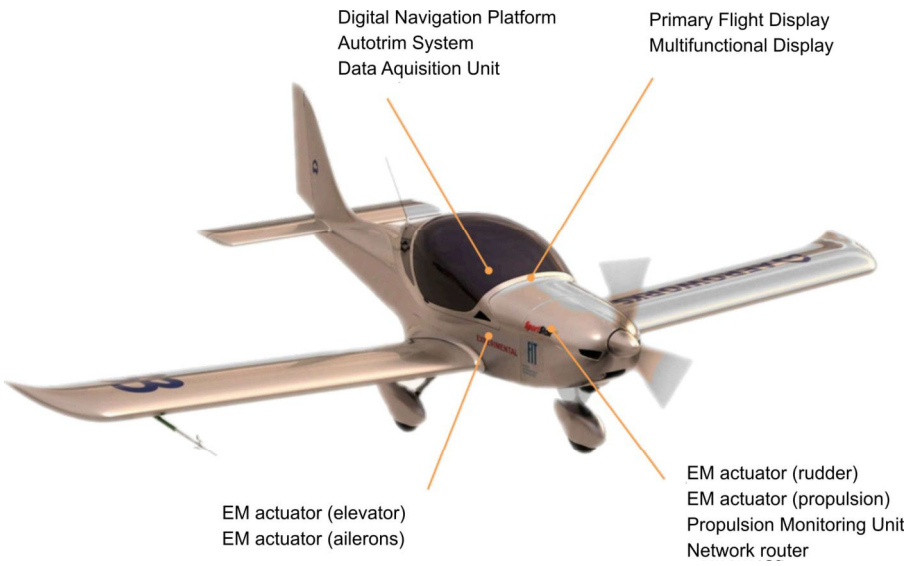

Figure E.3: Position of digital FCS components. Source [17]

E.1 SYSTEM FUNCTIONS DESCRIPTION

This section introduces the PFD and MFD system functions description. The logic of activating the digital FCS uses following steps. The pilot has to arm the whole system using the A/P switch on the instrument panel. Then the pilot enables the FCS by pushing the A/P button on the control stick. Initial flight quantities as airspeed, altitude or heading are automatically set when the FCS is enabled. The FCS is engaged when the pilot pushes the A/P button for the second time. There are few ways to disconnect the FCS either by pushing the A/P button on the control stick or HOME button on the instrument panel or turning off the A/P switch.

E.1.1 *PFD Interface Description*

The Primary Flight Display (PFD) is the main display positioned in front of the aircraft pilot. It combines various flight instruments into one display and presents the flight quantities as airspeed, altitude, heading, vertical speed and attitude angles along with synthetic 3D terrain in a clear layout. The PFD also contains a moving minimap in the lower-left corner and an engine state indication in a lower right corner.

Figure E.4: Primary Flight Display layout. Source [17]

E.1.2 *MFD Interface Description*

The major part of the Multifunction display (MFD) is occupied by the moving map, which indicates the terrain elevation through different colors. The second large part of the MFD is dedicated to the engine variables provided by the Propulsion Monitoring Unit (PMU). The pilot can also enter the Options mode that enables various system settings. Alternatively, the pilot can enter Flight Plan mode, enabling the definition of waypoints for an automatic flight along a predefined trajectory.

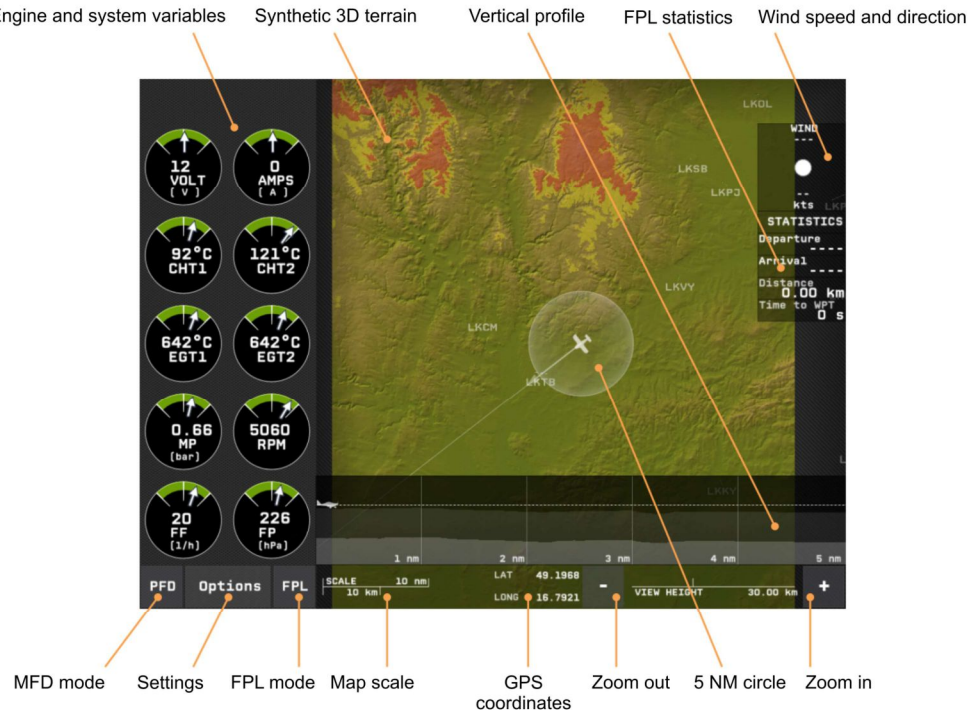

Figure E.5: Multifunction Display layout. Source [17]

E.1.3 *Flight Plan Interface Description*

This interface is a different mode of the MFD, which allows the pilot to set a flight plan defined by a series of waypoints. The definition of the trajectory starts with entering the departure airport, followed by entering the airport of arrival. The pilot can choose the departure and arrival airports from an airport database. Other waypoints can be added directly by a touch enabled command into the moving map.

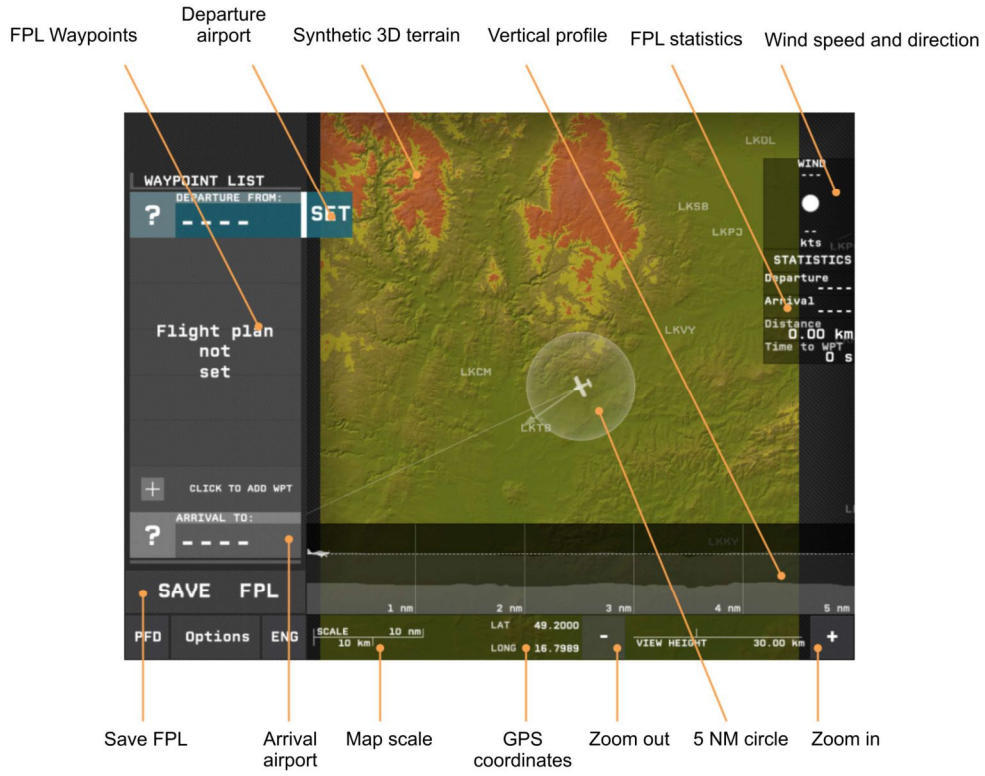

Figure E.6: Flight plan interface. Source [17]

E.1.4 *Adjustable A/P Flight Variables*

Setting of the FCS target variables and operational variables is performed via PFD and MFD touch interface. Table E.2 contains a list of all parameters that can be set via the display and Figure E.7 shows the layout of control elements at the PFD.

Table E.2: Adjustable flight variables.

Flight variable	**Increment**
Indicated airspeed [kts]	10
Altitude [ft]	100 or 1000
Track [°]	1 or 10
QNH [hPa]	1

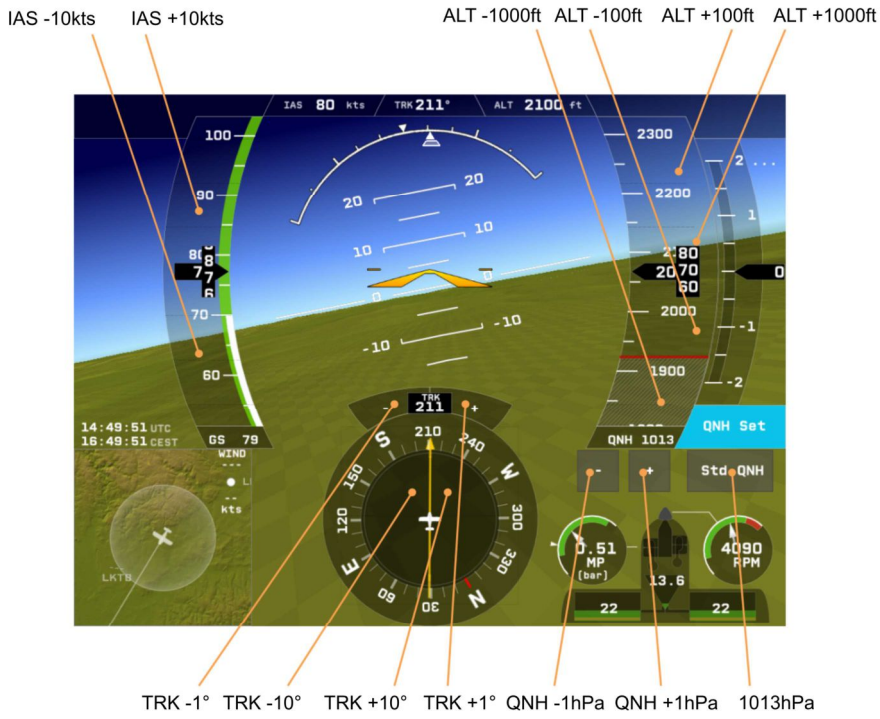

Figure E.7: PFD in A/P setting mode. Source [17]

E.2 SENSORS

The experimental aircraft was equipped with a set of sensors for measuring different types of data. Table E.3 contains a list of all measured variables together with respective measurement device, range and units.

Table E.3: List of measured variables. Source [17]

Flight variable	**Abbr.**	**Device**	**CAN ID**	**Range**
Indicated airspeed [m·s^{-1}]	IAS	DNP	315	<0;100>
Pressure altitude [m]	ALT	DNP	322	<0;3100>
Dynamic pressure [hPa]	P_{DYN}	DNP	325	<0;345>
Static pressure [hPa]	P_{STAT}	DNP	326	<0;2068>
Pitch angle [°]	Theta	DNP	311	<-90;90>
Roll angle [°]	Phi	DNP	312	<-90;90>
Magnetic heading [°]	HDG	DNP	321	<0;360>
Roll rate [°·s^{-1}]	p	DNP	304	<-300;300>
Pitch rate [°·s^{-1}]	q	DNP	303	<-300;300>
Yaw rate [°·s^{-1}]	r	DNP	305	<-300;300>
Axial acceleration [m·s^{-2}]	a_x	DNP	300	<-49;49>
Side acceleration [m·s^{-2}]	a_y	DNP	301	<-49;49>
Normal acceleration [m·s^{-2}]	a_z	DNP	302	<-49;49>
GPS Track [°]	TRK	PFD	1040	<0;360>
Geodetic longitude [°]	LON	DNP	1037	<-180;180>
Geodetic latitude [°]	LAT	DNP	1036	<-90;90>
Height above ellipsoid [m]	HGT	DNP	1038	<0;10000>
GPS velocity N [m·s^{-1}]	V_n	DNP	1131	<0;515>
GPS velocity E [m·s^{-1}]	V_e	DNP	1130	<0;515>
GPS velocity U [m·s^{-1}]	V_u	DNP	1132	<0;515>
Elevator deflection [°]	δ_e	EMA	308	<-25;20>
Rudder deflection [°]	δ_r	EMA	306	<-30;30>
Aileron deflection [°]	δ_a	EMA	310	<-15;20>
Throttle lever deflection [1]	δ_T	EMA	414	<0;1>

Flight variable	Abbr.	Device	CAN ID	Range
Angle of attack [°]	AoA	DAQ	329	<-30;30>
Angle of sideslip [°]	AoS	DAQ	347	<-30;30>
Manifold pressure [hPa]	MP	PMU	528	<0;2000>
Battery voltage [V]	VOLTS	PMU	920	<0;24>
Current [A]	AMPS	PMU	930	<-120;120>
Cylinder head temperature [°C]	CHT	PMU	540	<0;160>
Exhaust gas temperature [°C]	EGT	PMU	628,630	<0;925>
Oil temperature [°C]	OT	PMU	N/A	<0;160>
Oil pressure [hPa]	OP	PMU	N/A	<0;22000>
Fuel pressure [hPa]	FP	PMU	684	<0;2200>
Fuel flow [$l \cdot h^{-1}$]	FF	PMU	524	<3;225>
Engine revolutions [1]	RPM	PMU	315	<0;100>

E.3 ACTUATION SYSTEM

The actuation system is composed of 4 digitally controlled electromechanical actuators shown in Figure E.8, which are mechanically linked to aircraft control surfaces. An electromechanical actuator's mechanical assembly includes a stepper motor with a custom-built gearbox with an optional electromagnetic clutch. The control board electronics consists of Commercial of the Shelf (COTS) microcontroller, a stepper motor driver, a galvanically isolated CAN driver and a switch. This configuration is supported by an external high precision rotary potentiometer used as a source of angular position information. In order to utilize the potential of the digital control, the following main operational functions have been implemented on the electromechanical actuator's microcontroller [19]:

- position measurement of an electromechanically actuated control surface,
- commanding of the stepper motor through the stepper motor driver,
- commanding of the electromechanical clutch (optional),
- monitoring of the state outputs at the drivers integrated circuit.

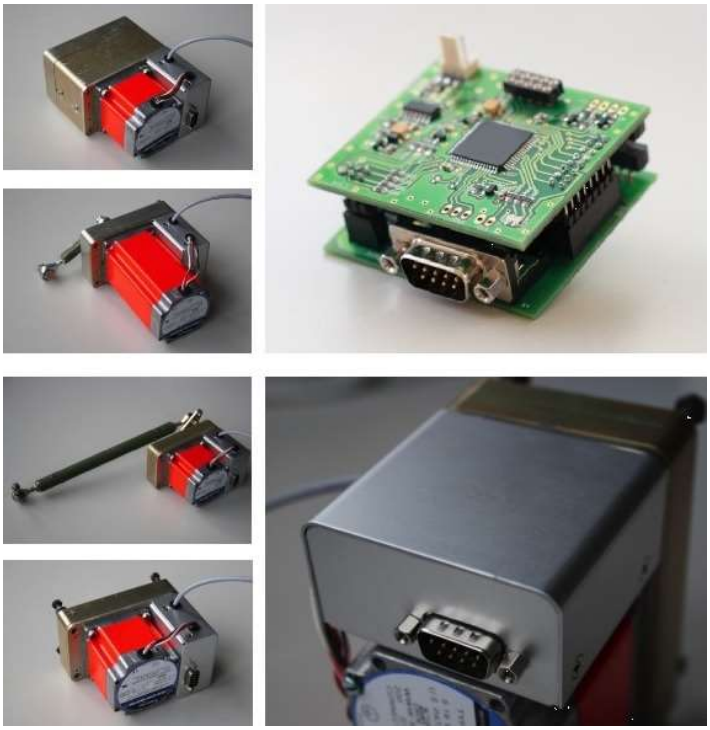

Figure E.8: Actuation system of a 4-axis FCS. Source [19].

Figure E.9: Experimental LSA with control surface operated by EMAs.

BIBLIOGRAPHY

[1] Sanjay Acharya. *Honeywell C-1 Autopilot Control Panel*. URL: https://commons.wikimedia.org/wiki/File:Honeywell%5C_C-1%5C_Autopilot%5C_Control%5C_Panel.jpg (visited on 05/04/2020).

[2] Smithsonian Air and Space Museum. *Pioneer RQ-2A UAV*. URL: https://airandspace.si.edu/collection-objects/pioneer-rq-2a-uav/nasm_A20000794000 (visited on 08/31/2020).

[3] Airwolfhound. *B17 - Chino Airshow 2014*. URL: https://cs.wikipedia.org/wiki/Boeing_B-17_Flying_Fortress#/media/Soubor:B17_-_Chino_Airshow_2014_(framed).jpg (visited on 08/31/2020).

[4] Scott Alban. *The Curtiss Pusher Model D Biplane*. URL: https://cz.pinterest.com/pin/366199013434470701/?nic_v2=1a6YGBzbU (visited on 08/31/2020).

[5] B.D.O. Anderson and J.B. Moore. *Optimal Filtering*. Dover Books on Electrical Engineering. Dover Publications, 2012. ISBN: 9780486136899.

[6] A. M. Annaswamy and Jo-Ey Wong. "Adaptive control in the presence of saturation non-linearity." In: *International Journal of Adaptive Control and Signal Processing* 11.1 (1997), pp. 3–19. DOI: 10.1002/(SICI)1099-1115(199702)11:1<3::AID-ACS391>3.0.CO;2-T.

[7] ANSI/AIAA. *Recommended Practice for Atmospheric and Space Flight Vehicle Coordinate Systems*. Recommendation Practice. Version R-004-1992. Washington, DC, 1992.

[8] C.E. Billings. *Human-Centered Aviation Automation: Principles and Guidelines*. 1996.

[9] H. Blomberg and R. Ylinen. *Algebraic theory for multivariable linear systems, Volume 166 (Mathematics in Science and Engineering)*. Academic Press, 1983. ISBN: 0121071502.

[10] J.L. Boiffier. *The Dynamics of Flight, The Equations*. The Dynamics of Flight. Wiley, 1998. ISBN: 9780471942375.

[11] S.P. Boyd and C.H. Barratt. *Linear controller design: limits of performance*. Prentice Hall Information and System Sciences Series. Prentice Hall PTR, 1991. ISBN: 9780135386873.

[12] A. Chatfield. *Fundamentals of High Accuracy Inertial Navigation (Progress in Astronautics and Aeronautics)*. American Institute of Aeronautics and Astronautics, 1997. ISBN: 1-56347-243-0.

[13] Ben M. Chen, Zongli Lin, and Yacov Shamash. *Linear Systems Theory: A Structural Decomposition Approach (Control Engineering)*. Birkhäuser, 2004. ISBN: 0817637796.

[14] P. Chudy, J. Vlk, and P. Dittrich. "Prototyping framework for digital flight control systems." In: *2013 IEEE/AIAA 32nd Digital Avionics Systems Conference (DASC)*. 2013, 7A3-1-7A3–12.

[15] Peter Chudý and Petr Dittrich. *Letové ověření. Letové ověření systému „chytrého autopilota"*. Tech. rep. Version AWEXP 1.2018. Brno, Czech Republic, 2013.

[16] Peter Chudý, Petr Dittrich, and Jan Vlk. *Dynamický model letounu. Dynamický model letounu kategorie ULL/LSA*. Tech. rep. Version AWDM 2.2011. Brno, Czech Republic, 2011.

[17] Peter Chudý, Milan Prustoměrský, and Jan Vlk. *Autonomous Light Aircraft Demonstrator Initiative "ALADIN". Popis ověření experimentálního digitálního systému řízení letu*. Tech. rep. Version AWALA 1.2018. Brno, Czech Republic, 2013.

[18] Peter Chudý and Jan Vlk. *Systém řízení letu pro „Chytrý autopilot". Souhrnný popis návrhu implementace řízení pro „Chytrého autopilota"*. Tech. rep. Version AWFCS 1.2013. Brno, Czech Republic, 2013.

[19] Peter Chudy et al. "HW in-the-loop simulation of light aircraft's autopilot." In: Aug. 2013. DOI: 10.2514/6.2013-4829.

[20] C.K. Chui and G. Chen. *Kalman Filtering: With Real-Time Applications*. Springer series in information sciences. Springer, 2009. ISBN: 9783540878483.

[21] Monroe Conner. *NASA Armstrong Fact Sheet: Global Hawk High-Altitude Long-Endurance Science Aircraft*. URL: https://www.nasa.gov/centers/armstrong/news/FactSheets/FS-098-DFRC.html (visited on 08/31/2020).

[22] Wikipedia contributors. *Fly-by-wire - Wikipedia, The Free Encyclopedia*. 2020. URL: https://en.wikipedia.org/w/index.php?title=Fly-by-wire&oldid=944018500 (visited on 05/03/2020).

[23] U.S. Department of Defense. *Flying Qualities of Piloted Aircraft, Department of Defense Handbook. MIL-HDBK-1797*. Tech. rep. Washington, DC, 1997.

[24] J. Doyle. "Guaranteed margins for LQG regulators." In: *IEEE Transactions on Automatic Control* 23.4 (1978), pp. 756–757.

[25] J. Doyle and G. Stein. "Multivariable feedback design: Concepts for a classical/modern synthesis." In: *IEEE Transactions on Automatic Control* 26.1 (1981), pp. 4–16.

[26] Laurent ERRERA. *Airbus A320-100 Air France*. URL: https://en.wikipedia.org/wiki/Airbus_A320_family#/media/File:Airbus_A320-100_Air_France_(AFR)_F-GFKQ_-_MSN_002_(10655931213).jpg (visited on 08/31/2020).

[27] Bernard Etkin and Lloyd Duff Reid. *Dynamics of Flight: Stability and Control*. Wiley, 1995. ISBN: 0-471-03418-5.

[28] Pieter Eykhoff. *System identification : parameter and state estimation*. English. Wiley-Interscience, 1974. ISBN: 0-471-24980-7.

[29] Wouter Falkena. "Investigation of Practical Flight Control Systems for Small Aircraft." PhD thesis. Delft, Netherlands: Delft University of Technology, Faculty Aerospace Engineering, 2012. ISBN: 978-94-6203-258-3.

[30] Florian Fisch. "Development of a Framework for the Solution of High-Fidelity Trajectory Optimization Problems and Bilevel Optimal Control Problems." PhD thesis. Munich, Germany: Technical University of Munich, 2011.

[31] *Flying Magazine*. URL: https://books.google.cz/books?id=UaLnwFjU0AoC&lpg=PA18&dq=F-5%20automatic%20pilot%20lear&hl=cs&pg=PA1#v=onepage&q=F-5%20automatic%20pilot%20lear&f=false (visited on 05/03/2020).

[32] G.F. Franklin, J.D. Powell, and A. Emami-Naeini. *Feedback control of dynamic systems*. Addison-Wesley series in electrical and computer engineering: Control engineering. Addison-Wesley, 1994.

[33] Graham C. Goodwin and Robert L. Payne. *Dynamic system identification : experiment design and data analysis / Graham C. Goodwin and Robert L. Payne*. Academic Press New York, 1977. ISBN: 0122897501.

[34] Robert Goyer. *LSA safety picture emerging*. URL: https://www.flyingmag.com/pilot-reports/lsa/sport/lsa-safety-picture-emerging/ (visited on 07/19/2020).

[35] Robert A. Granger. *Fluid Mechanics (Dover Books on Physics)*. Dover Publications, 1995. ISBN: 0486683567.

[36] Christoph Hahn. *Code Generation: Run MATLAB Code and Simulink Models Anywhere!* URL: https://blogs.mathworks.com/racing-lounge/2019/01/02/code-generation-online-tutorial/ (visited on 08/27/2020).

[37] J.P. Hespanha. *Linear Systems Theory*. Princeton University Press, 2009. ISBN: 9781400831890.

[38] Pavel Holoborodko. *Smooth noise-robust differentiators*. URL: http://www.holoborodko.com/pavel/numerical-methods/numerical-derivative/smooth-low-noise-differentiators/ (visited on 07/24/2020).

[39] Florian Holzapfel. *Lecture notes in Flight Control I*. 2015.

[40] Florian Holzapfel. *Lecture notes in Nonlinear and Adaptive Flight Control*. 2015.

[41] Florian Holzapfel. "Nichtlineare adaptive Regelung eines unbemannten Fluggerätes." PhD thesis. Munich, Germany: Technical University of Munich, 2014.

[42] IEEE. *IEEE Standard Specification Format Guide and Test Procedure for Single-Axis Laser Gyros*. Standard. Version 647-2006. New York, NY, 2006.

[43] P. Ioannou and B. Fidan. *Adaptive Control Tutorial*. Advances in Design and Control. Society for Industrial and Applied Mathematics (SIAM, 3600 Market Street, Floor 6, Philadelphia, PA 19104), 2006. ISBN: 9780898718652. URL: https://books.google.cz/books?id=wyBbyTnxpawC.

[44] P.A. Ioannou and J. Sun. *Robust Adaptive Control*. Dover Books on Electrical Engineering Series. Dover Publications, Incorporated, 2012. ISBN: 9780486498171.

[45] ISO. *Flight dynamics – Concepts, quantities and Symbols—Part 1: Aircraft motion relative to the air*. Standard. Version 1151-1:1988. Geneva, Switzerland, 1988.

[46] ISO. *Quantities and Units—Part 1: General*. Standard. Version 80000-1:2009. Geneva, Switzerland, 2009.

[47] ISO. *Quantities and Units—Part 2: Mathematical signs and symbols to be used in the natural sciences and technology*. Standard. Version 80000-2:2009. Geneva, Switzerland, 2009.

[48] ISO. *Standard Atmosphere*. Standard. Version 2533:1975. Geneva, Switzerland, 1975.

[49] Ravindra V. Jategaonkar. *Flight Vehicle System Identification (Progress in Astronautics and Aeronautics)*. American Institute of Aeronautics and Astronautics, 2006. ISBN: 1-56347-836-6.

[50] R. E. Kalman and R. S. Bucy. "New results in linear filtering and prediction theory." In: *TRANS. ASME, SER. D, J. BASIC ENG* (1961), p. 109.

[51] Vladislav Klein and Eugene A. Morelli. *Aircraft System Identification: Theory And Practice*. American Institute of Aeronautics and Astronautics, 2006. ISBN: 1-56347-832-3.

[52] M. E. Kügler and F. Holzapfel. "Autoland for a novel UAV as a state-machine-based extension to a modular automatic flight guidance and control system." In: (2017), pp. 2231–2236.

[53] Ajoy Kumar Kundu. *Aircraft Design (Cambridge Aerospace Series)*. Cambridge University Press, 2010. ISBN: 978-0-521-88516-4.

[54] H. Kwakernaak and R. Sivan. *Linear optimal control systems*. Wiley-Interscience publication. Wiley Interscience, 1972. ISBN: 9780471511106.

[55] P. de Larminat. *Analysis and Control of Linear Systems*. Wiley, 2007. ISBN: 9781905209354.

[56] J. LaSalle. "Some Extensions of Liapunov's Second Method." In: *IRE Transactions on Circuit Theory* 7.4 (1960), pp. 520–527.

[57] E. Lavretsky and K. Wise. *Robust and Adaptive Control: With Aerospace Applications*. Advanced Textbooks in Control and Signal Processing. Springer London, 2012. ISBN: 9781447143963.

[58] *Lawrence Sperry: Genius on Autopilot*. URL: https://www.historynet.com/lawrence-sperry-autopilot-inventor-and-aviation-innovator.htm (visited on 05/03/2020).

[59] Miguel Leitao, Florian Peter, and Florian Holzapfel. "Adaptive Augmentation of a Fighter Aircraft Autopilot Using a Nonlinear Reference Model." In: (Jan. 2013).

[60] Sadie P. Livingston and William Gracey. *Tables of Airspeed, Altitude, and Mach Number Based on Latest International Values for Atmospheric Properties and Physical Constants*. Technical Note. Version D-822. Langley Field, VA, 1961.

[61] L. Ljung. *System Identification: Theory for the User*. Prentice Hall information and system sciences series. Prentice Hall PTR, 1999. ISBN: 9780136566953.

[62] Lennart Ljung and Torsten Söderström. *Theory and practice of recursive identification*. Vol. 4. The MIT press series in signal processing, optimization, and control. MIT Press, 1983. ISBN: 0-262-12095-X.

[63] R. V. Monopoli. "Adaptive control for systems with hard saturation." In: *1975 IEEE Conference on Decision and Control including the 14th Symposium on Adaptive Processes*. 1975, pp. 841–843.

[64] K.S. Narendra and A.M. Annaswamy. *Stable Adaptive Systems*. Dover Books on Electrical Engineering. Dover Publications, 2012. ISBN: 9780486141428.

[65] NASA. *F-8C FBW*. URL: https://en.wikipedia.org/wiki/File:F-8C%5C_FBW.jpg (visited on 05/04/2020).

[66] NASA. *Fly by wire*. URL: https://en.wikipedia.org/wiki/File:Fly%5C_by%5C_wire.jpg (visited on 05/04/2020).

[67] Russel Naughton. *The Radioplane Target Drone*. URL: http://www.ctie.monash.edu.au/hargrave/rpav_radioplane4.html (visited on 08/31/2020).

[68] I. Newton, A. Motte, and J. Machin. *The Mathematical Principles of Natural Philosophy*. The Mathematical Principles of Natural Philosophy sv. 1. B. Motte, 1729.

[69] NIMA. *World Geodetic System 1984—Its Definition and Relationships with Local Geodetic Systems*. NIMA. Version TR8350.2. St. Louis, MO, 2000.

[70] J.P. Norton. *An Introduction to Identification*. Dover Books on Electrical Engineering Series. Dover Publications, 2009. ISBN: 9780486469355.

[71] W.F. Phillips. *Mechanics of Flight*. Engineering case studies online. Wiley, 2004. ISBN: 9780471334583.

[72] Lt. Col. Leslie Pratt. *MQ-9 Reaper UAV*. URL: https://commons.wikimedia.org/wiki/File:MQ-9_Reaper_UAV_(cropped).jpg (visited on 08/31/2020).

[73] J.R. Raol and J. Singh. *Flight Mechanics Modeling and Analysis*. Taylor & Francis, 2009. ISBN: 9781420067538.

[74] Robert M. Rogers. *Applied Mathematics in Integrated Navigation Systems, Third Edition (AIAA Education)*. American Institute of Aeronautics and Astronautics, 2007. ISBN: 1-56347-927-3.

[75] Jan Roskam. *Airplane Flight Dynamics and Automatic Flight Controls: Part 2*. Darcorporation, 2003. ISBN: 1-884885-18-7.

[76] SAE-International. *AS94900: General Specification For Aerospace - Flight Control Systems - Design, Installation and Test of Piloted Military Aircraft*. Tech. rep. 2007.

[77] J.P.L. Salle, J.P. LaSalle, and S. Lefschetz. *Stability by Liapunov's Direct Method: With Applications*. Mathematics in science and engineering : a series of monographs and textbooks. Academic Press, 1961.

[78] R.S. Sánchez-Peña and M. Sznaier. *Robust Systems Theory and Applications*. Adaptive and Cognitive Dynamic Systems: Signal Processing, Learning, Communications and Control. Wiley, 1998. ISBN: 9780471176275.

[79] Abraham. Savitzky and M. J. E. Golay. "Smoothing and Differentiation of Data by Simplified Least Squares Procedures." In: *Analytical Chemistry* 36.8 (1964), pp. 1627–1639. DOI: 10.1021/ac60214a047.

[80] Loyd Searle. "The Bombsight War: Norden vs Sperry." In: (1989).

[81] Athanasios Sideris and Raymond E. De Gaston. "Multivariable stability margin calculation with uncertain correlated parameters." In: *1986 25th IEEE Conference on Decision and Control* (1986), pp. 766–771.

[82] D. Siegel, Massachusetts Institute of Technology. Department of Aeronautics, and Astronautics. *Development of an Autoland System for General Aviation Aircraft*. Massachusetts Institute of Technology, Department of Aeronautics and Astronautics, 2012.

[83] Z. S. Spakovszky. *Thermodynamics and Propulsion: Performance of Propellers*. URL: https://web.mit.edu/16.unified/www/FALL/thermodynamics/notes/node86.html (visited on 07/01/2020).

[84] G. Stein and M. Athans. "The LQG/LTR procedure for multivariable feedback control design." In: *IEEE Transactions on Automatic Control* 32.2 (1987), pp. 105–114.

[85] R.F. Stengel. *Flight Dynamics*. Princeton University Press, 2015. ISBN: 9781400866816.

[86] Robert F. Stengel. *Stochastic Optimal Control: Theory and Application*. Wiley-Interscience, 1986. ISBN: 0-471-86462-5.

[87] Brian L. Stevens and Frank L. Lewis. *Aircraft Control and Simulation*. Wiley-Interscience, 2003. ISBN: 0-471-37145-9.

[88] Air Force Technology. *Predator RQ-1 / MQ-1 / MQ-9 Reaper UAV*. URL: https://www.airforce-technology.com/projects/predator-uav/ (visited on 08/31/2020).

[89] Ashish Tewari. *Atmospheric and Space Flight Dynamics: Modeling and Simulation with MATLAB® and Simulink® (Modeling and Simulation in Science, Engineering and Technology)*. Birkhäuser, 2007. ISBN: 0-8176-4373-7.

[90] *The amazing story of how the Airbus A320 became the Boeing 737's greatest rival*. URL: https://www.businessinsider.com/airbus-a320-history-boeing-737-rival-2018-9 (visited on 05/04/2020).

[91] J. Vande Vegte. *Feedback Control Systems*. Prentice-Hall international editions. Prentice-Hall, 1986. ISBN: 9780133129434.

[92] UAS Vision. *USAF Buys Four More Predator B's and Control Stations*. URL: https://www.uasvision.com/2019/03/26/usaf-buys-four-more-predator-bs-and-control-stations/ (visited on 08/31/2020).

[93] J. Vlk and P. Chudy. "Adaptive Augmentation of an Unmanned Aerial Vehicle's Flight Control System." In: *2018 IEEE/AIAA 37th Digital Avionics Systems Conference (DASC)*. 2018, pp. 1–9.

[94] J. Vlk and P. Chudy. "General aviation digital autopilot design based on LQR/LQG control strategy." In: *2017 IEEE/AIAA 36th Digital Avionics Systems Conference (DASC)*. 2017, pp. 1–9.

[95] J. Vlk, P. Chudy, and M. Prustomersky. "Light Sport Aircraft Auto-Land System." In: *2019 IEEE/AIAA 38th Digital Avionics Systems Conference (DASC)*. 2019, pp. 1–10.

[96] Kevin Wise and Eugene Lavretsky. "Asymptotic Properties of LQG/LTR Controllers in Flight Control Problems." In: Aug. 2012. ISBN: 978-1-60086-938-9. DOI: 10.2514/6.2012-4889.

[97] P. C. YOUNG and J. C. WILLEMS. "An approach to the linear multivariable servomechanism problem." In: *International Journal of Control* 15.5 (1972), pp. 961–979. DOI: 10.1080/00207177208932211.

COLOPHON

This document was typeset using the typographical look-and-feel `classicthesis` developed by André Miede. The style was inspired by Robert Bringhurst's seminal book on typography *"The Elements of Typographic Style"*. It is available for LaTeX via CTAN as `classicthesis`.